MAGNETOM Flash

Issue Number 76 · 1/2020
ISMRM Edition

siemens.com/magnetom-world

6-Minute Volumetric Whole Brain Exam Using Wave-CAIPI

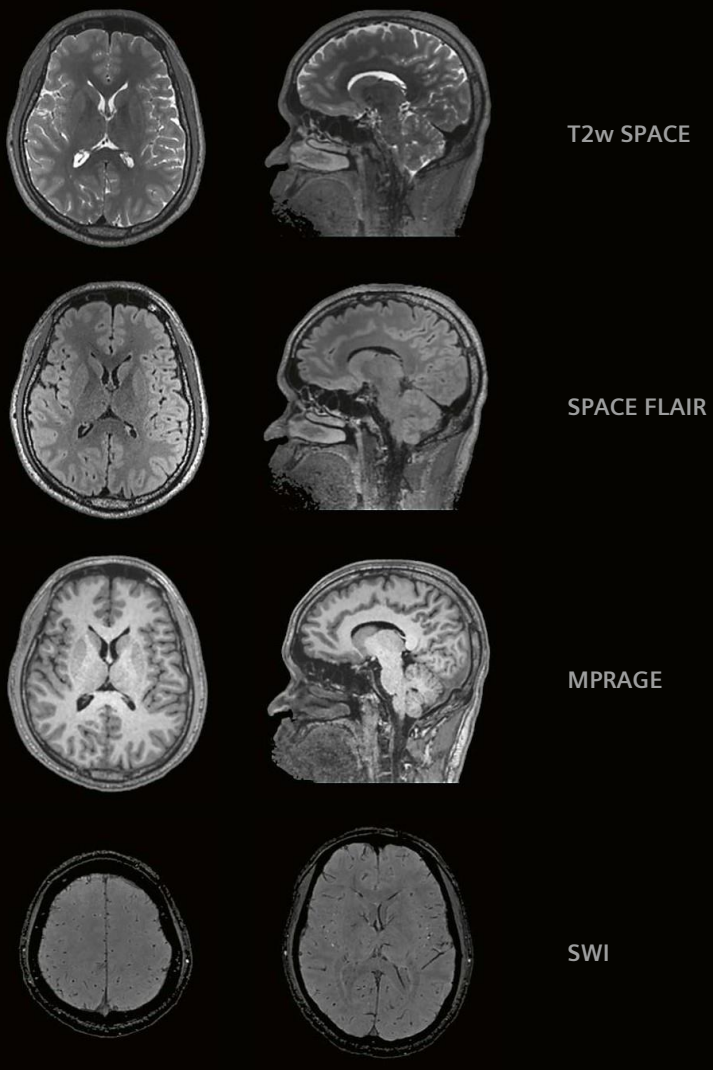

SIEMENS Healthineers

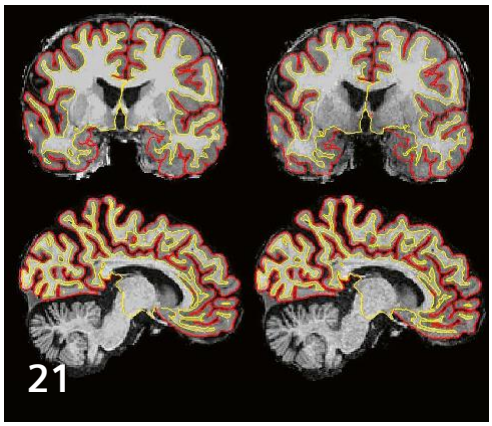

Clinical Evaluation of Wave-CAIPI

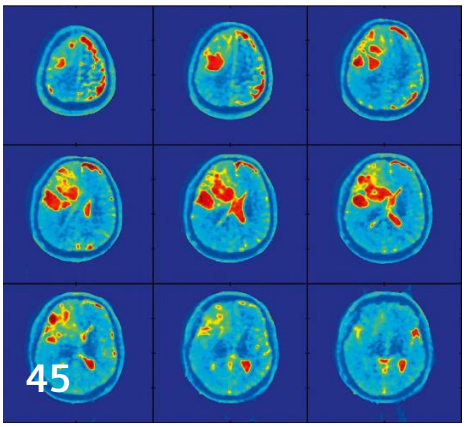

X-Nuclei MRI on a 7T MAGNETOM Terra

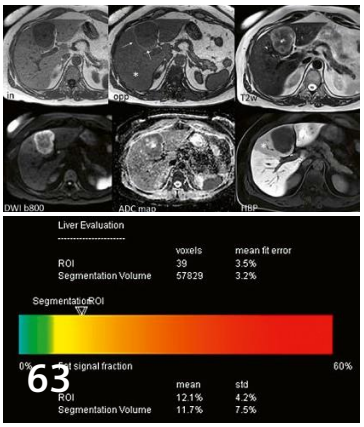

Liver Fat and Iron Quantification using LiverLab

Editorial Comment

Spotlight

Neurology

Musculoskeletal Imaging

Consistency in Prostate MRI Exams

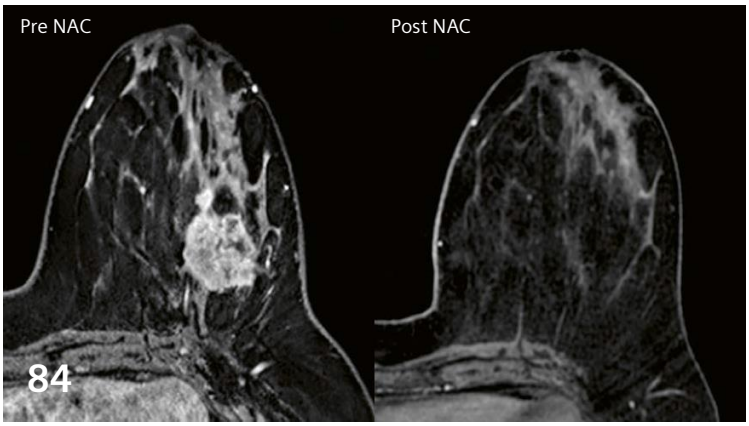

Assessing Breast Cancer Phenotypes with MRI Biomarkers

Abdominal Imaging

Oncological Imaging

Business

A History of Innovations

Meet Siemens Healthineers

Cover courtesy of Kawin Setsompop, Lawrence Wald, Berkin Bilgic, Stephen Cauley et al. (Martinos Center for Biomedical Imaging, Dept. of Radiology, Massachusetts General Hospital, Charlestown, MA, USA)

[1]*Work in progress: the application is currently under development and is not for sale in the U.S. and in other countries. Its future availability cannot be ensured.*

Univ. Prof. Dr. Siegfried Trattnig graduated from the University of Vienna Medical School in 1985. He trained in Radiology and subsequently served as Assistant Medical Director and Acting Medical Director for the Section of Neuroradiology in the Department of Radiology, Medical University of Vienna. He was appointed as an Associate Professor in Radiology 1993 becoming the Acting Medical Director at the Clinical Magnetic Resonance Institute at the University of Vienna. Since 2003 Prof. Trattnig has the position of the Medical Director of the Centre of Excellence in High-Field MR at the Medical University of Vienna. In 2010 he was appointed as a full Professor for Radiology with special focus on High field MR. Prof. Trattnig has pioneered the field of multi parametric or biochemical MR imaging of cartilage. He is currently the lead researcher on the clinical 7T & 3T projects at the Medical University in Vienna. Based on the results of clinical comparison studies between 3 and 7T his Center of Excellence for High Field MR was appointed as the international Reference Center for 7 Tesla by Siemens Healthcare, the leading vendor in the ultra-high-field MR. He is editorial board member of 8 scientific journals, is or was member of 35 committees and working groups within the ISMRM, ESR, ESMRMB and the ICRS among them he has been Executive Board member of the ESMRMB, member of the ESR Research Committee Board and Chairperson of the ESR European Imaging Biomarker Alliance (EIBALL) and Director of the School of MRI of the ESMRMB. He is an author of 532 articles in peer reviewed scientific journals and contributed to 25 scientific books. Additionally he has held 26 peer reviewed scientific grants with a total of funding money of 13.5 Mio €, received 12 scientific awards and is a reviewer for 35 scientific journals.

Exploring New Frontiers in MRI 7-Tesla MRI Goes Clinical – a Personal View

Dear readers and colleagues,

I have been asked to introduce this ISMRM edition of MAGNETOM Flash by taking a look to the future of MRI. The articles cover a range of aspects that reflect the latest developments. They also look at AI and the wide field of digitalization in healthcare – developments that no longer lie ahead, but are already happening. Winkel and colleagues, for instance, describe Prostate AI[1]. This end-to-end concept enables a standardized workflow with reproducible and fast data acquisition, optimized imaging sequences, and AI-powered data analysis. It includes automated detection, classification, and reporting of suspicious lesions in biparametric prostate MRI examinations. Elizabeth Morris's assessment of breast cancer phenotypes using MRI biomarkers in clinical practice shows how machine learning and radiomics are already influencing professionals and the patient experience. Other articles reflect how quantification has reached clinical routine: Frittoli and colleagues describe quantifying liver fat and iron using LiverLab, while Gregor Körzdörfer shares new developments in the success story of MR Fingerprinting[2]. With a focus on reaching underserved populations and using MRI in settings such as the emergency room, field strength might also be under discussion going forward. Salameh and Sarracanie address this topic in their article on re-envisioning low-field MRI. At the other end of the spectrum, ultra-high-field MRI is attracting increasing interest because of the improved clinical results it can deliver thanks to its morphological, functional, and metabolic capabilities.

Our High Field MR Centre (HFMRC) in Vienna is an interdisciplinary platform for methodological development and basic science research in the field of whole-body high-field MR (3 tesla and 7 tesla) with a clinically oriented approach. The flagship resource of the HFMRC is a 7T research system (Siemens Healthcare, Erlangen, Germany) with multinuclear capability and 8-channel parallel transmit. In addition, the centre houses two state-of-the-art 3T MRI scanners which are used for research.

Compared to other ultra-high-field installations, the HFMRC has the advantage of being located close to Vienna General Hospital, one of the largest university hospitals in Europe. This proximity makes it possible to combine method development with translational and clinically applied research.

[1]Work in progress: the application is currently under development and is not for sale in the U.S. and in other countries. Its future availability cannot be ensured.
[2]MR Fingerprinting is not commercially available in some countries. Due to regulatory reasons its future availability cannot be guaranteed. Please contact your local Siemens organization for further details.

In this particular field, not only may basic research be of interest, but also clinically oriented patient trials that demonstrate the clinical feasibility of nuclei other than protons and their clinical benefit as unique features of 7T.

When we started operating our 7T research system more than ten years ago, my group and I realized that, in contrast to many other 7T sites which were focused on hardware development, our strength at the Vienna site was clinically oriented research at 7T with large departments at Vienna General Hospital and many clinical experts in different fields.

Collaboration is key

Since I personally experienced the fast development of 3T from pure research scanners to commercially available routine scanners – the shift from 1.5T to 3T took only a few years – my vision as a radiologist for 7T was to see a similar transition from 3T to 7T. To make this crucial step, several elements were necessary. First, we needed excellent collaboration with the MR scanner vendor, Siemens Healthineers. This would enable us to develop and optimize routine clinical MR protocols for 7T which could use the additional signal-to-noise ratio for higher resolution protocols at 7T in the same scan time as 3T, with a consecutive benefit in morphological imaging. In a series of sequences, patient comparison studies in neuro and MSK routine imaging at both field strengths had to be performed to evaluate the diagnostic confidence at 3T and at 7T. In addition, and in parallel to these basic studies, unique features of 7T had to be demonstrated in clinical trials. Beyond morphological imaging, another strength of 7T is the X-nuclei option, i.e., the application of other nuclei such as sodium imaging, phosphorus spectroscopy, and carbon spectroscopy at 7T. In this particular field, not only may basic research be of interest, but also clinically oriented patient trials that demonstrate the clinical feasibility of nuclei other than protons and their clinical benefit as unique features of 7T.

My vision became reality when Siemens Healthineers made the strategically important decision to develop an ultra-high-field clinical MR scanner: the MAGNETOM Terra system. Our abovementioned comparison studies examined 40 patients with neurological disorders and 40 patients with knee pain using 11 sequences at 3T and at 7T. They clearly showed higher diagnostic confidence at 7T than 3T, and were very helpful in acquiring FDA approval and CE certification for the MAGNETOM Terra system in 2017 [1, 2].

Advanced therapy results

Our ultra-high-field clinical research has contributed to a variety of fields.

As the signal-to-noise ratio scales supralinearly with the field strength (B_0) of the scanner, the most obvious application at 7T is for obtaining higher spatial resolution in the brain, musculoskeletal system, and breast. When imaging the hippocampus, we could demonstrate that even subfields of the internal hippocampal anatomy and pathology can be visualized with excellent resolution, which provides a predictive marker for surgical outcome in patients with intractable temporal lobe epilepsy [3]. The dynamic and static blood oxygenation level-dependent contrast increases supralinearly with the field strength. This significantly improves the presurgical evaluation of eloquent areas before tumor removal, especially in critical cases where the tumor is very close to vital regions of the brain and high fMRI accuracy and spatial resolution are required [4]. Using susceptibility-weighted imaging, the plaque-vessel relationship and iron accumulation in multiple sclerosis plaques could be visualized for the first time. The detection rate of chronic MS lesions surrounded by iron rims is significantly higher at 7T than at 3T, and

Partners can attain optimal outcomes in research and translational medicine that will ultimately benefit the patient by improving diagnoses and enabling noninvasive monitoring of different treatment regimens.

their presence is associated with an increase in volume over several years, which corresponds to slowly expanding MS lesions [5]. This noninvasive follow-up of patients with slow-progressing MS is of great interest to the pharmaceutical industry for evaluating drug efficacy. High-resolution MR spectroscopic imaging has become feasible at 7T, which enables the additional mapping of pathological processes in MS on a biochemical level and reveals even well-delineated (sub)cortical MS lesions down to ~3 mm in regions that are inconspicuous on conventional MRI [6]. Regions of myo-inositol (mIns) were often larger than on FLAIR and NAA maps, suggesting that an increase in mIns may provide an earlier imaging biomarker for neuroinflammation or lesion development than with conventional MR. A further improvement is patch-based super-resolution (PBSR), an up-sampling method shown to work better than standard interpolation techniques for MRSI maps. PBSR uses imaging data to search for similar neighboring voxels during up-sampling for increased fidelity. The first application of PBSR to glioma measurements, reaching an in-plane-resolution of less than 1 mm, provided better resolution of tumor metabolism than ever before [7]. The article by Hyunsuk Shim in this issue of MAGNETOM Flash describes how to make MRSI standard in clinical imaging. *In vivo* detection of gamma-aminobutyric acid (GABA) and glutamate (Glu), both major neurotransmitters in the human brain, benefits from the higher sensitivity and SNR at 7T compared to lower field strengths [8].

Optimized clinical operations

In MR mammography, high spatial and temporal resolutions are feasible simultaneously at 7T, which improves breast cancer detection rates, allows better differentiation between benign and malignant breast lesions, and may help to avoid unnecessary breast biopsies [9]. Multinuclear clinical applications such as sodium imaging can help evaluate the quality of repair tissue after different cartilage repair therapies and can monitor maturation over time [10]. Again, large pharmaceutical companies are now interested in these methods for monitoring the efficacy of newly developed cartilage regeneration drugs, and are increasingly accepting imaging as a primary endpoint for their clinical trials. With 7T, it is possible to perform proof-of-method studies on a small scale, which if successful can then be transferred to 3T for trials with larger patient cohorts. Sodium imaging provides insight into the negative effects of a systemic disease like type 1 diabetes mellitus on joint structures such as tendons and cartilage, even in young DM1 patients [11]. Finally, we were also able to demonstrate and quantify drug side effects on the composition of musculoskeletal structures, such as tendon weakening which may result in tendinosis and tears quantified by sodium imaging [12]. At 7T, ^{31}P spectroscopy can help to noninvasively differentiate between non-alcoholic benign liver disease and potentially progressive steatohepatitis; this was previously only possible with an invasive liver biopsy [13]. The article by Armin Nagel and colleagues describes his first experiences with X-nuclei on the clinical 7T MAGNETOM Terra system.

These results can only be achieved by close collaboration between the academic institution and the MR vendor. Both partners must have a clear vision, be prepared to take risks in a newly developing field, and be willing to join forces and share resources. In doing so, the partners can attain optimal outcomes in research and translational medicine that will ultimately benefit the patient by improving diagnoses and enabling non-invasive monitoring of different treatment regimens.

I hope you enjoy reading this issue and exploring the various aspects of precision medicine, healthcare delivery, and improved patient experience presented in the articles.

Siegfried Trattnig

References

1 Springer E, Dymerska B, Cardoso PL, et al. Comparison of Routine Brain Imaging at 3 T and 7 T. Invest Radiol. 2016; 51(8):469–82.
2 Springer E, Bohndorf K, Juras V, et al. Comparison of Routine Knee Magnetic Resonance Imaging at 3T and 7T. Invest Radiol. 2017; 52(1):42–54.
3 Stefanits H, Springer E, Pataraia E, et al. Seven-Tesla MRI of Hippocampal Sclerosis: An In Vivo Feasibility Study With Histological Correlations. Invest Radiol. 2017; 52(11):666–671.
4 Beisteiner R, Robinson S, Wurnig M, et al. Clinical fMRI: evidence for a 7T benefit over 3T. Neuroimage. 2011; 57(3):1015–21.
5 Dal-Bianco A, Grabner G, Kronnerwetter C, et al. Slow expansion of multiple sclerosis iron rim lesions: pathology and 7 T magnetic resonance imaging. Acta Neuropathol. 2017; 133(1):25–42.
6 Hangel G, Jain S, Springer E, et al. High-resolution metabolic mapping of gliomas via patch-based super-resolution magnetic resonance spectroscopic imaging at 7T. Neuroimage. 2019; 191:587–595.
7 Heckova E, Strasser B, Hangel GJ, et al. 7 T Magnetic Resonance Spectroscopic Imaging in Multiple Sclerosis: How Does Spatial Resolution Affect the Detectability of Metabolic Changes in Brain Lesions? Invest Radiol. 2019; 54(4):247–254.
8 Moser P, Hingerl L, Strasser B, et al. Whole-slice mapping of GABA and GABA+ at 7T via adiabatic MEGA-editing, real-time instability correction, and concentric circle readout. Neuroimage. 2019; 184:475–489.
9 Pinker K, Baltzer P, Bogner W, et al. Multiparametric MR Imaging with High-Resolution Dynamic Contrast-enhanced and Diffusion-weighted Imaging at 7 T Improves the Assessment of Breast Tumors: A Feasibility Study. Radiology. 2015; 276(2):360–70.
10 Trattnig S, Welsch GH, Juras V, et al. 23Na MR Imaging at 7T after Knee Matrix-associated Autologous Chondrocyte Transplantation Preliminary Results. Radiology. 2010; 257:175–84.
11 Marik W, Nemec SF, Zbýň Š, et al. Changes in Cartilage and Tendon Composition of Patients With Type I Diabetes Mellitus: Identification by Quantitative Sodium Magnetic Resonance Imaging at 7 T. Invest Radiol. 2016; 51(4):266–72.
12 Juras V, Winhofer Y, Szomolanyi P, et al. Multiparametric MR Imaging Depicts Glycosaminoglycan Change in the Achilles Tendon during Ciprofloxacin Administration in Healthy Men: Initial Observation. Radiology. 2015; 275(3):763–71.
13 Traussnigg S, Kienbacher C, Gajdošík M, et al. Ultra-high-field magnetic resonance spectroscopy in non-alcoholic fatty liver disease: Novel mechanistic and diagnostic insights of energy metabolism in non-alcoholic steatohepatitis and advanced fibrosis. Liver Int. 2017; 37(10):1544–1553.

We appreciate your comments.
Please contact us at magnetomworld.team@siemens-healthineers.com

Editorial Board

Review Board

Re-Envisioning Low-Field MRI

Najat Salameh, Ph.D. and Mathieu Sarracanie, Ph.D.

Center for Adaptable MRI Technology, Department of Biomedical Engineering, University of Basel, Switzerland

The Center for Adaptable MRI Technology (AMT) aims to develop disruptive MRI technology to push the boundaries of diagnosis and monitoring in environments and settings usually out of reach. This task faces at least two major challenges.

The first concerns scaling down and opening up the MRI device. One way to achieve this is to leverage magnetic field strengths at lower orders of magnitude than today's MRI devices, which are particularly heavy and expensive, have extreme siting requirements and high costs, and offer limited access for patients.

The second concerns enhancing the flexibility of MRI. The AMT Center aims to develop methods and instruments that perform in heterogeneous environments and compensate for the impeded signal sensitivity naturally available at lower magnetic fields.

The AMT center's research focuses on four different areas:

1. **Tools and methods for low-field MRI:** With a unique platform including multiple scanners operating at variable fields, this area focuses on developing new MR sequences and detectors for specific applications.
2. **Image-guided therapies:** Research in this area involves the development of MRI sequences and instruments compatible with therapeutic settings/devices.
3. **Quantitative and functional MRI:** These techniques will provide quantified metrics of organ function.
4. **Fast multiparametric MRI:** The aim here is to accelerate quantitative diagnosis.

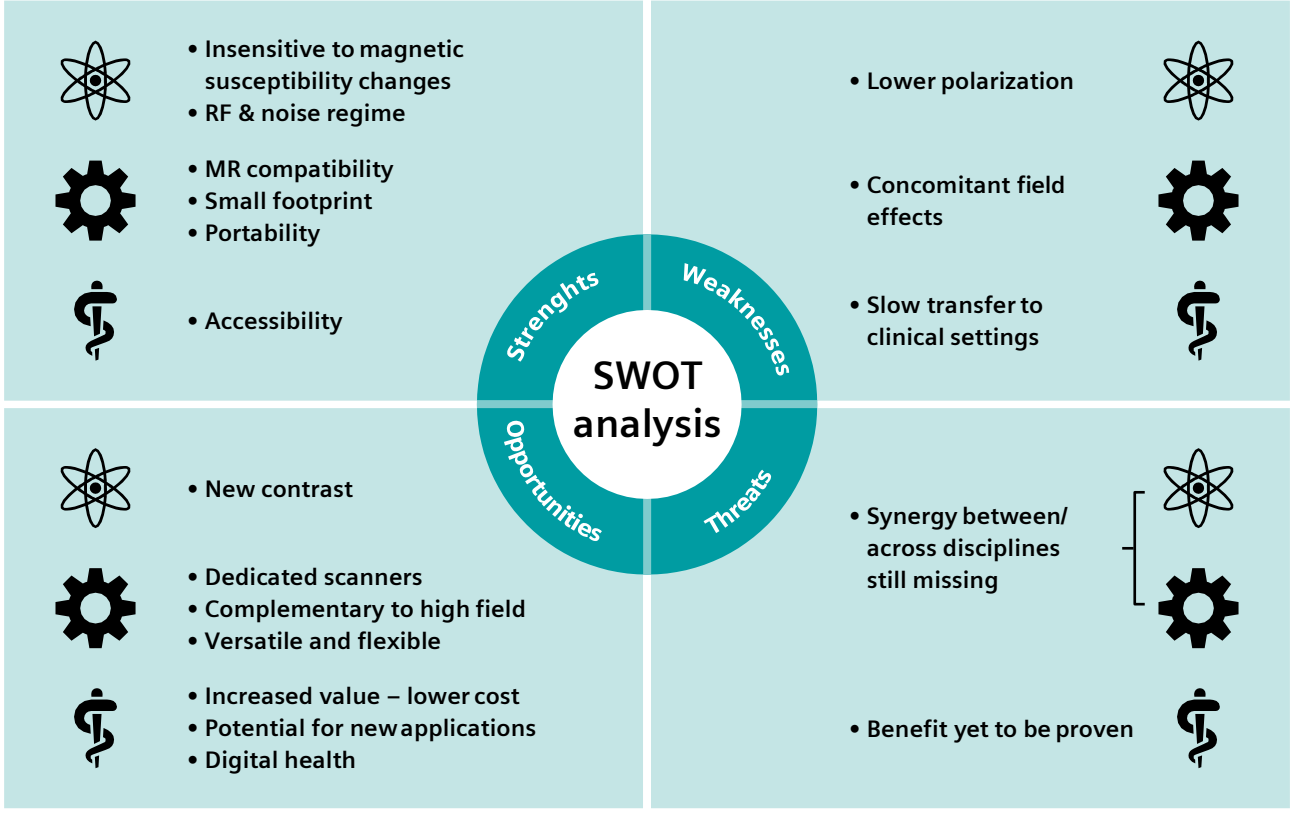

1 SWOT analysis of low-field MRI.

MRI has without doubt revolutionized medical imaging. In addition to delivering anatomical images with incomparable soft-tissue contrast, it also enables quantification of metabolic processes and of physiological and mechanical properties in a completely non-invasive and non-ionizing manner. In the late 1990s, the progress made in sequence development, hardware, and computing capabilities even led users to believe that MRI might ultimately replace all other imaging and diagnostic modalities [1].

This did not happen, however, for a number of reasons: The signal in conventional MR techniques comes from the spin polarization of hydrogen nuclei present in the body, and the Boltzmann law defines the total magnetic moment usable for nuclear magnetic resonance (NMR). Despite a high natural abundance and gyromagnetic ratio of ^{1}H nuclei, the sensitivity in NMR is known to be low, particularly when compared to other imaging modalities. In addition, spatial encoding is a necessity, as direct imaging with electromagnetic wavelengths much larger than the human body and individual body parts is not allowed, making MRI a rather slow technique.

Other reasons why MRI has stalled with regards to certain applications include the very important fact that, in parallel to developments in MRI, major technological progress has also been achieved in most other imaging modalities. In addition, MRI scanners as we know them today have mostly remained one-size-fits-all devices, confined to use in radiology departments and within specific and restricted environments. While many clinicians' needs (including those outside of radiology) and potential patient benefits have therefore been overlooked in MRI over the years, they have been addressed, at least partially, using ultrasound or X-ray devices across a large spectrum of applications. The reasons why MRI has not embraced such paradigm shifts are diverse. They are most likely financial and cultural, and certainly not limited to constraints of technical feasibility. We will try to describe why the MRI paradigm could now be at a turning point and why re-envisioning low-field MRI could play a role in the changes to come.

The right time

The advantages of low-field MRI have been highlighted multiple times in recent decades, but the technique has never succeeded in spreading to clinical settings. Recent work in the field shows that the MRI community is entering another of these cycles, and one may wonder why this new decade should be more favorable for a breakthrough in low-field MRI. We see two main reasons for this to be the case. The first is based on technological progress and developments made in the last 40 years, not only with respect to magnetics, but also concerning power electronics, RF detection, sequence programming, and image processing. Altogether, these developments have proven that magnetic field alone is not the key to good quality images. This is easily visible if one compares the first images acquired at 1.5T in the 1980s with today's routine scans. Another factor that could encourage the deployment of low-field MRI today is the increased awareness that one-size-fits-all scanners cannot help in all circumstances. As an example, many groups are now developing mobile, point-of-care solutions [2–6] that leverage low-field technology. These groups include teams that earned their reputation from their work at ultra-high magnetic fields. This recent trend may indicate that low-field MRI should no longer be considered a niche.

More concretely, time is also crucial in MRI when it comes to the signal-to-noise ratio (SNR). Since the early days of MRI, engineers and physicists have pushed high-field MRI because it provides higher polarization and higher spectral dispersion, which respectively enable higher SNR per unit time and advanced spectroscopy measurements. In the past, basic imaging sequences were used, but they were obviously not as time efficient as today's standards. Over the years, researchers and scientists have developed advanced acquisition schemes that are routinely used today and have improved the image quality in terms of sharpness, contrast, and also speed. It is rather challenging to directly compare past and current performance based on the heterogeneous information available in the literature. If, however, we (very roughly) assume equivalent SNR and contrast-to-noise ratio, one could compare the SNR per unit time and volume of T2-weighted images acquired in the human brain in 1986 [7]. The outcome yields an acceleration factor superior to 7 for an equivalent voxel size. Wald recently highlighted the various revolutions, beyond the magnetic field, that have occurred in MRI [8]. When combined with lower magnetic field strengths, these revolutions would certainly democratize MRI and make it as versatile as other established modalities (e.g., ultrasound or X-ray technologies). After 40 years of development, it is now becoming clear that the quest for ever-higher field strengths is weakening, leaving room to also explore the physics of low- to ultra-low-field MRI.

The right tool

High-field MRI has transformed the medical imaging landscape, producing images with high soft-tissue contrast in reasonable acquisition times. Beyond simple images, MRI has ventured into a broad range of areas, from time-resolved 3D imaging of moving body parts to imaging of cerebral function, flow and motion, and even temperature changes within interventional settings. This progress is unfortunately restricted to cases that are compatible with conventional MR environments, and access is limited

to applications that can be physically bound to radiology suites. Immense efforts have been invested in developing MR-compatible devices and surgical instruments that continue to broaden the range of envisioned applications within MRI facilities. However, they also raise the overall cost of an MRI examination. This ultimately affects accessibility from a financial perspective, and therefore makes MRI an even more exclusive modality.

It is known that lowering magnetic field strength is a path to relaxing both engineering and siting requirements for MRI scanners. It also comes with many extra benefits, such as a smaller footprint and lower power consumption, fewer magnetic susceptibility issues, and increased compatibility within a variety of environments. However, lowering the magnetic field naturally leads to lower nuclear spin polarization and therefore reduces SNR per unit time, raising questions about low-field capabilities and opening debates about what would define the most relevant field strengths in clinical settings. The latter point is worth commenting on, as this type of debate only exists in the MRI community. X-ray and ultrasound have already been successfully adapted to fit different applications, while technological progress in MRI (for the most part) continues to revolve around the same 30-year-old geometry that fits all body parts and sits in a complex shielded environment. Over the years, scientists have explored NMR at different magnetic field strengths, yet these have almost exclusively been higher-field regimes, up to what are now commonly called the ultra-high fields (7T and higher). Beyond sensitivity and potential achievable resolution, the main advantages offered by these regimes mostly relate to metabolic imaging and susceptibility mapping. Surprisingly, the discussion about field strength at the other end of the spectrum has never really been fueled, and is often reduced to practical considerations. In most minds today, low-field MRI is restricted to mid-field MRI (from 0.25 to 1.0T); these open geometries are mainly justified for obese and claustrophobic patients, or to guide biopsies. This is a valid approach, but possibly not disruptive enough for real breakthroughs. Indeed, such field strengths are still too high to harness the real advantages of low-field MRI, and siting requirements (in particular for permanent magnet designs) are still the same as for high-field scanners. The next section will set out the pros and cons of low-field MRI, and describe how it can complement conventional MRI.

Low-field MRI under the microscope

A simple way to illustrate and discuss the potential development of low-magnetic-field MRI is using a SWOT analysis. A summary is presented in Figure 1, and the different aspects are discussed below.

Strengths

Physics

Using lower field strengths has the obvious advantage of reducing MR-compatibility issues and susceptibility artifacts. Images are no longer prone to chemical shift artifacts, imaging can be performed near implants, and MR-guided procedures become possible. Contrast is also a key feature in low-field MRI and will play a major role in how fast the technique is adopted in clinical settings. It is well known from the early days of MRI that lower field strengths offer a wider dispersion in T1 relaxation times [9] and have the potential to reveal endogenous contrasts that are relevant for very specific applications. As low-field MRI has quickly been abandoned in the past, this area of research is still rather untouched and deserves to be explored. Recent work from Broche and colleagues supports this fact and shows different T1 behaviors during Fast Field-Cycling (FFC) experiments applied to different human body parts *in vivo* [10]. Another major advantage concerns noise domination in different frequency regimes [11]. Sample noise dominates at high field and can be neglected at low field, meaning that the noise level can be favorably influenced by adequately designing and building the different elements of the acquisition chain. Finally, specific absorption rate (SAR) is not an issue in low-frequency regimes.

Engineering

Magnetic field strength is what currently drives the cost of MRI machines. Reducing field strength has a direct impact on cost, as it enables technological solutions in magnet construction that no longer require superconductive technologies and cryogenics. New magnet geometries could be designed (moving away from the current one-size-fits-all design) and MRI technologies could be adapted to dedicated applications. Finally, shielding will not be as demanding as it is today, enabling multiple scanners with smaller footprints to be deployed in a given area [12, 13].

Weaknesses

Physics and engineering

As already mentioned, the major limitation of low-field MRI is that its nuclear polarization is intrinsically lower than conventional MR, which naturally leads to lower SNR per unit time if embraced in the same way as for high-field MRI. Another weakness is the maximum magnetic field gradient strength achievable at a given static main magnetic field, B_0. If gradient strength cannot be increased to achieve finer spatial resolutions because of concomitant field effects, time is the only way of achieving smaller voxel sizes, and this will negatively impact total acquisition times. However, this can also be seen as an opportunity to develop research into these types of regime.

Medicine

As mentioned in the Strengths section, contrast could be a game changer at low field. This added benefit opens up new perspectives, but it also requires radiologists to adapt their skills for interpreting images according to the field strength. Perhaps other practitioners will also have to develop basic skills for reading images, if the goal is to decongest radiology departments using point-of-care units. Multisite studies will be needed to fine-tune the learning process, and this step will inevitably slow down the transfer of technology to clinical routine. It goes without saying that the technology will also need to prove useful in order to attract physicians' interest and maximize their learning curve.

Opportunities

Physics, engineering, and computing

MRI has made many technological leaps forward since it was first introduced in the 1970s, and images produced almost 30 years ago at 1.5T look very different than those obtained today. Low-field MRI can benefit from all these technological advances, as illustrated in two recent papers: Sarracanie et al. performed a six-minute 3D scan of the human brain *in vivo* at 6.5mT using time-efficient b-SSFP sequences and custom-built low-frequency RF resonators [6] (see Figure 2A). In a 2019 publication in Radiology, Campbell and colleagues showed very promising images of different body parts using a mid-field scanner operating at 0.55T[1]. The authors employed a commercial 1.5T scanner with a ramped-down field, existing RF coils simply detuned to the corresponding Larmor frequency, and state-of-the-art MR sequences [14] (c.f. Figure 2B). These recent works show that, rather than being considered as a niche, low-field MRI should perhaps now be viewed as a serious contender in the field of medical imaging.

Applications

Various applications have been described in the past [15]. We will focus only on recent research efforts. Portable and point-of-care devices appear to offer the most promising benefits when considering low magnetic field strengths.

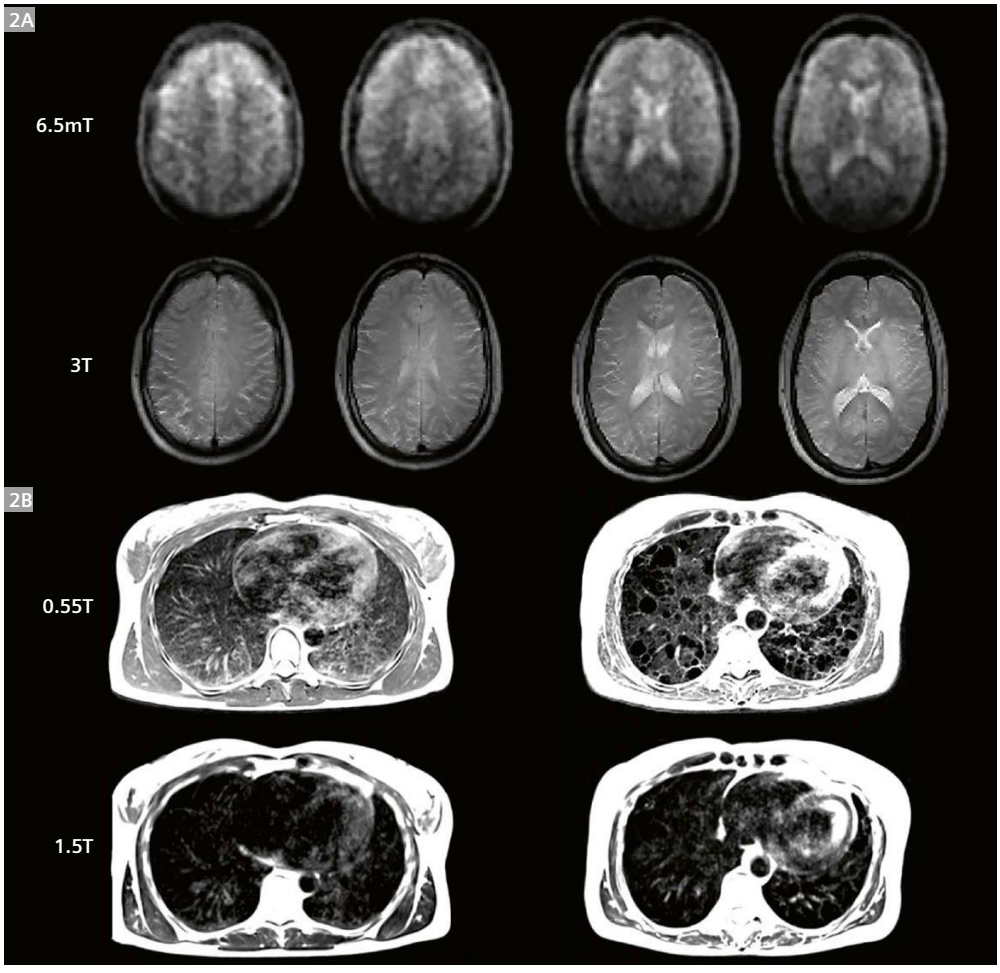

2 Images acquired recently at lower field strengths: **(2A)** Brain images from Sarracanie et al., acquired in the same volunteer at 6.5mT (upper row) and 3T (bottom row) [6]; **(2B)** T2-weighted lung images acquired at 0.55T and 1.5T in a healthy control (left) and in a patient with lymphangioleiomyomatosis (right) [14]. *(2A) Images modified from [6], head under Creative Commons license CC-BY 4.0; (2B) images modified with permission from [14].*

[1] *Work in progress: the application is currently under development and is not for sale in the U.S. and in other countries. Its future availability cannot be ensured.*

Publications on this topic, as well as new sessions at international conferences, are good indicators of this current trend [2–6, 16–18]. Interventional MR, and lung and multimodal imaging are also relevant applications, as low-field techniques lower the MR-compatibility hurdle and reduce magnetic susceptibility artifacts [14, 19–24]. The risk-benefit balance is another key criterion guiding the use of imaging modalities, and while MRI is considered very safe, it is usually not indicated in patients with implanted cardiac devices, or in pregnant women and neonates. Lower magnetic field strength, with its intrinsic SAR reduction, could prove extremely useful for these patients and improve their outcomes. Finally, future directions will be defined along the way, as new contrast might reveal key applications for low-field MRI. Even considering that scientists cannot currently reach spatial resolutions equivalent to those of conventional scanners, we already have indications that low-field MRI could provide high-sensitivity, high-specificity diagnoses in patients with cancer, stroke, osteoarthritis, or edema [10]. Has the spatial resolution of nuclear medicine ever been discussed for cancer diagnosis? This is a path worth exploring.

Value

Value in MR has attracted interest recently and is being discussed by all parties, including academics, clinicians, radiologists, and MRI vendors. The topic was discussed during a three-day ISMRM workshop in 2019. It was addressed from different angles with a focus on exploring opportunities to increase value in MRI, with value defined as the ratio of outcome to cost. Cost is probably the main barrier, as MRI machines are usually worth about €1 million per tesla. As a result, MR examinations have been shortened drastically so that more patients can be scanned per day, leading to an increase in burnout cases among radiologists and technologists [25]. Surprisingly, examination time was the first aspect to be adjusted in order to reduce cost. This completely overlooked the fact that, for a given scanning protocol, variability exists that is caused by human, not technical, factors [26]. What if this paradigm were to change and the direct cost of MRI scanners was reduced instead of examination time? Staff would be under less pressure, more time would be allocated per patient, and/or more personnel could be hired. Again, one way to decrease the cost of an MRI scanner is to lower the magnetic field strength – not only for permanent magnets but also for resistive or hybrid technologies – to avoid dealing with heavy equipment that requires special handling and siting. In addition to reducing costs, lowering field strength is also relevant because it enables siting in areas with restricted space [12, 13], making MRI more accessible in highly populated regions. Market trends alone indicate a clear need for this technology, as mid-field scanners represent about 50% of sales in Asia [27], against 6% in Europe and North America [28]. The added value of ubiquitous MRI could also play an important role in the new realm of digital health, producing truly big data and channeling artificial intelligence. Ultimately, true value would stem from MRI becoming available in places where it is currently not an option.

Threats

History shows that the major threat regarding low-field MRI is the lack of added outcome to increase the overall value of the technique. Lowering cost is clearly crucial, but it is not enough to convince clinicians and governments to use different tools if the benefit for the patient does not increase significantly. Various past attempts have shown a high potential for creativity and originality in MRI developments, especially in magnet design. However, the images often had low SNR and took an extremely long time to produce. The technology now seems able to circumvent such limitations. The capacity to secure better outcomes at low field will also come from a general willingness to pool skills and expertise across various fields, from combining state-of-the-art MR sequences with the best RF detectors and magnet design, and from advanced computing resources. Only then will low-field MRI achieve its breakthrough.

Conclusion

Many indicators show that MRI is ready to undergo a transition. In the near future, we anticipate that there will no longer be one type (or just a few types) of MRI, but rather a range of systems that can serve a variety of applications and needs. Since its invention, MRI has made tremendous technological and methodological progress, delivering highly valuable images that provide anatomical, functional, and metabolic information. Yet this information is available in restricted areas only, either due to affordability or logistics, since MRI is expensive and highly demanding in terms of siting and compatibility. The original landscape has already started to evolve, and economically powerful actors are showing that alternative models are possible, with lower-field MRI already earning large market shares. MRI must become more accessible, widespread, and versatile in order to benefit patients as much as possible. The need for low-cost, high-performance low-field MRI is clear, and it is only a matter of time before new technologies become available.

References

1 Kaufman L. The impact of Radiology's culture on the cost of Magnetic Resonance Imaging. J Magn Reson Imaging. 1996; 6(1):67–71.
2 Cooley CZ, Stockmann JP, Armstrong BD, et al. Two-dimensional imaging in a lightweight portable MRI scanner without gradient coils. Magn Reson Med. 2015; 73(2):872–83.
3 O'Reilly T, Teeuwisse WM, Webb AG. Three-dimensional MRI in a homogenous 27 cm diameter bore Halbach array magnet. J Magn Reson. 2019; 307:106578.
4 McDaniel PC, Cooley CZ, Stockmann JP, Wald LL. The MR Cap: A single-sided MRI system designed for potential point-of-care limited field-of-view brain imaging. Magn Reson Med. 2019; 82(5):1946–1960.
5 Nakagomi M, Kajiwara M, Matsuzaki J, et al. Development of a small car-mounted magnetic resonance imaging system for human elbows using a 0.2 T permanent magnet. J Magn Reson. 2019; 304:1–6.
6 Sarracanie M, LaPierre CD, Salameh N, et al. Low-Cost High-Performance MRI. Sci Rep. 2015; 5:15177.
7 Zimmerman RA, Bilaniuk LT, Hackney DB, et al. Head injury: early results of comparing CT and high-field MR. AJR Am J Roentgenol. 1986; 147(6):1215–22.
8 Wald LL. Ultimate MRI. J Magn Reson. 2019; 306:139–144.
9 Fischer HW, Rinck PA, Van Haverbeke Y, et al. Nuclear relaxation of human brain gray and white matter: analysis of field dependence and implications for MRI. Magn Reson Med. 1990; 16(2):317–34.
10 Broche LM, Ross PJ, Davies GR, et al. A whole-body Fast Field-Cycling scanner for clinical molecular imaging studies. Sci Rep. 2019; 9(1):10402.
11 Darrasse L, Ginefri JC. Perspectives with cryogenic RF probes in biomedical MRI. Biochimie. 2003; 85(9):915–37.
12 Salameh N, Sarracanie M. Low magnetic field MRI. ISMRM Workshop on MR Value. 2019.
13 Salameh N, Sarracanie M. Low magnetic field MR imaging. Magn Reson Mater Phy. 2019; 32:S79.
14 Campbell-Washburn AE, Ramasawmy R, Restivo MC, et al. Opportunities in Interventional and Diagnostic Imaging by Using High-Performance Low-Field-Strength MRI. Radiology. 2019; 293(2):384–393.
15 Klein HM. Clinical Low Field Strength Magnetic Resonance Imaging. Basel: Springer International Publishing; 2016.
16 McDaniel PC, Cooley CZ, Stockmann JP, Wald LL. A target-field shimming approach for improving the encoding performance of a lightweight Halbach magnet for portable brain MRI. Proc Intl Soc Mag Reson Med. Montreal. 2019.
17 Wald LL, McDaniel PC, Witzel T, et al. Low-cost and portable MRI. J Magn Reson Imaging. 2019; 4:31.
18 Lother S, Schiff SJ, Neuberger T, et al. Design of a mobile, homogeneous, and efficient electromagnet with a large field of view for neonatal low-field MRI. Magn Reson Mater Phy. 2016; 29(4):691–8.
19 Arbogast-Ravier S, Gangi A, Choquet P, et al. An in vitro study at low field for MR guidance of a biopsy needle. Magn Reson Imaging. 1995; 13(2):321–4.
20 Goetz C, Breton E, Choquet P, et al. SPECT low-field MRI system for small-animal imaging. J Nucl Med. 2008; 49(1):88–93.
21 Senft C, Ulrich CT, Seifert V, et al. Intraoperative magnetic resonance imaging in the surgical treatment of cerebral metastases. J Surg Oncol. 2010; 101(5):436–41.
22 Senft C, Seifert V, Hermann E, et al. Surgical treatment of cerebral abscess with the use of a mobile ultralow-field MRI. Neurosurg Rev. 2009; 32(1):77–85.
23 Iturri-Clavero F, Galbarriatu-Gutierrez L, Gonzalez-Uriarte A, et al. "Low-field" intraoperative MRI: a new scenario, a new adaptation. Clin Radiol. 2016; 71(11):1193–8.
24 Klüter S. Technical design and concept of a 0.35 T MR-Linac. Clin Transl Radiat Oncol. 2019; 18:98–101.
25 Harolds JA, Parikh JR, Bluth EI, et al. Burnout of Radiologists: Frequency, Risk Factors, and Remedies: A Report of the ACR Commission on Human Resources. J Am Coll Radiol. 2016; 13(4):411–16.
26 Avey GD, Belden DS, Zea RD, et al. Factors predicting the time-length variability of identically protocoled MRI exams. J Magn Reson Imaging. 2019; 49(7):e265–e270.
27 Rinck PA. MR Imaging: Quo Vadis? Rinckside. 2019; 30(3):5–8.
28 Moser E, Laistler E, Schmitt F, et al. Ultra-High Field NMR and MRI—The Role of Magnet Technology to Increase Sensitivity and Specificity. Front Phys. 2017; 5:33.

Contact

Professor Najat Salameh
Center for Adaptable MRI Technology
Department of Biomedical Engineering
University of Basel
Gewerbestrasse 14
4123 Allschwil
Switzerland
Tel.: +41 61 207 54 52
najat.salameh@unibas.ch

Professor Mathieu Sarracanie
Center for Adaptable MRI Technology
Department of Biomedical Engineering
University of Basel
Gewerbestrasse 14
4123 Allschwil
Switzerland
Tel.: +41 61 207 54 53
mathieu.sarracanie@unibas.ch

GOBrain in Acute Neurological Emergencies: Diagnostic Accuracy and Impact on Patient Management

Philipp M. Kazmierczak, M.D.[1]; Max Dührsen, MS[1]; Robert Forbrig, M.D.[2]; Maximilian Patzig, M.D.[2]; Matthias Klein, M.D.[3]; Andreas Pomschar, M.D.[4]; Wolfgang G. Kunz, M.D.[1]; Daniel Puhr-Westerheide, M.D.[1]; Jens Ricke, M.D.[1]; Olga Solyanik, M.D.[1]*; Clemens C. Cyran, M.D.[1,4]*

***Olga Solyanik and Clemens C. Cyran contributed equally and share last authorship.**

[1]Klinik und Poliklinik für Radiologie, Klinikum der Universität München, Germany
[2]Institut für Neuroradiologie, Klinikum der Universität München, Germany
[3]Neurologische Klinik und Poliklinik, Klinikum der Universität München, Germany
[4]DIE RADIOLOGIE, München, Germany

Introduction

Even though computed tomography (CT) of the head is the primary imaging modality used in the majority of institutions to rule out intracranial pathologies in acute neurological emergencies, magnetic resonance imaging (MRI) remains the imaging reference standard for the detection and differential diagnosis of intracranial lesions. However, the use of MRI in the acute setting is still limited by long acquisition times for multi-sequence protocols. This drawback may now be overcome by a novel ultra-fast brain MRI protocol, which allows for the acquisition of five standard sequences in just 04:33 min (GOBrain, Siemens Healthcare, Erlangen, Germany, optimized for use in our institution, including sagittal T1-weighted gradient echo (GRE), axial T2-weighted turbo spin echo (TSE), axial T2-weighted TSE fluid-attenuated inversion recovery (FLAIR), axial diffusion-weighted (DWI) single-shot echo-planar imaging (EPI), axial T2*-weighted EPI-GRE). To validate the GOBrain protocol for use in the emergency setting, we hypothesized that

a. image quality and diagnostic performance of GOBrain for the detection of intracranial pathologies are non-inferior to the standard-length brain MRI protocol,
b. GOBrain leads to a change in patient management compared to CT alone.

Sequences		Image Quality						GWM Differentiation			
		Scores						Scores			
		1	2	3	4	5	Median	0	1	2	Median
T1-weighted	Conventional	0	0	1	58	0	4	0	6	53	2
	GOBrain	0	0	0	59	0	4	0	7	52	2
T2-weighted	Conventional	0	0	3	54	2	4	0	34	25	1
	GOBrain	0	0	2	57	0	4	0	39	20	1
FLAIR	Conventional	0	0	2	56	1	4	0	32	27	1
	GOBrain	0	0	1	58	0	4	0	31	28	1
DWI	Conventional	0	0	0	59	0	4	NA	NA	NA	NA
	GOBrain	0	0	0	59	0	4	NA	NA	NA	NA
T2*	Conventional	0	0	6	53	0	4	NA	NA	NA	NA
	GOBrain	0	2	56	1	0	3	NA	NA	NA	NA

Table 1: Image quality assessments (consensus reading). NA = not applicable; GWM = gray-white matter.

Materials and methods

A total of 449 consecutive patients presenting to our emergency department with acute non-traumatic neurological symptoms were evaluated [1]. Of these, 238 patients underwent a head CT scan to exclude an intracranial pathology. In case of a negative head CT scan, patients were included in this prospective single-center trial and were transferred to the 3T MRI suite (MAGNETOM Skyra, Siemens Healthcare, Erlangen, Germany). A total of 60 patients (30 female, 30 male; mean age 61 years) were successfully included. The MRI examinations were performed using a 20-channel receiver head coil.
Two brain MRI protocols (GOBrain and a standard-length protocol serving as reference standard) including the following five non-contrast standard sequences were acquired in randomized order:

1. **Sagittal T1-weighted GRE**
   (GOBrain 00:41 min; standard-length: 01:34 min)
2. **Axial T2-weighted TSE**
   (GOBrain 01:02 min; standard-length: 03:45 min)
3. **Axial T2-weighted TSE FLAIR**
   (GOBrain 01:52 min; standard-length: 04:02 min)
4. **Axial T2*-weighted EPI-GRE**
   (GOBrain 00:06 min; standard-length: 04:44 min)
5. **Axial DWI SS-EPI**
   (GOBrain 00:38 min; standard-length: 01:06 min)

Total acquisition times: GOBrain 04:19 min, standard-length protocol 15:11 min, localizer 00:14 min (same for both protocols). Two blinded board-certified neuroradiologists independently analyzed the image datasets with regard to overall image quality (5-point Likert scale: 1 – non-diagnostic, 2 – substantial artifacts, 3 – satisfactory, 4 – minor artifacts, 5 – no artifacts) and gray-white matter differentiation as a surrogate of image quality (T1-weighted, T2-weighted, and FLAIR images; 0 = no visible gray-white matter differentiation, 1 = unclear but recognizable borders, 2 = clear differentiation) [2]. In case of divergent results, a consensus reading was performed by a third reader. To calculate the parameters of diagnostic accuracy for the GOBrain protocol, image datasets were read regarding six defined intracranial pathology categories: acute ischemia, chronic infarction, intracranial hemorrhage/microbleeds, edema, white matter lesion, and miscellaneous. A consensus reading was performed in case of divergent reading results. Due to severe motion artifacts, one patient was excluded and 59 patients were successfully included in the statistical analysis.

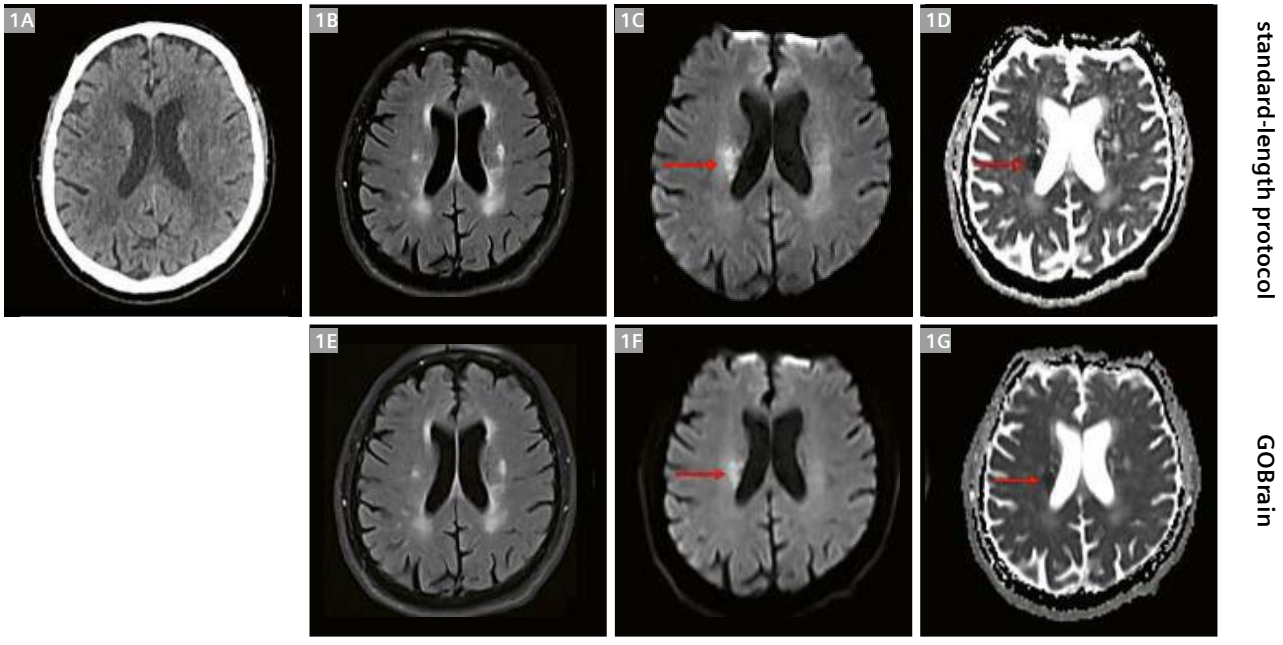

1 CT-occult acute ischemia (right corona radiata). Axial non-contrast head CT scan **(1A)**, FLAIR **(1B, E)**, DWI **(1C, F)**, ADC map **(1D, H)** from the standard-length protocol (top row) and GOBrain (bottom row) in a 72-year-old man presenting with acute left facial paralysis, dysarthria, and left-body coordination disorder. No evidence of ischemia or hemorrhage on non-contrast CT. MRI revealed an acute ischemia in the right internal capsule and the corona radiata (red arrow). Note the equivalent image quality and lesion conspicuity of both protocols.

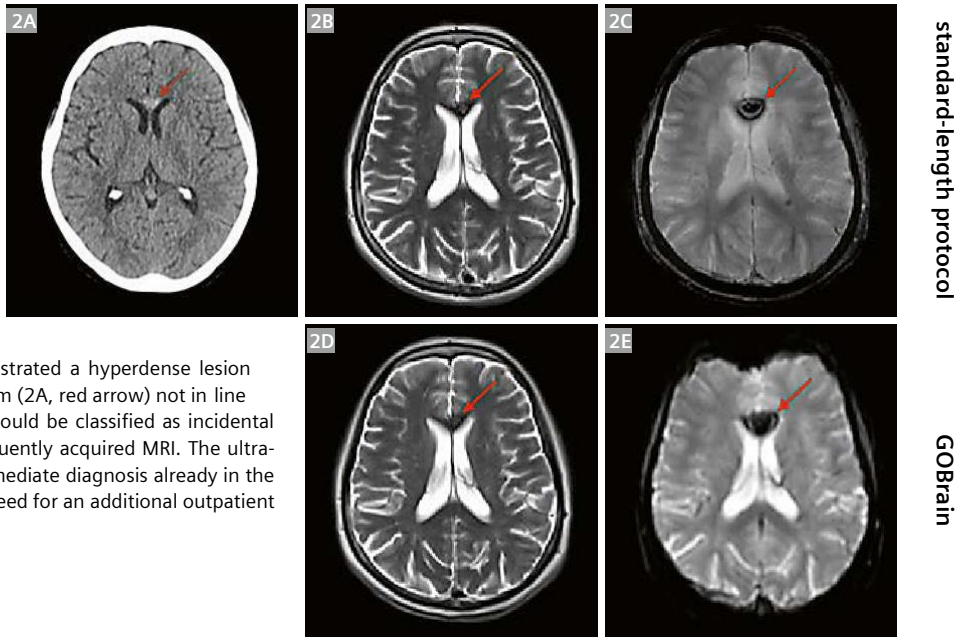

2 Incidental cavernoma (genu of the corpus callosum). Axial non-contrast head CT scan **(2A)**, axial T2 TSE **(2B, D)**, axial T2* **(2C, E)** from the standard-length protocol (top row) and GOBrain (bottom row) of a 62-year-old woman reporting temporary visual disturbance in the right eye. No correlation of the symptoms in both imaging modalities. However, non-contrast CT imaging demonstrated a hyperdense lesion in the genu of the corpus callosum (2A, red arrow) not in line with acute hemorrhage, which could be classified as incidental cavernoma based on the subsequently acquired MRI. The ultra-fast MRI protocol enabled an immediate diagnosis already in the emergency setting without the need for an additional outpatient MRI scan a few days later.

Results

Image quality of the GOBrain protocol was equivalent to the standard-length protocol: Results of image quality and gray-white matter differentiation assessments are listed in Table 1. Compared to CT imaging, 93 additional intracranial lesions were detected using the ultra-fast protocol (n = 21 acute ischemia, n = 27 intracranial hemorrhage/microbleeds, n = 2 edema, n = 38 white matter lesion, n = 3 chronic infarction, n = 2 others) while 101 additional intracranial lesions were detected using the standard-length protocol (n = 24 acute ischemia, n = 32 intracranial hemorrhage/microbleeds, n = 2 edema, n = 38 white matter lesion, n = 3 chronic infarction, n = 2 others). GOBrain demonstrated high diagnostic accuracy in detecting intracranial pathologies, with a sensitivity of 0.939 (95% CI: 0.881; 0.972) and a specificity of 1.000 (95% CI: 0.895; 1.000). Figures 1 and 2 demonstrate representative clinical cases in which GOBrain proved to be equivalent to the standard-length protocol reference standard. A change in patient management based on the MRI was noted in 10% (6 / 59; admission to a dedicated stroke unit in 6 / 59 patients, initiation of acetyl-salicylic acid treatment in 3 / 6 stroke unit patients).

Discussion

In this prospective study, we investigated a novel ultra-fast (04:33 min / 5 sequences) brain MRI protocol in the neurological emergency setting. Image quality and diagnostic performance of the GOBrain protocol demonstrated to be non-inferior to a standard-length brain MRI protocol. Furthermore, MRI led to a change in patient management in 10% of cases compared to CT imaging alone. Our data provide evidence for the standard use of the ultra-fast GOBrain protocol as a valid alternative to CT imaging for the detection and differential diagnosis of intracranial pathologies in selected acute neurological emergency patients. The ultra-fast MRI protocol may be individualized by adding sequences, such as dedicated brain stem DWI or constructive interference in steady state (CISS) sequences for optimized diagnosis of infratentorial pathologies, a contrast-enhanced T1-weighted sequence for suspected tumor or neuroinflammatory disease, or MR angiography to exclude vascular pathologies.

Contact

PD Dr. med. Philipp M. Kazmierczak, MD
Klinik und Poliklinik für Radiologie
Klinikum der Universität München
Marchioninistr. 15
81377 München
Germany
Tel.: +49 89 4400 73620
Fax: +49 89 4400 78832
philipp.kazmierczak@med.uni-muenchen.de

References

1 Kazmierczak PM, Dührsen M, Forbrig R, et al. Ultrafast Brain Magnetic Resonance Imaging in Acute Neurological Emergencies: Diagnostic Accuracy and Impact on Patient Management. Invest Radiol 2020;55:181-189.
2 Prakkamakul S, Witzel T, Huang S, et al. Ultrafast Brain MRI: Clinical Deployment and Comparison to Coventional Brain MRI at 3T. J Neuroimaging 2016;26:503-510.

Ultrafast Multi-contrast High-resolution 3D Brain MRI: a Technical Description of Wave-CAIPI

Daniel Polak[1,2]; Stephen Cauley[1,3]; Berkin Bilgic[1,3,4]; Lawrence Wald[1,3,4]; Kawin Setsompop[1,3,4]

[1]Martinos Center for Biomedical Imaging, Department of Radiology, Massachusetts General Hospital, Charlestown, MA, USA
[2]Siemens Healthineers, Erlangen, Germany
[3]Department of Radiology, Harvard Medical School, Boston, MA, USA
[4]Harvard-MIT Health Sciences and Technology, Massachusetts Institute of Technology, Cambridge, MA, USA

Introduction

Parallel imaging techniques (e.g., SENSE [1], GRAPPA [2], etc.) have enabled substantial scan time reduction in Magnetic Resonance Imaging (MRI) while retaining high spatial resolution and appropriate imaging contrast. These methods leverage the spatial information afforded by multi-channel receiver arrays to minimize the time-consuming gradient encoding. However, the performance of these acceleration techniques is limited by the spatial encoding capability of the coil sensitivities which are related to the coil design and coil geometry (adjacent coil elements typically have similar coil sensitivity). In the case of conventional 2D slice-by-slice imaging, the close spatial proximity of aliased voxels usually constrains clinical applications to moderate acceleration factors, even when a modern high-channel-count receive array is used.

Several new imaging technologies have been developed to address the increasing encoding burden at high resolution and enable faster scanning. This represents a move towards volumetric imaging, where Simultaneous MultiSlice (SMS) and efficient 3D-encoding have enabled dramatic increases in acquisition speed. These imaging techniques can also make better use of the coil sensitivity information in multi-channel receiver arrays, i.e. through employing controlled aliasing along multiple spatial dimensions. The 2D-CAIPIRINHA technique [3] was developed to enable higher acceleration for 3D acquisitions by employing a staggered k_y-k_z undersampling pattern. This increases the distance between aliased voxels in the phase-partition encoding plane allowing for better utilization of the available variation in the coil sensitivity profiles.

The recently proposed Wave-CAIPI[1] technique [4] expands controlled aliasing to the full 3D extent. This has enabled even greater parallel imaging encoding capability for structural scans while retaining good image quality and SNR.

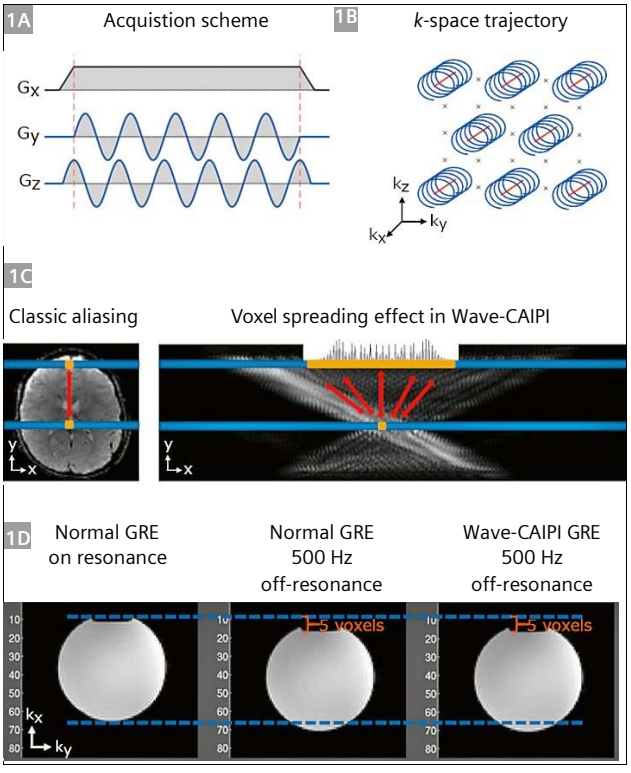

1 Wave-CAIPI:
(1A) Wave-CAIPI utilizes sinusoidal gradients during the frequency encoding. **(1B)** The sinusoidal waveforms incur corkscrew trajectories in *k*-space which are staggered due to the 2D-CAPIRINHA sampling **(1C)** In the image domain Wave-encoding results in voxel spreading along the readout direction. This increases the distance between collapsing voxels when compared to classic aliasing. **(1D)** Wave-CAIPI exhibits the same off-resonance shifts along the readout direction as standard Cartesian acquisitions (here shown for GRE at 500 Hz off-resonance and bandwidth 100 Hz/px).

[1]*Work in progress: the application is currently under development and is not for sale in the U.S. and in other countries. Its future availability cannot be ensured.*

Wave-CAIPI

Wave-CAIPI [4] generalizes 2D-CAIPIRINHA and Bunch Phase Encoding/Zig-Zag sampling [5, 6] to create a controlled aliasing concept that encompasses all three spatial dimensions (including the readout direction). Figure 1A demonstrates the acquisition scheme for Wave-CAIPI. Two sinusoidal gradients G_y and G_z are played during the readout with a quarter cycle phase shift. Combined with 2D-CAIPIRINHA sampling, this results in staggered corkscrew trajectories through *k*-space (Fig. 1B). In the image domain the additional phase deposition results in voxel-spreading along the readout direction which varies linearly as a function of the spatial y and z position (Fig. 1C). When combined with the interslice shifts from 2D-CAIPIRINHA, a well distributed aliasing pattern is created across all three spatial dimensions. This allows Wave-CAIPI to take full advantage of the 3D coil sensitivity information and enables up to an order of magnitude increase in acquisition speed with negligible parallel imaging noise amplification and artifact penalty [4, 7–9].

Wave-CAIPI also has several desirable properties that enable high quality reconstruction. In contrast to other rapid acquisition techniques such as EPI or spiral imaging, Wave-CAIPI is not susceptible to image blurring and distortion artifacts caused by inhomogeneity of the main magnetic field (B0) [9]. This can be attributed to the constant rate of *k*-space traversal along the readout direction (k_x) for Wave-CAIPI. As a result, phase evolution from B0 inhomogeneity only evolves as a function of k_x, resulting in the same chemical shift effect as observed in conventional Cartesian imaging sequences. This effect is demonstrated in Figure 1D. At 500 Hz off-resonance a Wave-CAIPI gradient echo (GRE) acquisition shows the same voxel shift along the readout direction as a standard acquisition. Moreover, intravoxel dephasing is negligible in Wave-CAIPI acquisitions as sinusoidal waveforms prevent large accrual of the gradient moment [4].

Figure 2 compares the encoding efficiency of Wave-CAIPI, 2D-CAIPIRINHA and standard acquisitions at R = 3 x 3 acceleration and 1 mm³ isotropic resolution using a Siemens Healthineers 32-channel head coil. Wave-CAIPI offers high quality reconstructions and negligible noise amplification penalty as evidenced by the reciprocal *g*-factor maps (measure of noise amplification due to lack of spatial encoding). In contrast, 2D-CAIPIRINHA and standard sampling provide insufficient encoding capability at R = 9-fold acceleration causing residual aliasing artifacts and large noise amplification especially in the center of the brain.

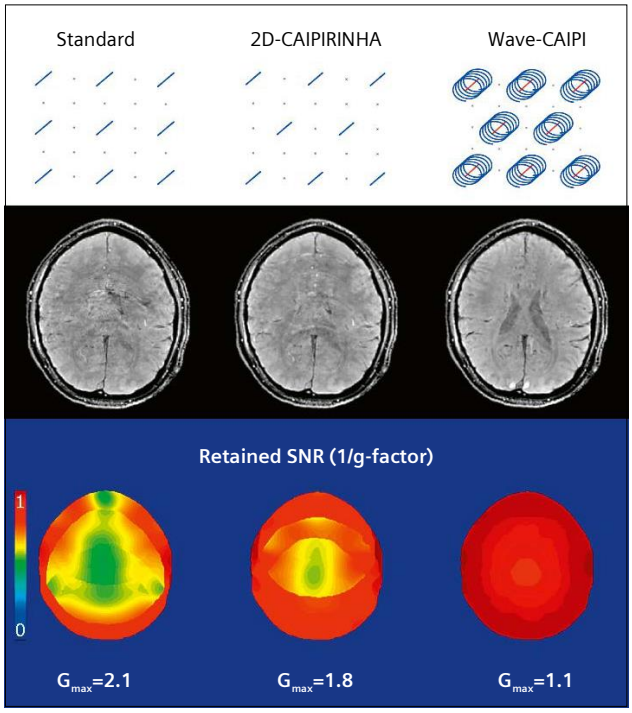

2 ***G*-factor comparison at R = 3 x 3:**
At R = 3 x 3 acceleration, standard and 2D-CAIPIRINHA sampling result in residual aliasing artifacts and large noise amplification especially in the center of the brain. In contrast, Wave-CAIPI yields high quality reconstructions without artifacts and close to perfect *g*-factor.

Auto-calibrated image reconstruction

Wave-CAIPI acquisitions can be reconstructed efficiently using a generalized SENSE framework thus avoiding the need for *k*-space gridding [4]. This is made possible as the non-Cartesian corkscrew trajectory can be represented as additional phase deposition in Cartesian *k*-space. Using a simple point spread function framework, the voxel spreading effect from Wave-CAIPI is either modeled as a spatially varying convolution in the image domain or more efficiently as a phase modulation in hybrid space (k_x, y, z). Due to this spatially invariant encoding property, the SENSE-based reconstruction also remains highly separable. This allows for efficient parallelization as separate linear systems can be solved for each set of collapsing readout lines. Moreover, Wave-CAIPI does not require internal calibration data, as volumetric ESPIRiT [10] coil sensitivity maps are typically computed from a rapid low-resolution 3D gradient echo (GRE) scan (acquisition time roughly two seconds).

The separable Wave-CAIPI reconstruction also facilitates the automatic estimation and correction of any minor gradient deviations from the nominal trajectory without the need for additional calibration scans. This auto-calibrated technique [11] relies on a compact representation of the Wave-encoding's sinusoidal phase modulation (including minor deviations) which can be accurately described using a limited number of frequency coefficients. To accurately determine the exact *k*-space

trajectory, the auto-calibrated reconstruction optimizes the frequency coefficients and aliased voxels jointly to reduce the data consistency error of the generalized SENSE encoding model. By limiting this non-linear search to a small representative set of collapsing readout lines, the computational demand of this optimization problem is substantially reduced while mitigating artifacts globally. This has enabled rapid convergence (roughly after 10 seconds) for arbitrary acquisition protocols using standard scanner computation hardware.

Applications

The Wave-CAIPI acquisition and reconstruction framework can be broadly applied and has been shown to enable up to an order of magnitude higher acceleration for both SMS and 3D imaging sequences [4, 7–9] with negligible *g*-factor noise amplification. This scan efficiency has allowed for the development of a six-minute high-resolution volumetric brain exam comprising of the clinical contrasts T1w MPRAGE, T2w SPACE, T2w SPACE-FLAIR and T2*w SWI. Detailed optimization of the Wave corkscrew was performed for each structural scan to achieve optimal performance with respect to SNR and image quality [8]. Figure 3 illustrates example slices acquired at 3T (MAGNETOM Skyra, Siemens Healthcare, Erlangen, Germany) using a product Siemens Healthineers 32-channel head coil. Good SNR and contrast are provided in each of the rapid volumetric acquisitions (scan time 1–2 minutes each). Due to the isotropic resolution ($1 \times 1 \times 1$ mm^3) of MPRAGE and SPACE (T2w and FLAIR) these datasets can also be reformatted and viewed in arbitrary orientations without loss of spatial resolution.

The encoding capability of Wave-CAIPI can also be deployed in clinical standard protocols with high in-plane resolution and thick slices [12]. In Figure 4, Wave-CAIPI SPACE-FLAIR (R = 3 x 2, 0.8 x 0.8 x 3 mm^3) was acquired in axial orientation and compared to standard clinical T2w TSE (R = 2). Despite substantial speed-up from Wave-encoding, comparable contrast and image quality is maintained.

At present, clinical validation of the rapid Wave-CAIPI sequences for brain imaging is being led by the Neuroradiology Department of the Massachusetts General Hospital (Boston, MA, USA). The objective of these ongoing assessments is to establish non-inferior diagnostic quality between the Wave-CAIPI and standard clinical protocols routinely used at this institution. Progress towards this goal has been reported in several clinical evaluations [13–16] and is also summarized in "Ultrafast Multi-contrast

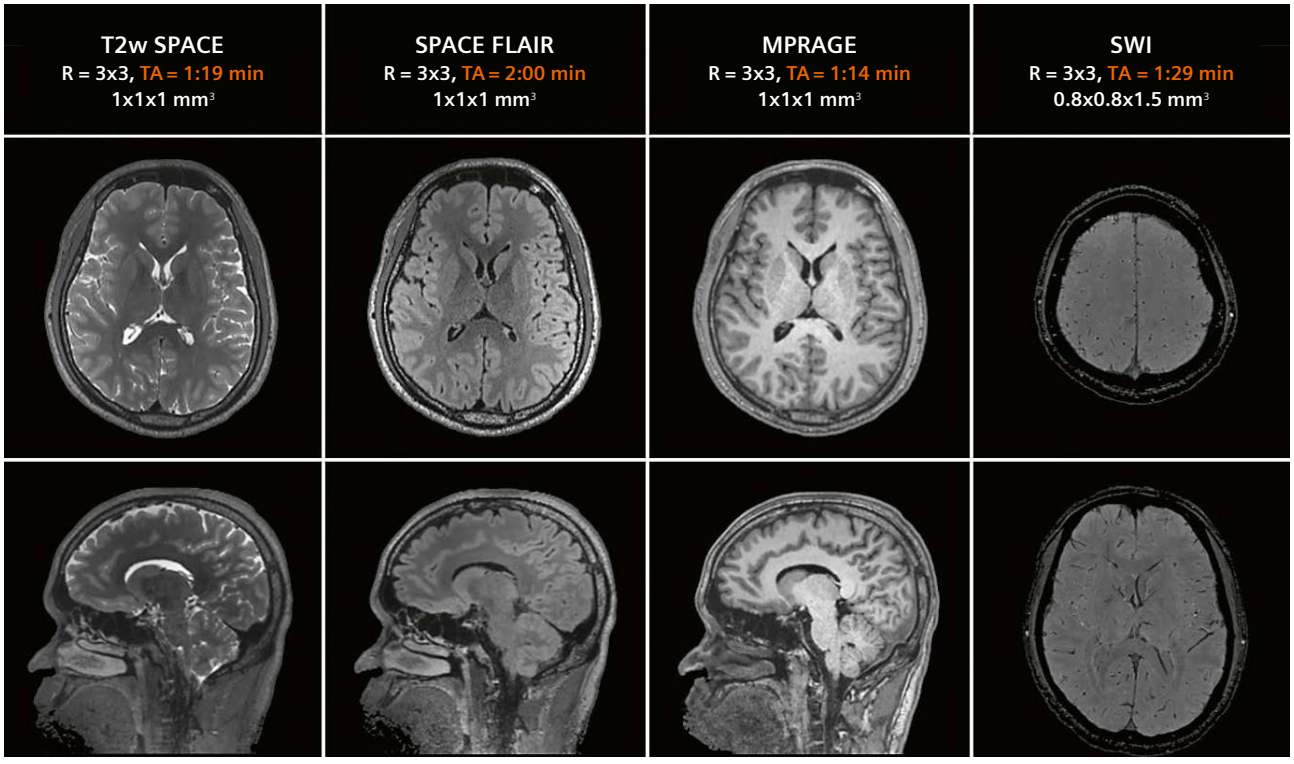

3 Six-minute volumetric whole brain exam using Wave-CAIPI:
Six-minute high-resolution whole-brain exam comprised of T2w SPACE, T2w SPACE-FLAIR, T1w MPRAGE and T2*w SWI at R = 9-fold acceleration.

High-resolution 3D Brain MRI: Clinical Evaluation of Wave CAIPI Acceleration in SWI, MPRAGE, FLAIR, SPACE" by Susie Huang et al. on page 21 of this issue.

Acknowledgments

The authors would like to thank Wei Liu, Daniel Nicolas Splitthoff, Borjan Gagoski, Wei-Ching Lo, Sinyeob Ahn, Thomas Beck, Thorsten Feiweier, Himanshu Bhat, Yulin Chang, Shivraman Giri and Keith Heberlein for their valuable support.

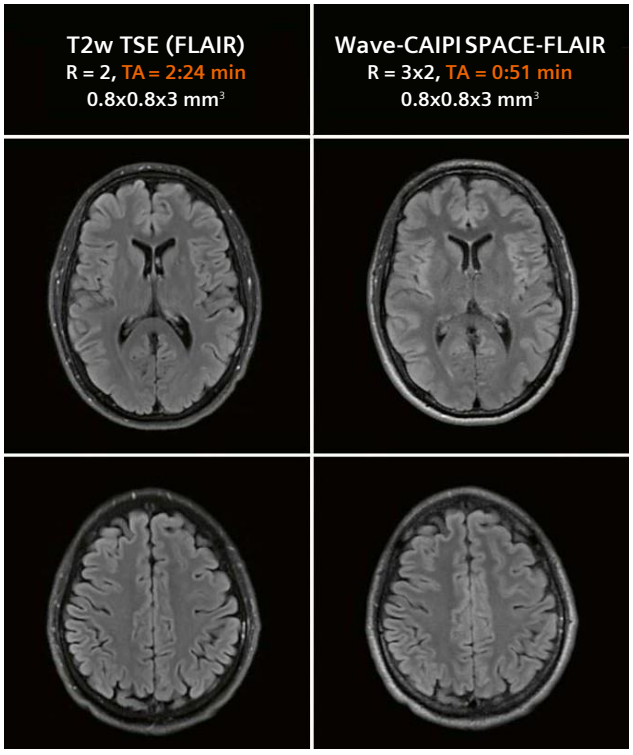

4 Comparing standard T2w TSE versus Wave-CAIPI SPACE-FLAIR: Standard clinical T2w TSE scan is compared to highly accelerated 3D Wave-CAIPI SPACE-FLAIR acquisition with high in-plane resolution and thick slices.

Contact

Kawin Setsompop
Massachusetts General Hospital
Martinos Center for Biomedical Imaging
Building 75, Room 2.102, 13th Street
Charlestown, MA, 02129, USA
Phone: +1 617-669-6640
kawin@nmr.mgh.harvard.edu

Daniel Polak
Siemens Healthineers
DI MR DL ORTH
daniel.polak@siemens.healthineers.com

References

1 K. P. Pruessmann, M. Weiger, M. B. Scheidegger, and P. Boesiger, "SENSE: Sensitivity encoding for fast MRI," Magn. Reson. Med., vol. 42, no. 5, pp. 952–962, 1999.
2 M. A. Griswold et al., "Generalized Autocalibrating Partially Parallel Acquisitions (GRAPPA)," Magn. Reson. Med., vol. 47, no. 6, pp. 1202–1210, 2002.
3 F. A. Breuer et al., "Controlled aliasing in volumetric parallel imaging (2D CAIPIRINHA)," Magn. Reson. Med., vol. 55, no. 3, pp. 549–556, 2006.
4 B. Bilgic et al., "Wave-CAIPI for highly accelerated 3Dimaging," Magn. Reson. Med., vol. 73, no. 6, pp. 2152–2162,2015.
5 H. Moriguchi and J. L. Duerk, "Bunched Phase Encoding (BPE): A new fast data acquisition method in MRI," Magn. Reson. Med., vol. 55, no. 3, pp. 633–648, 2006.
6 F. A. Breuer et al., "Zigzag sampling for improved parallel imaging," Magn. Reson. Med., 2008.
7 D. Polak et al., "Wave-CAIPI for highly accelerated MP-RAGE imaging," Magn. Reson. Med., vol. 79, no. 1, pp. 401–406, 2018.
8 D. Polak et al., "Highly-accelerated volumetric brain examination using optimized wave-CAIPI encoding," J. Magn. Reson. Imaging, vol. 50, no. 3, pp. 961–974, 2019.
9 B. A. Gagoski et al., "RARE/Turbo Spin Echo imaging with Simultaneous MultiSlice Wave-CAIPI," Magn. Reson. Med., vol. 73, no. 3, pp. 929–938, 2015.
10 M. Uecker et al., "ESPIRiT--an eigenvalue approach to autocalibrating parallel MRI: where SENSE meets GRAPPA.," Magn. Reson. Med., vol. 71, no. 3, pp. 990–1001, Mar. 2014.
11 S. F. Cauley, K. Setsompop, B. Bilgic, H. Bhat, B. Gagoski, and L. L. Wald, "Autocalibrated wave-CAIPI reconstruction; Joint optimization of k-space trajectory and parallel imaging reconstruction," Magn. Reson. Med., vol. 78, no. 3, pp. 1093–1099, 2017.
12 Wei-Ching Lo, et. al., "A comprehensive distortion-free 2-minute brain MR examination using BUDA and Wave-CAIPI", Accepted for oral presentation at ISMRM Annual Meeting 2020, Paris, France.
13 Conklin J, Longo MGF, Cauley SF, et al. Validation of Highly Accelerated Wave–CAIPI SWI Compared with Conventional SWI and T2*-Weighted Gradient Recalled-Echo for Routine Clinical Brain MRI at 3T. AJNR Am J Neuroradiol. 2019, 40:2073–80.
14 Longo MGF, Conklin J, Tian Q, et al. Validation of ultrafast Wave-CAIPI magnetization prepared rapid gradient-echo (MPRAGE) for quantitative evaluation of brain tissue volume in the workup of suspected neurodegenerative disease. American Society of Neuroradiology, 2019. Boston, MA.
15 Ngamsombat C, Longo MGF, Goncalves Filho ALM, et al. Evaluation of Ultrafast Wave-CAIPI Three-Dimensional Fluid-attenuated Inversion Recovery (3D FLAIR) Compared to Standard 3D FLAIR for Quantitative Analysis of Cerebral White Matter Lesions. Accepted for oral presentation at the Annual Meeting of the American Society of Neuroradiology, Las Vegas, Nevada. May 30–June 04, 2020.
16 Goncalves Filho ALM, Longo MGF, Conklin J, et al. Evaluation of Highly Accelerated Wave-CAIPI Post-Contrast 3D-T1 Sampling Perfection With Application Optimized Contrast Using Different Flip-Angle Evolutions (Wave-3D-T1 SPACE) Compared to Standard Post-Contrast 3D-T1 SPACE for Detection of Intracranial Enhancing Lesions. Accepted for oral presentation at the Annual Meeting of the American Society of Neuroradiology, Las Vegas, Nevada. May 30–June 04, 2020.

Ultrafast Multi-Contrast High-Resolution 3D Brain MRI: Clinical Evaluation of Wave-CAIPI Acceleration in SWI, MPRAGE, FLAIR, SPACE

Augusto Lio Goncalves Filho[1]; John Conklin[1,2]; Otto Rapalino[3]; Pamela Schaefer[3]; Susie Huang[1,3]

[1]Athinoula A. Martinos Center for Biomedical Imaging, Department of Radiology, Massachusetts General Hospital, Charlestown, MA, USA
[2]Division of Emergency Radiology, Department of Radiology, Massachusetts General Hospital, Boston, MA, USA
[3]Division of Neuroradiology, Department of Radiology, Massachusetts General Hospital, Boston, MA, USA

Magnetic Resonance Imaging (MRI) stands out among today's many medical imaging techniques as the best modality for studying the human brain. High field MRI scanners have improved many forms of structural and functional imaging by reducing voxel sizes and providing significant gains in signal-to-noise ratio (SNR) with an increase in image resolution [1]. Technological developments have also enabled more widespread use of 3D imaging sequences that allow for multiplanar image reconstruction with detailed anatomic depiction and high sensitivity in lesion detection. Traditionally, achieving high-resolution imaging has demanded long encoding and acquisition times that resulted in a lengthy total protocol.

With an eye toward limited scanner resources and the ever-growing demand for medical imaging, efforts have been made to reduce the duration of MRI acquisitions. Parallel imaging techniques such as generalized autocalibrating partially parallel acquisition (GRAPPA) and sensitivity encoding (SENSE) acquisitions have been successfully used to accelerate MRI acquisitions by two- to threefold in clinical practice by taking advantage of the inherent spatial encoding information of modern multichannel receiver arrays [1, 2]. Nevertheless, extreme accelerations have not been possible due to limitations in SNR imposed by higher *g*-factor penalties and aliasing artifacts. The Wave-CAIPI[1] method has recently been proposed as a

Table 1: Representative acquisition times of standard and accelerated 3D sequences performed on a 3T MAGNETOM scanner with 20-channel and 32-channel coil arrays. R = acceleration factor.

Sequence	Acquisition Time		
	Standard (GRAPPA)	3D Wave-CAIPI 20-ch coil	3D Wave-CAIPI 32-ch coil
SWI	5 min 21 s (*R* = 2)	1 min 37 s (*R* = 6)	1 min 6 s (*R* = 9)
MPRAGE	5 min 18 s (*R* = 2)	1 min 46 s (*R* = 6)	1 min 11 s (*R* = 9)
SPACE FLAIR	7 min 15 s (*R* = 2)	2 min 45 s (*R* = 6)	1 min 50 s (*R* = 9)
Post-contrast T1 SPACE	4 min 19 s (*R* = 4)	1 min 40 s (*R* = 9)	1 min 40 s (*R* = 9)

[1]*Work in progress: the application is currently under development and is not for sale in the U.S. and in other countries. Its future availability cannot be ensured.*

way to enable greater acceleration of high-resolution volumetric imaging by combining *k*-space undersampling of CAIPIRINHA with corkscrew readout gradient trajectories that optimally utilize the intrinsic spatial information of the coil array, enabling increased acquisition speed with reduced noise amplification and artifact [2]. Wave-CAIPI is specifically designed to accelerate 3D exams, which offer the potential for increased diagnostic information by avoiding thick imaging slices and slice gaps, while providing multiplanar views and eliminating the need for redundant acquisitions in different planes. With support of Siemens Healthineers MR, this article will demonstrate the clinical experience and translational studies being performed at Massachusetts General Hospital (MGH) to validate the use of Wave-CAIPI acquisitions in a high-volume tertiary care setting with satellite outpatient facilities serving the large, diverse population of the greater Boston area.

The development, optimization and translation of Wave-CAIPI technology has been carried out by a multi-disciplinary team of MR physicists, Siemens Healthineers engineers, and neuroradiologists at MGH. Following the optimization of sequence parameters and online reconstruction using an autocalibrated procedure [3], we have sought to evaluate systematically the diagnostic performance of 3D Wave-CAIPI sequences against standard clinical protocols acquired with conventional parallel imaging (GRAPPA). The validation approach comprises prospective comparative studies including inpatient and outpatient examinations with a variety of indications and undergoing different imaging protocols that include SWI, MPRAGE, SPACE FLAIR and post-contrast T1 SPACE sequences. Imaging was performed on 3T MAGNETOM Skyra and MAGNETOM Prisma MRI scanners (Siemens Healthcare, Erlangen, Germany) using Siemens 20- and 32-channel head coils. Acceleration factors were tailored for each pulse sequence and RF coil to balance scan time (Table 1) with an acceptable SNR for each coil configuration.

The approach to optimize and clinically validate diagnostic protocols incorporating Wave-CAIPI technology included the following steps:

1. Optimization of acquisition parameters for each sequence, including optimization of the Wave corkscrew to reduce noise amplification and blurring artifacts.
2. Establishing the ideal balance between maximum acceleration and adequate visualization of abnormal findings without loss of diagnostic capability compared to the standard exam.
3. Execution of an Institutional Review Board approved study to assess the head-to-head performance of the rapid MR protocol to the conventional exam with blinded reads by at least two board-certified neuroradiologists. The imaging evaluation incorporates a semiquantitative grading system to compare predetermined criteria on the Wave-CAIPI sequences with the standard sequence, including factors such as image quality, presence of artifacts, and diagnostic findings appropriate for the indication. The statistical demonstration of noninferiority of the Wave-CAIPI sequence compared to the standard sequence was used to validate the clinical utility of the accelerated imaging sequence, with an emphasis on preserving diagnostic performance.

→ Don't miss the technical description of Wave-CAIPI in the article by Kawin Setsompop, et al.

"Ultrafast Multi-contrast High-resolution 3D Brain MRI: a Technical Description of Wave-CAIPI"

Go to page 17 in this edition of MAGNETOM Flash.

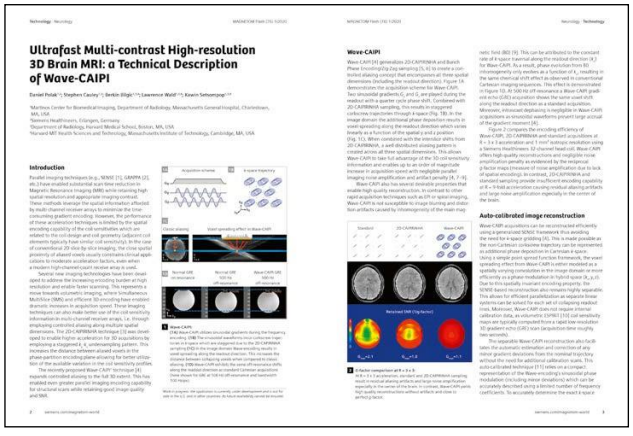
Ultrafast Multi-contrast High-resolution 3D Brain MRI: a Technical Description of Wave-CAIPI

Clinical experience with Wave-CAIPI sequences:

Wave-SWI[1]

Wave-CAIPI SWI has been validated for routine clinical brain imaging at 3T and 1.5T. The results of a recent study have shown that Wave-SWI provided superior visualization of pathology and overall diagnostic quality compared with T2*-weighted GRE and was noninferior to standard SWI with reduced scan time (Table 2) and reduced motion artifacts [4] (Fig. 1).

Given the predominance of 1.5T scanners in clinical practice, we have also conducted a smaller scale clinical study of Wave-SWI at 1.5T. The results of this study show comparable diagnostic performance of Wave-SWI to standard SWI at 1.5T (Fig. 2), thereby supporting the broad clinical adoption of Wave-SWI at both 1.5T and 3T.

Table 2: Representative acquisition parameters of standard and accelerated 3D SWI sequences performed on a 3T MAGNETOM scanner with 20-channel and 32-channel coil arrays.

	FOV read (mm)	FOV phase (%)	Matrix size	Slice thickness (mm)	TR/TE (msec)	Flip angle (degree)	Acceleration factor *R*		Scan time	
							20-ch	32-ch	20-ch	32-ch
Standard SWI	240	75.0	256 x 182	1.8	30 / 20	12	GRAPPA, *R* = 2	GRAPPA, *R* = 2	4 min 56 s	5 min 21 s
Wave-SWI	240	87.5	288 x 189	1.8	40 / (13 and 30; effective TE 21.5)	15	Wave-CAIPI, *R* = 6	Wave-CAIPI, *R* = 9	1 min 37 s	1 min 6 s

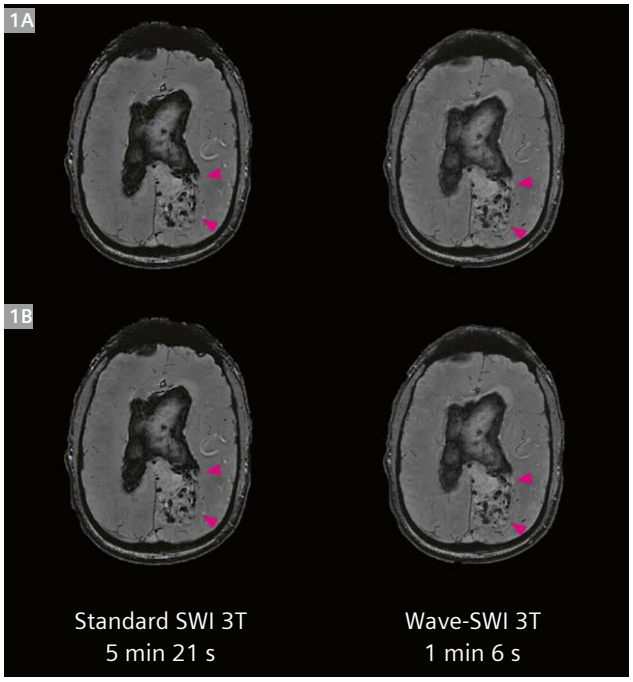

1 Representative images comparing standard susceptibility-weighted imaging (Standard SWI) and Wave-CAIPI SWI (Wave-SWI) at 3T with a 32-channel coil array. **(1A)** Extensive intraventricular hemorrhage and serpiginous foci of susceptibility effect corresponding to an arteriovenous malformation. **(1B)** Focal subarachnoid hemorrhage in the left superior frontal sulcus and the pre-central sulcus.

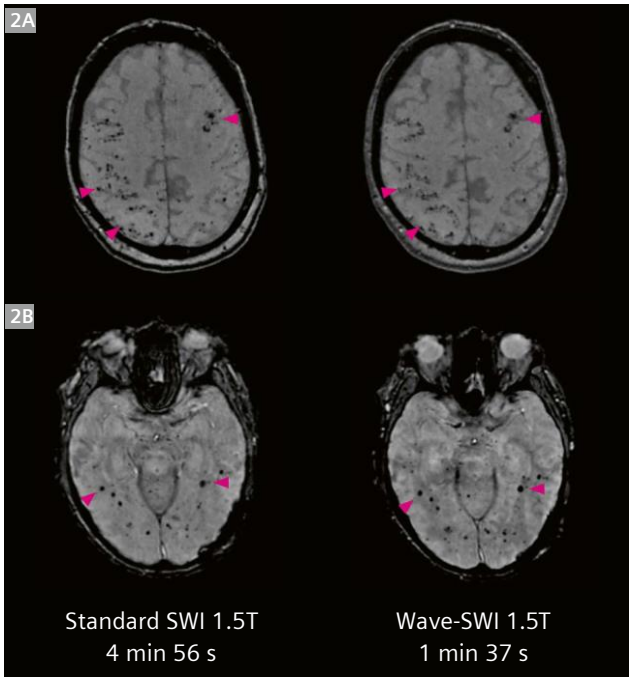

2 Representative images comparing standard susceptibility-weighted imaging (Standard SWI) and Wave-CAIPI SWI (Wave-SWI) at 1.5T with a 20-channel coil array. **(2A)** Cortical and juxtacortical punctate susceptibility foci due to amyloid angiopathy. **(2B)** Multiple small hemangioblastomas within the temporal and occipital lobes in a 57-year-old man with von Hippel Lindau syndrome.

Wave-MPRAGE[1]

Wave-CAIPI has been optimized for brain imaging with MPRAGE and has demonstrated potential in accelerating the evaluation of cortical volume in healthy volunteers [6]. In a recent study, Wave-MPRAGE[1] was evaluated in a clinical setting among patients undergoing evaluation for suspected neurodegenerative disease. The results revealed similar reliability to standard MPRAGE for regional evaluation of brain atrophy using automated segmentation of brain tissue volumes, cortical thickness measurements, and semi-quantitative visual rating scales, despite a 3- to 5-fold decrease in acquisition time [7] (Table 3, Fig. 3). Therefore, adoption of Wave-MPRAGE over standard MPRAGE for volumetric imaging of patients with suspected neurodegenerative diseases could improve utilization of MRI resources in both clinical and research settings.

Table 3: Representative acquisition parameters of standard and accelerated 3D MPRAGE sequences performed on a 3T MAGNETOM scanner with 20-channel and 32-channel coil arrays.

	FOV read (mm)	FOV phase (%)	Matrix size	Slice thickness (mm)	TR/TE/TI (msec)	Flip angle (degree)	Acceleration factor *R*		Scan time	
							20-ch	32-ch	20-ch	32-ch
Standard MPRAGE	240 x 240	100	256 x 256	0.89	2300 / 2.32 / 900	8	GRAPPA, *R* = 2	GRAPPA, *R* = 2	5 min 19 s	5 min 18 s
Wave-MPRAGE	256 x 256	100	256 x 256	1.0	2500 / 3.48 / 1100	7	Wave-CAIPI, 3 x 2	Wave-CAIPI, 3 x 3	1 min 46 s	1 min 11 s

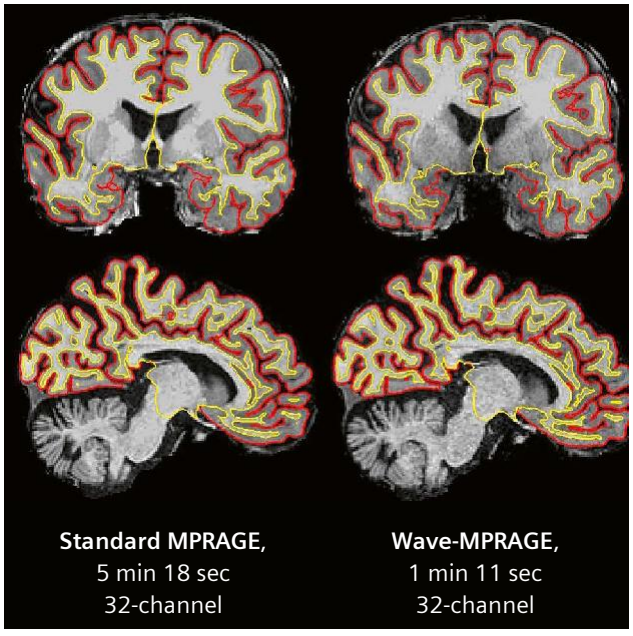

3 Comparison of Wave-MPRAGE images in a patient with biparietal atrophy. Cortical volumes were generated by the FreeSurfer longitudinal processing stream. The lines represent the automated FreeSurfer outputs for the pial surface (red) and gray-white matter surface (yellow). These outputs demonstrate the accuracy of the longitudinal stream in both Wave-MPRAGE and standard MPRAGE images.

Wave-SPACE FLAIR[1]

Quantitative and qualitative evaluation of cerebral white matter lesions in a clinical setting has been explored using different flip angle evolution (SPACE) FLAIR sequences with Wave-CAIPI encoding (Wave-SPACE FLAIR) in comparison to standard SPACE FLAIR [7]. Preliminary results show excellent agreement in lesion detection between Wave-CAIPI and standard SPACE-FLAIR in patients undergoing clinical evaluation for multiple sclerosis (MS) and epilepsy, in less than half the acquisition time (Table 4, Fig. 4). Additionally, Wave-CAIPI SPACE FLAIR eliminates flow artifacts in the posterior fossa and middle cranial fossa that are commonly seen in the standard SPACE-FLAIR sequence (Fig. 5) which can confound the detection of subtle lesions in both MS and epilepsy.

Table 4: Representative acquisition parameters of standard and accelerated 3D SPACE FLAIR sequences performed on a 3T MAGNETOM scanner with 20-channel and 32-channel coil arrays.

	FOV read (mm)	FOV phase (%)	Matrix size	Slice thickness (mm)	TR/TE/TI (msec)	Flip angle (degree)	Acceleration factor *R*		Scan time	
							20-ch	32-ch	20-ch	32-ch
Standard SPACE FLAIR	256	100	256 x 256	1	5000 / 390 / 1800	120	GRAPPA, *R* = 2	GRAPPA, *R* = 2	7 min 15 s	7 min 15 s
Wave-SPACE FLAIR	256 x 256	100	256 x 256	1	5000 / 392 / 1800	120	Wave-CAIPI, *R* = 6	Wave-CAIPI, *R* = 9	2 min 45 s	1 min 50 s

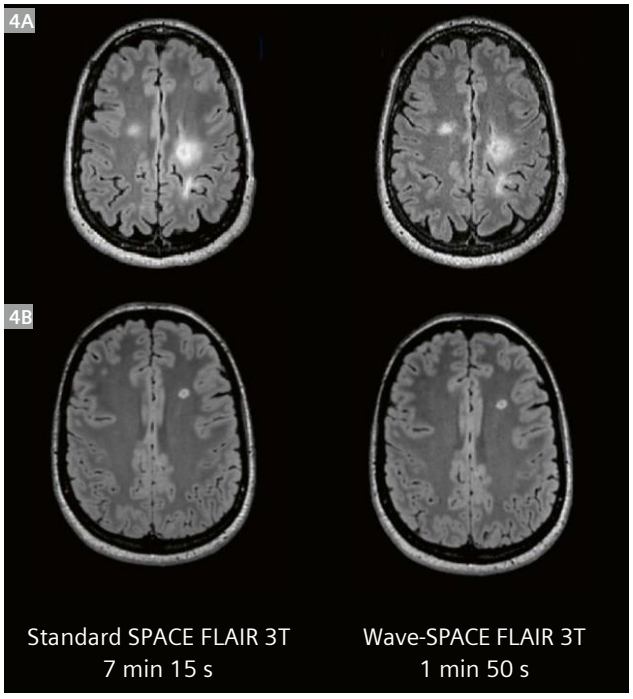

4 White matter lesions in **(4A)** multiple sclerosis and **(4B)** suspected multiple sclerosis on Standard SPACE FLAIR and Wave-SPACE FLAIR at 3T with a 32-channel coil.

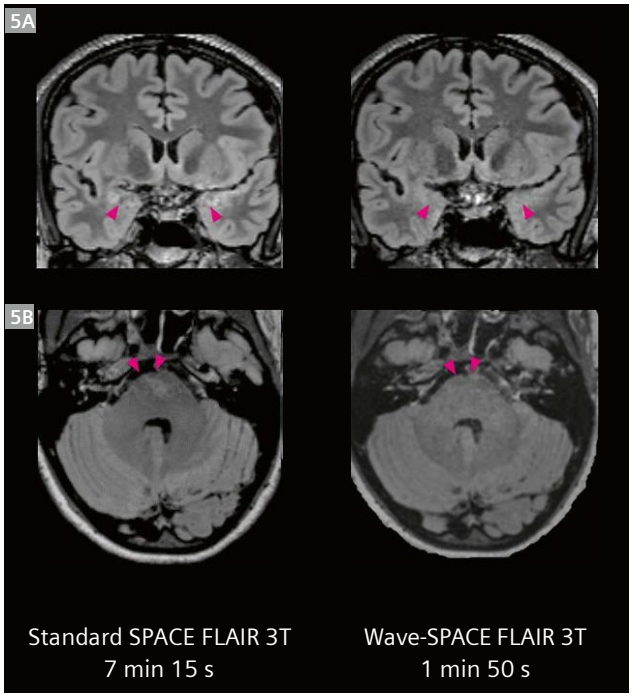

5 Representative images showing flow artifacts in the **(5A)** mesial temporal lobes and **(5B)** posterior fossa on the standard SPACE-FLAIR images that are not seen on the Wave-SPACE FLAIR images. In (5B), a pseudolesion in the central pons related to flow artifact around is not seen on the Wave-SPACE FLAIR image. Images were acquired at 3T on a 32-channel coil.

Wave-T1 SPACE[1]

Evaluation of diagnostic performance and image quality of highly accelerated Wave-CAIPI post-contrast 3D-T1 SPACE (Wave-T1 SPACE) compared to standard post-contrast 3D-T1 SPACE has also been performed for the detection of intracranial enhancing lesions [8]. There was no significant difference in the visualization of parenchymal, leptomeningeal, dural or ependymal enhancement (Fig. 6). Although Wave-T1 SPACE images demonstrated slightly greater image noise, there was no impact on the overall diagnostic quality.

Rapid acquisition techniques not only shorten scan times to increase scanning efficiency but also provide higher-quality data through reducing vulnerability to motion (Fig. 7), artifacts arising from dynamic physiological changes, and blurring that accumulates with time during the image encoding [9]. We have observed further benefits in motion prone populations such as infants and children[2], and individuals with clinical conditions that limit their cooperation for long lasting exams (e.g., critically ill patients in the emergency department or intensive care unit).

Table 5: Representative acquisition parameters of standard and accelerated 3D T1 SPACE sequences performed on a 3T MAGNETOM scanner with 20-channel and 32-channel coil arrays.

	FOV read (mm)	FOV phase (%)	Matrix size	Slice thickness (mm)	TR/TE (msec)	Flip angle (degree)	Acceleration factor *R*		Scan time	
							20-ch	32-ch	20-ch	32-ch
Standard T1 SPACE	230	89.8	256 x 256	0.9	700 / 11	120	GRAPPA, *R* = 4	GRAPPA, *R* = 4	4 min 19 s	4 min 19 s
Wave-T1 SPACE	240	100	256 x 256	1	700 / 12	120	Wave-CAIPI, *R* = 9	Wave-CAIPI, *R* = 9	1 min 40 s	1 min 40 s

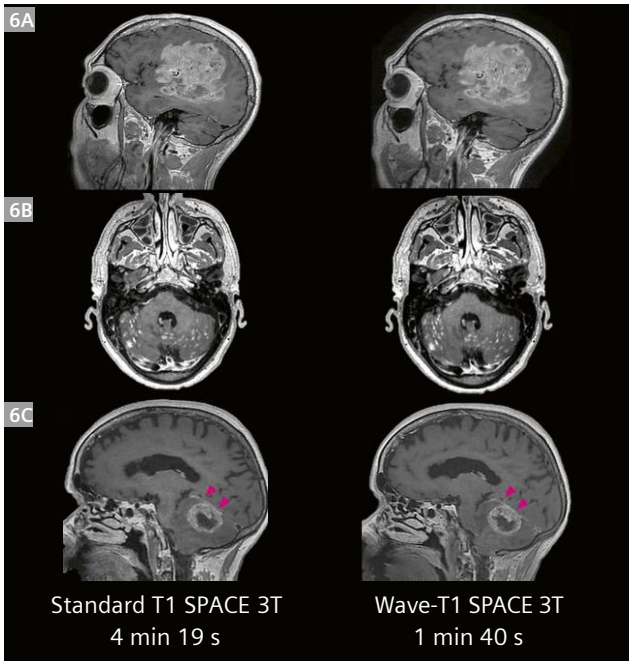

6 Comparison of abnormal enhancement in **(6A)** glioblastoma presenting as a large parenchymal mass in the cerebral hemisphere, **(6B)** multiple nodular leptomeningeal enhancing lesions due to leptomeningeal spread of lymphoma throughout the bilateral cerebellar hemispheres, and **(6C)** a heterogeneously enhancing melanoma metastasis in the cerebellar hemisphere with dural enhancement in the overlying tentorium (arrowheads) on standard T1 SPACE and Wave-T1 SPACE at 3T with a 32-channel coil array.

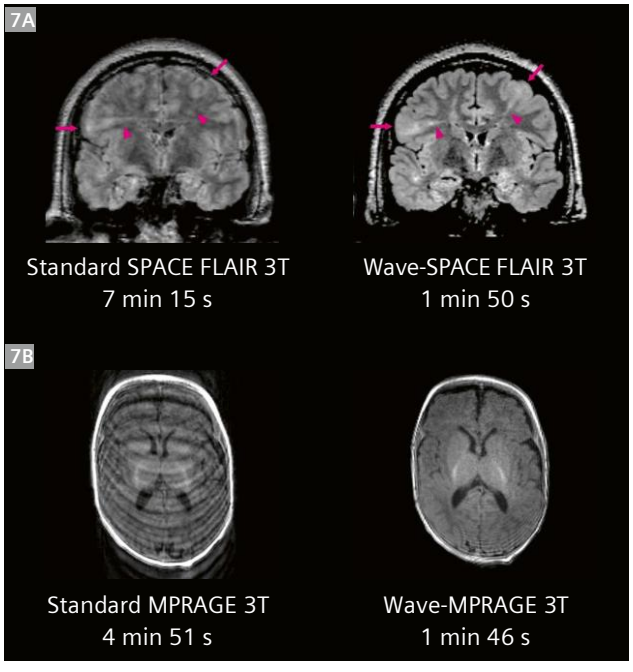

7 Rapid acquisition with Wave-CAIPI reduces vulnerability to motion artifacts, demonstrated by **(7A)** coronal standard SPACE FLAIR vs. Wave-SPACE FLAIR, exhibiting image degradation that impairs the evaluation of cortical tubers (arrows) and radial bands (arrowheads) in a patient diagnosed with tuberous sclerosis complex. **(7B)** Axial standard MPRAGE vs. Wave-MPRAGE demonstrating intense motion artifacts in a 3-month-old infant[2] being evaluated after seizures, showing an age-appropriate pattern of T1 hyperintense myelinated white matter in the posterior limbs of the internal capsules that is much better seen on the Wave-MPRAGE exam.

Conclusion

We have successfully used Wave-CAIPI to enable encoding-intensive high-resolution isotropic acquisitions across a variety of contrasts and clinical indications. The highly accelerated Wave-CAIPI examinations preserve image quality and achieve comparable diagnostic performance to the comparison standard protocol with a 2- to 5-fold reduction in scan time, depending on the pulse sequence, RF coil and field strength. The increasing interest and demand for fast brain imaging examinations ensures that Wave-CAIPI technology will benefit a widerange of individuals including motion-prone populations while decreasing the time that patients are in the scanner, thereby improving patient comfort, throughput and facilitating the more efficient use of valuable MRI resources.

Acknowledgments

The authors would like to thank Maria Gabriela Longo, John Kirsch, Chanon Ngamsombat, Paul Caruso, Michael Gee, and Azadeh Tabari for their valuable support.

References

1 Setsompop K, Feinberg DA, Polimeni JR.
Rapid brain MRI acquisition techniques at ultra-high fields.
NMR Biomed. 2016, 29: 1198–1221.

2 Bilgic B, Gagoski BA, Cauley SF, et al.
Wave-CAIPI for Highly Accelerated 3D Imaging.
Magn Reson Med. 2015, 73: 2152–2162.

3 Cauley SF, Setsompop K, Bilgic B, Bhat H, Gagoski B, Wald LL.
Autocalibrated wave-CAIPI reconstruction; Joint optimization of k-space trajectory and parallel imaging reconstruction.
Magn Reson Med. 2017;78(3):1093-1099. doi:10.1002/mrm.26499

4 Conklin J, Longo MGF, Cauley SF, et al.
Validation of Highly Accelerated Wave–CAIPI SWI Compared with Conventional SWI and T2*-Weighted Gradient Recalled-Echo for Routine Clinical Brain MRI at 3T.
AJNR Am J Neuroradiol. 2019, 40:2073–80.

5 Polak D, Setsompop K, Cauley SF, et al.
Wave-CAIPI for highly accelerated MP-RAGE imaging.
Magn Reson Med. 2018;79(1):401-406.

6 Longo MGF, Conklin J, Tian Q, et al.
Validation of ultrafast Wave-CAIPI magnetization prepared rapid gradient-echo (MPRAGE) for quantitative evaluation of brain tissue volume in the workup of suspected neurodegenerative disease.
American Society of Neuroradiology, 2019. Boston, MA.

7 Ngamsombat C, Longo MGF, Goncalves Filho ALM, et al.
Evaluation of Ultrafast Wave-CAIPI Three-Dimensional Fluid-attenuated Inversion Recovery (3D FLAIR) Compared to Standard 3D FLAIR for Quantitative Analysis of Cerebral White Matter Lesions.
Accepted for oral presentation at the Annual Meeting of the American Society of Neuroradiology, Las Vegas, Nevada.
May 30–June 04, 2020.

8 Goncalves Filho ALM, Longo MGF, Conklin J, et al.
Evaluation of Highly Accelerated Wave-CAIPI Post-Contrast 3D-T1 Sampling Perfection With Application Optimized Contrast Using Different Flip-Angle Evolutions (Wave-3D-T1 SPACE) Compared to Standard Post-Contrast 3D-T1 SPACE for Detection of Intracranial Enhancing Lesions. Accepted for oral presentation at the Annual Meeting of the American Society of Neuroradiology, Las Vegas, Nevada. May 30–June 04, 2020.

9 Polak D, Cauley SF, Huang SY, et al.
Highly-Accelerated Volumetric Brain Examination Using Optimized Wave-CAIPI Encoding.
J. MAGN. RESON. IMAGING. 2019, 50:961–974.

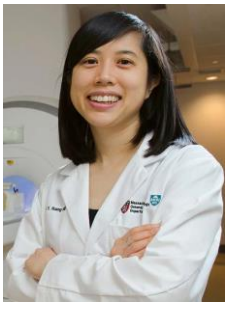

Contact

Susie Y. Huang, MD, PhD
Assistant Professor of Radiology, Harvard Medical School
Radiologist, Division of Neuroradiology
Director of Translational MR Imaging
Athinoula A. Martinos Center for Biomedical Imaging
Department of Radiology, Massachusetts General Hospital
Building 149, Room 2.301
Charlestown, MA 02129
USA
susie.huang@mgh.harvard.edu

[2]*MR scanning has not been established as safe for imaging fetuses and infants less than two years of age. The responsible physician must evaluate the benefits of the MR examination compared to those of other imaging procedures.*

Novelties in MR Fingerprinting

Gregor Körzdörfer

Siemens Healthineers, Erlangen, Germany

Magnetic Resonance Fingerprinting in brief

Magnetic Resonance Fingerprinting (MRF)[1] is a fast and precise technique for multiparametric quantitative MRI [1]. With MRF several tissue properties can be identified simultaneously in a single acquisition. Sequence parameters are varied pseudorandomly throughout the acquisition, to generate distinguishable tissue signals. These measured signals are then compared with a dictionary of pre-simulated signals. Each signal is unique and can therefore be considered a fingerprint for certain tissue properties. Comparing a measured fingerprint with all dictionary entries allows the most similar simulated fingerprint to be identified, revealing the fingerprint's properties.

Since its first publication in 2013, MRF has sparked much research interest. Besides clinical research with MRF, which is now facilitated by a commercially available implementation, a variety of technical aspects of the concept and extensions have been explored. While a commercially available MR Fingerprinting version requires a high-performance integration on the scanner as well as thorough validation to be ready for use in clinical studies, it should be clear that MR Fingerprinting continues to evolve vividly in the research arena. This includes modifying the acquisition scheme, for example with different *k-s* pace trajectories and extending the MRF concept to provide additional information such as magnetization transfer [2], diffusion [3], susceptibility and B0 [4] and B1+ [5, 6]. Another research area is optimal sequence design for specific MRF implementations, which can be addressed with optimization algorithms [7, 8].

This article sheds light on some novel developments driven by Siemens Healthineers. Please refer to the referenced literature for further reading.

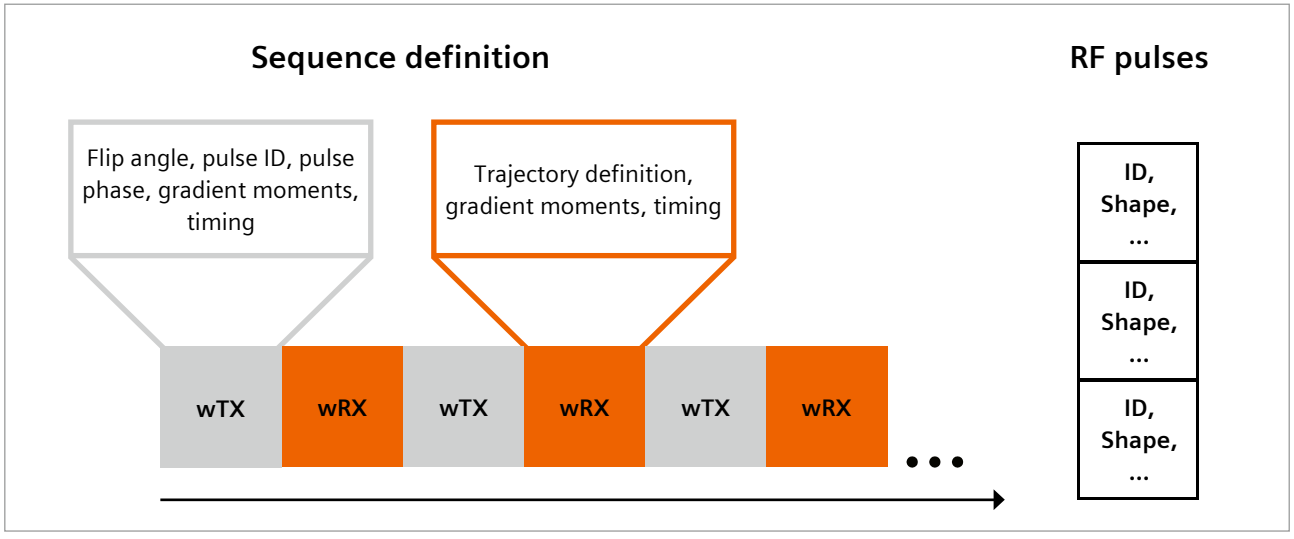

1 A sequence definition and a list of RF pulses labeled with a unique ID. The sequence definition consists of an arbitrary series of warp&TX events (wTX) and warp&RX events (wRX). In each wTX block the gradient moments and timing before the RF pulse are recorded, as is the specified RF pulse ID (linked from the RF pulse list) with its prescribed flip angle and phase. The wRX block contains information on the gradient moments and timing before the signal is sampled and the echo sampling time. Trajectory information can be contained or defined later at the scanner.

[1] *The product/feature (mentioned herein) is not commercially available in some countries. Due to regulatory reasons its future availability cannot be guaranteed.*

Promoting research: MRF development kit

One strength of the MRF idea is the freedom to combine different sequences and sampling schemes to optimize and extend MRF. However, quantitative MRI in general requires carefully considered sequence design and attention to detail, as it is highly sensitive to deviations between real experiment and limited theoretical models. Common effects are deviations in sampling trajectory, inhomogeneities of B0 and B1+, and effects not included in the signal model in general. Much effort needs to be spent in programming sequences, performing simulations for the dictionary, and implementing reconstruction algorithms and further infrastructure to handle the large amount of data, using performant data structures and interfaces. Some specific pitfalls are:

- The sequence scheme is replicated offline for the dictionary simulation and so may deviate from the actual scheme played out on the scanner in small but crucial details, such as RF-pulse profiles or the exact gradient moments. This of course also applies to conventional mappings where a simplistic signal model may not reflect the physical reality.
- A variety of Bloch simulators or extended phase graph algorithms exist that may lead to varying results for the same sequence input. These can be arbitrarily parametrized, which might further alter results between different handcrafted simulators.
- Once there is more than a single MRF version employed, special provisions are required to safely link each measured raw data file to the corresponding dictionary file. The same applies to changes of sequence parameters "on the fly", which may render the designated dictionary invalid. Reconstructions with a wrong dictionary will result in wrong mapping results, and the error may be hard to detect, so this must be avoided.

To simplify and harmonize the development of novel MRF implementations, we provide a framework that elegantly solves the aforementioned problems. This framework provides data structures for describing an MR sequence in a generic way.

A sequence is described by a chain of warp&TX (wTX) and warp&RX (wRX) blocks (Fig. 1). A wTX block consists of the gradient moments before a transmit pulse, as well as the gradient during the pulse, and the pulse ID. RF pulses can be stored in a different data structure, so that the same RF pulse can be used in multiple wTX events (Fig. 1). The wRX events contain similar gradient moment information, and also information about when signals are to be sampled. Blocks can contain trajectory information, but generally do not need to, because the assumption underlying today's MRF approaches is that simulated fingerprints are independent of in-plane pixel position – so trajectory information is usually not important for signal generation or for simulation, and it can be defined later directly at the scanner.

This sequence definition can be represented by a simple data structure, which can be easily filled using different programming languages such as Python, C++ and MATLAB. Together with a definable set of tissues, and ranges for physical parameters such as T1, T2, and B1+, it is then handed over to a fast C++ standalone Bloch simulator that rapidly creates a dictionary.

Both the sequence definition and dictionary are then wrapped together into an MRF container (Fig. 2). This container can be run on the scanner using an interpreter that executes the sequence definition. Acquired data is reconstructed in the ICE (Image Calculation Environment) environment utilizing the dictionary stored in the container, and finally DICOM images are generated.

The package facilitates the development of new MRF applications, and especially their direct application in

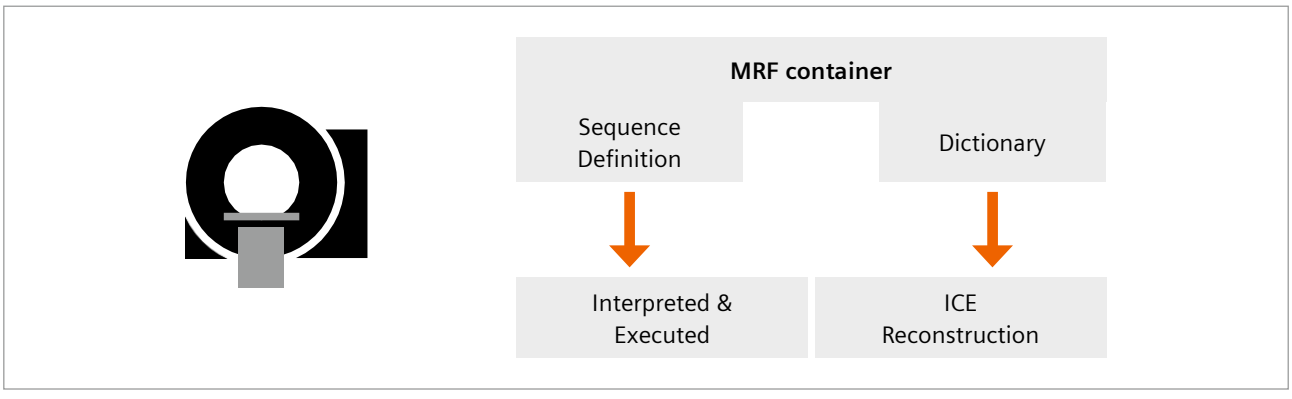

2 An MRF container with sequence definition and corresponding dictionary can be loaded onto the scanner. The sequence definition is interpreted and executed, and then tissue parameters are reconstructed using the dictionary for this sequence directly in ICE, generating DICOM maps.

clinical studies, due to its full scanner integration. Users also benefit from other features such as integrated correction methods for non-Cartesian sampling trajectories, and advanced reconstruction methods described later in this article.

One convenient and beginner-friendly application is parametrizing a spiral FISP MRF [9] sequence (Fig. 3). The user can specify repetition times, flip angles and phases of the pulses, as well as the parameters T1, T2, and B1+. A C++ standalone program then writes a FISP MRF sequence definition and dictionary files, which can be simply copied to the scanner for execution.

3D MRF

The framework idea also applies to 3D sequences. 3D acquisitions provide significant speedup and improved resolution for MRF. In addition to higher signal to noise ratio (SNR), a potentially more efficient undersampling along all three spatial dimensions can be employed. Examples are 3D Cartesian [10] or spiral projection sampling schemes. A 3D spiral stack FISP MRF sequence has recently been successfully applied in clinical studies for detecting epileptic lesions [11] and hippocampal sclerosis [12].

Novel reconstruction methods for MRF

MRF estimates parameter maps from highly undersampled signals. Assuming that spatial undersampling artifacts can be treated as noise in the temporal signal domain, dictionary matching can even be performed without any further measures. However, more advanced techniques aim to reconstruct better quality parameter maps by taking the effect of undersampling into account. An example is CS-MRF [13] which is an iterative gradient proximal algorithm for MRF, that uses the concepts of compressed sensing. An estimated image series is calculated in three steps: a gradient step to enforce data consistency; fingerprint dictionary matching; and spatial regularization via total variation regularization. CS-MRF extends the iterative reconstruction algorithm AIR MRF [14] with this spatial regularization. This provides parameter maps free of undersampling artifacts, as well as maps with lower noise, while fine structures and boundaries between tissues are preserved. Figure 4 shows an example of a volunteer's brain acquired at 3 mm slice thickness (acquisition time per slice: 21 seconds at 1 mm in-plane resolution) reconstructed with and without CS-MRF. Especially fine details are better visible, and the overall image impression is better with CS-MRF due to reduced noise.

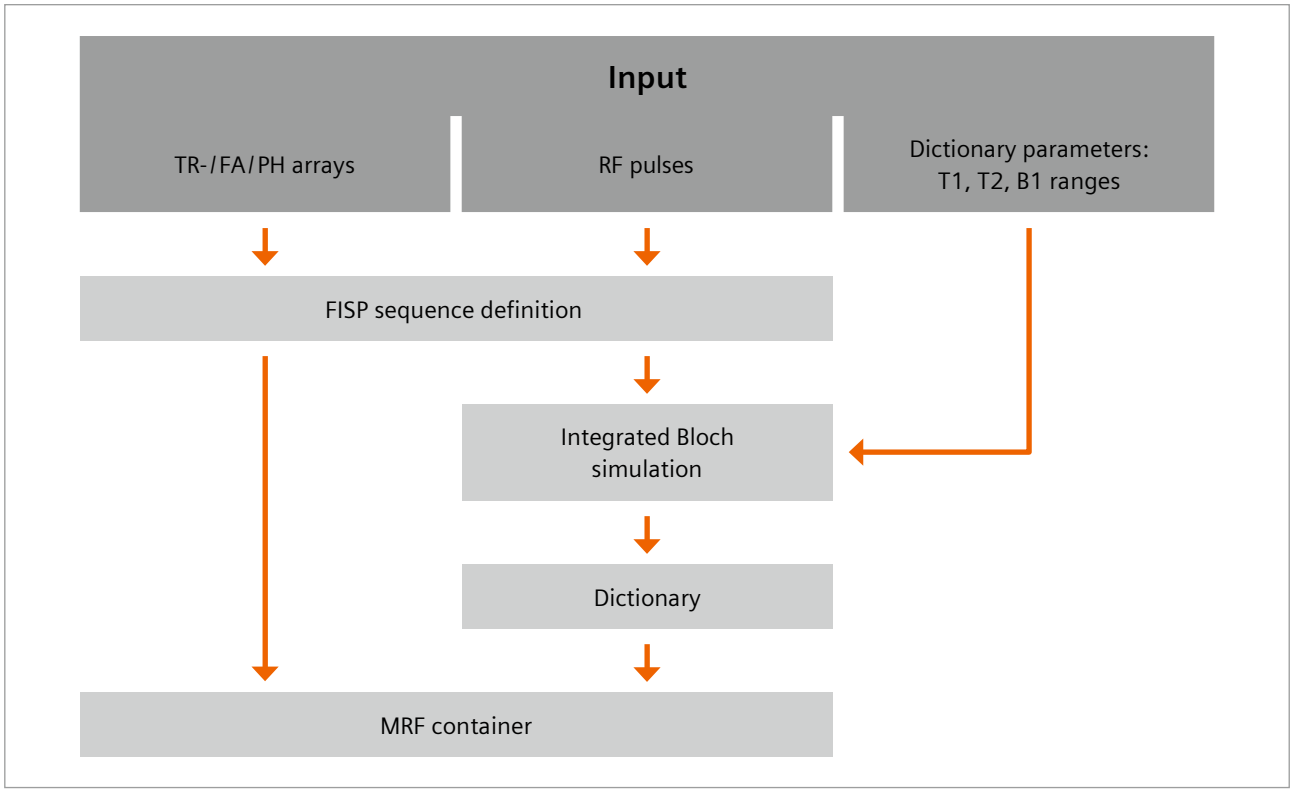

3 Example of a user-friendly use case for the MRF development kit. The user defines repetition time (TR), flip angle (FA) and pulse phase (PH) arrays, RF pulses, and the dictionary parameter ranges for T1, T2, and B1. With this information a precompiled program writes a spiral FISP MRF sequence definition, calculates the matching dictionary, and packs both together into an MRF container.

Another challenge for MRF reconstructions is the high computational effort, in particular if the dictionary increases in size. Every measured signal must be compared with every dictionary entry. Since every dictionary can only have a finite number of entries, the resulting maps are limited to this discrete set of entries, and are therefore intrinsically inaccurate. Furthermore, the more entries the dictionary contains, the more reconstruction time is required. Deep learning (DL) can be used to provide continuous parameter estimations, accelerate the MRF reconstruction process, and eliminate the burden of high storage requirements during the reconstruction. Reconstruction with DL algorithm is performed by passing the signal (or a set of signals from e.g., neighboring voxels) through a network, which predicts the T1 and T2 relaxation times from the input. Proposed approaches include fully connected neural networks (FCNs) and convolutional neural networks (CNNs). However, even state-of-the-art DL algorithms have their drawbacks. FCNs tend to overfit because of the huge number of optimizable parameters. CNNs are not optimally suited for time-resolved tasks.

To overcome these limitations, we recently evaluated recurrent neural networks (RNNs) due to their ability to better capture the continuous time dependency in typical MRF signals [15, 16]. RNNs (Fig. 5) were evaluated on *in vivo* data from several volunteers' brains. The results show that with this approach, precise parameter maps can be reconstructed in an extremely short time. RNNs are especially promising for large dictionaries comprising multiple dimensions, where conventional matching algorithms are limited due to the exponential character of the problem. Another promising approach is to separate the DL reconstruction into two networks: a first artifact reduction network cleans and restores the input signals, which are then fed into the regression network [17].

Motion detection for MRF

Motion artifacts in MRI are usually accompanied by visible image artifacts. In quantitative MRI, results may be affected in a more subtle way: values in the parametric maps can be corrupted without obvious hints in the appearance of the maps. MRF has a certain inherent robustness regarding motion due to the applied pattern matching approach. However, while MRF is indeed fairly insensitive to in-plane motion (as excited signal remains in the imaging plane), several works suggest that 2D FISP MRF is more sensitive to strong through-plane motion (as new spins enter the imaging plane during the acquisition).

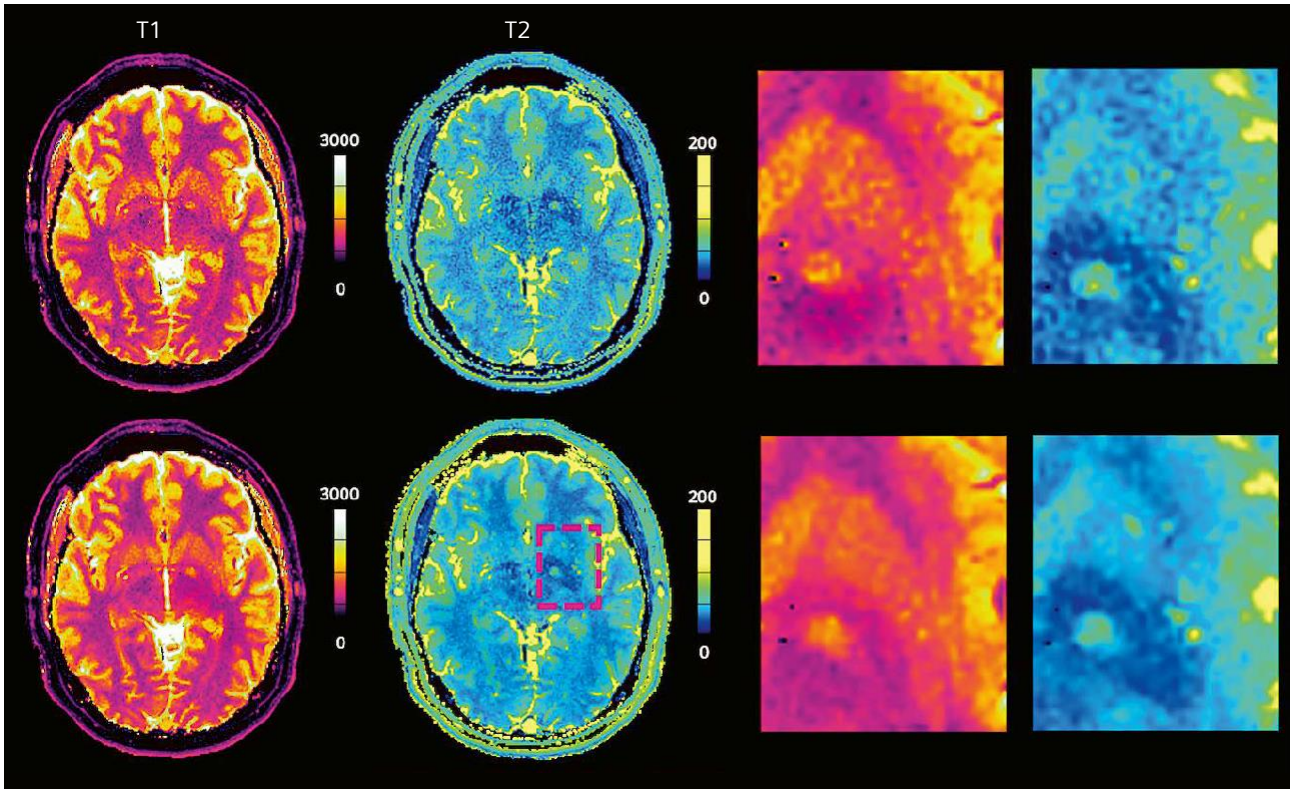

4 Top row: conventionally reconstructed FISP MRF T1 (first column) and T2 (second column) maps (21 seconds acquisition time per slice, slice thickness 3 mm, in-plane resolution 1 mm) with a zoomed excerpt on the right. Bottom row: The same slice parameter maps reconstructed using CS-AIR have substantially less noise while image details and tissue boundaries are preserved as observable in the excerpt on the right.

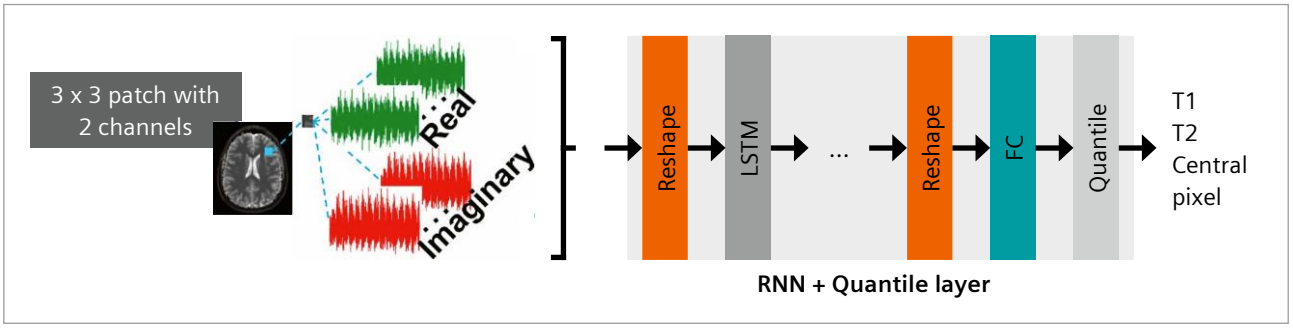

5 Architecture of the neural network for quantifying T1 and T2 from signals in MRF. A patch of complex signals is used as input and fed through a recurrent neural network (RNN) plus a quantile layer. (LSTM: long-short-term memory layer, FC: fully connected layer)

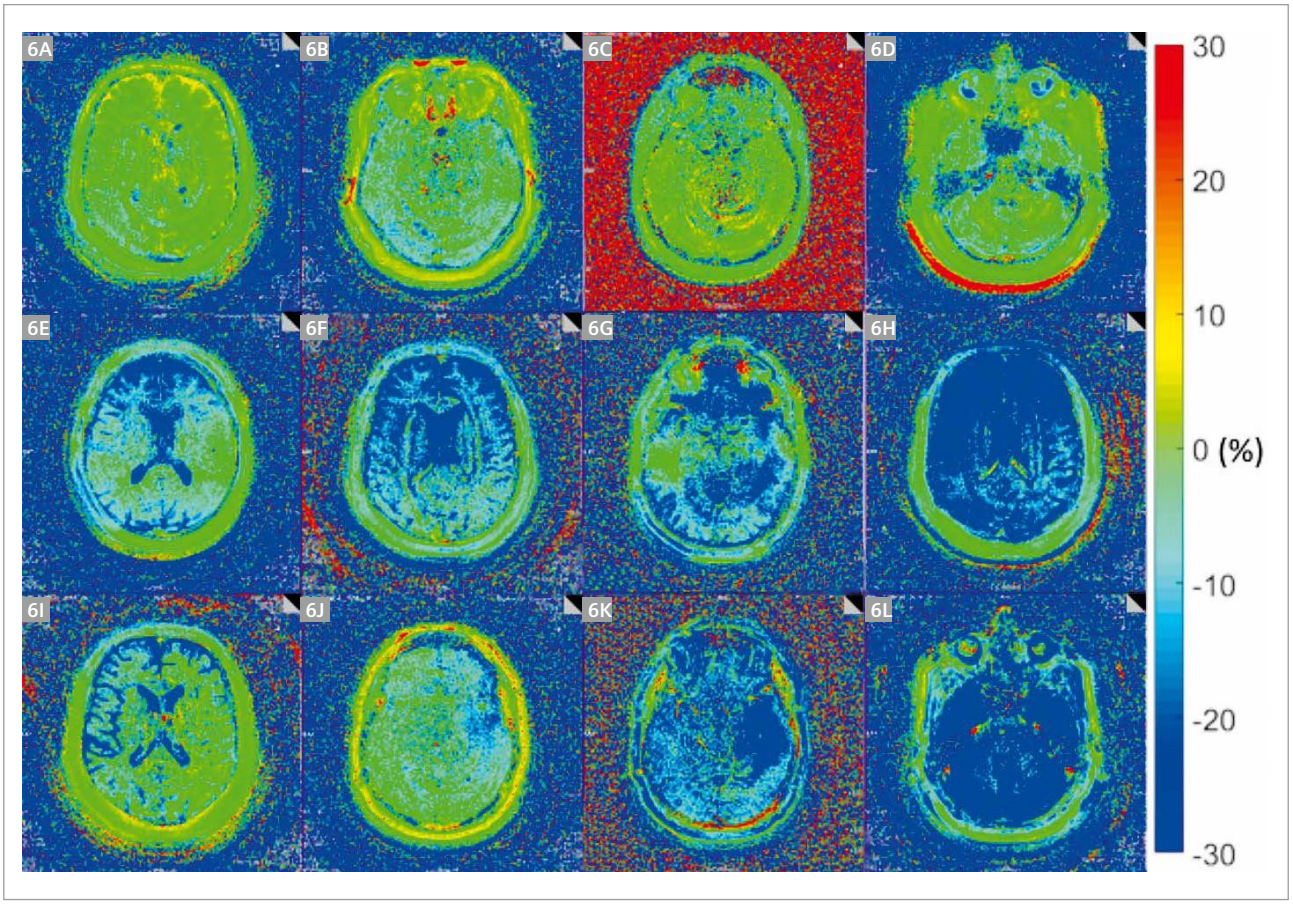

6 Exemplary residual maps (rel. deviation in %) obtained from patient brain MRF scans. 6A–D show residual maps where no motion occurred. 6E shows a pattern that corresponds to slight nodding; 6F and G medium nodding; 6H strong nodding. 6I and J show tilting of the head. 6K shows a slight stretching movement, and 6L a strong one.

Consequently, there should be a way to at least detect the presence of motion-related errors. A prototype method [18] demonstrates that this is feasible without any additional navigator scans or camera devices. It relies on the fact that bulk movement of the head is rigid (flowing CSF is not considered), and that signal alterations due to motion have high frequency compared with dictionary signals. The concept consists in comparing measured signals with the corresponding matched dictionary signals at different timepoints. This is possible due to the high sampling rate of spiral FISP MRF [9], where approximately every 600 microseconds a fully sampled image can be reconstructed from a set of single spiral frames.

These images do not provide a well-defined contrast, as the signal in MRF also varies strongly on short time scales, but they do enable the calculation of spatially and temporally resolved residuals with respect to the predicted ideal signal from the dictionary. These residuals exhibit certain patterns characteristic of typical head movements such as nodding, tilting, and stretching. Examples are shown in Figure 6. These can be evaluated manually or automatically, using a fitting algorithm such as a neural network. By doing a weighted sum of all detected motion patterns, an overall estimate (non, low, medium, strong) of the motion effect in a slice can be determined.

The technique was evaluated in volunteers and 32 patients with suspicion of glioma. Two MRF acquisitions were performed, so the difference between the two acquisitions could be related to the detected motion. Where there was no detected motion, the average difference of parameter values from the two acquisitions was approximately 2%. For acquisition pairs where one was not motion corrupted and the other exhibited low, medium, or strong motion, the average differences were 3%, 5% and 25% respectively. With the help of the algorithm, motion corrupted scans could be identified reliably. Overall in 77% of all measured slices no motion, in 8.8% low motion, in 9.4% medium motion, and in 4.8% strong motion was detected.

References

1 D. Ma, V. Gulani, N. Seiberlich, K. Liu, J. L. Sunshine, J. L. Duerk, and M. A. Griswold, "Magnetic resonance fingerprinting," Nature, vol. 495, no. 7440, pp. 187–192, 2013.

2 Hilbert, T, Xia, D, Block, KT, et al. Magnetization transfer in magnetic resonance fingerprinting. Magn Reson Med. 2019; 00: 1–14.

3 Jiang, Yun, et al. "Simultaneous T1, T2 and Diffusion Quantification using Multiple Contrast Prepared Magnetic Resonance Fingerprinting." Proceedings of the 25th Annual Meeting of ISMRM, Honolulu, HI, USA. 2017.

4 Körzdörfer, G, Jiang, Y, Speier, P, et al. Magnetic resonance field fingerprinting. Magn Reson Med. 2019; 81: 2347–2359.

5 Cloos, M., Knoll, F., Zhao, T. et al. Multiparametric imaging with heterogeneous radiofrequency fields. Nat Commun 7, 12445 (2016).

6 Buonincontri, G. and Sawiak, S.J. (2016), MR fingerprinting with simultaneous B1 estimation. Magn. Reson. Med., 76: 1127–1135.

7 Zhao, Bo, et al. "Optimal Experiment Design for Magnetic Resonance Fingerprinting: Cramer-Rao Bound ´Meets Spin Dynamics" in IEEE Transactions on Medical Imaging, vol. 38, no. 3, pp. 844–861, 2019.

8 Cohen, Ouri, et al. "Algorithm comparison for schedule optimization in MR fingerprinting" in Magnetic Resonance Imaging, vol. 41, pp. 15–21, 2017.

9 Y. Jiang, D. Ma, N. Seiberlich, V. Gulani, and M. A. Griswold, "MR fingerprinting using fast imaging with steady state precession (FISP) with spiral readout," Magnetic resonance in medicine, vol. 74, no. 6, pp. 1621–1631, 2015.

10 Jiang, Yun, et al. "Fast 3D MR Fingerprinting with Pseudorandom Cartesian Sampling." Proceedings of the 27th Annual Meeting of ISMRM, Montréal, Canada. 2019.

11 Ma, D., Jones, S.E., Deshmane, A., Sakaie, K., Pierre, E.Y., Larvie, M., McGivney, D., Blümcke, I., Krishnan, B., Lowe, M., Gulani, V., Najm, I., Griswold, M.A. and Wang, Z.I., "Development of high-resolution 3D MR fingerprinting for detection and characterization of epileptic lesions". J. Magn. Reson. Imaging, 49: 1333–1346, 2019

12 Congyu Liao, Kang Wang, Xiaozhi Cao, Yueping Li, Dengchang Wu, Huihui Ye, Qiuping Ding, Hongjian He, and Jianhui Zhong, "Detection of Lesions in Mesial Temporal Lobe Epilepsy by Using MR Fingerprinting", Radiology 2018 288:3, 804–812.

13 S. Arberet, X. Chen, B. Mailhé, P. Speier, and M. S. Nadar, "CS-MRF: Sparse & low-rank iterative reconstruction for magnetic resonance fingerprinting" in ISMRM Workshop on Magnetic Resonance Fingerprinting, 2017.

14 Christopher C. Cline, Xiao Chen, Boris Mailhe, Qiu Wang, Josef Pfeuffer, Mathias Nittka, Mark A. Griswold, Peter Speier, Mariappan S. Nadar, AIR-MRF: Accelerated iterative reconstruction for magnetic resonance fingerprinting, Magnetic Resonance Imaging, 74: 29–40, 2017.

15 Hoppe, Elisabeth, et al. "Deep learning for magnetic resonance fingerprinting: Accelerating the reconstruction of quantitative relaxation maps." Proceedings of the 26th Annual Meeting of ISMRM, Paris, France. 2018.

16 Hoppe, Elisabeth, et al. "RinQ Fingerprinting: Recurrence-Informed Quantile Networks for Magnetic Resonance Fingerprinting." International Conference on Medical Image Computing and Computer-Assisted Intervention. Springer, Cham, 2019.

17 Xu, Yiling, et al. "Learning how to Clean Fingerprints – Deep Learning based Separated Artefact Reduction and Regression for MR Fingerprinting." Proceedings of the 28th Annual Meeting of ISMRM, Paris, France. 2020.

18 Körzdörfer, Gregor, et al. "Data-driven Motion Detection for MR Fingerprinting" Proceedings of the 28th Annual Meeting of ISMRM, Paris, France. 2020.

Contact

Gregor Körzdörfer
Siemens Healthineers
SHS DI MR DL Orth
Erlangen, Germany
Tel.: +49 (0) 9131 84-7192
Gregor.Koerzdoerfer@siemens-healthineers.com

A Path to Establishing MRSI as a Clinical Standard Imaging

Mohammed Goryawala[1]; Hui Han[2]; Zahra Hosseini[3]; Sinyeob Ahn[3]; Gerald R. Moran[4]; Hyunsuk Shim[5]

[1]Department of Radiology, University of Miami, Miami, FL, USA
[2]Biomedical Imaging Research Institute, Cedars-Sinai Medical Center, Los Angeles, CA, USA
[3]Siemens Healthineers, Malvern, PA, USA
[4]Siemens Healthineers, Oakville, ON, Canada
[5]Department of Radiation Oncology and Radiology and Imaging Sciences, Winship Cancer Institute, Emory University School of Medicine, Atlanta, GA, USA

Abstract

This article introduces the evolution of technology for magnetic resonance spectroscopic imaging (MRSI) of the brain, and in particular describes 3D proton spectroscopic MRI with whole-brain coverage and its application to patients with brain tumors. Unfortunately, vendor-provided MRS technology for clinical use typically lags behind the capabilities developed in research labs and to date is limited to either single voxel or multi-voxel localization with very limited spatial coverage and resolution. Here, a multisite effort to transform this technology toward clinical standard imaging is described.

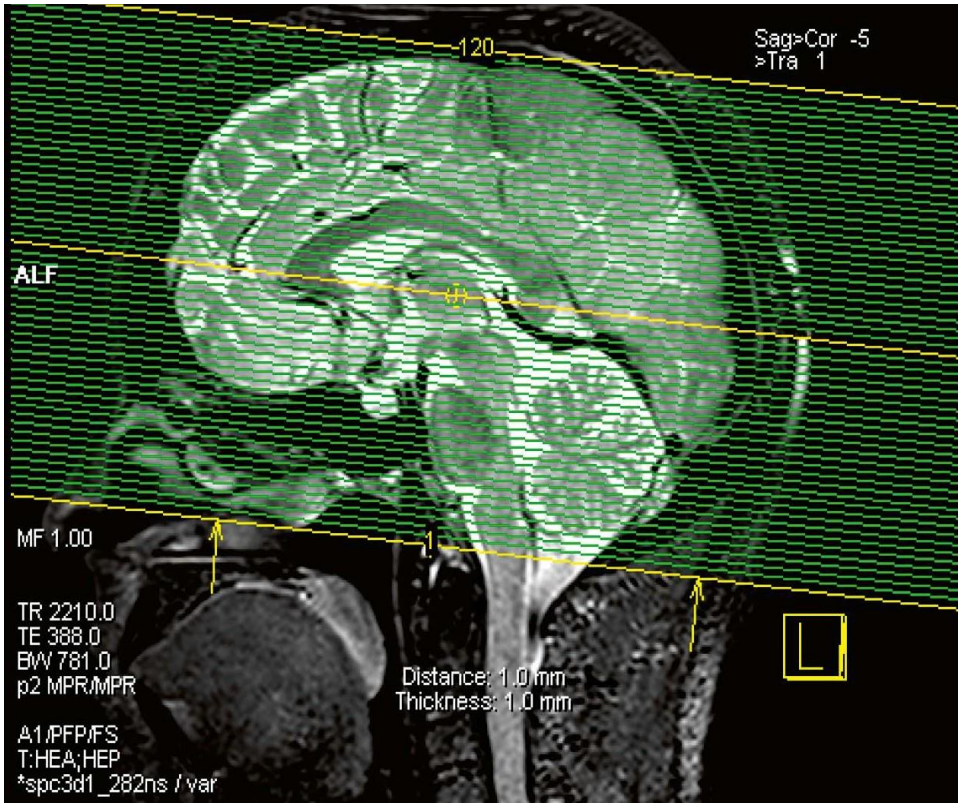

1 Example setup (graphical prescription) for a GRAPPA-encoded EPSI acquisition as described in the text.

The concepts and information presented in this paper are based on research and not commercially available.

Proton MRS-detectable metabolites of brain

Because of the relatively low sensitivity of *in vivo* ^{1}H magnetic resonance spectroscopy (MRS), in order for a compound to be detectable following successful water and lipid suppression, its concentration must be in the millimolar range, and it must be a small, mobile molecule. The information from a brain spectrum depends on several factors, such as the field strength used, echo time, and type of pulse sequence. On a 1.5T scanner with long echo times (e.g., 140 or 280 ms), only choline (Cho), creatine (Cr), and N-acetyl aspartate (NAA) are observable in the healthy brain, while compounds such as lactate (Lac), alanine, or others may be detectable if their concentrations are elevated above normal levels due to abnormal metabolic processes [1–3]. At short echo times (≤ 35 ms), more compounds become detectable. These include glutamine and glutamate, but these are not resolved from each other at 1.5T. In addition, myo-inositol, lipids, and macromolecules are detectable.

The largest signal in the healthy brain spectrum is the acetyl group of NAA that resonates at 2.0 ppm [4, 5]. NAA is often referred to as a healthy neuronal biomarker. The Cho signal (3.2 ppm) is involved in membrane synthesis and degradation and is commonly elevated in many types of tumors, including the brain, prostate, breast, liver, and other tumors [6]. The Cr at 3.0 ppm is involved in energy metabolism via the Cr kinase reaction, generating ATP. Cr shows quite large regional variations, with lower levels in white matter than gray matter in normal brain, as well as higher levels in the cerebellum compared to supratentorial regions [7]. The individual/regional variations in Cr levels are higher than NAA or Cho in normal brains. In a healthy brain, the methyl resonance of Lac (1.33 ppm) is barely detectable under normal conditions. Increased levels of brain lactate have been observed in a variety of conditions, including ischemia and tumor [1, 8]. Lac may be difficult to distinguish from overlapping lipids which have similar chemical shifts, either originating from the brain itself, or spatial contamination from the scalp. Myo-inositol (mI) is one of the larger signals in short echo time spectra (≤ 35 ms), occurring around 3.5–3.6 ppm. mI is a pentose sugar, which is part of the inositol triphosphate intracellular second messenger system. mI levels have been found to be increased in Alzheimer's dementia [9] and demyelinating diseases [10]. The exact pathophysiological significance of alterations in mI is uncertain, but a leading hypothesis is that elevated mI reflects increased populations of glial cells [11, 12], which may be linked to both degenerative and inflammatory diseases. mI has also been reported to be elevated in low-grade gliomas [13] and also correlates with depression status of GBM patients [14–16]. There are more than 25 additional compounds that have been assigned in ^{1}H MRS of the human brain. Some of these compounds are present in the normal brain but are difficult to detect routinely because they are too small and/or have overlapping peaks. Some examples of these compounds include aspartate, glycine, glutathione, ethanolamine, purine nucleotides, GABA, histidine, taurine, scyllo-inositol, and glucose [17]. Others may only be present under abnormal or pathological conditions, for instance, alanine, 2-hydroxyglutarate, phenylalanine, and ketone bodies. Occasionally exogenous compounds such as mannitol, ethanol or methyl-sulfonyl methane, all of which freely cross the blood-brain barrier, may also be observed in the spectrum.

Current state-of-the-art 3D MRSI

Multi-voxel (2D, or 3D) MRSI sequences are commonly available on commercial MR scanners [18], but their application has a number of problems, such as chemical shift displacement effects and restricted coverage due to the rectangular excitation of the voxel. Lipid signal bleeding from these effects can confound data quality and difficulty of appropriate data analysis. To avoid these problems, an alternative approach is to use a spin-echo sequence with outer volume suppression (OVS) pulses to suppress the lipid signals from the scalp, which can be readily extended to a multi-slice approach to obtain improved brain coverage [19]. These conventional Cartesian 2D or 3D phase-encoding approaches can give excellent quality data but are too time-consuming for clinical routine use because of the large number of phase-encoding steps to be collected. Therefore, a number of different approaches for fast MRSI have been developed (reviewed in [20–22]); however, so far these techniques have had a limited clinical impact, mainly because they are not commercially available nor mature enough for clinical applications. To reduce scan time, several *k*-space under-sampling strategies such as parallel imaging or compressed sensing have been applied to conventional MRSI, which involve tradeoffs for data quality, scan time, and spatial resolution [23–25].

Echo-planar spectroscopic imaging (EPSI) is a promising method for acceleration of whole-brain MRSI [26–29]. 3D EPSI has been used to study numerous different brain pathologies over the last two decades [30, 31]. The data displayed in the remainder of this chapter were obtained using 3D EPSI with whole-brain coverage, combined with GRAPPA and elliptical *k*-space encoding on a 3T MRI scanner with either 20- or 32-channel head coil arrays (Fig. 1). After the routine field map-based automated shim procedure on the scanner [32], it is strongly recommended to check the water linewidth to be less than ~25–28 Hz. If it is higher than 30 Hz, a brief 1st order manual shimming (x-, y-, and z-directions only) is recommended to reduce water linewidth, which can significantly improve the signal-to-noise ratio (SNR) and water/lipid suppression,

thus critical to obtain high-quality 3D data. A 3 pulse 'WET' [33] water suppression scheme is used along with lipid suppression by using a slab selective short TI (198 ms) inversion recovery (STIR) scheme [34, 35]. The EPSI pulse sequence also includes an interleaved small flip angle (20˚) water reference excitation [36] and GRAPPA spatial encoding [37] to shorten scan time (~15 minutes). The scan parameters used for images presented in this article are as follows: TR/TE/TI = 1710/17.6/198 ms, matrix size 50 x 50 x 18; 280 x 280 x 180 mm^3 FOV; 155 mm excitation slab thickness; interpolated matrix of 64 x 64 x 32 (Fig. 1) [38]. The quality of an acquired spectrum is critically dependent on the success of adjusting the field homogeneity (shimming), setting the scanner center frequency (on-resonance with water), and adjusting the flip angle(s) of the water suppression pulses. The failure of any one of these processes can lead to an uninterpretable spectrum. In the early days of MRS, many of these steps were performed manually by an operator, but for the current sequence, these steps are usually performed in an automated procedure offering greater ease and versatility for the application of the developed imaging methods in clinical environments.

Raw data are processed using the Metabolite Imaging and Data Analysis System (MIDAS[1], University of Miami, USA) [39]. This included B_0 and phase correction using the water reference data prior to any further processing in the frequency domain. The relative gray- and white-matter tissue and cerebrospinal fluid (CSF) contents in each SI voxel were estimated by downsampling the tissue segmentation maps, which were obtained using FSL/FAST algorithm [40], using the spatial response function of the EPSI acquisition. Additional processing included generating masks for brain and lipid regions, *k*-space extrapolation to reduce the contribution of extracranial lipid into the brain [41], linear registration between the T1-weighted MR and MRSI (TE = 50 ms), and signal intensity normalization following the creation of individual metabolite maps. Automated spectral analysis was carried out for 3 metabolites (NAA, Cr, Cho) or 6 metabolites (NAA, Cr, Cho, mI, lactate, and Glu/Gln (Glx)) [42]. Additional maps are generated for the fitted spectral linewidth and the Cramer-Rao lower bounds (CRLB) of fitting for each metabolite. Generated metabolite maps are overlaid on clinical images with a nominal voxel size of 4.4 x 4.4 x 5.6 mm are shown in Figure 2. The red contour represents two times elevated Cho/NAA ratio compared to the contralateral side. As apparent in Figure 2, not all metabolically active tumors are visible in standard MRIs (contrast-enhanced T1w-MRI and T2-SPACE). The MIDAS program package[1], developed by Dr. Maudsley and his team at the University of Miami is distributed together with the EPSI sequence at no cost under the GNU General Public License. For further information, the readers can reach out to their local Siemens Healthineers Collaborations Scientist.

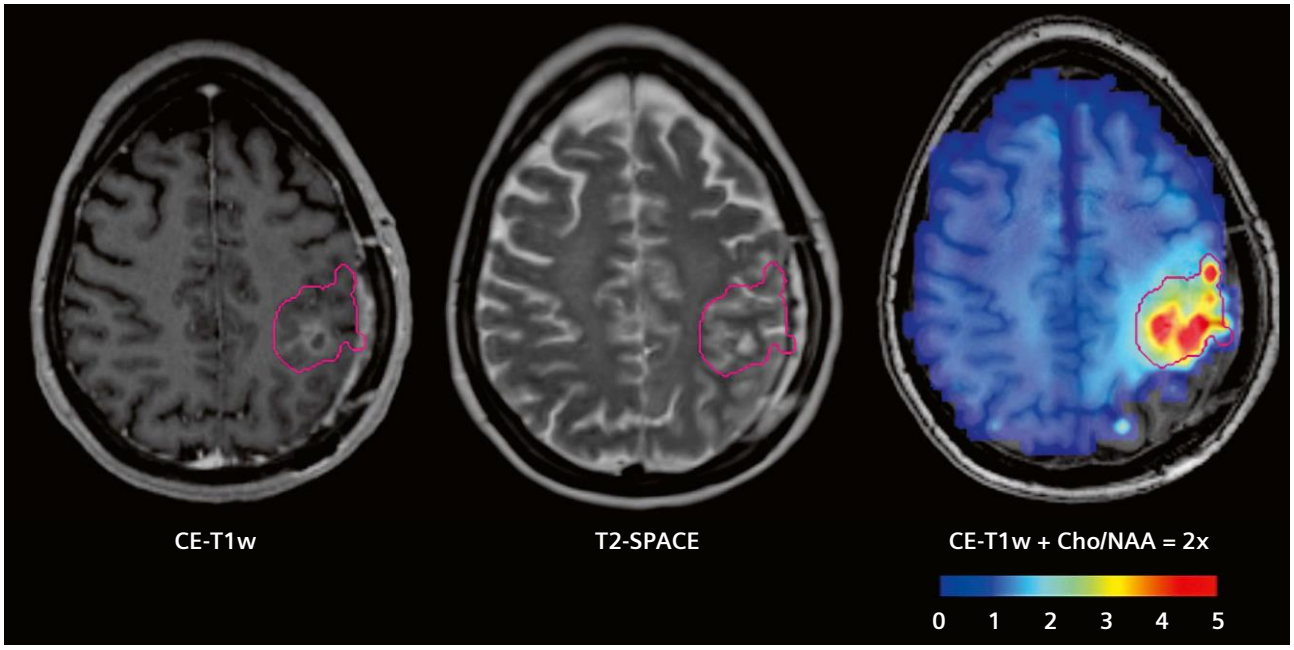

2 Views of anatomical and metabolite data with Cho/NAA ratio contour in red (2-fold over normal contralateral white matter). **(2A)** Contrast-enhanced T1w MRI; **(2B)** T2-SPACE MRI; **(2C)** Cho/NAA ratio map overlaid on T1w MRI. Cho/NAA ratio heat map shows metabolic abnormalities beyond CE-T1w or T2-SPACE MRIs and gives insight into the metabolic heterogeneity of the tumor and surrounding tissue. TE = 50 ms was used.

[1]*The information shown herein refers to products of a 3rd party and thus are in their regulatory responsibility. Please contact the 3rd party for further information.*

Developing the next generation of clinical spectroscopic MRI for patients with brain tumors

During the past decade, technological developments have transformed a single slice or multislice collection of 2D multivoxel chemical shift imaging (CSI) into a robust 3D imaging modality with the increased availability of 3T scanners, multichannel detector systems, new encoding methods, accelerated processing methods, automated artifact removal, and new approaches for obtaining whole-brain metabolite maps co-registered/overlaid with other clinical MR images. These developments allow MRSI to be addressed as "spectroscopic MRI", which is a significant improvement over standard vendor-provided 2D CSI techniques.

While MRSI has been shown to be capable of providing clinically useful information associated with disease processes or treatment, it has not had much impact on clinical care and its use remains largely confined to the research community. Technological advancements are required towards the acquisition, processing, interpretation, and dissemination of the MRSI data for true integration of spectroscopic MRI in the clinic. The current methods in whole-brain EPSI for water and lipid suppression are limited in their performance and are difficult to use for high-resolution whole-brain metabolite mapping due to SNR constraints. Improvements in methods for lipid and water suppression can offer a significant improvement in spatial resolution. Further, the adoption of methods that do not rely on inversion recovery for lipid suppression can improve imaging time and spatial coverage. The addition of these changes to the acquisition methods has the potential to elevate MRSI to true whole-brain technique with > 85% brain coverage with enhanced performance in critical cortical areas that are vital to a number of neurological applications.

Together with improved imaging, optimized reconstruction techniques play a vital role in more effective integration of spectroscopic imaging in the clinical environment. The current pipelines for EPSI data processing require time-consuming data transfer of multi-gigabyte datasets and processing on offline computers/servers which can be challenging for wider adaptation. In addition, to be able to fit the clinical workflow, the entire processing pipeline, including co-registration of metabolite and ratio maps with conventional anatomical MR images, should take less than an hour in order for the timely generation of the radiology report in the clinic. In currently available processing packages (such as MIDAS), one of the major bottlenecks is the time taken by the quantitative fitting routines which extract information on metabolite peak areas (proportional to concentrations) from the spectral data. As most fitting methods are based on iterative parametric modeling and the incorporation of a priori metabolite spectral information, one voxel at a time, and since high-resolution EPSI with whole-brain coverage generates several thousand spectra that need to be fit, it is virtually impossible to complete the entire processing pipeline in one hour on commonly available scanner computers. Furthermore, the complexity of MRSI technology requires on-site MRS experts to supervise the scanning of patients, process and analyze the data, and interpret the results with the clinicians involved. A particularly important role of on-site MRS experts is to recognize artifactual spectra and eliminate them before clinical decision making. Finally, the programs developed to process and display MRSI results are primarily for MRS experts, and not appropriate for general use by clinicians or other staff who do not have specialist training in MRS. Current multisite efforts at improving MRSI focus on a multi-faceted approach that aim to significantly improve processes from acquisition to the clinical deployment of spectroscopic MR imaging for its wider acceptance in clinical workflows based on NIH/NIBIB U01 funding (Han/Maudsley/Li/Cooper/Shim).

I. High-resolution mapping of brain metabolites

Brain metabolite concentrations are on the order of 10 mM or less, whereas water protons in the brain at approximately 80 M and lipid protons in peri-cranial fat, also at very high concentrations, are also present. The current methods in whole-brain EPSI for water and lipid suppression are limited in their performance and are difficult to use for high-resolution whole-brain metabolite mapping due to SNR constraints. To overcome these issues a novel acquisition scheme that increases SNR to enable the generation of higher-resolution MRSI metabolite maps using dual-band water and lipid suppression has been developed. Volumetric whole-brain MRSI can be acquired with TR = 950 ms and TE of 17.6 or 50 ms. Water and lipid suppression were carried out using the hypergeometric dual-band pulses [43] to create a passband between 1.8 and 4.2 ppm with Mz/Meq > 0.99 with Bloch equation simulations to derive the parameters for the individual hypergeometric pulses. Real-time frequency measurement and adjustment were carried out by sampling the water frequency every TR. The removal of inversion-based lipid nulling resulted in a significant improvement in SNR that enabled higher spatial sampling in the phase encoding direction to yield nominal voxel volume of 75.16 mm^3 and a zero-filled interpolated resolution of 1.3 x 2.0 x 2.5 mm with a FOV of 170 x 260 x 120 mm left-right, anterior-posterior, and head-foot directions, respectively with an acquisition time of 15 minutes using a GRAPPA factor of 1.3 in the phase-encoding direction. In conjunction with new sequence development, novel post-processing methods for tissue segmentation to improve masks for brain and lipid, lipid suppression using a frequency-

selective filtering technique using Hankel Lanczos singular value decomposition (HLSVD), and methods for estimation of regional metabolite ratios significantly improve the quality of generated high-resolution metabolite maps. The new acquisition methods have delivered excellent spectral quality as seen in Figure 3 with Figure 3A showing a short TE spectrum from normal white matter areas in a control subject whereas Figure 3B shows a TE 50 ms spectrum from a patient with high-grade glioma. The Ernst angle of the excitation pulse was set according to the TR for both acquisitions. SNR estimated as the ratio of the area under the NAA (or Cho in the absence of NAA) peak to the standard deviation of the noise, estimated between 0 to 1.2 ppm [44] is reported besides the spectra. SNR is expressed in decibels (dB) as 10*log10 (SNR).

Good coverage was observed across the brain with improved performance compared to previous lower resolution implementations of the EPSI sequence as evident from metabolite maps for a patient with high-grade glioma (Fig. 4). Brain coverage (defined as the percentage of brain voxels with linewidths of < 13 Hz) of as high as 80% was obtained in control subjects. Previous MRSI methods that employ multiple OVS bands to reduce lipid signals, or those using sparse reconstruction-based techniques, are often limited in their ability to map cortical regions. Moreover, lower resolution whole-brain approaches also perform poorly in cortical regions due to lipid signal bleeding and partial volume effects [45]. The high-resolution MRSI in the glioma case of Figure 4 shows the potential for better delineation of tumor boundaries, for instance for improved guidance of biopsies or radiation treatment planning.

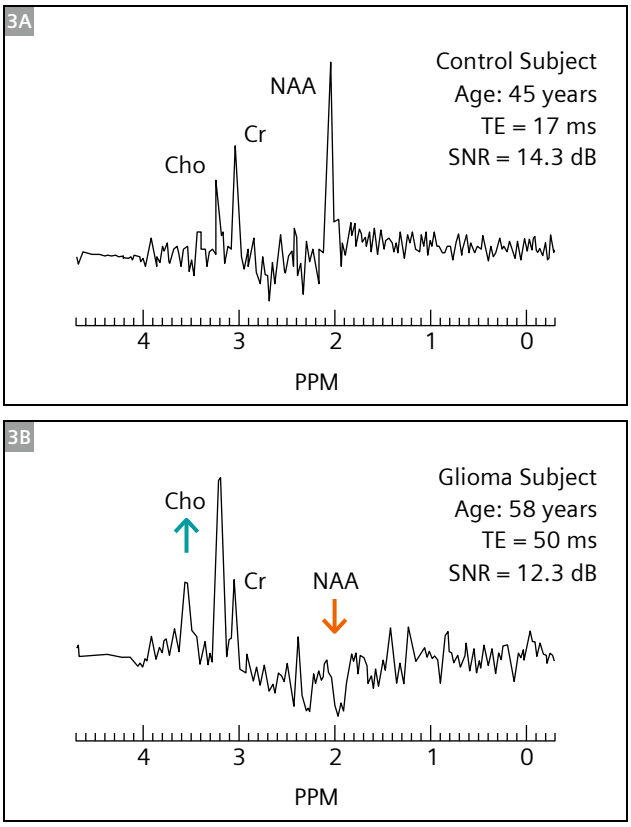

3 Representative spectra obtained using the proposed whole-brain MRSI. **(3A)** White matter spectra in a control subject acquired at TE = 17.6 ms. **(3B)** Tumor spectra in a high-grade glioma patient acquired at TE = 50 ms. Tumor spectra show lowered NAA (red arrow) and increased Cho (blue arrow).

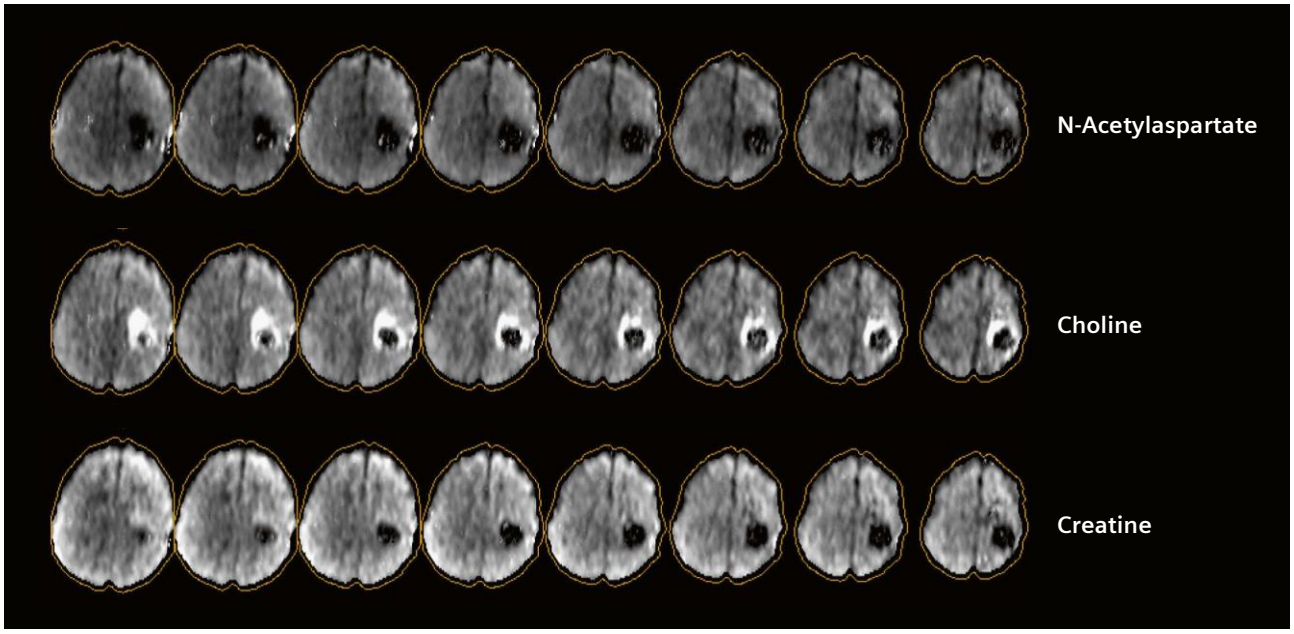

4 N-Acetylaspartate, Choline, and Creatine maps obtained using the high-resolution whole-brain MRSI sequence in a high-grade glioma patient acquired at TE = 50 ms.

II. Accelerated processing for rapid reconstruction
With the aim of fitting the entire MRSI pipeline, from the acquisition of the data to presentation of metabolite maps to the neuroradiologist within a clinically acceptable timeline (1 hour), the EPSI sequence was enhanced to perform the bulk of the time-consuming post-processing components on Siemens Healthineers platform. On-scanner processing pipelines were developed to perform data curation, echo correction, GRAPPA reconstruction and coil combination. The advantages of performing the operations on the scanner is a significant reduction (4-fold) of reconstruction time as compared to using remote systems in addition to significant reduction of data size needed to be transferred to secondary systems that fit the spectra for metabolite quantification. In this scenario, the on-scanner reconstructed data are of the order of 1 gigabyte in size as compared to ~30 gigabytes of raw data which results in significant reductions in transfer times. Moreover, intelligent pipelines have been developed that perform data reconstruction during the acquisition of other clinical sequences allowing complete on-scanner reconstruction possible before a patient leaves the facility. Furthermore, automated data transfer can be achieved by utilizing the Siemens Healthineers provided BOLD addin to transfer on-scanner processed data to remote computers/servers for further processing. Further processing carried out on the remote computer (or clouds) using MIDAS the Brain Imaging Collaboration Suite (BrICS) can be fully automated and generates metabolic images that can be sent to the institutional Picture Archiving and Communication System (PACS) for review by a radiologist in time to generate radiology report.

III. Accelerated spectral fitting using machine learning
A variety of methods have been developed for frequency domain analysis for single or multivoxel MRS [42, 46, 47]. Common analysis methods include parametric curve-fitting routines, using various model functions such as Lorentzian and Gaussian [48, 49] and fitting algorithms (simplex, non-linear least squares, etc.). The most sophisticated method, and one which is widely used, is the linear combination model ('LCModel') that fits the spectrum as a linear combination of the spectra of pure compounds known to exist in the spectrum [50]. Although LCModel works well for single-voxel and conventional MRSI data, it cannot process other types of fast MRSI data (such as EPSI). The MIDAS package for processing EPSI data [26] includes a spectral fitting routine that utilizes iterative expectation-maximization algorithms to estimate peak area parameters; however, it currently takes 40–60 minutes to execute on a high-end multicore workstation, which hampers the adaptation of MRSI into the routine clinical workflow. To overcome this, a novel fitting algorithm based on convolutional networks (FastFit) was developed, which provides rapid fitting of thousands of spectra from each EPSI data set in under 1 min using typical-performance computers that are found on MR scanners [51]. FastFit incorporates a priori knowledge of spectral physics into a deep learning algorithm that computes coefficients for a wavelet-based baseline and Lorentzian-Gaussian peak functions, published by Soher et al. [42]. Results suggest that this method is also more tolerable to baseline and other artifacts than traditional curve-fitting methods, and can effectively produce maps of metabolites and metabolite ratio 3D volumes for clinical interpretation in a timely manner [51].

IV. Development of automated artifact removing filter
As stated above, the clinical application of MRSI has been hampered due to challenges arising from: (a) artifacts in the data, which can produce erroneous classifications of tissue; and (b) a lack of consistent and validated models for spectral quality assessment.

The MIDAS program package includes first-pass multiple filters to eliminate poor quality spectra; (1) data are not included for spectral analysis if the water linewidth is > 18 Hz; and (2) following spectral fitting measures of linewidth (typically < 13 Hz), Cramer-Rao lower bounds (CRLB) (e.g., < 20% for Cr), and spectral outlier detection are used. Despite these first-pass filtering, many exceptions still occur and can lead to false-positive or false-negative detection of 'abnormal' spectra (e.g., based on ratios of Cho/NAA). Therefore, confirmation of true metabolic abnormality requires a manual review of individual spectrum by MRS experts, rather than a mere observation of maps of metabolite distributions alone. However, with several thousands of spectra in a single whole-brain EPSI scan, manual review by qualified MRS expert(s) is impractical and not scalable. To adopt whole-brain EPSI data into the clinical workflow, it is, therefore, necessary to develop additional automated spectral quality algorithms. Since there are no consistently accepted metrics for spectral quality [52], a novel algorithm for identifying and filtering spectral artifacts that arise from field inhomogeneities has recently been developed and validated [53]. This approach uses a convolutional neural network (CNN) trained using a curated dataset of 10,000 voxels derived from GBM patients and labeled by multiple MRS experts. The resulting filter can accurately recognize the broad range of spectral artifacts (e.g., due to poor water suppression, lipid suppression, low SNR, or baseline shifts) and provides highly specific and sensitive (AUC = 0.95) artifact classification to remove voxels with poor quality. This CNN-based filter complements the existing quality evaluation methods currently provided by MIDAS. In addition, an anatomical filter can exclude spectra from certain regions of the brain that have different normal metabolite levels and ratios than the cerebrum, using atlas-based registration [54].

V. Development of image viewing platform specialized for EPSI acquisition for non-MRS experts

Most programs to process/display EPSI data are not user-friendly and require significant training. They are challenging for clinicians or other non-MRS experts to use. To better facilitate the use of 3D whole-brain spectroscopic information in a clinically useful manner and promote real-time collaboration/support from MRS experts who are not necessarily available on-site, a web-based software platform has been developed for EPSI data display and real-time collaborative use in multisite clinical trials [55]. The Brain Imaging Collaboration Suite enables clinicians to manage, analyze, and visualize volumetric spectroscopic MRI (sMRI) with data from other clinical imaging sequences [55]. BrICS currently overlays metabolic information on anatomical images (i.e. CT or MRI) and enables browsing in whole-brain volumes, automated lesion segmentation, and spectral quality and fitting of individual spectrum all within a web browser. Metabolite information first gets co-registered into the space of a high-resolution T1w MRI and FLAIR. The end-user can select from various individual metabolite maps (in the case of GBM: NAA, Cho, Cr, and the Cho/NAA ratio maps) with interchangeable panels for enlarged views with editing capability of the segmented lesions (Fig. 5).

In order to make BrICS available to a larger collaboration community, we intend to exploit digital platforms that can support multiple users as well as a scanner-to-PACS interface without compromising patient information. MRI vendors have started to offer such digital solutions. For example, Siemens Healthineers teamplay platform enables the interfacing of MRI scanners with PACS and offers various FDA approved digital tools, called "Companions", that are specifically designed to facilitate such manual operations by radiologists as segmentation. BrICS can be built into the teamplay platform, as a radiation therapy planning Companion, to enable a large network of collaborators to work together in improving upon and translating this tool into the clinic.

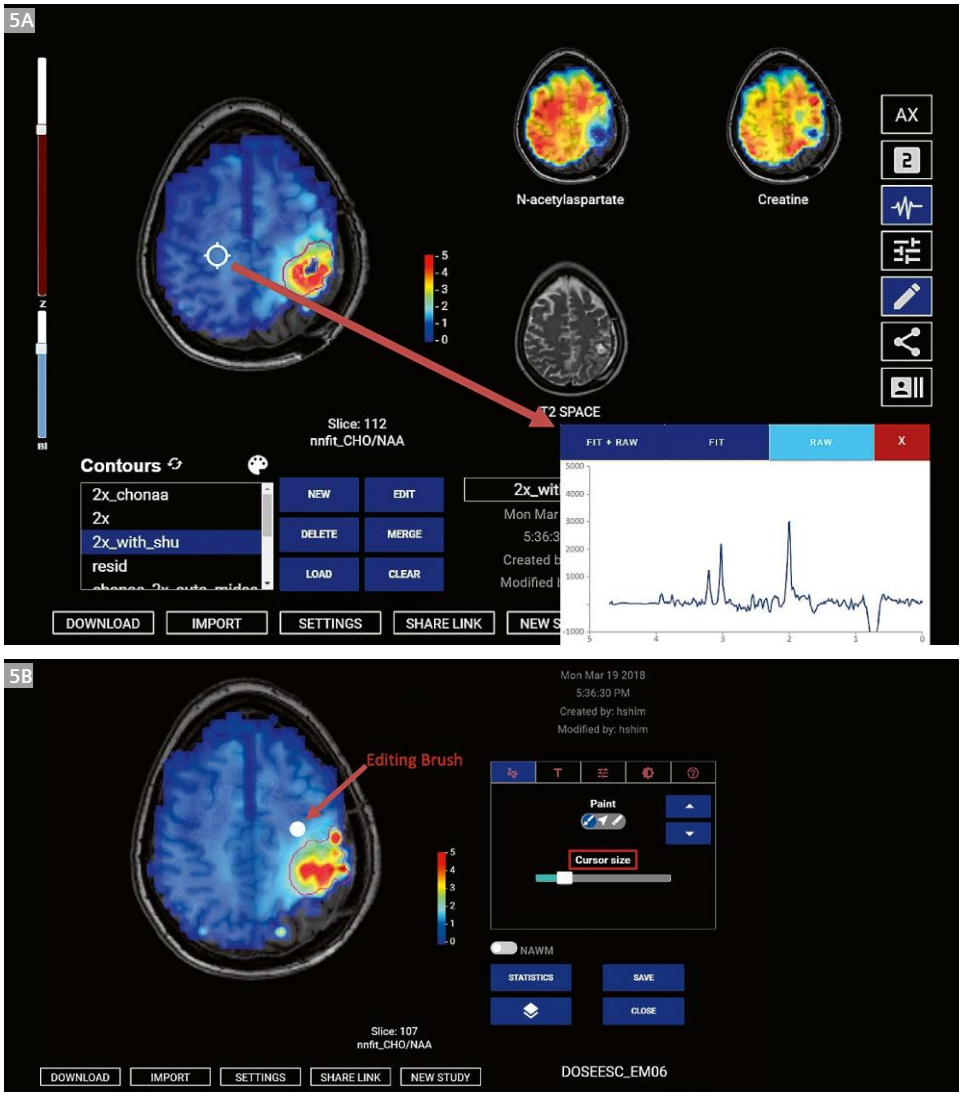

5 An example screenshot of BrICS (the same patient as Figure 2). BrICS allows metabolic information overlaid on anatomical images (i.e. CT or MRI), browsing the whole-brain volume, automated lesion segmentation, and spectral quality and fitting/viewing of individual spectrum for selected location (red arrow), all within a web browser. Metabolite information first gets co-registered into the space of a high-resolution T1w MRI and FLAIR (or any clinical MRIs). The end-user can select from various individual metabolite maps (in the case of GBM: NAA, Cho, Cr, and the Cho/NAA ratio maps) with interchangeable panels **(5A)** and edit the segmented lesions using various cursor size of paint brush (red arrow) in a separate screen in enlarged views **(5B)**.

VI. Advancing magnetic field B_0 homogeneity to improve MRSI quality and reproducibility

Owing to the theoretical doubling of overall signal-to-noise ratio (SNR), 3T MRI now plays the same role for clinical imaging that was occupied by 1.5T systems in the past. The static main (B_0) field inhomogeneity is mostly caused by magnetic susceptibility differences between soft tissues, air, and bone and is proportional to the B_0 field strength, which can lead to image distortion and signal loss. Static field (frequency) variations found at 3T are twice as large as those at 1.5T. To address this problem, advanced MR scanners use built-in shim coils in the magnet bore to provide shimming capability up to the 2nd order spherical harmonics (SH) for brain scans. Although this can address part of the issue, organs with an air-tissue interface or larger field-of-view, such as the heart, abdomen and the whole brain, are often subject to higher-order magnetic field disturbance and make the current vendor-provided solution insufficient. This remains a major challenge in spectroscopic MRI. The primary limitation to more widespread clinical implementation of spectroscopic MRI technology has been the inability to achieve good magnetic field homogeneity over the entire brain volume, as well as the variability in shimming between patients. Recently a new concept has been proposed and developed, so-called integrated parallel reception, excitation, and shimming (iPRES) [56, 57], using the same single coil array for simultaneous B_0 shimming and RF reception by adding DC currents to RF reception coil loops (Fig. 6). The close proximity of the shared shim-RF loops to the subject allows to increase the RF reception sensitivity and also provide additional local B_0 shimming. It relies on a novel circuit design (Fig. 6A) that allows an RF current (for reception) and a DC current (for B_0 shimming) to coexist independently in the same coil element. Compared to conventional RF array coils [58], the integrated RF-Shim array provides a powerful add-on ability for multi-coil local B_0 shimming [59]. The integrated shim-RF technology is currently pursued by several groups [60–63]. The innovative circuit design first implemented in a proof-of-concept two-channel RF/shim array [56], was applied to arrays with more channels [61, 62], where either 16 or 32 elements of commercial 32-channel RF head coils were modified for successful experiments on humans. The RF sensitivity was found not largely compromised compared to conventional RF array coil [58]. The iPRES concept has received considerable attention in the community and its potential impact in several MR applications recognized, including fMRI, MRS, and ultra-high-field MRI [64–72]. It also draws considerable attention from vendors since it can simplify scanner design and considerably improve its shimming function. The decreased distance from shim coils to the targeted organ increases shimming effectiveness compared to distantly located magnet bore shim coils. The integrated shim-RF coil does not compromise patient comfort compared to a clinical coil (Fig. 6). Additionally, the novel coil based shimming does not require more scan times, sequence modification or additional image reconstruction. The local shimming protocol essentially has no significant difference from vendor-supplied shimming protocols. The only difference is the shim coils being changed from the shim coils built in the magnet bore to a local shim-RF coil. As such, there will be no increase in exam times compared to existing protocols after the software is integrated into the MR scanner console.

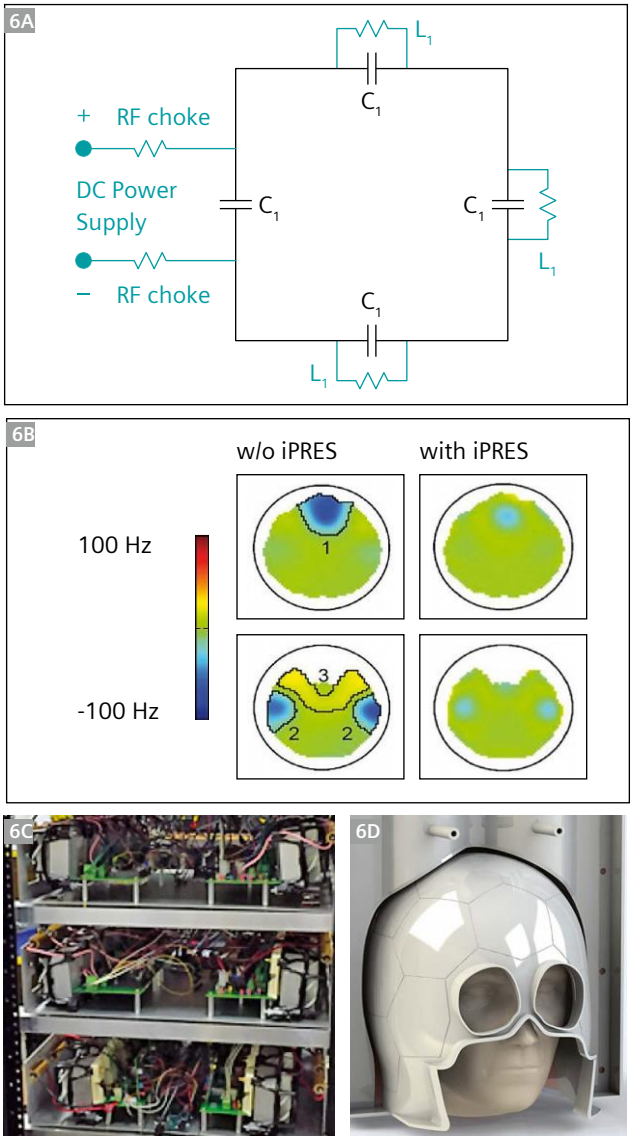

6 Integrated shim-RF head coil as a potential clinical technology. **(6A)** Shared RF/shim loop as used in iPRES. **(6B)** Field homogenization in frontal and temporal lobes. **(6C)** Homemade low cost multi-channel shim current amplifiers. **(6D)** The helmet CAD model for 3D printing has similar geometry as for product coils. Integrated coils have no compromise in patient comfort by integrating shim/RF into a standard-size head coil assembly.

Further advanced technology such as Unified Coil (UNIC) can provide even higher-order local shimming using a standard-size coil assembly, which may potentially achieve the true full brain coverage and allow metabolic evaluation of the entire brain. Such coils can be widely used and thus benefit the entire MR community by advancing B_0 shimming technology, and negligible eddy current effects make it very suitable for dynamic shimming. It will help catalyze the clinical acceptance of spectroscopic MRI. As a background, Siemens Healthineers has introduced the new generation MRI scanner MAGNETOM Vida with BioMatrix technology in 2017. Such integrated shim-RF coils fit the scope of the endeavor in better addressing one of the greatest challenges of imaging – variability of anatomies and physiologies among different patients – and further advance initiatives in precision medicine in MRI.

Conclusions and future prospects

To be able to utilize spectroscopic MRI in routine clinical workflow, there are still a number of improvements to be made, including; (1) accelerated processing pipeline to meet neuroradiology reading time; (2) whole-brain coverage; (3) fully automated and reliable artifact removal; and (4) improvement in resolution. Excitingly, an ultrahigh-resolution EPSI sequence is under development by Maudsley et al., which provides improved interpolated resolution of 1.3 x 2.0 x 2.5 mm^3 with 128 x 128 x 48 *k*-space points (currently under validation). This will enable imaging smaller tumors/regions of the brain and provides better brain coverage due to decreased sensitivity to field inhomogeneity and better fat suppression using smaller voxel size. Acquisition time is reduced by optimizing the sequence to acquire 50% fewer spectral points without affecting spectral quality and the field-of-view is decreased by 1/3 in the z-direction. With a shorter TR (950 ms) (previously 1700 ms), there was no increase in imaging time compared to the earlier sequence. On-scanner preprocessing modules are also under development to perform echo combination, GRAPPA reconstruction, coil combination, and spatial Fourier transform. Running these preprocessing modules on the scanner can significantly reduce post-processing times and the size of data required to be transferred, stored and processed. Since the ultrahigh-resolution sequence has more demanding computational requirements and may prolong reconstruction times, the reconstruction pipelines are modified to use parallel/distributed computing, which promises a significant reduction in processing times along with implementing the recently developed neural-network-based accelerated spectral fitting [51]. The value of spectroscopic MRI becomes evident when considering the shortcomings of conventional MRI exams in delineating disease progression versus treatment effect. Figure 7 shows the Cho/NAA = 2x volume in BrICS from a 16-year-old patient with high-grade glioma, using the ultrahigh-resolution sequence (the same patient in Figure 4) with an interpolated resolution of 6.5 µl. While there was hardly any enhancement visible in the CE T1w-MRI following surgery, the Cho map shows a significant elevation of choline in the anterior aspect of the resection cavity and the Cho/NAA ratio map revealed a 19.2 ml region consistent with a residual tumor. It is expected that by combining the software and improved hardware technologies described above, many of the obstacles of the implementation of MRSI in the clinic will be overcome, and it will gradually become accepted as an important modality for the evaluation of patients with brain tumors and other neurological diseases.

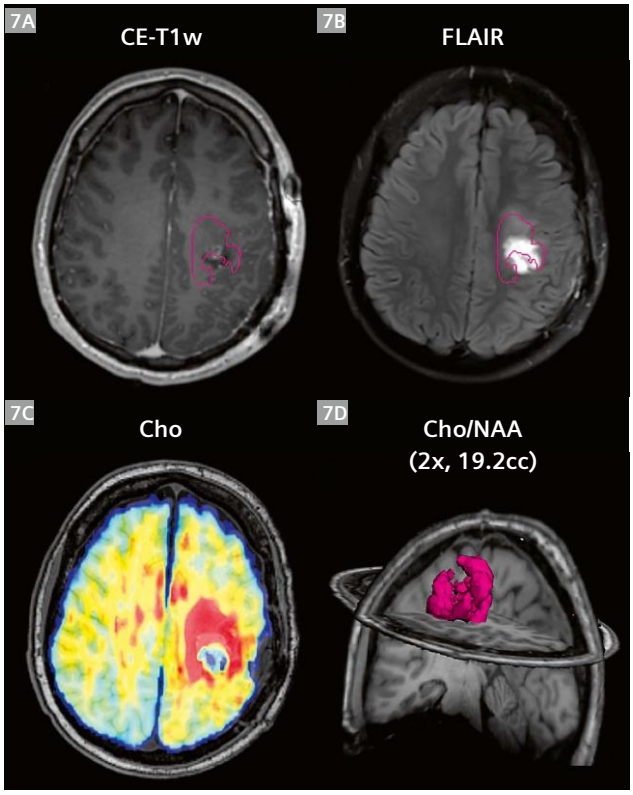

7 Conventional MRI including T1w **(7A)** and FLAIR **(7B)** showing an infiltrative mass in the left insula and posterior limb of the internal capsule. The complete extent of the mass is difficult to appreciate. Cho sMRI **(7C)** shows much larger spectroscopic abnormality encompassing a significant region of elevated Cho involving the temporal stem, insula, and cerebral peduncle **(7D)**.

Acknowledgment

This work has been supported by the National Institutes of Health grant: U01 EB028145.

References

1 Barker PB, Gillard JH, van Zijl PC, Soher BJ, Hanley DF, Agildere AM, Oppenheimer SM, Bryan RN. Acute stroke: evaluation with serial proton MR spectroscopic imaging. Radiology. 1994;192(3):723-32.

2 Lin DD, Crawford TO, Barker PB. Proton MR spectroscopy in the diagnostic evaluation of suspected mitochondrial disease. AJNR Am J Neuroradiol. 2003;24(1):33-41.

3 Remy C, Grand S, Lai ES, Belle V, Hoffmann D, Berger F, Esteve F, Ziegler A, Le Bas JF, Benabid AL, Decorps M, Segebarth CM. 1H MRS of human brain abscesses in vivo and in vitro. Magn Reson Med. 1995;34(4):508-14.

4 Frahm J, Michaelis T, Merboldt KD, Hanicke W, Gyngell ML, Bruhn H. On the N-acetyl methyl resonance in localized 1H NMR spectra of human brain in vivo. NMR Biomed. 1991;4(4):201-4.

5 Pouwels PJ, Frahm J. Differential distribution of NAA and NAAG in human brain as determined by quantitative localized proton MRS. NMR Biomed. 1997;10(2):73-8.

6 Barker P, Breiter S, Soher B, Chatham J, Forder J, Samphilipo M, Magee C, Anderson J. Quantitative Proton Spectroscopy of Canine Brain: In vivo and in vitro correlations. Magn Reson Med. 1994;32:157-63.

7 Jacobs MA, Horska A, van Zijl PC, Barker PB. Quantitative proton MR spectroscopic imaging of normal human cerebellum and brain stem. Magn Reson Med. 2001;46(4):699-705.

8 Petroff OA, Graham GD, Blamire AM, al-Rayess M, Rothman DL, Fayad PB, Brass LM, Shulman RG, Prichard JW. Spectroscopic imaging of stroke in humans: histopathology correlates of spectral changes. Neurology. 1992;42(7):1349-54.

9 Shonk TK, Moats RA, Gifford P, Michaelis T, Mandigo JC, Izumi J, Ross BD. Probable Alzheimer disease: diagnosis with proton MR spectroscopy. Radiology. 1995;195(1):65-72.

10 Kruse B, Hanefeld F, Christen HJ, Bruhn H, Michaelis T, Hanicke W, Frahm J. Alterations of brain metabolites in metachromatic leukodystrophy as detected by localized proton magnetic resonance spectroscopy in vivo. J Neurol. 1993;241(2):68-74.

11 Brand A, Richter-Landsberg C, Leibfritz D. Multinuclear NMR studies on the energy metabolism of glial and neuronal cells. Dev Neurosci. 1993;15(3-5):289-98.

12 Flogel U, Willker W, Leibfritz D. Regulation of intracellular pH in neuronal and glial tumour cells, studied by multinuclear NMR spectroscopy. NMR Biomed. 1994;7(4):157-66.

13 Castillo M, Smith JK, Kwock L. Correlation of myo-inositol levels and grading of cerebral astrocytomas. AJNR Am J Neuroradiol. 2000;21(9):1645-9.

14 Gurbani SS, Yoon Y, Weinberg BD, Salgado E, Press RH, Cordova JS, Ramesh KK, Liang Z, Velazquez Vega J, Voloschin A, Olson JJ, Schreibmann E, Shim H, Shu HG. Assessing Treatment Response of Glioblastoma to an HDAC Inhibitor Using Whole-Brain Spectroscopic MRI. Tomography. 2019;5(1):53-60.

15 Shim H, Wei L, Holder CA, Guo Y, Hu XP, Miller AH, Olson JJ. Use of high-resolution volumetric MR spectroscopic imaging in assessing treatment response of glioblastoma to an HDAC inhibitor. AJR Am J Roentgenol. 2014;203(2):W158-65.

16 Wei L, Hong S, Yoon Y, Hwang SN, Park JC, Zhang Z, Olson JJ, Hu XP, Shim H. Early prediction of response to vorinostat in an orthotopic glioma rat model. NMR Biomed. 2012; In Press.

17 van Zijl PCM, Barker PB. Magnetic Resonance Spectroscopy and Spectroscopic Imaging for the Study of Brain Metabolism. Imaging Brain Structure and Function. Annals of the New York Academy of Sciences. 820. New York, N.Y.1997. p. 75-96.

18 Nelson SJ. Analysis of volume MRI and MR spectroscopic imaging data for the evaluation of patients with brain tumors. Magn Reson Med. 2001;46(2):228-39.

19 Duyn JH, Gillen J, Sobering G, van Zijl PC, Moonen CT. Multisection proton MR spectroscopic imaging of the brain. Radiology. 1993;188(1):277-82.

20 Pohmann R, von Kienlin M, Haase A. Theoretical evaluation and comparison of fast chemical shift imaging methods. J Magn Reson. 1997;129(2):145-60.

21 Kurhanewicz J, Vigneron DB, Nelson SJ. Three-dimensional magnetic resonance spectroscopic imaging of brain and prostate cancer. Neoplasia. 2000;2(1-2):166-89.

22 Zhu H, Barker PB. MR spectroscopy and spectroscopic imaging of the brain. Methods Mol Biol. 2011;711:203-26.

23 Nassirpour S, Chang P, Avdievitch N, Henning A. Compressed sensing for high-resolution nonlipid suppressed (1) H FID MRSI of the human brain at 9.4T. Magn Reson Med. 2018;80(6):2311-25.

24 Strasser B, Povazan M, Hangel G, Hingerl L, Chmelik M, Gruber S, Trattnig S, Bogner W. (2 + 1)D-CAIPIRINHA accelerated MR spectroscopic imaging of the brain at 7T. Magn Reson Med. 2017;78(2):429-40.

25 Thomas MA, Nagarajan R, Huda A, Margolis D, Sarma MK, Sheng K, Reiter RE, Raman SS. Multidimensional MR spectroscopic imaging of prostate cancer in vivo. NMR Biomed. 2014;27(1):53-66.

26 Ebel A, Soher BJ, Maudsley AA. Assessment of 3D proton MR echo-planar spectroscopic imaging using automated spectral analysis. Magn Reson Med. 2001;46(6):1072-8.

27 Ebel A, Maudsley AA. Improved spectral quality for 3D MR spectroscopic imaging using a high spatial resolution acquisition strategy. Magn Reson Imaging. 2003;21(2):113-20.

28 Mansfield P. Spatial mapping of chemical shift in NMR. Magn Reson Med. 1984;1:370-86.

29 Posse S, Cuenod CA, Risinger R, Le Bihan D, Balaban RS. Anomalous transverse relaxation in 1H spectroscopy in human brain at 4 Tesla. Magn Reson Med. 1995;33(2):246-52.

30 Govindaraju V, Gauger GE, Manley GT, Ebel A, Meeker M, Maudsley AA. Volumetric proton spectroscopic imaging of mild traumatic brain injury. AJNR Am J Neuroradiol. 2004;25(5):730-7.

31 Pelletier D, Nelson SJ, Grenier D, Lu Y, Genain C, Goodkin DE. 3-D echo planar (1)HMRS imaging in MS: metabolite comparison from supratentorial vs. central brain. Magn Reson Imaging. 2002;20(8):599-606.

32 Nassirpour S, Chang P, Fillmer A, Henning A. A comparison of optimization algorithms for localized in vivo B_0 shimming. Magn Reson Med. 2018;79(2):1145-56.

33 Ogg RJ. WET, a T1- and B1-Insensitive Water-Suppression Method for in Vivo Localized 1H NMR Spectroscopy. J Magn Reson B. 1994;104:1-10.

34 Ebel A, Maudsley AA. Comparison of methods for reduction of lipid contamination for in vivo proton MR spectroscopic imaging of the brain. Magn Reson Med. 2001;46(4):706-12.

35 Hetherington HP, Mason GF, Pan JW, Ponder SL, Vaughan JT, Twieg DB, Pohost GM. Evaluation of cerebral gray and white matter metabolite differences by spectroscopic imaging at 4.1T. Magn Reson Med. 1994;32(5):565-71.

36 Maudsley AA, Domenig C, Govind V, Darkazanli A, Studholme C, Arheart K, Bloomer C. Mapping of brain metabolite distributions by volumetric proton MR spectroscopic imaging (MRSI). Magn Reson Med. 2009;61(3):548-59.

37 Zhu X, Ebel A, Ji JX, Schuff N. Spectral phase-corrected GRAPPA reconstruction of three-dimensional echo-planar spectroscopic imaging (3D-EPSI). Magn Reson Med. 2007;57(5):815-20.

38 Cordova JS, Shu HK, Liang Z, Gurbani SS, Cooper LA, Holder CA, Olson JJ, Kairdolf B, Schreibmann E, Neill SG, Hadjipanayis CG, Shim H. Whole-brain spectroscopic MRI biomarkers identify infiltrating margins in glioblastoma patients. Neuro Oncol. 2016;18(8):1180-9.

39 Maudsley AA, Darkazanli A, Alger JR, Hall LO, Schuff N, Studholme C, Yu Y, Ebel A, Frew A, Goldgof D, Gu Y, Pagare R, Rousseau F, Sivasankaran K, Soher BJ, Weber P, Young K, Zhu X. Comprehensive processing, display and analysis for in vivo MR spectroscopic imaging. NMR Biomed. 2006;19(4):492-503.

40 Zhang Y, Brady M, Smith S. Segmentation of brain MR images through a hidden Markov random field model and the expectation-maximization algorithm. IEEE Trans Med Imaging. 2001;20(1):45-57.

41 Haupt CI, Schuff N, Weiner MW, Maudsley AA. Removal of lipid artifacts in 1H spectroscopic imaging by data extrapolation. Magn Reson Med. 1996;35(5):678-87.

42 Soher BJ, Young K, Govindaraju V, Maudsley AA. Automated spectral analysis III: application to in vivo proton MR spectroscopy and spectroscopic imaging. Magn Reson Med. 1998;40(6):822-31.

43 Zhu H, Ouwerkerk R, Barker PB. Dual-band water andlipid suppression for MR spectroscopic imaging at 3 Tesla. Magn Reson Med. 2010;63(6):1486-92.

44 Goryawala MZ, Sheriff S, Maudsley AA. Regional distributions of brain glutamate and glutamine in normal subjects. NMR Biomed. 2016;29(8):1108-16.

45 Goryawala MZ, Sheriff S, Stoyanova R, Maudsley AA. Spectral decomposition for resolving partial volume effects in MRSI. Magn Reson Med. 2018;79(6):2886-95.

46 Soher BJ, van Zijl PC, Duyn JH, Barker PB. Quantitative proton MR spectroscopic imaging of the human brain. Magn Reson Med. 1996;35(3):356-63.

47 Mierisova S, Ala-Korpela M. MR spectroscopy quantitation: a review of frequency domain methods. NMR Biomed. 2001;14(4):247-59.

48 Marshall I, Bruce SD, Higinbotham J, MacLullich A, Wardlaw JM, Ferguson KJ, Seckl J. Choice of spectroscopic lineshape model affects metabolite peak areas and area ratios. Magn Reson Med. 2000;44(4):646-9.

49 Soher BJ, Maudsley AA. Evaluation of variable line-shape models and prior information in automated 1H spectroscopic imaging analysis. Magn Reson Med. 2004;52(6):1246-54.

50 Provencher SW. Estimation of metabolite concentrations from localized in vivo proton NMR spectra. Magn Reson Med. 1993;30(6):672-9.

51 Gurbani SS, Sheriff S, Maudsley AA, Shim H, Cooper LAD. Incorporation of a spectral model in a convolutional neural network for accelerated spectral fitting. Magn Reson Med. 2019;81(5):3346-57.

52 Kreis R. Issues of spectral quality in clinical 1H-magnetic resonance spectroscopy and a gallery of artifacts. NMR Biomed. 2004;17:361-81.

53 Gurbani SS, Schreibmann E, Maudsley AA, Cordova JS, Soher BJ, Poptani H, Verma G, Barker PB, Shim H, Cooper LAD. A convolutional neural network to filter artifacts in spectroscopic MRI. Magn Reson Med. 2018.

Contact

Hyunsuk Shim, Ph.D.
Winship Cancer Institute
of Emory University
Department of Radiation Oncology
1701 Uppergate Drive
Atlanta, GA 30322
USA
hshim@emory.edu

54 Schreibmann E, Gurbani S, Shim H, editors. Building an anatomical filter to facilitate 3D whole brain spectroscopic MRI into GBM treatment planning. American Association for Physicists in Medicine Annual Meeting; 2017; Denver, CO.

55 Gurbani S, Weinberg B, Mellon E, Schreibmann E, Sheriff S, Maudsley A, Cooper L, Shu HK, Shim H. The brain imaging collaboration suite (BrICS): a cloud platform for integrating whole-brain spectroscopic MRI into the radiation therapy planning workflow. Tomography. 2019;5(1):184-91.

56 Han H, Song AW, Truong TK. Integrated parallel reception, excitation, and shimming (iPRES). Magn Reson Med. 2013;70(1):241-7.

57 Han H, Truong TK, Song AW. Magnetic resonance imaging systems for integrated parallel reception, excitation and shimming and related methods and devices. US Patent 9,874,6162018.

58 Roemer PB, Edelstein WA, Hayes CE, Souza SP, Mueller OM. The NMR phased array. Magn Reson Med. 1990;16(2):192-225.

59 Juchem C, Nixon TW, McIntyre S, Boer VO, Rothman DL, de Graaf RA. Dynamic multi-coil shimming of the human brain at 7 T. J Magn Reson. 2011;212(2):280-8.

60 Darnell D, Truong TK, Song AW. Integrated parallel reception, excitation, and shimming (iPRES) with multiple shim loops per radio-frequency coil element for improved B_0 shimming. Magn Reson Med. 2017;77(5):2077-86.

61 Stockmann JP, Witzel T, Keil B, Polimeni JR, Mareyam A, LaPierre C, Setsompop K, Wald LL. A 32-channel combined RF and B_0 shim array for 3T brain imaging. Magn Reson Med. 2016;75(1):441-51.

62 Truong TK, Darnell D, Song AW. Integrated RF/shim coil array for parallel reception and localized B_0 shimming in the human brain. Neuroimage. 2014;103:235-40.

63 Winkler SA, Schmitt F, Landes H, de Bever J, Wade T, Alejski A, Rutt BK. Gradient and shim technologies for ultra high field MRI. Neuroimage. 2018;168:59-70.

64 Budinger TF, Bird MD, Frydman L, Long JR, Mareci TH, Rooney WD, Rosen B, Schenck JF, Schepkin VD, Sherry AD, Sodickson DK, Springer CS, Thulborn KR, Ugurbil K, Wald LL. Toward 20 T magnetic resonance for human brain studies: opportunities for discovery and neuroscience rationale. MAGMA. 2016;29(3):617-39.

65 Cloos MA, Knoll F, Zhao T, Block KT, Bruno M, Wiggins GC, Sodickson DK. Multiparametric imaging with heterogeneous radiofrequency fields. Nat Commun. 2016;7:12445.

66 Deistung A, Schweser F, Reichenbach JR. Overview of quantitative susceptibility mapping. NMR Biomed. 2017;30(4).

67 Esmaeili M, Bathen TF, Rosen BR, Andronesi OC. Three-dimensional MR spectroscopic imaging using adiabatic spin echo and hypergeometric dual-band suppression for metabolic mapping over the entire brain. Magn Reson Med. 2017;77(2):490-7.

68 Feinberg DA, Vu AT, Beckett A. Pushing the limits of ultra-high resolution human brain imaging with SMS-EPI demonstrated for columnar level fMRI. Neuroimage. 2018;164:155-63.

69 Hangel G, Strasser B, Povazan M, Heckova E, Hingerl L, Boubela R, Gruber S, Trattnig S, Bogner W. Ultra-high resolution brain metabolite mapping at 7 T by short-TR Hadamard-encoded FID-MRSI. Neuroimage. 2018;168:199-210.

70 Ma C, Lam F, Ning Q, Johnson CL, Liang ZP. High-resolution (1) H-MRSI of the brain using short-TE SPICE. Magn Reson Med. 2017;77(2):467-79.

71 Sclocco R, Beissner F, Bianciardi M, Polimeni JR, Napadow V. Challenges and opportunities for brainstem neuroimaging with ultrahigh field MRI. Neuroimage. 2018;168:412-26.

72 Webb AG, Van de Moortele PF. The technological future of 7 T MRI hardware. NMR Biomed. 2016;29(9):1305-15.

X-Nuclei MRI on a 7T MAGNETOM Terra: Initial Experiences

Tobias Wilferth[1]; Lena V. Gast[1,2]; Sebastian Lachner[1]; Nicolas G. R. Behl[3]; Manuel Schmidt[4]; Arnd Dörfler[4]; Michael Uder[1]; Armin M. Nagel[1,2,5]

[1]Institute of Radiology, University Hospital Erlangen, Friedrich-Alexander-Universität Erlangen-Nürnberg (FAU), Erlangen, Germany
[2]Institute of Medical Physics, Friedrich-Alexander-Universität Erlangen-Nürnberg (FAU), Erlangen, Germany
[3]Siemens Healthcare GmbH, Erlangen, Germany
[4]Department of Neuroradiology, University Hospital Erlangen, Friedrich-Alexander-Universität Erlangen-Nürnberg (FAU), Erlangen, Germany
[5]Division of Medical Physics in Radiology, German Cancer Research Center (DKFZ), Heidelberg, Germany

Introduction

Ions such as sodium (Na^+), potassium (K^+) and chlorine (Cl^-) play a vital role in many cellular processes. Healthy tissue contains very little extracellular K^+ ($[K^+]_e$ = 2.5–3.5 mM) but a large amount of intracellular K^+ ($[K^+]_i$ = 140 mM). The Na^+ gradient is reversed and a little less pronounced ($[Na^+]_i$ = 10–15 mM; $[Na^+]_e$ = 145 mM). Cl^- is the most abundant anion in the human body.

Cellular exchange processes, such as the Na^+/K^+-ATPase pump [1] maintain chemical and electrical gradients across the cell membrane – essential for regulating cell volume, energy production and consumption, as well as excitation of muscle or neuronal cells. Independent of its origin, loss of ATPase function leads to breakdown of the resting transmembrane potential difference, and finally to cell death as well as increase of the extracellular volume fraction.

As a result, changes in ion homeostasis can be early markers for many disease processes [2], and MRI can reveal such changes non-invasively. Nuclei other than ^1H are denoted X-nuclei and among them sodium (^{23}Na) provides the best properties for *in vivo* MRI. ^{23}Na MRI has been performed since the 1980s, even at low field strengths [3], and it is established as a non-invasive technique in clinical research [4, 5]. Numerous studies on sodium MRI have promised new metabolic information for many diseases such as stroke [6, 7], tumors [8], and multiple sclerosis [9, 10], epilepsy [11], osteoarthritis [12], diabetes [13], hypertension [14], muscular dystrophies [15], and muscular channelopathies [16].

However, X-nuclei imaging is challenging for several reasons. First of all, the signal-to-noise ratio (SNR) is several orders of magnitude lower compared to proton (^1H) MRI. In most situations relevant for human imaging, noise is dominated by the sample. And for low frequencies, which is usually the case for X-nuclei MRI, a linear noise model can be assumed. In this case, the SNR depends on the concentration c, the magnetic spin moment I and the gyromagnetic ratio γ of the nucleus as given in Equation 1 [17]:

Equation 1

$$SNR \propto c \cdot I\,(I + 1) \cdot \gamma^2$$

Due to the intrinsically reduced NMR sensitivity, which results from the lower gyromagnetic ratio and the low *in vivo* concentrations of X-nuclei, compared to ^1H, their SNR is considerably lower (see Table 1). To achieve sufficient SNR for imaging, large voxel volumes are required. In addition, long acquisition times and ultra-high magnetic field strengths ($B_0 \geq 7T$) both increase SNR.

Depending on the noise model, the SNR shows at least a linear increase with the main magnetic field strength B_0 [17] (see Figure 1A-C). MRI at field strengths of 7 Tesla and above enable imaging of nuclei such as ^{35}Cl and ^{39}K that have even lower SNR than ^{23}Na (see Table 1). Due to its low SNR, ^{39}K MRI was not considered to be practical in a clinical setting for many years [24]. This changed with the advent of ultra-high field (UHF) MR systems, and the feasibility of

^{35}Cl and ^{39}K MRI has been shown using 7T and 9.4T UHF systems [22, 23, 25]. Even the feasibility of cardiac ^{39}K MRI has now been demonstrated [26]. As an investigation of the *in vivo* ion homeostasis in healthy and pathological tissue by non-invasive MRI quantification is of high medical interest, further advancements of these methods are highly desirable. For this purpose, UHF systems with approval as a medical device such as MAGNETOM Terra, which first entered the market in 2017, are of great importance.

Furthermore, X-nuclei with a spin $I > 1/2$ (e.g., ^{23}Na, ^{39}K) generally experience very rapid relaxation. Therefore, acquisition techniques enabling ultra-short echo times such as density-adapted projection reconstruction [27] or twisted projection imaging [28] are essential for efficient imaging of fast relaxing nuclei [29].

Sodium MRI using a 32-channel phased array head coil

The following measurements were performed with a 7T MAGNETOM Terra MR system (Siemens Healthcare, Erlangen, Germany) using a dual tuned proton/sodium (^{1}H/^{23}Na) birdcage head coil (RAPID Biomedical, Rimpar, Germany) with 32 additionally integrated receive-only elements for ^{23}Na MRI. All ^{23}Na images were acquired using a density adapted 3D radial projection pulse sequence [27] (TR/TE = 120 ms/0.3 ms, FA = 90°, T_{RO} = 9.98 ms, T_{AQ} = 14:00 min, (2.5 mm)^3 nominal isotropic resolution).

In addition to providing higher static magnetic fields, phased array coils can further increase SNR compared with volume coils (see Figure 1C, D and Figure 2A, B) because they consist of many small receiver elements [30–32].

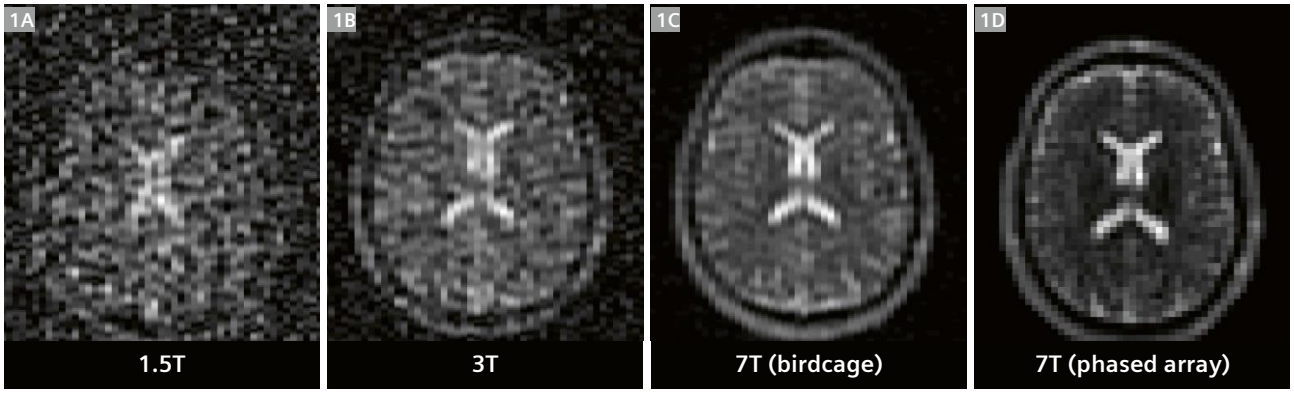

1 ^{23}Na MR brain images acquired at 1.5T **(1A)**, 3T **(1B)** and 7T **(1C, D)** using a density adapted 3D radial projection pulse sequence. At 7T, one image was acquired using a birdcage volume coil **(1C)** and one image using a 32-channel phased array coil **(1D)**. All data sets have a nominal isotropic resolution of (4 mm)^3. The SNR increases with magnetic field strength and the phased array coil yields higher SNR than the birdcage coil. Parameters: TE (1.5T and 3T) = 0.2 ms, TE (7T) = 0.5 ms, TR = 50 ms, FA = 77°, T_{RO} = 5 ms, T_{AQ} = 10:50 min.

Nucleus	Spin I	Natural Abundance [%]	Typical *in vivo* concentrations c [mol/L]	γ/2π [MHz/T]	Relative *in vivo* SNR[a] [%]
^{1}**H**	1/2	99.99	79[b]	42.58	100
^{23}**Na**	3/2	100	0.041 / 0.3[c]	11.27	$1.8 \cdot 10^{-2}$ / $1.3 \cdot 10^{-1}$
^{35}**Cl**	3/2	75.78	0.027[d]	4.18	$2.2 \cdot 10^{-3}$
^{39}**K**	3/2	93	0.108[e]	1.99	$1.6 \cdot 10^{-3}$

Table 1: Physical properties of selected X-nuclei and ^{1}H for comparison [17, 18].
[a]SNR values derived from Equation [1]
[b]Derived from measured water content (71%) of brain white matter [19]
[c]Measured ^{23}Na concentration of healthy brain white matter [20] and healthy articular cartilage [21] (highest ^{23}Na content among all tissues)
[d]Measured ^{35}Cl concentration of healthy brain white matter [22]
[e]Measured ^{39}K concentration of skeletal muscle tissue [23]

However, phased array coils are only rarely used in ^{23}Na MRI, most likely due to the more complex coil design and the need to correct for the receive profile enabling ^{23}Na quantification. The latter can be addressed by optimized intensity correction methods [33].

The signal measured using the phased array coil is corrected with the receive profile of the phased array coil to obtain the real magnetization of the object. In order to determine the receive profile, a homogeneous reference image is acquired, for example via the integrated birdcage coil. A 3D sensitivity map can be obtained by dividing the low-pass filtered phased array image (which may be reconstructed via adaptive combination reconstruction [34, 35]) by the low-pass filtered reference image. Under the assumption of negligible noise, dividing the phased array image by the sensitivity map yields the intensity corrected image.

As the correction via a birdcage reference image requires additional acquisition time, a different approach using a universal sensitivity map has been evaluated [33]. The universal sensitivity map was determined by averaging individually calculated receive profiles of eight volunteers, obtained following the procedure described above.

Both approaches were applied to correct the receive profile of ^{23}Na *in vivo* measurements of the human brain, and validated by calculating of an averaged signal intensity ratio between the outer and inner CSF compartment (CSF_{out}:CSF_{in}) after performing a partial volume correction [20]. Both methods correct the intensity of the lateral ventricles in the center of the brain, which is most affected by the inhomogeneous receive profile (see Figure 3 for example data on one volunteer). No remaining intensity modulations are apparent in the ratios between the homogeneous birdcage image and the corrected phased array images. Furthermore, the signal intensities for the outer and inner CSF compartment converge. Averaged over the results of eight examined subjects, the ratio CSF_{out}:CSF_{in}

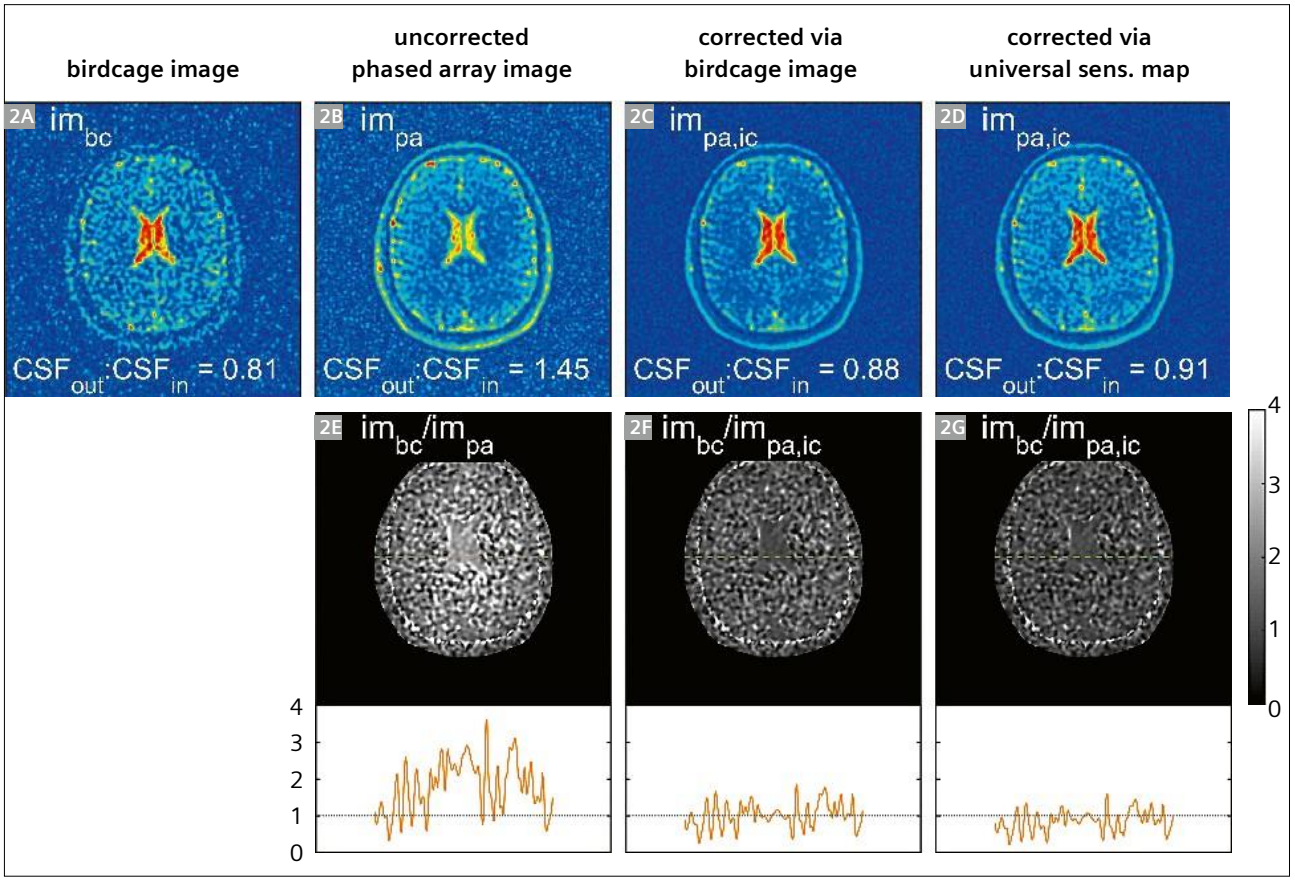

2 Representative intensity correction of a measured ^{23}Na MRI *in vivo* data, using a birdcage image **(2C)** and a universal sensitivity map **(2D)**. The ratio between the uncorrected phased array image **(2B)** and the birdcage image **(2A)** indicates an intensity modulation due to the inhomogeneous receive profile **(2E)**. For the corrected phased array images **(2C, D)** the ratios **(2F, G)** indicate a good performance of the applied correction methods.

for the uncorrected phased array image is 1.71 due to underestimation of the signal intensity in the center of the brain. For the birdcage image the averaged ratio is 0.89. After applying the intensity correction using a birdcage image, an averaged ratio of 1.00 is obtained. Using the universal sensitivity map instead of the individual birdcage image results in an averaged ratio of 1.05 [33].

So the method utilizing a birdcage image performs better but requires considerably longer acquisition time [33], while the universal sensitivity map performs only slightly worse. As there only seems to be a small subject dependency of the coil sensitivities, even a low number of averaged *in vivo* datasets should be sufficient to determine the universal sensitivity map (here n = 8).

Figure 3 shows an intensity-corrected ^{23}Na MRI dataset (using the universal sensitivity map) of a glioblastoma patient. The intensity of the right lateral ventricle in the center of the brain is increased in the corrected phased array image as compared to the uncorrected phased array image, and comparable to the intensity in the outer CSF compartment (see Figure 3A). In Figure 3B concentration maps of different slices are shown. The concentration values were normalized to 145 mM in the CSF of the ventricles, which were used as internal reference.

Iterative reconstruction

As mentioned above, the low SNR of ^{23}Na MRI results in low spatial resolution and long acquisition time. One way to counteract this is Compressed Sensing (CS) image reconstruction. The 3D radial trajectory used for ^{23}Na MRI is well suited for CS, since resulting undersampling artifacts appear noise-like. On the other hand, the inherent low SNR in the data is not ideal for CS approaches. One way to get the most out of ^{23}Na MRI reconstructions is to undersample the radial data and invest the time gained into averaging [36]. Figure 4 shows the standard reconstruction (NUFFT) and the Dictionary Learning CS reconstruction (3D-DLCS) of ^{23}Na MRI volunteer data, with a nominal resolution of 2 mm isotropic. The data are 10-fold undersampled and 10-fold averaged.

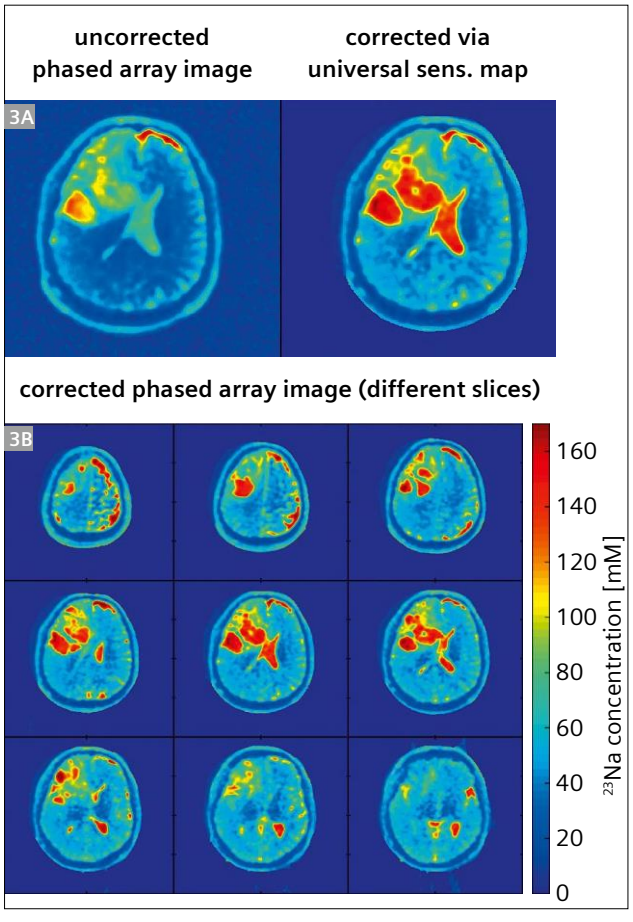

3 ^{23}Na MRI of a glioblastoma patient using a 32-channel phased array head coil and intensity correction via a universal sensitivity map (spatial resolution: isotropic (2.5 mm)^3, T_{AQ} = 14:00 min). The region of the tumor shows higher sodium concentration.

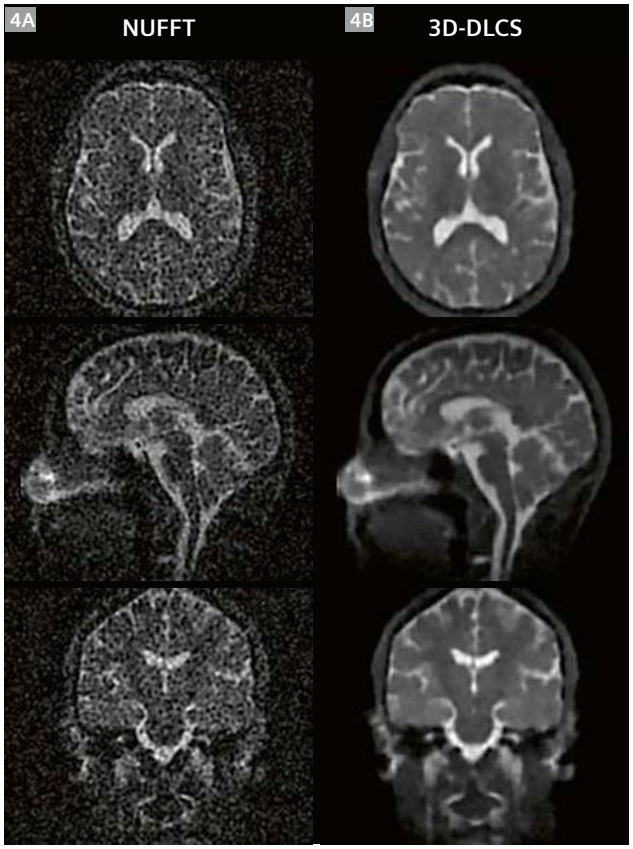

4 Reconstructions of 10-fold undersampled and 10-fold averaged ^{23}Na MRI data with a nominal resolution of 2 mm isotropic. While the NUFFT reconstruction **(4A)** displays strong noise contamination, image noise is markedly reduced in the 3D-DLCS reconstruction **(4B)**.

Combined ^{23}Na/^{39}K MRI of human skeletal muscle

Due to the inverse Na^+ and K^+ ion distribution between the intracellular and extracellular spaces, a combined determination of their tissue concentrations using ^{23}Na and ^{39}K MRI might give interesting insights into the physiology. While alterations in tissue sodium content (TSC) have been examined in various diseases using ^{23}Na MRI [14, 15, 37–39], in clinical practice, K^+ concentrations are currently only determined using extracellular body fluids such as blood samples. However, changes in total K^+ content in the human body are mainly buffered in the intracellular space [40], so a direct detection of tissue potassium content (TPC) using ^{39}K MRI might be beneficial.

For combined ^{23}Na/^{39}K MRI, we used a dual tuned, circular polarized ^{23}Na/^{39}K calf coil[1] with inner diameter of 20 cm (Rapid Biomedical, Rimpar, Germany). With this coil, imaging of both nuclei can be realized without repositioning the leg. However, no ^{1}H channel is included for the acquisition of anatomical images. Moreover, B_0 shimming in X-nuclei imaging is usually performed using the ^{1}H channel of a dual tuned (e.g., ^{23}Na/^{1}H) coil, or using a ^{1}H body coil. If no ^{1}H channel is available, B_0 shimming cannot be performed using vendor-provided B_0 shimming techniques as they are generally based on B_0 maps acquired by ^{1}H MRI. As a homogeneous B_0 field is indispensable, especially for quantitative measurements [41], a custom B_0 shimming routine based on ^{23}Na MRI data was implemented [42]. To verify this shimming approach, we compared its performance with conventional vendor-provided ^{1}H MRI based B_0 shimming routines, and used the double resonant 32-channel ^{23}Na/^{1}H head coil (Rapid Biomedical, Rimpar, Germany) described above.

^{23}Na B_0 maps are acquired using a double-echo 3D density-adapted radial readout (DA-3D-RAD) scheme [27]. Shim values are calculated using the constrained regularized pseudo-inversion approach (ConsTru) proposed by Nassirpour et al. [43]. The volume of interest to be shimmed is defined by a three-dimensional mask calculated by thresholding based on the magnitude image corresponding to the first echo. Reconstruction and post-processing of the radial datasets, as well as shim value calculation, are performed on the host computer of the MR system using MATLAB (TheMathworks, Natick, MA, USA).

B_0 shimming of the human head was performed both based on ^{23}Na MRI and using the vendor-provided ^{1}H MRI based GRE Brain shimming routine. For better comparability, only one iteration of shimming was performed each for the ConsTru and the GRE Brain shim in all measurements. Additionally, the acquisition duration of the ^{23}Na images used for the shim value calculation was chosen to match

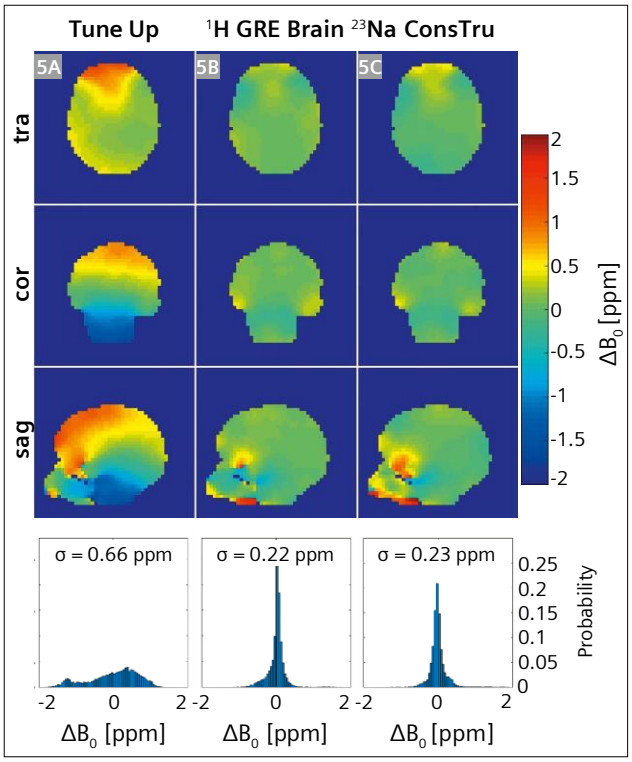

5 B_0 homogeneity in the human brain using: system default shim settings (denoted as Tune Up shim settings) **(5A)**, shim values calculated by the vendor-provided ^{1}H GRE Brain shim **(5B)** implemented ^{23}Na MRI based ConsTru shim **(5C)**. The last two routines show similar resulting B_0 homogeneity with a reduction of the B_0 variations over the entire volume of interest by 67% (GRE Brain shim) and 65% (^{23}Na ConsTru). Similar data can be found in Gast et al. [42].

the acquisition duration of the GRE Brain shimming B_0 map acquisition (N_{proj} = 300). The resulting B_0 homogeneity is shown in Figure 5. Over six examined volunteers, we observed a very similar performance of both shimming routines with a mean reduction of the B_0 variations σ by 53 ± 7% (^{1}H GRE Brain) and 52 ± 7% (^{23}Na ConsTru) over the entire head volume. Therefore, we conclude that B_0 shimming based on ^{23}Na MRI is feasible in clinically acceptable acquisition durations with satisfactory outcome.

For quantitative ^{23}Na and ^{39}K imaging, human lower legs are positioned on a five-compartment reference tube holder filled with different combinations of NaCl and K_2HPO_4 solution, corresponding to different Na^+ (10–40 mM) and K^+ (120–240 mM) concentrations. K_2HPO_4 solution has lower electrical conductivity than KCl solution, and is therefore expected to produce fewer image artifacts. Images are acquired using an acquisition-weighted stack-of-stars (AW-SOS) scheme [44]. Parameters (^{23}Na/^{39}K): TR = 120/40 ms, TE = 0.3/0.4 ms, T_{RO} = 10/5 ms, FA = 90°, rectangular excitation pulse of 500 ms duration,

[1] *The information shown herein refers to products of 3rd party manufacturer's and thus are in their regulatory responsibility. Please contact the 3rd party manufacturer for further information.*

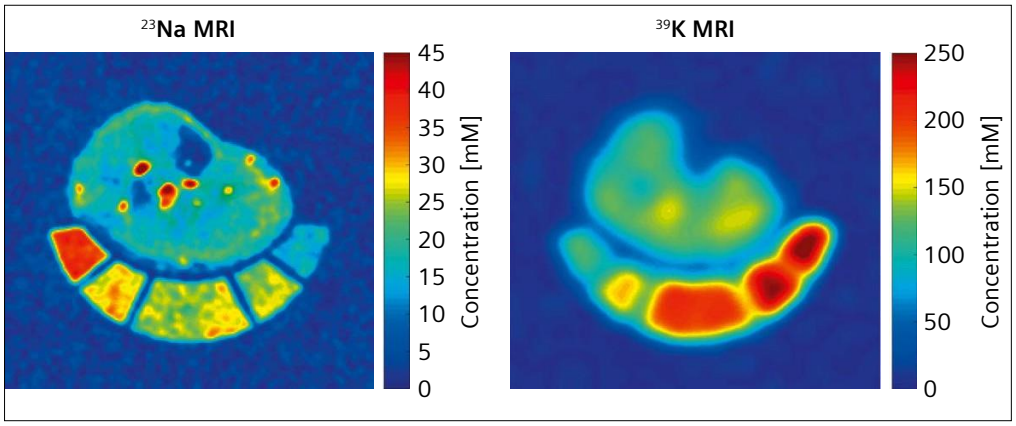

6 Exemplary ^{23}Na and ^{39}K concentration maps of healthy human lower leg calculated from ^{23}Na and ^{39}K MRI datasets. Concentration calibration was performed by a linear regression, based on the signal intensity within the reference compartments containing NaCl and K_2HPO_4 solution.

nominal spatial resolution Δx = 2.5 x 2.5 x 10 mm³ / 7.5 x 7.5 x 30 mm³, averages = 1/4, total acquisition time T_{AQ} = 10:54 / 8:06 min.

Concentration calibration is performed by linear regression of the ^{23}Na and ^{39}K signal intensities within the reference compartments to their nominal concentrations. Resulting ^{23}Na and ^{39}K concentration maps of healthy lower leg are shown in Figure 6. However, for precise quantification of Na^+ and K^+ concentrations based on ^{23}Na and ^{39}K images, several signal corrections are required. For ^{39}K especially, low image resolution leads to a strong partial volume effect. Moreover, muscle tissue has significantly shorter T2* and T1 relaxation times than the reference solutions both for ^{23}Na and ^{39}K, so a relaxation correction is needed.

So far, ^{39}K concentration maps have been acquired only for healthy muscle tissue. However, examining potassium concentrations would be of interest in various diseases, for example renal impairment and muscular diseases, to help reveal underlying physiological processes.

Conclusion

Introducing clinically approved UHF scanners such as MAGNETOM Terra, together with suitable RF coils and sequences, was an important step for X-nuclei imaging, which benefits from the increased SNR and resultant higher spatial resolution or shorter acquisition time. This paves the way for ^{23}Na MRI to move from research into clinical applications. Tissue sodium concentration might evolve into a useful biomarker for a large variety of diseases such as kidney diseases [45], muscular diseases [46], and neurodegeneration [9]. Moreover, MRI of other nuclei such as ^{39}K becomes possible in a clinical environment with feasible measurement times. Compared with morphological ^{1}H MRI, these nuclei provide additional information that will provide insights into many physiologically relevant processes, resulting in various potential clinical research applications.

References

1 Robinson JD, Flashner MS. The (Na+ + K+)-activated ATPase. Enzymatic and transport properties. Biochim Biophys Acta 1979;549(2):145-176.
2 Rose AM, Valdes R, Jr. Understanding the sodium pump and its relevance to disease. Clin Chem 1994;40(9):1674-1685.
3 Hilal SK, Maudsley AA, Ra JB, Simon HE, Roschmann P, Wittekoek S, Cho ZH, Mun SK. In vivo NMR imaging of sodium-23 in the human head. J Comput Assist Tomogr 1985;9(1):1-7.
4 Madelin G, Regatte RR. Biomedical applications of sodium MRI in vivo. J Magn Reson Imaging 2013;38(3):511-529.
5 Thulborn KR. Quantitative sodium MR imaging: A review of its evolving role in medicine. Neuroimage 2018;168:250-268.
6 Thulborn KR, Gindin TS, Davis D, Erb P. Comprehensive MR imaging protocol for stroke management: tissue sodium concentration as a measure of tissue viability in nonhuman primate studies and in clinical studies. Radiology 1999;213(1):156-166.
7 Hussain MS, Stobbe RW, Bhagat YA, Emery D, Butcher KS, Manawadu D, Rizvi N, Maheshwari P, Scozzafava J, Shuaib A, Beaulieu C. Sodium imaging intensity increases with time after human ischemic stroke. Ann Neurol 2009;66(1):55-62.
8 Schepkin VD. Sodium MRI of glioma in animal models at ultrahigh magnetic fields. NMR Biomed 2016;29(2):175-186.
9 Huhn K, Engelhorn T, Linker RA, Nagel AM. Potential of Sodium MRI as a Biomarker for Neurodegeneration and Neuroinflammation in Multiple Sclerosis. Front Neurol 2019;10:84.
10 Petracca M, Fleysher L, Oesingmann N, Inglese M. Sodium MRI of multiple sclerosis. NMR Biomed 2016;29(2):153-161.
11 Ridley B, Marchi A, Wirsich J, Soulier E, Confort-Gouny S, Schad L, Bartolomei F, Ranjeva JP, Guye M, Zaaraoui W. Brain sodium MRI in human epilepsy: Disturbances of ionic homeostasis reflect the organization of pathological regions. Neuroimage 2017;157:173-183.
12 Zbyn S, Mlynarik V, Juras V, Szomolanyi P, Trattnig S. Evaluation of cartilage repair and osteoarthritis with sodium MRI. NMR Biomed 2016;29(2):206-215.
13 Kopp C, Linz P, Maier C, Wabel P, Hammon M, Nagel AM, Rosenhauer D, Horn S, Uder M, Luft FC, Titze J, Dahlmann A. Elevated tissue sodium deposition in patients with type 2 diabetes on hemodialysis detected by ^{23}Na magnetic resonance imaging. Kidney Int 2018;93(5):1191-1197.
14 Kopp C, Linz P, Dahlmann A, Hammon M, Jantsch J, Muller DN, Schmieder RE, Cavallaro A, Eckardt KU, Uder M, Luft FC, Titze J. 23Na magnetic resonance imaging-determined tissue sodium in healthy subjects and hypertensive patients. Hypertension 2013;61(3):635-640.

15 Gerhalter T, Gast LV, Marty B, Martin J, Trollmann R, Schussler S, Roemer F, Laun FB, Uder M, Schroder R, Carlier PG, Nagel AM. (23) Na MRI depicts early changes in ion homeostasis in skeletal muscle tissue of patients with duchenne muscular dystrophy. J Magn Reson Imaging 2019;50(4):1103-1113.
16 Weber MA, Nagel AM, Marschar AM, Glemser P, Jurkat-Rott K, Wolf MB, Ladd ME, Schlemmer HP, Kauczor HU, Lehmann-Horn F. 7-T Cl and Na MR Imaging for Detection of Mutation-dependent Alterations in Muscular Edema and Fat Fraction with Sodium and Chloride Concentrations in Muscular Periodic Paralyses. Radiology 2016;280(3):848-859.
17 Ladd ME, Bachert P, Meyerspeer M, Moser E, Nagel AM, Norris DG, Schmitter S, Speck O, Straub S, Zaiss M. Pros and cons of ultra-high-field MRI/MRS for human application. Prog Nucl Magn Reson Spectrosc 2018;109:1-50.
18 Harris RK, Becker ED, Cabral de Menezes SM, Goodfellow R, Granger P. NMR Nomenclature: Nuclear Spin Properties and Conventions for Chemical Shifts. IUPAC Recommendations 2001. Solid State Nucl Magn Reson 2002;22(4):458-483.
19 Neeb H, Zilles K, Shah NJ. A new method for fast quantitative mapping of absolute water content in vivo. Neuroimage 2006;31(3):1156-1168.
20 Niesporek SC, Hoffmann SH, Berger MC, Benkhedah N, Kujawa A, Bachert P, Nagel AM. Partial volume correction for in vivo (23)Na-MRI data of the human brain. Neuroimage 2015;112:353-363.
21 Madelin G, Lee JS, Regatte RR, Jerschow A. Sodium MRI: methods and applications. Prog Nucl Magn Reson Spectrosc 2014;79:14-47.
22 Nagel AM, Lehmann-Horn F, Weber MA, Jurkat-Rott K, Wolf MB, Radbruch A, Umathum R, Semmler W. In vivo 35Cl MR imaging in humans: a feasibility study. Radiology 2014;271(2):585-595.
23 Umathum R, Rosler MB, Nagel AM. In vivo 39K MR imaging of human muscle and brain. Radiology 2013;269(2):569-576.
24 Parrish TB, Fieno DS, Fitzgerald SW, Judd RM. Theoretical basis for sodium and potassium MRI of the human heart at 1.5 T. Magn Reson Med 1997;38(4):653-661.
25 Atkinson IC, Claiborne TC, Thulborn KR. Feasibility of 39-potassium MR imaging of a human brain at 9.4 Tesla. Magn Reson Med 2014;71(5):1819-1825.
26 Wenz D, Nagel AM, Lott J, Kuehne A, Niesporek SC, Niendorf T. In vivo potassium MRI of the human heart. Magn Reson Med 2020;83(1):203-213.
27 Nagel AM, Laun FB, Weber MA, Matthies C, Semmler W, Schad LR. Sodium MRI using a density-adapted 3D radial acquisition technique. Magn Reson Med 2009;62(6):1565-1573.
28 Boada FE, Gillen JS, Shen GX, Chang SY, Thulborn KR. Fast three dimensional sodium imaging. Magn Reson Med 1997;37(5):706-715.
29 Konstandin S, Nagel AM. Measurement techniques for magnetic resonance imaging of fast relaxing nuclei. MAGMA 2014;27(1):5-19.
30 Roemer PB, Edelstein WA, Hayes CE, Souza SP, Mueller OM. The NMR phased array. Magn Reson Med 1990;16(2):192-225.
31 Wiggins GC, Brown R, Lakshmanan K. High-performance radiofrequency coils for (23)Na MRI: brain and musculoskeletal applications. NMR Biomed 2016;29(2):96-106.
32 Bangerter NK, Kaggie JD, Taylor MD, Hadley JR. Sodium MRI radiofrequency coils for body imaging. NMR Biomed 2016;29(2):107-118.
33 Lachner S, Ruck L, Niesporek SC, Utzschneider M, Lott J, Hensel B, Dorfler A, Uder M, Nagel AM. Comparison of optimized intensity correction methods for (23)Na MRI of the human brain using a 32-channel phased array coil at 7 Tesla. Z Med Phys 2019; in press.
34 Benkhedah N, Hoffmann SH, Biller A, Nagel AM. Evaluation of adaptive combination of 30-channel head receive coil array data in 23Na MR imaging. Magn Reson Med 2016;75(2):527-536.
35 Walsh DO, Gmitro AF, Marcellin MW. Adaptive reconstruction of phased array MR imagery. Magn Reson Med 2000;43(5):682-690.
36 Behl NG, Gnahm C, Bachert P, Ladd ME, Nagel AM. Three-dimensional dictionary-learning reconstruction of (23)Na MRI data. Magn Reson Med 2016;75(4):1605-1616.
37 Weber MA, Nagel AM, Jurkat-Rott K, Lehmann-Horn F. Sodium (23Na) MRI detects elevated muscular sodium concentration in Duchenne muscular dystrophy. Neurology 2011;77(23):2017-2024.
38 Nagel AM, Amarteifio E, Lehmann-Horn F, Jurkat-Rott K, Semmler W, Schad LR, Weber MA. 3 Tesla sodium inversion recovery magnetic resonance imaging allows for improved visualization of intracellular sodium content changes in muscular channelopathies. Invest Radiol 2011;46(12):759-766.
39 Hammon M, Grossmann S, Linz P, Seuss H, Hammon R, Rosenhauer D, Janka R, Cavallaro A, Luft FC, Titze J, Uder M, Dahlmann A. 3 Tesla (23)Na Magnetic Resonance Imaging During Acute Kidney Injury. Acad Radiol 2017;24(9):1086-1093.
40 Palmer BF. Regulation of Potassium Homeostasis. Clin J Am Soc Nephrol 2015;10(6):1050-1060.
41 Lu A, Atkinson IC, Claiborne TC, Damen FC, Thulborn KR. Quantitative sodium imaging with a flexible twisted projection pulse sequence. Magn Reson Med 2010;63(6):1583-1593.
42 Gast LV, Henning A, Hensel B, Uder M, Nagel AM. Localized B0 shimming based on (23) Na MRI at 7 T. Magn Reson Med 2020;83(4):1339-1347.
43 Nassirpour S, Chang P, Fillmer A, Henning A. A comparison of optimization algorithms for localized in vivo B0 shimming. Magn Reson Med 2018;79(2):1145-1156.
44 Müller M, Gast LV, Hensel B, Uder M, Nagel AM. Comparison of anisotropic UTE sequences for 23Na/39K imaging in the human calf at 7T. Proc Intl Soc Mag Reson Med 27 2019.
45 Dahlmann A, Dorfelt K, Eicher F, Linz P, Kopp C, Mossinger I, Horn S, Buschges-Seraphin B, Wabel P, Hammon M, Cavallaro A, Eckardt KU, Kotanko P, Levin NW, Johannes B, Uder M, Luft FC, Muller DN, Titze JM. Magnetic resonance-determined sodium removal from tissue stores in hemodialysis patients. Kidney Int 2015;87(2):434-441.
46 Strijkers GJ, Araujo ECA, Azzabou N, Bendahan D, Blamire A, Burakiewicz J, Carlier PG, Damon B, Deligianni X, Froeling M, Heerschap A, Hollingsworth KG, Hooijmans MT, Karampinos DC, Loudos G, Madelin G, Marty B, Nagel AM, Nederveen AJ, Nelissen JL, Santini F, Scheidegger O, Schick F, Sinclair C, Sinkus R, de Sousa PL, Straub V, Walter G, Kan HE. Exploration of New Contrasts, Targets, and MR Imaging and Spectroscopy Techniques for Neuromuscular Disease – A Workshop Report of Working Group 3 of the Biomedicine and Molecular Biosciences COST Action BM1304 MYO-MRI. J Neuromuscul Dis 2019;6(1):1-30.

Contact

Professor Armin Nagel
Institute of Radiology
University Hospital Erlangen
Maximiliansplatz 3
91054 Erlangen
Germany
Tel.: +49 (0)9131 85-25900
armin.nagel@uk-erlangen.de

The concepts and information presented (in this paper) are based on research and are not commercially available.

How I do it: Imaging Morton's Neuroma

Dag Sjølie

Diakonhjemmet Hospital, Radiology Department, Oslo, Norway

Patient history

Patient presented with pain underneath the metatarsophalangeal (MTP) joint as well as numbness and tingling in the three middle toes. The pain was aggravated by running and walking. Tentative diagnosis: Morton's neuroma.

Imaging findings

All images were acquired using a 1.5T MAGNETOM Aera MRI scanner with software version *syngo* MR E11C (Siemens Healthcare, Erlangen, Germany). Figures 1 and 2 demonstrate why imaging of Morton's neuroma should be acquired in the prone position. These two images show the same patient with 10 minutes between acquisitions. Morton's neuroma is clearly depicted between the 3rd and the 4th digits. In the supine position, the neuroma is in between the MTP joints, but in the prone position, it protrudes like a mushroom on the plantar side of the foot. This makes it much easier to measure. An accurate measurement of size is important in assessing whether or not an operative intervention is required.

Optimization and discussion

We always perform this examination in the prone position, but how can we improve it even more? Which coil provides the best SNR and fits the forefoot?

In our experience, the 16-channel Hand/Wrist coil is the perfect coil for this type of examination. It allows the acquisition of higher quality images in a shorter scan time. Our previous protocol scan time with the 15-channel Tx/Rx Knee coil was 20:26 minutes. Using the Hand/Wrist coil, we both improved image quality and reduced scan time by almost 30% with a total scan time of 14:33 minutes (details in Table 1).

An added advantage is that most patients find it more comfortable and experience better support with the 16-channel Hand/Wrist coil than with the Knee coil. For positioning hints see Figure 6. Many radiographers do not think that a large foot will fit in the Hand/Wrist coil; however, we have successfully scanned a patient with EU 46-sized feet and weighing 130 kg. In our opinion, most forefeet will fit into the coil. We use it for Morton's neuroma, but other examinations requiring high resolution images of the forefoot can also potentially benefit from improved image quality due to the better SNR with the Hand/Wrist coil.

	#slices	Slice thickness (mm)/gap	TR	TE	Turbo factor	Voxel size (mm)	FOV (mm)	Averages	BW	Flip angle	TA (min:sec)
COR T1	25	2.5/0%	564	12	3	0.2 x 0.2 x 2.5	160 x 95	2	181	170	2:16
COR PD FS	25	2.5/0%	2000	39	9	0.17 x 0.19 x 2.5	130 x 93	2	221	153	2:50
TRA T1	20	2/30%	414	11	3	0.2 x 0.2 x 2	165 x 113	2	217	150	2:18
SAG T1	26	2.5/30%	489	9.9	3	0.3 x 0.3 x 2.5	180 x 124	1	217	150	2:01
SAG T1 FS + Gd	26	2.5/30%	637	11	3	0.3 x 0.3 x 2.5	175 x 115	1	178	150	1:58
COR T1 FS + Gd	25	2.5/0%	482	10	3	0.2 x 0.2 x 2.5	175 x 115	1	200	150	2:40

Table 1: Sequence parameters with Hand/Wrist 16 coil.

The concepts and information presented in this paper are based on research and are not commercially available.

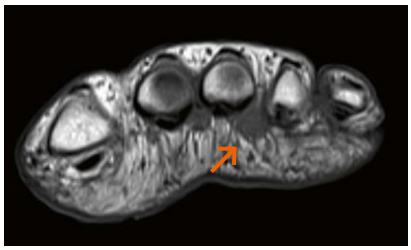

1 Prone T1-weighted image in 15-channel Tx/Rx Knee coil.

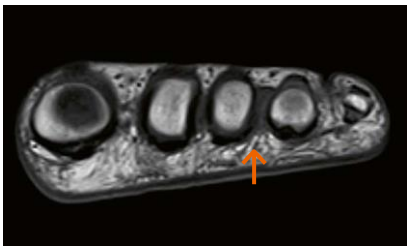

2 Supine T1-weighted image in 16-channel Foot/Ankle coil.

3 Prone position with 16-channel Hand/Wrist coil; PD FS coronal short-axis.

4 Prone position with 16-channel Hand/Wrist coil; T1-weighted transversal.

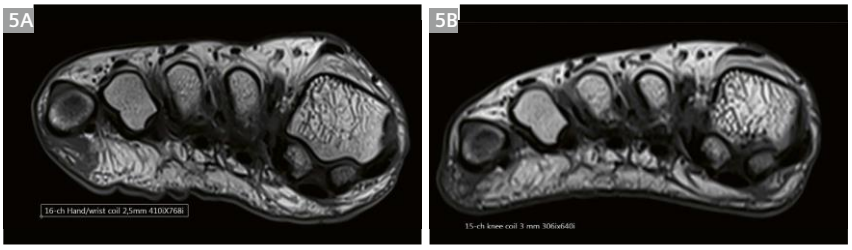

5 Image quality comparison Hand/Wrist coil vs. Knee coil in a healthy volunteer.
(5A) 16-channel Hand/Wrist coil, SL 2.5 mm, 410 x 768 mm isotropic.
(5B) 15-channel Knee coil, SL 3 mm, 306 x 640 mm isotropic.

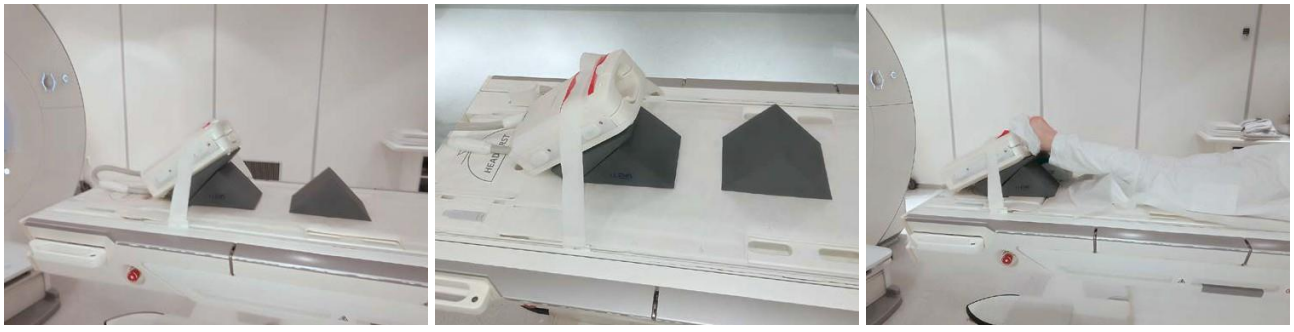

6 Positioning of the patient with Hand/Wrist 16 coil.

Conclusion

Position the patient prone for best depiction of Morton's neuroma. Use the 16-channel Hand/Wrist coil for improved SNR, a significantly shorter scan time, and more comfortable patient positioning.

Acknowledgments

I would like to thank Dr. David Strohe, Dr. Erik Haavardsholm, and Vegard Gjersdal for helping me out. And to all my dedicated friends in the MRI community for their help and support.

Contact

Dag Sjølie, BSc, RT(R)(MR)
Senior Radiographer
Diakonhjemmet Hospital
Radiology Department
Diakonveien 12
0370 Oslo
Norway
Tel. +47 90556528
dag.sjolie@gmail.com

The DICOM files are available for download at www.siemens.com/magnetom-world
> Clinical Corner > Protocols > DICOM Images

Imaging of Osteomyelitis with FDG PET-MR

Cristina Mitea[1]; Tineke van de Weijer[1]; Lieke van de Meer[1]; Linda Jacobi[1]; Daan Loeffen[1]; Dennis Hulsen[2,3]; Jan Geurts[3]; Rik Moonen[1]

[1]Department of Radiology and Nuclear Medicine, Maastricht University Medical Centre Maastricht, The Netherlands
[2]MICT Department, Jeroen Bosch Ziekenhuis, 's-Hertogenbosch, The Netherlands
[3]Department of Orthopaedic Surgery, Maastricht University Medical Centre, Maastricht, The Netherlands

Introduction

Osteomyelitis is an inflammatory process accompanied by bone destruction, and is caused by microorganism infection. The infection can be limited to a single portion of the bone or can involve several compartments such as marrow, cortex, periosteum and the surrounding soft tissue. Osteomyelitis can be (1) spread locally from a focal source of infection, (2) secondary to vascular insufficiency, or (3) caused by hematogenous spread of the microorganism from a different source.

For osteomyelitis in the extremities, the most common pathogen is Staphylococcus aureus. In skull-base osteomyelitis (SBO) it is Pseudomonas aeruginosa (50–90% of cases) [1]. Osteomyelitis of the skull base most often occurs as a complication of otitis externa, and can be categorized within the first category of focal infections. However, it is perceived as a special case due to the severe complications that can arise, given the location. The bacterial infection causes bone erosions, and uses fascial planes and venous sinuses for distant tissue invasion. It then can progress and spread to the surrounding osseous and soft tissues via the skull base.

Clinical presentation

Patients can present with a variety of symptoms, ranging from an open wound exposing fractured bone, or an indolent draining fistula, to no skin lesion but local swelling and bone pain. In the acute phase after surgery, infection can usually easily be recognized by clinical examination (fever, redness, swelling, wound leakage, pain and disability of the affected body part). In the later phases there can be clear signs of disease (fistula, purulent discharge), but often signs are subtler (slightly elevated temperature of the skin, diffuse pain) or not present at all, and then diagnosis may be very difficult.

Typical symptoms of patients with skull base osteomyelitis are: itching, otalgia, and/or otorrhea. Through possible bone erosions the infection can spread to the surrounding osseous and soft tissues, causing cranial nerve palsy and intracranial involvement.

Diagnosis

A great variety of imaging techniques can be used in diagnosing osteomyelitis [2].

Conventional radiological film (X-ray) is one of the most used techniques for the evaluation of osteomyelitis, mainly because it is cheap and fast. Plain film can show secondary signs of infection, for example edema of the soft tissue, bone destruction, and periosteal reaction. However, in general 30 to 50% of bone mineral content must be compromised to produce noticeable changes on plain radiographs, so this approach has low sensitivity in early diagnosis of osteomyelitis (sensitivity 63% and specificity 87% evaluated for diabetic foot osteomyelitis [3]).

Ultrasound is useful for evaluating the soft tissues and joints next to the infected bone. It can visualize soft tissue abscesses, cellulitis, subperiosteal collections, and joint effusion collections, which are seen in acute infections. However, it is less effective in evaluating bone erosions.

CT and MRI have far better resolution than conventional X-ray film or ultrasound, and provide information about destruction of the bone cortex, involvement of the medulla, periosteal reaction, and articular and soft tissue involvement. CT is superior to MRI in depicting bony margins and cortical erosions, and identifying sequestration [4]. CT imaging also has excellent spatial resolution for evaluating peripheral bone. It can be used to detect small foci of gas and areas of cortical erosion and destruction.

However, conventional CT imaging has limited value in early osteomyelitis. Its overall sensitivity and specificity is low, even for chronic osteomyelitis – reported to be 67% and 50%, respectively [5]. Another limitation is that single-energy CT imaging does not confidently detect bone marrow edema. While dual-energy CT imaging may be more effective, it is not available in most centers. Another problem was image degradation by streak artifacts when metallic implants are present, but this has been largely solved with the introduction of metal artifact reduction techniques.

MRI is superior to CT in delineating soft tissue involvement, including muscular structures, synovial and bone marrow involvement; and is superior even to dual-energy

CT imaging in bone marrow edema detection. For this reason, MRI is considered of value in diagnosing osteomyelitis [6]. It has a reported sensitivity of 70–90% and gives an excellent anatomic delineation of the infected or edematous area and the surrounding soft tissue [5, 7]; although specificity is relatively low (40–80%), and the images can lead to overestimated severity and extent of infection [5, 6].

Nuclear medicine imaging techniques are useful in evaluating specific physiological mechanisms of osteomyelitis. Three-phase bone scintigraphy is an imaging technique using bone-seeking tracers. It can visualize perfusion and bone formation reacting to destructive changes in osteomyelitis. Detection of osteomyelitis is highly sensitive (90%) and also highly specific (about 90%) in bones not affected by other conditions. In post-traumatic patients and after surgery, specificity is lower (circa 35%), as post-operative effects can increase perfusion and induce reactive bone changes [7].

Labeled leukocyte imaging is based on the recruitment of leukocytes by infections. The leukocytes will accumulate at the site of infection and can be visualized with SPECT-CT imaging. This technique has high sensitivity (94–95%) and specificity (89–100%) in expert hands, but it is time demanding for the patient, and not available in all nuclear medicine departments [8].

Pathologies with increased glucose metabolism, including osteomyelitis, can be visualized with ^{18}F-FDG PET-CT/MRI. FDG is a positron-emitting glucose analog, which is taken up by cells. Most malignant tumors as well as inflammatory processes have relatively high metabolic activity, meaning they take up more of the FDG. Detecting this with PET-CT has excellent sensitivity for infections, normally reaching or exceeding 95%, with high specificities above 87%. In spondylitis and spondylodiscitis, FDG PET-CT provides both a high sensitivity and a high specificity [9]. The CT component in hybrid PET-CT helps to differentiate between the different causes of FDG accumulation, including malignancy and trauma.

Recently, hybrid PET-MRI has become commercially available. It combines accurate functional imaging (PET) with high-resolution anatomical information (MRI), and shows promise in improving sensitivity and specificity in musculoskeletal infections, as these conditions require high soft-tissue contrast and resolution for accurate diagnosis. MRI is superior to CT imaging for soft tissue detail and resolution. Furthermore, MRI can visualize thrombosis and intracranial spread in SBO, which CT imaging cannot. Last, radiation burden for the patient is lower in PET-MRI imaging than in PET-CT, especially important in longitudinal follow-up. This technique cannot be used in patients with MRI-incompatible implants such as some defibrillators and pacemakers. Prostheses and osteosynthetic materials may cause artifacts on the MRI, but metal-artifact correction sequences may open PET-MRI for such patients.

Osteomyelitis in the extremities

Scan protocol:
After injection of ^{18}F-FDG (dosage 2 MBq/kg), patients rest for 45 minutes before the start of the PET-MRI scan. The arm or leg is stabilized with a vacuum pillow. A PET-compatible flexible surface coil (a single body matrix coil or flex coil, depending on the size and desired field of view) is placed on top. Multiple bed positions may be required, e.g., for a femur, and the PET acquisition time is 15 minutes per bed position. MRI is acquired simultaneously, including Dixon attenuation correction (soft tissue, fat, air, lung, bone) and a dedicated protocol such as the example in Table 1. Acquisitions are typically made in two anatomical planes, based on the anatomical location of the suspected lesion.

	TR/TE (ms)	FA (°)	FOV (mm)	Slices	Voxel size (mm)	TA (min)
T1 TSE bilateral	876/10	160	500 x 500 x 153.6	35	1.0 x 1.0 x 4.0	2:25
T1 TSE*	700/13	120	250 x 250 x 239	40	0.5 x 0.5 x 5.0	5:01 (bp)
T2 TSE FatSat*	6160/70	150	250 x 250 x 239	40	0.4 x 0.4 x 5.0	4:26 (bp)
DWI RESOLVE*	7110/ TE1: 53 TE2: 79	–	250 x 250 x 250.8	35	2.2 x 2.2 x 6.0	5:43 (bp)
T1 TSE STIR	5000/29	130	500 x 500 x 167.2	35	1.6 x 1.6 x 4.0	5:12
PD TSE FatSat	2500/20	150	500 x 250 x 193.2	44	0.8 x 0.8 x 4.0	3:22
Postcontrast T1 TSE FatSat cor	750/10	160	500 x 500 x 153.6	35	0.5 x 0.5 x 4.0	3:06
Postcontrast T1 TSE FatSat tra	750/13	120	250 x 250 x 239	40	0.5 x 0.5 x 5.0	5:23 (bp)

Table 1: MRI protocol for osteomyelitis of the femur.
**Scans during PET acquisition. bp: per bed position*

In a pilot study, 5 patients were scanned both by PET-CT and subsequently by PET-MRI, to assess the validity and quality of PET-MRI scans. Details can be found in the paper of Hulsen et al. [10].

Osteomyelitis diagnoses based on PET-MR and PET-CT images were identical for all the patients included in this study, but for one patient the PET-CT failed to detect a fistula which was diagnosed on the PET-MRI.

The regions with high signal detected by MRI, and with increased FDG accumulation by PET, were mostly congruent, except for adjacent segment bone marrow. Based on MRI only, it was impossible to differentiate between reactive edema and bone marrow infection. This led to an overestimation of the infection extent by MRI as compared with PET. By including PET information it was possible to distinguish between reactive and infective edema. This will help an operating surgeon to determine the extent of the necessary debridement.

For the PET, the ratio of SUV max measured with PET-MRI to that measured with PET-CT was close to 1 (range 0.6–1.3).

Examples of FDG PET-MRI evaluations of patients diagnosed with osteomyelitis are shown in Figures 1 and 2. These two cases illustrate the strengths of PET-MRI, as additional information on soft tissue defects can be appreciated. Also, the extent of bone marrow infection in the PET images is clearly more limited than the extent of reactive bone marrow edema shown in the MRI. The combination of PET and MRI gives a convincing picture of the infection. In Figure 2, the MRI shows a fistula, which is of utmost importance for adequate treatment of the osteomyelitis.

FDG PET-MRI is of added value not only in the extremities, but also for the spine. Here, FDG PET-MRI has been studied in spondylodiscitis patients showing a sensitivity of 100% and specificity of 88.2% [11].

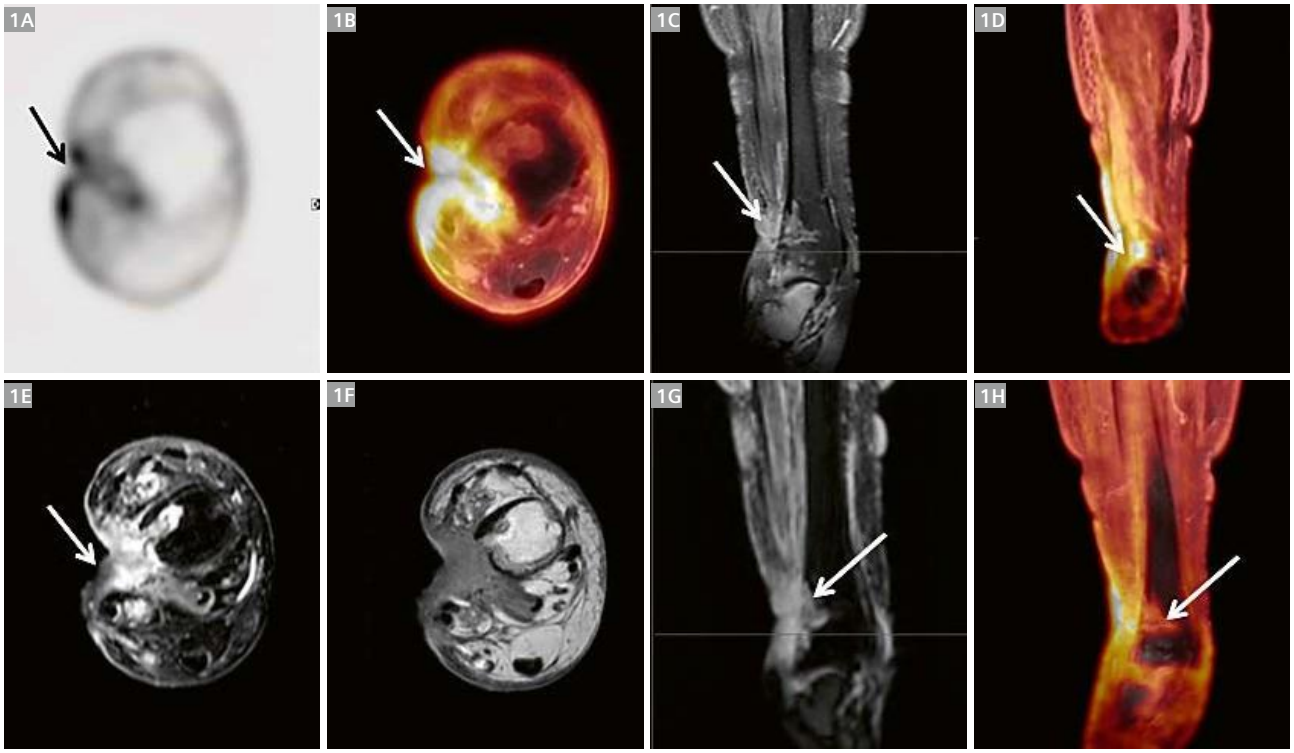

1 65-year-old woman with a skin lesion on the lateral malleolus of the right ankle. **(1A)** PET; **(1B)** FDG PET-MRI overlay; **(1C)** T1 FS; **(1D)** FDG PET-MRI overlay; **(1E)** T1 FS after gadolinium; **(1F)** T1 STIR; **(1G)** T2 FS; **(1H)** FDG PET-MRI overlay. The arrows show soft tissue defects with increased FDG accumulation on the lateral malleolus and extension in the distal tibia.

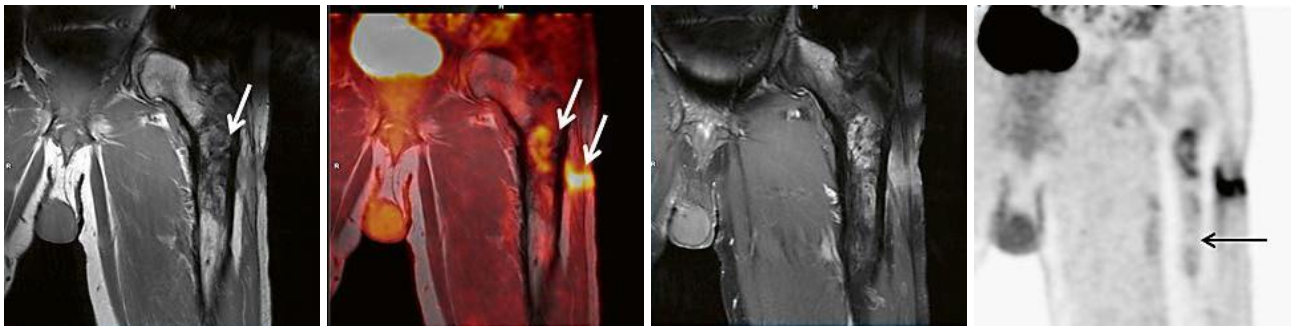

2 64-year-old man with a history of a femur fracture presents with pain in the left leg and wound leakage. He was diagnosed with an osteomyelitis with positive Staphylococcus aureus cultures.
(2A) T1; **(2B)** FDG PET-MRI overlay; **(2C)** T1 FS; **(2D)** PET. White arrows denote area of high FDG uptake, in both the bone marrow and an area in the soft tissue adjacent to the bone. Here a clear fistula was found in MRI. The black arrow denotes an area of moderate FDG uptake, with high signal intensity on the T2-weighted images, which was explained by reactive bone marrow.

Skull base osteomyelitis

One of the indications for an FDG PET-MRI in our center is skull base osteomyelitis (SBO). The scan is performed at initial diagnosis and for therapy evaluation, in most cases after 3 months of antibiotic therapy.

Scan protocol:
After injection of ^{18}F-FDG (dosage 2 MBq/kg), patients rest for 45 minutes before the start of the PET-MRI scan. In order to prevent motion artifacts, inflatable pillows are placed inside the head coil on both sides of the head. The PET acquisition time is 20 minutes and MRI is simultaneously acquired, with Dixon attenuation correction (soft tissue, fat, air, lung, bone) and the dedicated protocol in Table 2.

We use a combination of PET-MRI (sequences are described in Table 2) and a separate high-resolution CT scan. The CT scan is mainly added to evaluate cortical erosions, and does not have any added value in evaluating an active infection.

We studied 21 patients with SBO that were followed during and after treatment with PET-MRI and CT imaging. For three of these patients the diagnosis of SBO was made on the basis of the PET-MRI. One patient had thrombosis of the cavernous sinus as a complication, which was detected in the MRI but missed on the CT scan.

It is known that in MRI the abnormal bone marrow signal can still be present a relatively long time after remission. On the other hand, the PET will more rapidly reveal decreased inflammation, which results in lower FDG accumulation. However, spatial resolution of PET is

	TR/TE (ms)	FA (°)	FOV (mm)	Slices	Voxel size (mm)	TA (min)
T2 TSE (T2_tse_tra_512)	6000/100	150	220 x 220 x 69.3	28	0.4 x 0.4 x 5.0	2:26
T1 TSE	550/9.5	150	220 x 220 x 153.5	18	0.2 x 0.2 x 3.0	6:25
T2 TSE FatSat	4000/89	150	180 x 180 x 76.4	32	0.2 x 0.2 x 2.0	4:18
T2 3D SPACE	1400/158	120	210 x 210 x 28	–	0.2 x 0.2 x 0.5	4:21
T1 FLASH	250/2.48	70	220 x 220 x 170	31	0.7 x 0.7 x 5.0	2:10
DWI RESOLVE	5000/ TE1: 72 TE2: 122	–	220 x 220 x 118.4	27	1.0 x 1.0 x 4.0	3:17
Postcontrast T1 MPRAGE*	1800/2.73 TI: 900	9	240 x 210 x 172.8	–	0.9 x 0.9 x 0.9	5:54
Postcontrast T1 TSE FatSat*	550/9.5	150	220 x 220 x 69.3	18	0.2 x 0.2 x 3.0	6:25

Table 2: Skull-base osteomyelitis MRI protocol (Biograph mMR)
**Contrast injection and postcontrast scans were performed after PET acquisition*

relatively low, so correlation is needed with MRI anatomical information. For these reasons a hybrid PET-MRI is preferred for disease monitoring.

Examples of FDG PET-MRI evaluations of patients diagnosed with skull base osteomyelitis are shown in Figures 3 and 4. Here again the extent of the reactive edema and contrast enhancement on MRI is far greater than the region with active infection on FDG-PET. Furthermore, after treatment, clear remission in metabolic activity at the site of infection was observed, despite lingering edema and contrast enhancement on MRI. MRI helps to assess vascular structures and cortical erosions that cannot be depicted on PET alone. Nonetheless, a CT scan was performed to further evaluate the extent of bone destruction at the temporomandibular joint (TMJ).

Conclusion

PET-MRI is a useful imaging modality for musculoskeletal infections such as osteomyelitis, as it couples the molecular and physiological information acquired from PET with the unparalleled soft tissue resolution of MRI to provide a superior level of anatomic and functional patient information.

Hybrid PET-MRI reduces image acquisition time and misregistration artifacts. Additionally, using PET-MRI over PET-CT gives better appreciation of soft tissue involvement. It will add information on possible complications such as fistulas for the osteomyelitis of the extremities, and cerebral involvement in SBO. Furthermore, PET-MRI will substantially reduce ionizing radiation exposure for the patient, especially in those who require longitudinal follow-up.

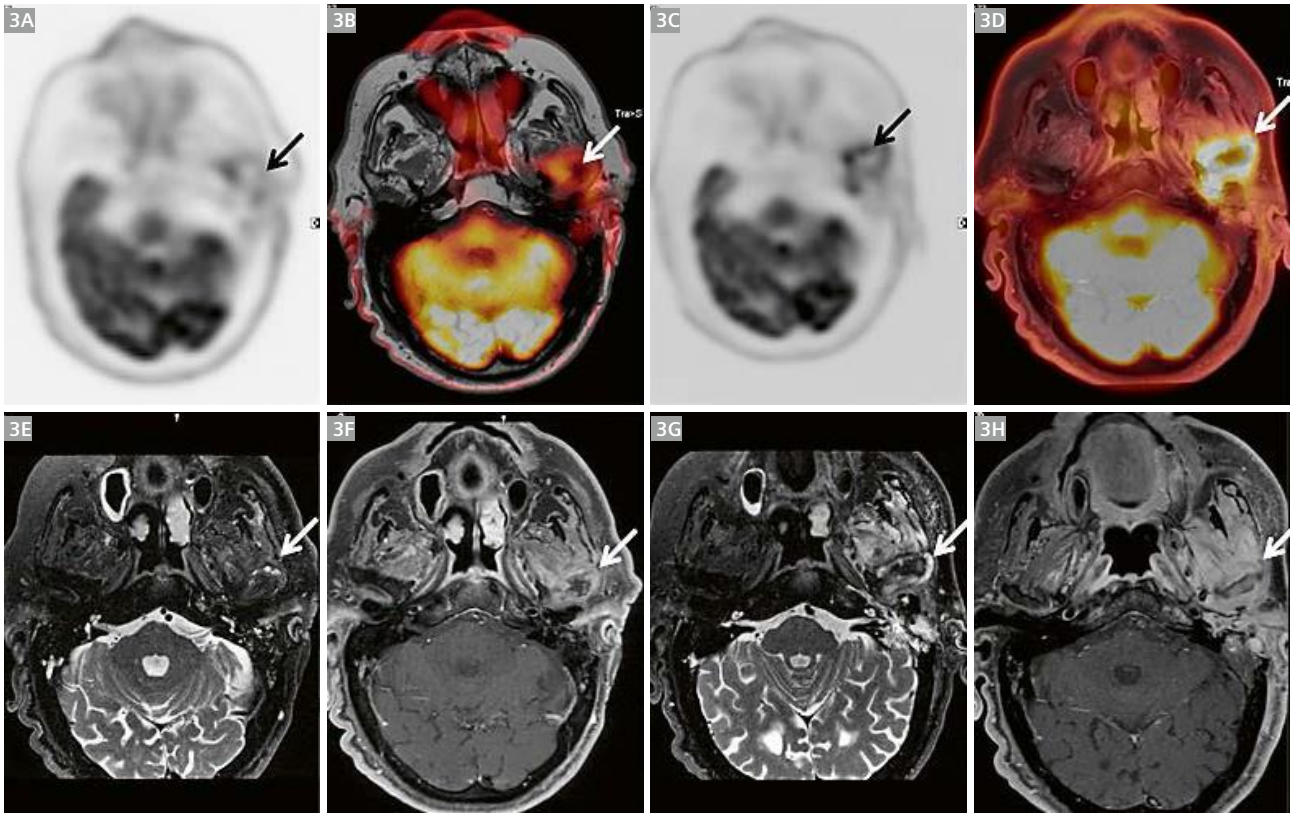

3 76-year-old diabetic patient with otalgia and otorrhea of the left ear. Cultures were positive for P. Aeruginosa. FDG PET-MRI was performed before (3C, D, G, and H) and after 3 months of antibiotic treatment (3A, B, E, and F). **(3A, C)** PET image; **(3B, D)** PET-MR overlay; **(3E, G)** MRI T2 FS; **(3F, H)** MRI T1 FS after gadolinium injection. Pre-treatment images show enhancement of the soft tissue of the middle ear and the mastoid cells, and enhancement of the os petrosum with bone erosion extending to the temporomandibular joint (TMJ). They also show infiltration of the soft tissue of the left infratemporal fossa, the masseter lodge, and the pterygoid and masseter muscles. Bone marrow edema is shown in the mandible and zygomatic arch at the left side.
The follow up images show decreased FDG accumulation around the TMJ compared with pre-treatment PET images. The MRI shows persistent edema in the mandible, and decreased enhancement around the TMJ and the surrounding muscles.

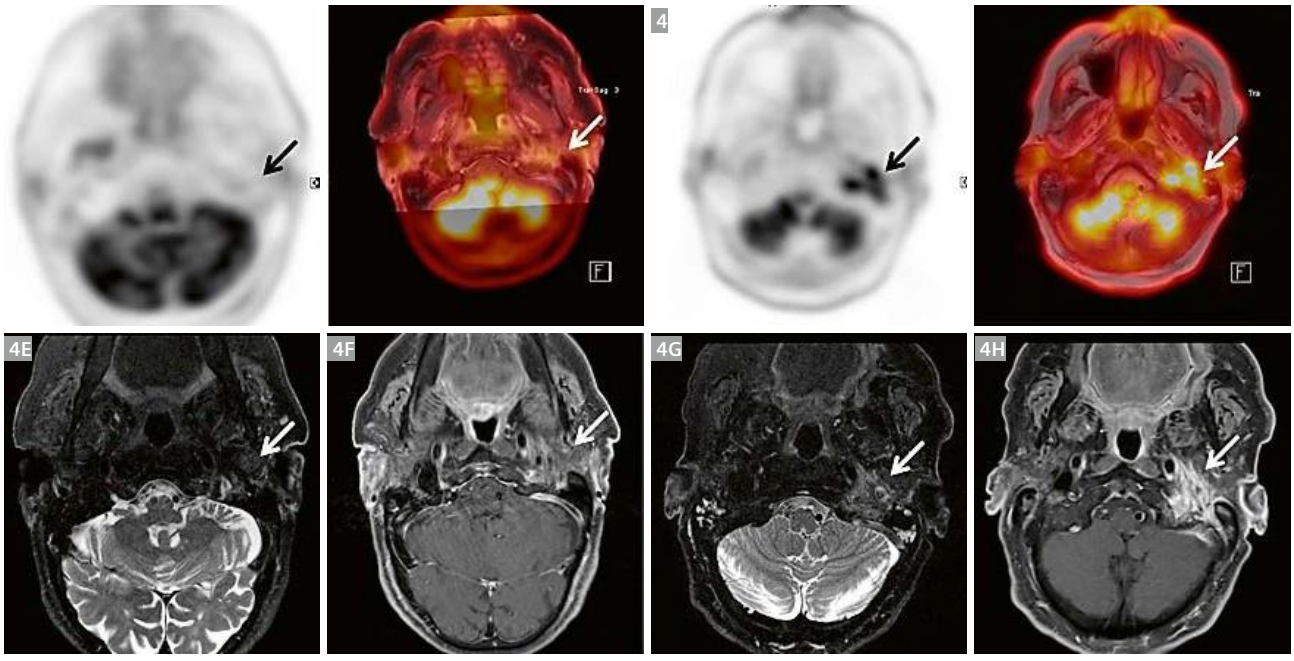

4 85-year-old patient with skull base osteomyelitis at the left side and paresis of the facial nerve. **(4A, C)** PET image; **(4B, D)** FDG PET-MRI overlay; **(4E, G)** T2 FS MRI; **(4F, H)** T1 FS after gadolinium injection MRI; 4A, B, E, and F follow-up after 3 months of antibiotic treatment. The arrows show contrast enhancement in the subtemporal soft tissue and around the styloid processes with engagement of the stylomastoid foramen. The follow-up scan shows decreased soft tissue enhancement and decreased FDG accumulation.

References

1 Grandis JR et al. The changing face of malignant (necrotising) external otitis: clinical, radiological and anatomic correlations. Lancet Infect Dis. 2004;4(1):34–39.
2 Pineda C et al. Imaging of osteomyelitis: current concepts. Infect Dis Clin North Am. 2006;20(4):789-825.
3 Nawaz A et al. Diagnostic Performance of FDG-PET, MRI, and Plain Film Radiography (PFR) for the Diagnosis of Osteomyelitis in the Diabetic Foot. Molecular Imaging and Biology. 2010;12(3):335–342.
4 Gold RH et al. Bacterial osteomyelitis: findings on plain radiography, CT, MR, and scintigraphy. American Journal of Roentgenology. 1991;157:365–370.
5 Termaat MF et al. The accuracy of diagnostic imaging for the assessment of chronic osteomyelitis: a systematic review and meta-analysis. J Bone Joint Surg Am. 2005;87-A(11):2464–2471.
6 Lee YJ et al. The imaging of osteomyelitis. Quant Imaging Med Surg. 2016;6(2):184–198.
7 van der Bruggen, W. (2010). PET and SPECT in Osteomyelitis and Prosthetic Bone and Joint Infections: A Systematic Review. Seminars in Nuclear Medicine, 3–15.
8 Erba PA et al. Image acquisition and interpretation criteria for 99mTc-HMPAO-labelled white blood cell scintigraphy: results of a multicentre study. European Journal of Nuclear Medicine and Molecular Imaging. 2014;41(4):615–623.
9 Gratz S et al. 18F-FDG hybrid PET in patients with suspected spondylitis. European Journal of Nuclear Medicine and Molecular Imaging. 2002;29(4):516–524.
10 Hulsen DJW et al. Hybrid FDG-PET/MR imaging of chronic osteomyelitis: a prospective case series. European Journal of Hybrid Imaging. 2019;3: article number 7.
11 Fahner J et al. Use of Simultaneous 18F-FDG PET/MRI for the Detection of Spondylodiskitis. J Nucl Med. 2016;57(9):1396–1401.

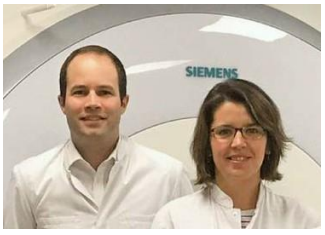

Contact

Rik Moonen
Department of Radiology and Nuclear Medicine
Maastricht University Medical Centre
Maastricht
The Netherlands
rik.moonen@mumc.nl

Cristina Mitea
Department of Radiology and Nuclear Medicine
Maastricht University Medical Centre
Maastricht
The Netherlands
cristina.mitea@mumc.nl

HIGHLIGHTS OF PRESCRIBING INFORMATION

These highlights do not include all the information needed to use Fludeoxyglucose F 18 Injection safely and effectively. See full prescribing information for Fludeoxyglucose F 18 Injection. Fludeoxyglucose F 18 Injection, USP For intravenous use Initial U.S. Approval: 2005

RECENT MAJOR CHANGES

Warnings and Precautions (5.1, 5.2)	7/2010
Adverse Reactions (6)	7/2010

INDICATIONS AND USAGE

Fludeoxyglucose F18 Injection is indicated for positron emission tomography (PET) imaging in the following settings:

- Oncology: For assessment of abnormal glucose metabolism to assist in the evaluation of malignancy in patients with known or suspected abnormalities found by other testing modalities, or in patients with an existing diagnosis of cancer.
- Cardiology: For the identification of left ventricular myocardium with residual glucose metabolism and reversible loss of systolic function in patients with coronary artery disease and left ventricular dysfunction, when used together with myocardial perfusion imaging.
- Neurology: For the identification of regions of abnormal glucose metabolism associated with foci of epileptic seizures (1).

DOSAGE AND ADMINISTRATION

Fludeoxyglucose F 18 Injection emits radiation. Use procedures to minimize radiation exposure. Screen for blood glucose abnormalities.

- In the oncology and neurology settings, instruct patients to fast for 4 to 6 hours prior to the drug's injection. Consider medical therapy and laboratory testing to assure at least two days of normoglycemia prior to the drug's administration (5.2).
- In the cardiology setting, administration of glucose-containing food or liquids (e.g., 50 to 75 grams) prior to the drug's injection facilitates localization of cardiac ischemia (2.3).

Aseptically withdraw Fludeoxyglucose F 18 Injection from its container and administer by intravenous injection (2).

The recommended dose:

- for adults is 5 to 10 mCi (185 to 370 MBq), in all indicated clinical settings (2.1).
- for pediatric patients is 2.6 mCi in the neurology setting (2.2).

Initiate imaging within 40 minutes following drug injection; acquire static emission images 30 to 100 minutes from time of injection (2).

DOSAGE FORMS AND STRENGTHS

Multi-dose 30mL and 50mL glass vial containing 0.74 to 7.40 GBq/mL (20 to 200 mCi/mL) Fludeoxyglucose F 18 Injection and 4.5mg of sodium chloride with 0.1 to 0.5% w/w ethanol as a stabilizer (approximately 15 to 50 mL volume) for intravenous administration (3).

CONTRAINDICATIONS

None

WARNINGS AND PRECAUTIONS

- Radiation risks: use smallest dose necessary for imaging (5.1).
- Blood glucose adnormalities: may cause suboptimal imaging (5.2).

ADVERSE REACTIONS

Hypersensitivity reactions have occurred; have emergency resuscitation equipment and personnel immediately available (6).

To report SUSPECTED ADVERSE REACTIONS, contact PETNET Solutions, Inc. at 877-473-8638 or FDA at 1-800-FDA-1088 or www.fda.gov/medwatch.

USE IN SPECIFIC POPULATIONS

Pregnancy Category C: No human or animal data. Consider alternative diagnostics; use only if clearly needed (8.1).

- Nursing mothers: Use alternatives to breast feeding (e.g., stored breast milk or infant formula) for at least 10 half-lives of radioactive decay, if Fludeoxyglucose F 18 Injection is administered to a woman who is breast-feeding (8.3).
- Pediatric Use: Safety and effectiveness in pediatric patients have not been established in the oncology and cardiology settings (8.4).

See 17 for PATIENT COUNSELING INFORMATION

Revised: 1/2011

FULL PRESCRIBING INFORMATION: CONTENTS*

*Sections or subsections omitted from the full prescribing information are not listed.

FULL PRESCRIBING INFORMATION

1 INDICATIONS AND USAGE

Fludeoxyglucose F 18 Injection is indicated for positron emission tomography (PET) imaging in the following settings:

1.1 Oncology

For assessment of abnormal glucose metabolism to assist in the evaluation of malignancy in patients with known or suspected abnormalities found by other testing modalities, or in patients with an existing diagnosis of cancer.

1.2 Cardiology

For the identification of left ventricular myocardium with residual glucose metabolism and reversible loss of systolic function in patients with coronary artery disease and left ventricular dysfunction, when used together with myocardial perfusion imaging.

1.3 Neurology

For the identification of regions of abnormal glucose metabolism associated with foci of epileptic seizures.

2 DOSAGE AND ADMINISTRATION

Fludeoxyglucose F 18 Injection emits radiation. Use procedures to minimize radiation exposure. Calculate the final dose from the end of synthesis (EOS) time using proper radioactive decay factors. Assay the final dose in a properly calibrated dose calibrator before administration to the patient [see Description (11.2)].

2.1 Recommended Dose for Adults

Within the oncology, cardiology and neurology settings, the recommended dose for adults is 5 to 10 mCi (185 to 370 MBq) as an intravenous injection.

2.2 Recommended Dose for Pediatric Patients

Within the neurology setting, the recommended dose for pediatric patients is 2.6 mCi, as an intravenous injection. The optimal dose adjustment on the basis of body size or weight has not been determined [see Use in Special Populations (8.4)].

2.3 Patient Preparation

- To minimize the radiation absorbed dose to the bladder, encourage adequate hydration. Encourage the patient to drink water or other fluids (as tolerated) in the 4 hours before their PET study.
- Encourage the patient to void as soon as the imaging study is completed and as often as possible thereafter for at least one hour.
- Screen patients for clinically significant blood glucose abnormalities by obtaining a history and/or laboratory tests [see Warnings and Precautions (5.2)]. Prior to Fludeoxyglucose F 18 PET imaging in the oncology and neurology settings, instruct patient to fast for 4 to 6 hours prior to the drug's injection.
- In the cardiology setting, administration of glucose-containing food or liquids (e.g., 50 to 75 grams) prior to Fludeoxyglucose F18 Injection facilitates localization of cardiac ischemia

2.4 Radiation Dosimetry

The estimated human absorbed radiation doses (rem/mCi) to a newborn (3.4 kg), 1-year-old (9.8 kg), 5-year-old (19 kg), 10-year-old (32 kg), 15-year-old (57 kg), and adult (70 kg) from intravenous administration of Fludeoxyglucose F 18 Injection are shown in Table 1. These estimates were calculated based on human[2] data and using the data published by the International Commission on Radiological Protection[4] for Fludeoxyglucose ^{18}F. The dosimetry data show that there are slight variations in absorbed radiation dose for various organs in each of the age groups. These dissimilarities in absorbed radiation dose are due to developmental age variations (e.g., organ size, location, and overall metabolic rate for each age group). The identified critical organs (in descending order) across all age groups evaluated are the urinary bladder, heart, pancreas, spleen, and lungs.

Table 1. Estimated Absorbed Radiation Doses (rem/mCi) After Intravenous Administration of Fludeoxyglucose F-18 Injection[a]

Organ	Newborn (3.4 kg)	1-year-old (9.8 kg)	5-year-old (19 kg)	10-year-old (32 kg)	15-year-old (57 kg)	Adult (70 kg)
Bladder wall[b]	4.3	1.7	0.93	0.60	0.40	0.32
Heart wall	2.4	1.2	0.70	0.44	0.29	0.22
Pancreas	2.2	0.68	0.33	0.25	0.13	0.096
Spleen	2.2	0.84	0.46	0.29	0.19	0.14
Lungs	0.96	0.38	0.20	0.13	0.092	0.064
Kidneys	0.81	0.34	0.19	0.13	0.089	0.074
Ovaries	0.80	0.8	0.19	0.11	0.058	0.053
Uterus	0.79	0.35	0.19	0.12	0.076	0.062
LLI wall *	0.69	0.28	0.15	0.097	0.060	0.051
Liver	0.69	0.31	0.17	0.11	0.076	0.058
Gallbladder wall	0.69	0.26	0.14	0.093	0.059	0.049
Small intestine	0.68	0.29	0.15	0.096	0.060	0.047
ULI wall **	0.67	0.27	0.15	0.090	0.057	0.046
Stomach wall	0.65	0.27	0.14	0.089	0.057	0.047
Adrenals	0.65	0.28	0.15	0.095	0.061	0.048
Testes	0.64	0.27	0.14	0.085	0.052	0.041
Red marrow	0.62	0.26	0.14	0.089	0.057	0.047
Thymus	0.61	0.26	0.14	0.086	0.056	0.044
Thyroid	0.61	0.26	0.13	0.080	0.049	0.039
Muscle	0.58	0.25	0.13	0.078	0.049	0.039
Bone surface	0.57	0.24	0.12	0.079	0.052	0.041
Breast	0.54	0.22	0.11	0.068	0.043	0.034
Skin	0.49	0.20	0.10	0.060	0.037	0.030
Brain	0.29	0.13	0.09	0.078	0.072	0.070
Other tissues	0.59	0.25	0.13	0.083	0.052	0.042

[a] MIRDOSE 2 software was used to calculate the radiation absorbed dose. Assumptions on the biodistribution based on data from Gallagher et al.1 and Jones et al.[2]

[b] The dynamic bladder model with a uniform voiding frequency of 1.5 hours was used.

*LLI = lower large intestine; **ULI = upper large intestine

2.5 Radiation Safety – Drug Handling

- Use waterproof gloves, effective radiation shielding, and appropriate safety measures when handling Fludeoxyglucose F 18 Injection to avoid unnecessary radiation exposure to the patient, occupational workers, clinical personnel and other persons.
- Radiopharmaceuticals should be used by or under the control of physicians who are qualified by specific training and experience in the safe use and handling of radionuclides, and whose experience and training have been approved by the appropriate governmental agency authorized to license the use of radionuclides.
- Calculate the final dose from the end of synthesis (EOS) time using proper radioactive decay factors. Assay the final dose in a properly calibrated dose calibrator before administration to the patient [see Description (11.2)].
- The dose of Fludeoxyglucose F 18 used in a given patient should be minimized consistent with the objectives of the procedure, and the nature of the radiation detection devices employed.

2.6 Drug Preparation and Administration

- Calculate the necessary volume to administer based on calibration time and dose.
- Aseptically withdraw Fludeoxyglucose F 18 Injection from its container.
- Inspect Fludeoxyglucose F 18 Injection visually for particulate matter and discoloration before administration, whenever solution and container permit.
- Do not administer the drug if it contains particulate matter or discoloration; dispose of these unacceptable or unused preparations in a safe manner, in compliance with applicable regulations. Use Fludeoxyglucose F 18 Injection within 12 hours from the EOS.

2.7 Imaging Guidelines

- Initiate imaging within 40 minutes following Fludeoxyglucose F 18 Injection administration.
- Acquire static emission images 30 to 100 minutes from the time of injection.

3 DOSAGE FORMS AND STRENGTHS

Multiple-dose 30 mL and 50 mL glass vial containing 0.74 to 7.40 GBq/mL (20 to 200 mCi/mL) of Fludeoxyglucose F 18 Injection and 4.5 mg of sodium chloride with 0.1 to 0.5% w/w ethanol as a stabilizer (approximately 15 to 50 mL volume) for intravenous administration.

4 CONTRAINDICATIONS

None

5 WARNINGS AND PRECAUTIONS

5.1 Radiation Risks

Radiation-emitting products, including Fludeoxyglucose F 18 Injection, may increase the risk for cancer, especially in pediatric patients. Use the smallest dose necessary for imaging and ensure safe handling to protect the patient and health care worker [see Dosage and Administration (2.5)].

5.2 Blood Glucose Abnormalities

In the oncology and neurology setting, suboptimal imaging may occur in patients with inadequately regulated blood glucose levels. In these patients, consider medical therapy and laboratory testing to assure at least two days of normoglycemia prior to Fludeoxyglucose F 18 Injection administration.

6 ADVERSE REACTIONS

Hypersensitivity reactions with pruritus, edema and rash have been reported in the post-marketing setting. Have emergency resuscitation equipment and personnel immediately available.

7 DRUG INTERACTIONS

The possibility of interactions of Fludeoxyglucose F 18 Injection with other drugs taken by patients undergoing PET imaging has not been studied.

8 USE IN SPECIFIC POPULATIONS

8.1 Pregnancy

Pregnancy Category C

Animal reproduction studies have not been conducted with Fludeoxyglucose F 18 Injection. It is also not known whether Fludeoxyglucose F 18 Injection can cause fetal harm when administered to a pregnant woman or can affect reproduction capacity. Consider alternative diagnostic tests in a pregnant woman; administer Fludeoxyglucose F 18 Injection only if clearly needed.

8.3 Nursing Mothers

It is not known whether Fludeoxyglucose F 18 Injection is excreted in human milk. Consider alternative diagnostic tests in women who are breast-feeding. Use alternatives to breast feeding (e.g., stored breast milk or infant formula) for at least 10 half-lives of radioactive decay, if Fludeoxyglucose F 18 Injection is administered to a woman who is breast-feeding.

8.4 Pediatric Use

The safety and effectiveness of Fludeoxyglucose F 18 Injection in pediatric patients with epilepsy is established on the basis of studies in adult and pediatric patients. In pediatric patients with epilepsy, the recommended dose is 2.6 mCi. The optimal dose adjustment on the basis of body size or weight has not been determined. In the oncology or cardiology settings, the safety and effectiveness of Fludeoxyglucose F 18 Injection have not been established in pediatric patients.

11 DESCRIPTION

11.1 Chemical Characteristics

Fludeoxyglucose F 18 Injection is a positron emitting radiopharmaceutical that is used for diagnostic purposes in conjunction with positron emission tomography (PET) imaging. The active ingredient 2-deoxy-2-[^{18}F]fluoro-D-glucose has the molecular formula of $C_6H_{11}{}^{18}FO_5$ with a molecular weight of 181.26, and has the following chemical structure:

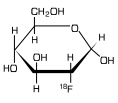

Fludeoxyglucose F 18 Injection is provided as a ready to use sterile, pyrogen free, clear, colorless solution. Each mL contains between 0.740 to 7.40GBq (20.0 to 200 mCi) of 2-deoxy-2-[^{18}F]fluoro-D-glucose at the EOS, 4.5 mg of sodium chloride and 0.1 to 0.5% w/w ethanol as a stabilizer. The pH of the solution is between 4.5 and 7.5. The solution is packaged in a multiple-dose glass vial and does not contain any preservative.

11.2 Physical Characteristics

Fluorine F 18 decays by emitting positron to Oxygen O 16 (stable) and has a physical half-life of 109.7 minutes. The principal photons useful for imaging are the dual 511 keV gamma photons, that are produced and emitted simultaneously in opposite direction when the positron interacts with an electron (Table 2).

Table 2. Pricipal Radiation Emission Data for Fluorine F18		
Radiation/Emission	% Per Disintegration	Mean Energy
Positron (b+)	96.73	249.8 keV
Gamma (±)*	193.46	511.0 keV

*Produced by positron annihilation

From: Kocher, D.C. Radioactive Decay Tables DOE/TIC-I 1026, 89 (1981)

The specific gamma ray constant (point source air kerma coefficient) for fluorine F 18 is 5.7 R/hr/mCi (1.35 x 10-6 Gy/hr/kBq) at 1 cm. The half-value layer (HVL) for the 511 keV photons is 4 mm lead (Pb). The range of attenuation coefficients for this radionuclide as a function of lead shield thickness is shown in Table 3. For example, the interposition of an 8 mm thickness of Pb, with a coefficient of attenuation of 0.25, will decrease the external radiation by 75%.

Table 3. Radiation Attenuation of 511 keV Photons by lead (Pb) shielding	
Shield thickness (Pb) mm	Coefficient of attenuation
0	0.00
4	0.50
8	0.25
13	0.10
26	0.01
39	0.001
52	0.0001

For use in correcting for physical decay of this radionuclide, the fractions remaining at selected intervals after calibration are shown in Table 4.

Table 4. Physical Decay Chart for Fluorine F18	
Minutes	Fraction Remaining
0*	1.000
15	0.909
30	0.826
60	0.683
110	0.500
220	0.250

*calibration time

12 CLINICAL PHARMACOLOGY

12.1 Mechanism of Action

Fludeoxyglucose F 18 is a glucose analog that concentrates in cells that rely upon glucose as an energy source, or in cells whose dependence on glucose increases under pathophysiological conditions. Fludeoxyglucose F 18 is transported through the cell membrane by facilitative glucose transporter proteins and is phosphorylated within the cell to [^{18}F] FDG-6-phosphate by the enzyme hexokinase. Once phosphorylated it cannot exit until it is dephosphorylated by glucose-6-phosphatase. Therefore, within a given tissue or pathophysiological process, the retention and clearance of Fludeoxyglucose F 18 reflect a balance involving glucose transporter, hexokinase and glucose-6-phosphatase activities. When allowance is made for the kinetic differences between glucose and Fludeoxyglucose F 18 transport and phosphorylation (expressed as the ‚lumped constant" ratio), Fludeoxyglucose F 18 is used to assess glucose metabolism. In comparison to background activity of the specific organ or tissue type, regions of decreased or absent uptake of Fludeoxyglucose F 18 reflect the decrease or absence of glucose metabolism. Regions of increased uptake of Fludeoxyglucose F 18 reflect greater than normal rates of glucose metabolism.

12.2 Pharmacodynamics

Fludeoxyglucose F 18 Injection is rapidly distributed to all organs of the body after intravenous administration. After background clearance of Fludeoxyglucose F 18 Injection, optimal PET imaging is generally achieved between 30 to 40 minutes after administration.

In cancer, the cells are generally characterized by enhanced glucose metabolism partially due to (1) an increase in activity of glucose transporters, (2) an increased rate of phosphorylation activity, (3) a reduction of phosphatase activity or, (4) a dynamic alteration in the balance among all these processes. However, glucose metabolism of cancer as reflected by Fludeoxyglucose F 18 accumulation shows considerable variability. Depending on tumor type, stage, and location, Fludeoxyglucose F 18 accumulation may be increased, normal, or decreased. Also, inflammatory cells can have the same variability of uptake of Fludeoxyglucose F 18.

In the heart, under normal aerobic conditions, the myocardium meets the bulk of its energy requirements by oxidizing free fatty acids. Most of the exogenous glucose taken up by the myocyte is converted into glycogen. However, under ischemic conditions, the oxidation of free fatty acids decreases, exogenous glucose becomes the preferred myocardial sub strate, glycolysis is stimulated, and glucose taken up by the myocyte is metabolized immediately instead of being converted into glycogen. Under these conditions, phosphorylated Fludeoxyglucose F 18 accumulates in the myocyte and can be detected with PET imaging.

In the brain, cells normally rely on aerobic metabolism. In epilepsy, the glucose metabolism varies. Generally, during a seizure, glucose metabolism increases. Interictally, the seizure focus tends to be hypometabolic.

12.3 Pharmacokinetics

Distribution: In four healthy male volunteers, receiving an intravenous administration of 30 seconds in duration, the arterial blood level profile for Fludeoxyglucose F 18 decayed triexponentially. The effective half-life ranges of the three phases were 0.2 to 0.3 minutes, 10 to 13 minutes with a mean and standard deviation (STD) of 11.6 (±) 1.1 min, and 80 to 95 minutes with a mean and STD of 88 (±) 4 min. Plasma protein binding of Fludeoxyglucose F 18 has not been studied.

Metabolism: Fludeoxyglucose F 18 is transported into cells and phosphorylated to [^{18}F]-FDG-6-phosphate at a rate proportional to the rate of glucose utilization within that tissue. [F18]-FDG-6-phosphate presumably is metabolized to 2-deoxy-2-[F18]fluoro-6-phospho-D-mannose([F 18]FDM-6-phosphate).

Fludeoxyglucose F 18 Injection may contain several impurities (e.g., 2-deoxy-2-chloro-D-glucose (ClDG)). Biodistribution and metabolism of ClDG are presumed to be similar to Fludeoxyglucose F 18 and would be expected to result in intracellular formation of 2-deoxy-2-chloro-6-phospho-D-glucose (ClDG-6-phosphate) and 2-deoxy-2-chloro-6-phospho-D-mannose (ClDM-6-phosphate). The phosphorylated deoxyglucose compounds are dephosphorylated and the resulting compounds (FDG, FDM, ClDG, and ClDM) presumably leave cells by passive diffusion. Fludeoxyglucose F 18 and related compounds are cleared from non-cardiac tissues within 3 to 24 hours after administration. Clearance from the cardiac tissue may require more than 96 hours. Fludeoxyglucose F 18 that is not involved in glucose metabolism in any tissue is then excreted in the urine.

Elimination: Fludeoxyglucose F 18 is cleared from most tissues within 24 hours and can be eliminated from the body unchanged in the urine. Three elimination phases have been identified in the reviewed literature. Within 33 minutes, a mean of 3.9% of the administrated radioactive dose was measured in the urine. The amount of radiation exposure of the urinary bladder at two hours post-administration suggests that 20.6% (mean) of the radioactive dose was present in the bladder.

Special Populations: The pharmacokinetics of Fludeoxyglucose F 18 Injection have not been studied in renally-impaired, hepatically impaired or pediatric patients. Fludeoxyglucose F 18 is eliminated through the renal system. Avoid excessive radiation exposure to this organ system and adjacent tissues. The effects of fasting, varying blood sugar levels, conditions of glucose intolerance, and diabetes mellitus on Fludeoxyglucose F 18 distribution in humans have not been ascertained [see Warnings and Precautions (5.2)].

13 NONCLINICAL TOXICOLOGY

13.1 Carcinogenesis, Mutagenesis, Impairment of Fertility

Animal studies have not been performed to evaluate the Fludeoxyglucose F 18 Injection carcinogenic potential, mutagenic potential or effects on fertility.

14 CLINICAL STUDIES

14.1 Oncology

The efficacy of Fludeoxyglucose F 18 Injection in positron emission tomography cancer imaging was demonstrated in 16 independent studies. These studies prospectively evaluated the use of Fludeoxyglucose F 18 in patients with suspected or known malignancies, including non-small cell lung cancer, colo-rectal, pancreatic, breast, thyroid, melanoma, Hodgkin's and non-Hodgkin's lymphoma, and various types of metastatic cancers to lung, liver, bone, and axillary nodes. All these studies had at least 50 patients and used pathology as a standard of truth. The Fludeoxyglucose F 18 Injection doses in the studies ranged from 200 MBq to 740 MBq with a median and mean dose of 370 MBq. In the studies, the diagnostic performance of Fludeoxyglucose F 18 Injection varied with the type of cancer, size of cancer, and other clinical conditions. False negative and false positive scans were observed. Negative Fludeoxyglucose F 18 Injection PET scans do not exclude the diagnosis of cancer. Positive Fludeoxyglucose F 18 Injection PET scans can not replace pathology to establish a diagnosis of cancer. Non-malignant conditions such as fungal infections, inflammatory processes and benign tumors have patterns of increased glucose metabolism that may give rise to false-positive scans. The efficacy of Fludeoxyglucose F 18 Injection PET imaging in cancer screening was not studied.

14.2 Cardiology

The efficacy of Fludeoxyglucose F 18 Injection for cardiac use was demonstrated in ten independent, prospective studies of patients with coronary artery disease and chronic left ventricular systolic dysfunction who were scheduled to undergo coronary revascularization. Before revascularization, patients underwent PET imaging with Fludeoxyglucose F 18 Injection (74 to 370 MBq, 2 to 10 mCi) and perfusion imaging with other diagnostic radiopharmaceuticals. Doses of Fludeoxyglucose F 18 Injection ranged from 74 to 370 MBq (2 to 10 mCi). Segmental, left ventricular, wall-motion assessments of asynergic areas made before revascularization were compared in a blinded manner to assessments made after successful revascularization to identify myocardial segments with functional recovery. Left ventricular myocardial segments were predicted to have reversible loss of systolic function if they showed Fludeoxyglucose F 18 accumulation and reduced perfusion (i.e., flow-metabolism mismatch). Conversely, myocardial segments were predicted to have irreversible loss of systolic function if they showed reductions in both Fludeoxyglucose F 18 accumulation and perfusion (i.e., matched defects). Findings of flow-metabolism mismatch in a myocardial segment may suggest that successful revascularization will restore myocardial function in that segment. However, false-positive tests occur regularly, and the decision to have a patient undergo revascularization should not be based on PET findings alone. Similarly, findings of a matched defect in a myocardial segment may suggest that myocardial function will not recover in that segment, even if it is successfully revascularized. However, false-negative tests occur regularly, and the decision to recommend against coronary revascularization, or to recommend a cardiac transplant, should not be based on PET findings alone. The reversibility of segmental dysfunction as predicted with Fludeoxyglucose F 18 PET imaging depends on successful coronary revascularization. Therefore, in patients with a low likelihood of successful revascularization, the diagnostic usefulness of PET imaging with Fludeoxyglucose F 18 Injection is more limited.

14.3 Neurology

In a prospective, open label trial, Fludeoxyglucose F 18 Injection was evaluated in 86 patients with epilepsy. Each patient received a dose of Fludeoxyglucose F 18 Injection in the range of 185 to 370 MBq (5 to 10 mCi). The mean age was 16.4 years (range: 4 months to 58 years; of these, 42 patients were less than 12 years and 16 patients were less than 2 years old). Patients had a known diagnosis of complex partial epilepsy and were under evaluation for surgical treatment of their seizure disorder. Seizure foci had been previously identified on ictal EEGs and sphenoidal EEGs. Fludeoxyglucose F 18 Injection PET imaging confirmed previous diagnostic findings in 16% (14/87) of the patients; in 34% (30/87) of the patients, Fludeoxyglucose F 18 Injection PET images provided new findings. In 32% (27/87), imaging with Fludeoxyglucose F 18 Injection was inconclusive. The impact of these imaging findings on clinical outcomes is not known. Several other studies comparing imaging with Fludeoxyglucose F 18 Injection results to subsphenoidal EEG, MRI and/or surgical findings supported the concept that the degree of hypometabolism corresponds to areas of confirmed epileptogenic foci. The safety and effectiveness of Fludeoxyglucose F 18 Injection to distinguish idiopathic epileptogenic foci from tumors or other brain lesions that may cause seizures have not been established.

15 REFERENCES

- 1. Gallagher B.M., Ansari A., Atkins H., Casella V., Christman D.R., Fowler J.S., Ido T., MacGregor R.R., Som P., Wan C.N., Wolf A.P., Kuhl D.E., and Reivich M. "Radiopharmaceuticals XXVII. ^{18}F-labeled 2-deoxy-2-fluoro-d-glucose as a radiopharmaceutical for measuring regional myocardial glucose metabolism in vivo: tissue distribution and imaging studies in animals," J Nucl Med, 1977; 18, 990-6.
- 2. Jones S.C., Alavi, A., Christman D., Montanez, I., Wolf, A.P., and Reivich M. "The radiation dosimetry of 2 [F-18] fluoro-2-deoxy-D-glucose in man," J Nucl Med, 1982; 23, 613-617.
- 3. Kocher, D.C. "Radioactive Decay Tables: A handbook of decay data for application to radiation dosimetry and radiological assessments," 1981, DOE/TIC-I 1026, 89.
- 4. ICRP Publication 53, Volume 18, No. I-4,1987, pages 75-76.

16 HOW SUPPLIED/STORAGE AND DRUG HANDLING

Fludeoxyglucose F 18 Injection is supplied in a multi-dose, capped 30 mL and 50 mL glass vial containing between 0.740 to 7.40 GBq/mL (20 to 200 mCi/mL), of no carrier added 2-deoxy-2-[F 18] fluoro-D-glucose, at end of synthesis, in approximately 15 to 50 mL. The contents of each vial are sterile, pyrogen-free and preservative-free.

NDC 40028-511-30; 40028-511-50

Receipt, transfer, handling, possession, or use of this product is subject to the radioactive material regulations and licensing requirements of the U.S. Nuclear Regulatory Commission, Agreement States or Licensing States as appropriate.

Store the Fludeoxyglucose F 18 Injection vial upright in a lead shielded container at 25°C (77°F); excursions permitted to 15-30°C (59-86°F).

Store and dispose of Fludeoxyglucose F 18 Injection in accordance with the regulations and a general license, or its equivalent, of an Agreement State or a Licensing State.

The expiration date and time are provided on the container label. Use Fludeoxyglucose F 18 Injection within 12 hours from the EOS time.

17 PATIENT COUNSELING INFORMATION

Instruct patients in procedures that increase renal clearance of radioactivity.

Encourage patients to:

- drink water or other fluids (as tolerated) in the 4 hours before their PET study.
- void as soon as the imaging study is completed and as often as possible thereafter for at least one hour.

Manufactured by: PETNET Solutions Inc. 810 Innovation Drive Knoxville, TN 37932

Distributed by: PETNET Solutions Inc.^ 810 Innovation Drive Knoxville, TN 37932^

PETNET Solutions

PN0002262 Rev. A

Marcg 1, 2011

Indications

Fludeoxyglucose F18 Injection is indicated for positron emission tomography (PET) imaging in the following settings:

Oncology: For assessment of abnormal glucose metabolism to assist in the evaluation of malignancy in patients with known or suspected abnormalities found by other testing modalities, or in patients with an existing diagnosis of cancer.

Cardiology: For the identification of left ventricular myocardium with residual glucose metabolism and reversible loss of systolic function in patients with coronary artery disease and left ventricular dysfunction, when used together with myocardial perfusion imaging.

Neurology: For the identification of regions of abnormal glucose metabolism associated with foci of epileptic seizures.

Important Safety Information

Radiation Risks: Radiationemitting products, including Fludeoxyglucose F18 Injection, may increase the risk for cancer, especially in pediatric patients. Use the smallest dose necessary for imaging and ensure safe handling to protect the patient and healthcare worker.

Blood Glucose Abnormalities: In the oncology and neurology setting, suboptimal imaging may occur in patients with inadequately regulated blood glucose levels. In these patients, consider medical therapy and laboratory testing to assure at least two days of normoglycemia prior to Fludeoxyglucose F18 Injection administration.

Adverse Reactions: Hypersensitivity reactions with pruritus, edema and rash have been reported; have emergency resuscitation equipment and personnel immediately available.

Dosage Forms and Strengths: Multiple-dose 30 mL and 50 mL glass vial containing 0.74 to 7.40 GBq/mL (20 to 200 mCi/mL) of Fludeoxyglucose F^{18} injection and 4.5 mg of sodium chloride with 0.1 to 0.5% w/w ethanolas a stabilizer (approximately 15 to 50 mL volume) for intravenous administration. Fludeoxyglucose F^{18} injection is manufactured by Siemens' PETNET Solutions, 810 Innovation Drive, Knoxville, TN 39732, USA.

Case Series: Clinical Application of Liver Fat and Iron Quantification using LiverLab

Barbara Frittoli, M.D.[1]; Martina Bertuletti, M.D.[1]; Valentina Angelini, M.D.[2]; Luigi Grazioli, M.D.[1]

[1]ASST-Spedali Civili di Brescia, Italy
[2]"Federico II" University, Naples, Italy

Background

In western countries in the last ten years, nonalcoholic fatty liver disease (NAFLD) has increased in incidence and prevalence, as has its advanced form, nonalcoholic steatohepatitis (NASH). These are complex metabolic alterations of liver function and structure. They have long term impacts on health and quality of life, raising the risk of cirrhosis and hepatocellular carcinoma. In the USA they are now the second indication for liver transplantation [1–5].

It has therefore become necessary to characterize and quantify the liver reversible modifications such as intrahepatic fat and iron overload associated with NAFLD and NASH. The ability to quantify liver fat will also benefit patients with chemotherapy-associated-steatohepatitis (CASH); and quantifying iron accumulation can benefit those with hemochromatosis, hemosiderosis, and chronic hepatopathy diseases [1–5].

These overload diseases usually have heterogeneous distribution within the liver, which is a challenge for liver biopsy. Biopsy is still considered by clinicians as the gold standard for diagnosis and quantification, despite being invasive. However, biopsy does not always show the real severity of the disease and its distribution within the parenchyma because it samples only one or a few sites.

Various noninvasive qualitative and quantitative techniques can be used to quantify liver steatosis, including ultrasound and computed tomography; but MRI is the most accurate and reproducible technique. MRI is also the only accurate method for detecting iron overload in the liver.

In recent years, software has been developed to automatically manage quantitative measurements and represent them with color parametric maps, which has simplified the use of quantitative MR imaging in everyday clinical practice [6].

Recent MRI methods for liver fat and iron quantification in the liver are based on the Dixon technique and spectroscopy. These methods are available as LiverLab on our magnetic resonance tomographs 1.5T MAGNETOM Aera and 3T MAGNETOM Skyra (Siemens Healthcare, Erlangen, Germany).

LiverLab comprises a fat and iron screening component (two-point e-Dixon), and two methods for evaluation: multi-echo Dixon VIBE (six point q-Dixon), an image-based method; and HISTO, a voxel-based spectroscopic method. It also provides clinical reports. In our experience with LiverLab, we take advantage of its very fast acquisition, reproducibility of results and interpretation immediacy [7, 8].

For our patients undergoing MR liver examination, the first sequences acquired during our liver protocol are T1 GRE in/opp. If liver signal intensity is hypointense in in-phase or opposed-phase acquisition, LiverLab is acquired before contrast media administration, in order to identify and quantify fat and/or iron deposition. It takes about 5–7 minutes if both Multi-echo Dixon VIBE and HISTO are acquired, and doesn't alter the regular workflow. Some hepatopathic and hematological patients are scheduled only for LiverLab acquisition by Hepatologists and Hematologists and then the complete MR examination takes about 10 minutes, with T2* map added to the protocol.

In our experience, LiverLab has become routinely useful in evaluating liver overload diseases in many clinical assets, bringing the advantages of rapid, accurate and reproducible acquisition. Here we show examples, in patients with fat accumulation (NAFLD/NASH, liver chronic hepatopathy, CASH in oncological patients), iron accumulation (hemochromatosis, hemosiderosis), and both (NAFLD/chronic hepatopathy). This technique is useful for follow-up and drugs effect monitoring, due to easy and rapid administration and accurate measurement.

Case 1

50-year-old male with incidental finding of cholestasis and hypercholesterolemia. Ultrasound examination of the liver had very heterogeneous aspect, with hyperechoic areas and pseudonodular hypoechoic areas. The patient was scheduled for an MRI examination to quantify steatosis and characterize pseudonodular lesions. Images were acquired by 1.5T MAGNETOM Aera.

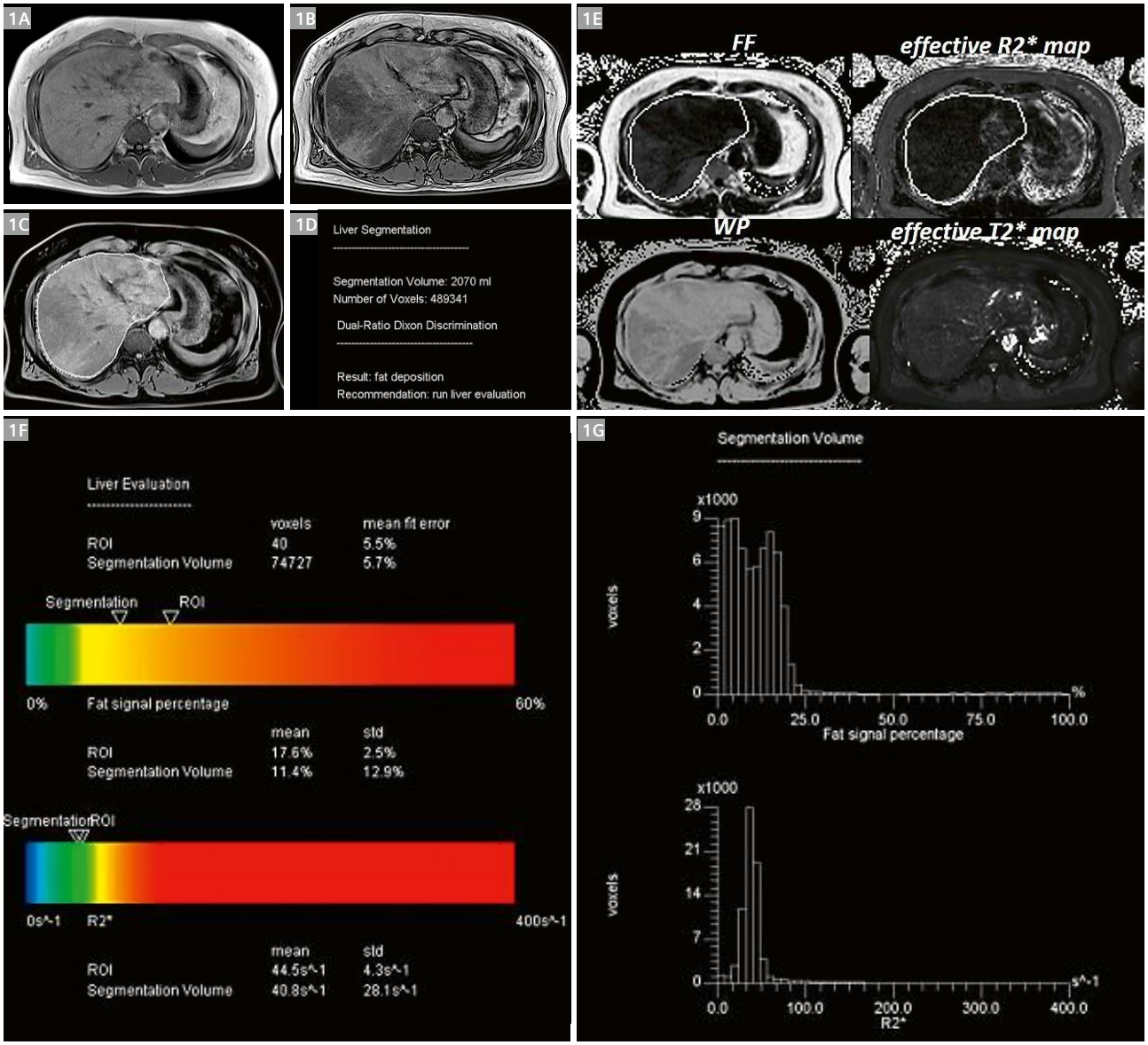

1 **(1A)** T1w GRE in-phase: liver of regular volume and morphology.
(1B) T1w GRE opp-phase: heterogeneous drop of signal within the liver parenchyma, in particular in the right lobe where some hypointense areas have pseudonodular aspect.
(1C) e-Dixon automatic liver segmentation.
(1D) e-Dixon report estimates liver volume and number of voxels, and reports the presence of intrahepatic fat.
(1E) Four of the five series of images from q-Dixon acquisition: FF (Fat Fraction), WF (Water Fraction), effective R2*, effective T2*.
(1F) q-Dixon report: color bars show the values of PDFF and R2* both for the whole liver volume segmented and for the ROI positioned in the right lobe. ROI value for PDFF is higher (17.6%) than segmentation value (11.4%) because of major fat accumulation in right lobe. Classification is grade 1–2 steatosis; R2* values are normal; no iron overload is detected.
(1G) q-Dixon report: histograms describe PDFF values and R2* values distribution.

Case 2

56-year-old male with steatosis. The patient was enrolled in a double-blind study in which steatosis was quantified by LiverLab performed on 3T MAGNETOM Skyra, before and after one year of therapy (drug versus placebo).

Qualitative imaging (in/opp or e-Dixon) could not correctly identify variation in fat overload; quantitative imaging (q-Dixon) could identify and measure PDFF before and after drug/placebo administration.

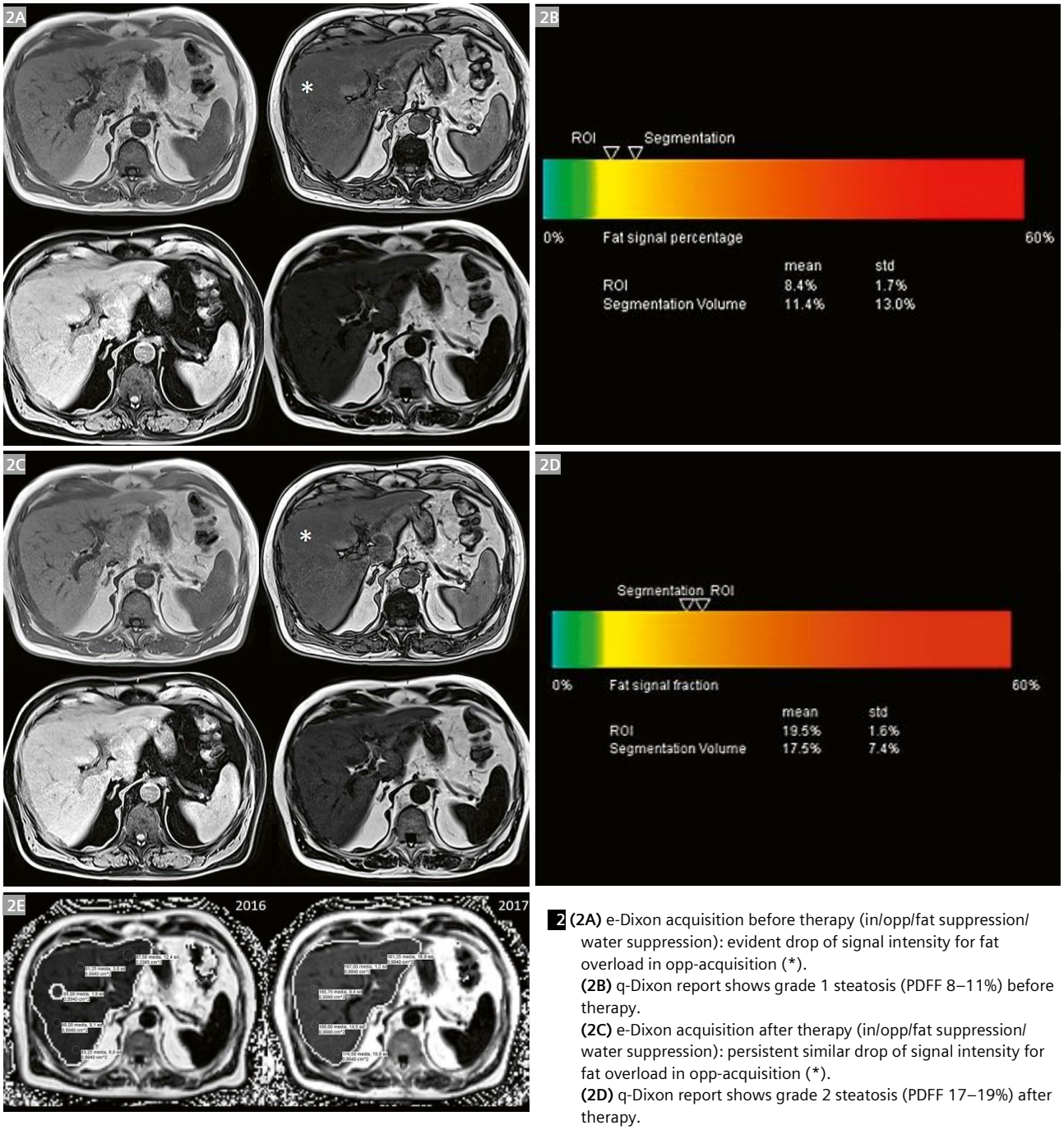

2 (2A) e-Dixon acquisition before therapy (in/opp/fat suppression/water suppression): evident drop of signal intensity for fat overload in opp-acquisition (*).
(2B) q-Dixon report shows grade 1 steatosis (PDFF 8–11%) before therapy.
(2C) e-Dixon acquisition after therapy (in/opp/fat suppression/water suppression): persistent similar drop of signal intensity for fat overload in opp-acquisition (*).
(2D) q-Dixon report shows grade 2 steatosis (PDFF 17–19%) after therapy.
(2E) q-Dixon FF series before and after therapy: multiple ROIs positioned in right liver lobe confirm PDFF values reported on colored bars.

Case 3

48-year-old female with single liver metastasis in S4 in obese patient with rectal cancer studied by MRI. The patient underwent chemotherapy and repeat MRI after three months to evaluate response to therapy: partial response was assessed but steatosis worsened and the patient could not go on with chemotherapy because of CASH. The multidisciplinary team decided to perform surgery "liver-first". The pathologic examination of liver surrounding resected metastasis confirmed grade 2 steatosis.

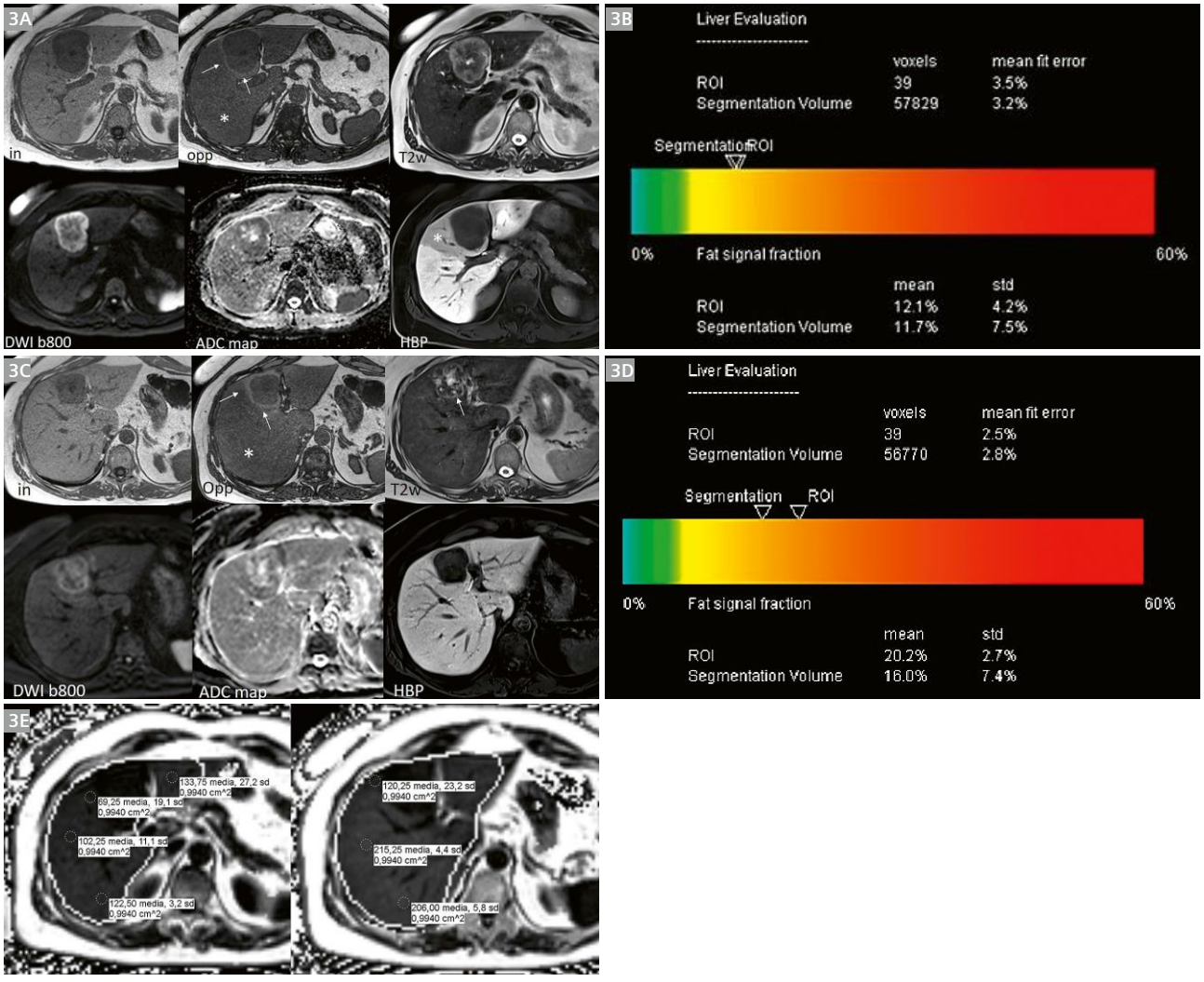

3 **(3A)** in-/opp, T2w, DWI (b800), ADC and hepatobiliary phase (HBP 15 min after EOB-DTPA injection) of the hepatic lesion at the initial staging: liver diffuse steatosis (* in opp); the lesion determines compression on left portal branch with consequent perilesional steatosis spare (arrows) and functional liver impairment (* in HBP).
(3B) q-Dixon report shows grade 1 steatosis (PDFF 11–12%) before chemotherapy.
(3C) in-/opp, T2w, DWI, ADC and HBP (15 min after EOB-DTPA injection) of the hepatic lesion after chemotherapy: liver diffuse steatosis persists (* in opp); the lesion is smaller but perilesional steatosis spare is still evident (arrows in opp); the signal of the lesion in T2w sequence is more heterogeneous (arrow) without any restriction of signal on DWI/ADC. The functional liver impairment is no easier to see during HBP.
(3D) q-Dixon report shows worsening of steatosis (grade 2, PDFF 16–21%) after chemotherapy.
(3E) q-Dixon FF series before and after (*) therapy: multiple ROIs in right liver lobe confirm PDFF values reported on colored bars of q-Dixon report.

Case 4

43-year-old female with incidental ultrasound finding of hypoechoic lesion in left lobe in hyperechoic liver – suspected steatosis. The patient was scheduled for MRI. With T1 GRE in/opp sequences, more hypointense signal of liver parenchyma was noted on T1 in-phase sequence. LiverLab was performed, and confirmed mild iron overload (LIC 4.4–4.7 mgFe/g). The lesion in the left lobe had signal intensity and pattern of enhancement typical for focal nodular hyperplasia (FNH). The patient was given specific blood tests, and heterozygosis for hemochromatosis was confirmed.

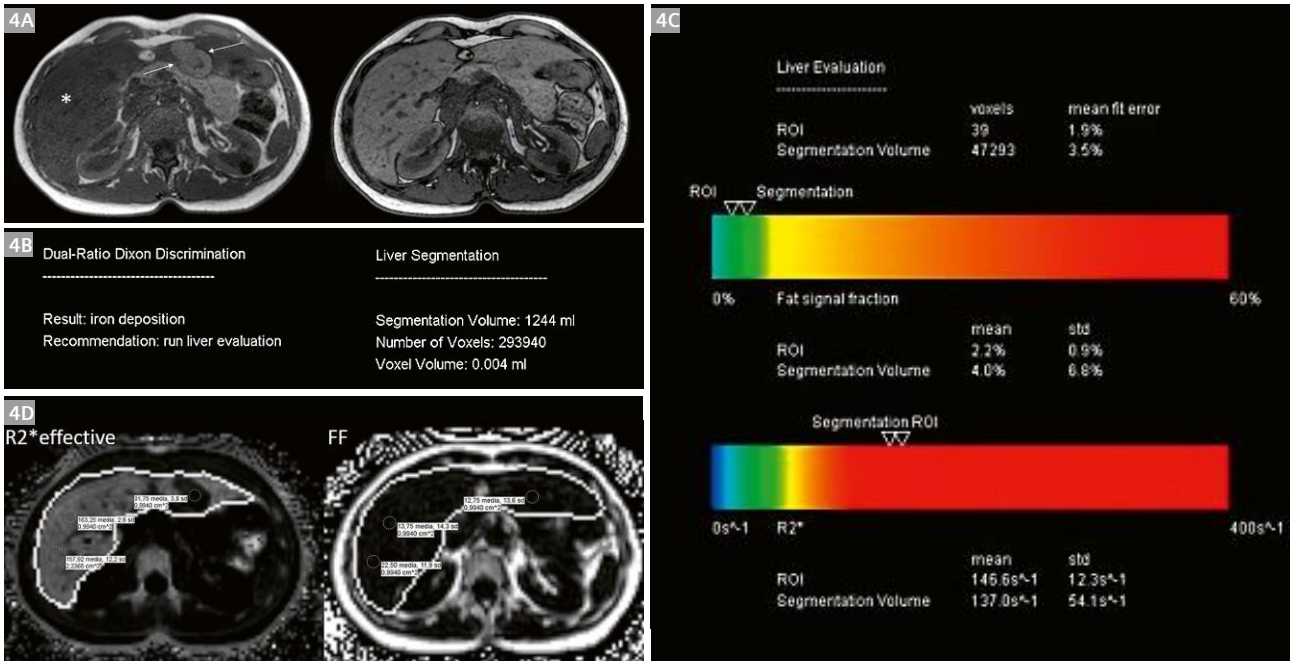

4 **(4A)** T1 GRE in/opp sequence: the signal intensity of liver parenchyma is lower in in-phase acquisition (*); in the left lobe an exophytic lesion shows as isointense in opp-phase and hyperintense in in-phase (arrows).
(4B) e-Dixon report confirms iron overload and provides an estimation of liver volume.
(4C) q-Dixon report shows mild iron overload, with R2* of 137–147 sec^{-1}, corresponding to LIC of 4.4–4.7 mgFe/g. PDFF is normal (<5%).
(4D) q-Dixon R2*effective and FF sequences: multiple ROIs in right liver lobe confirm R2* and PDFF values reported on colored bars. No fat or iron overload can be detected within the lesion in the left lobe.

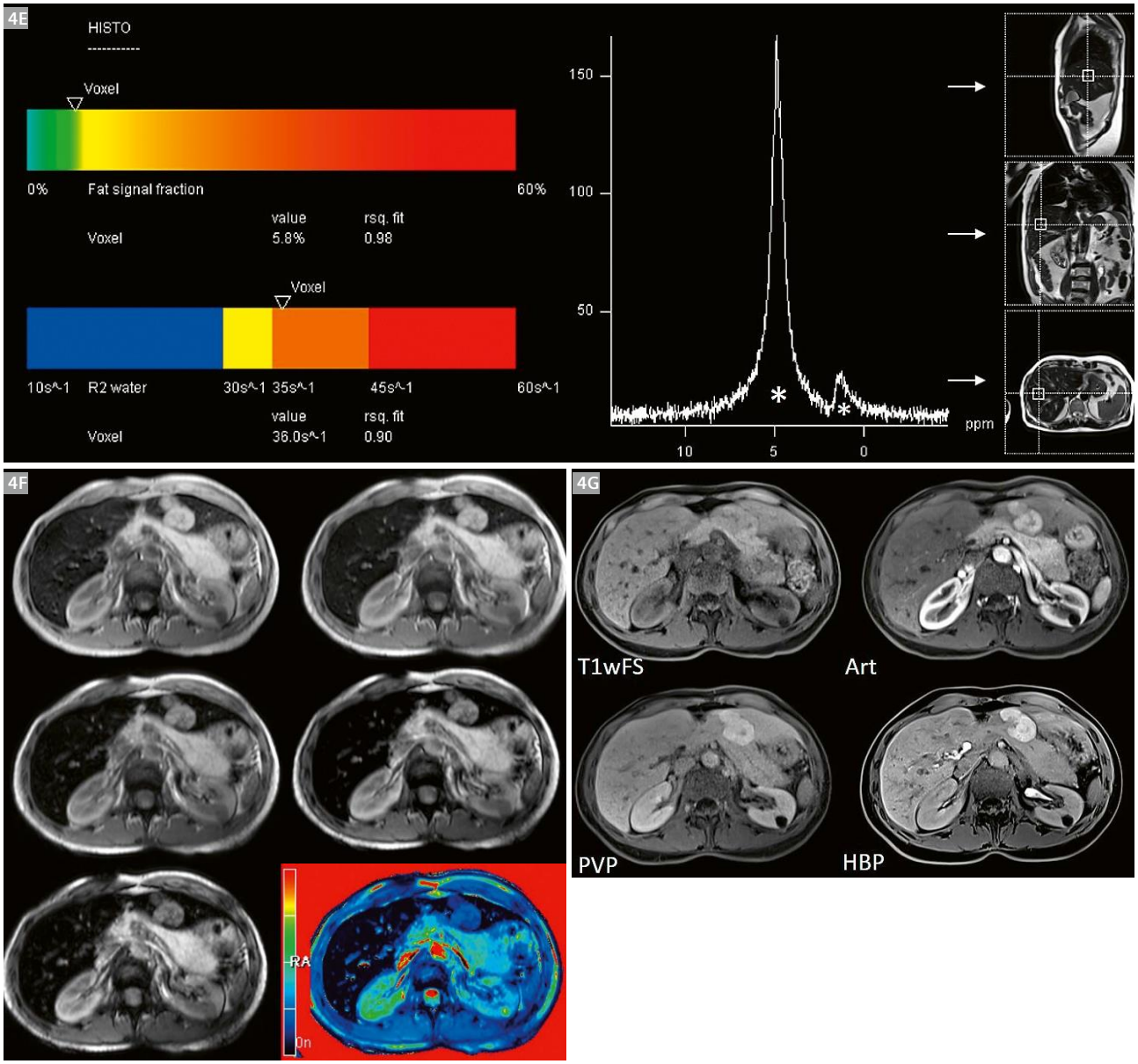

4 **(4E)** HISTO acquisition report confirms iron overload (R2 water 36 sec^{-1}; normal values <30 sec^{-1}) in the single voxel measured in right lobe (arrows indicate the site of the measured voxel in multiplanar vision). Asterisks represent T2-corrected peak areas for water and fat at each measured TE.
(4F) T2* multi-echo acquisition (TE = 9,53 – 14,29 – 19,05 – 23,81 and 28,58 seconds) and T2* colored map.
(4G) Characterization of the liver lesion before (T1w FatSat) and after contrast media administration (EOB-DTPA) during dynamic (arterial and portal venous phase) and hepatobiliary phase (HBP): focal nodular hyperplasia (FNH).

Case 5

68-year-old female with hemosiderosis. The patient undergoes MRI (LiverLab) to quantify iron overload and evaluate whether chelation therapy should be performed. After seven bloodletting sessions the patient was scheduled for LiverLab acquisition, which showed reduction of iron overload. Mild steatosis was associated with iron overload, and fat accumulation was reduced after therapy.

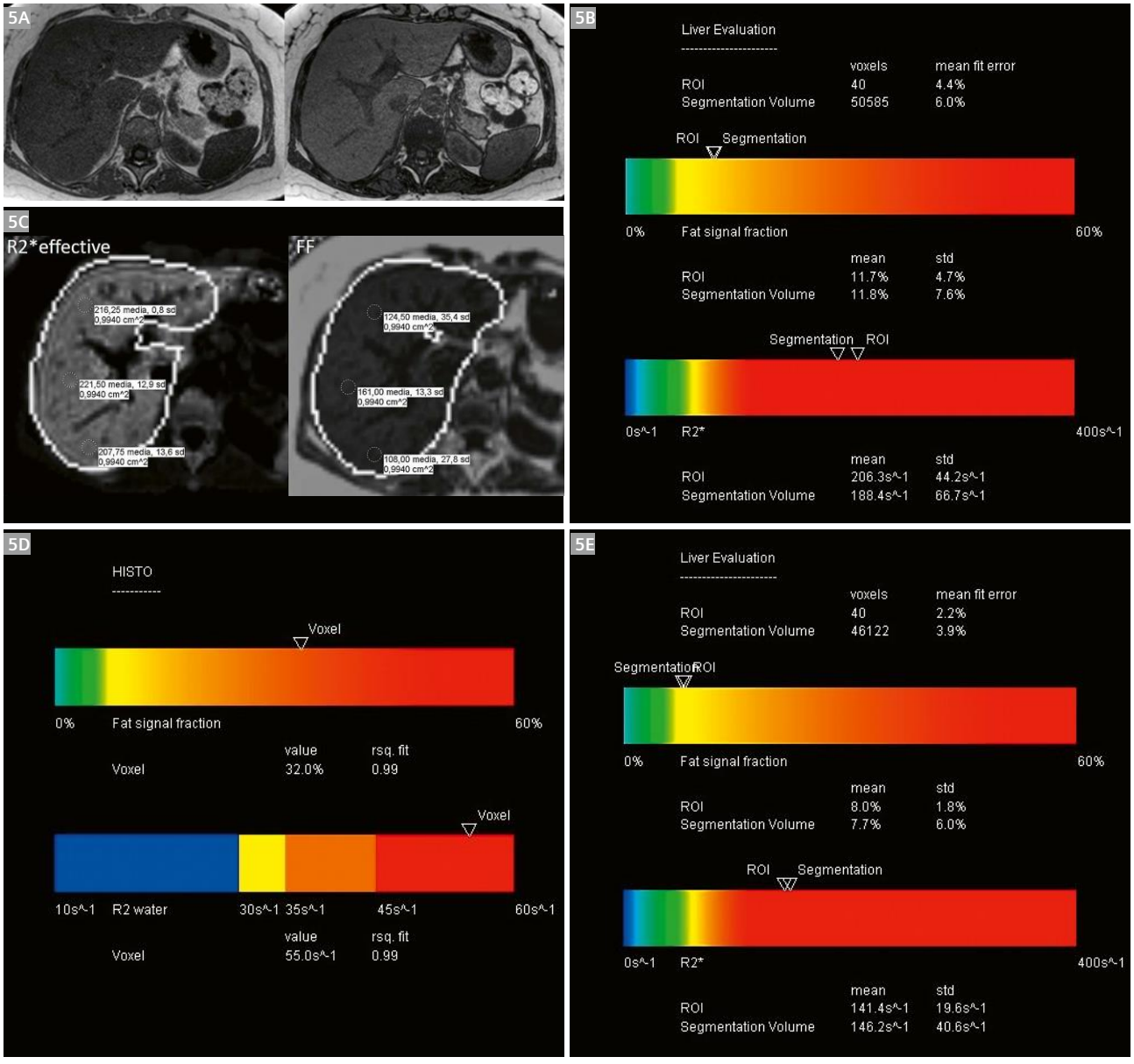

5 **(5A)** T1 GRE in/opp sequences
(5B) q-Dixon report shows iron overload, with R2* of 190–206 sec^{-1}, corresponding to LIC of 6.1–6.6 mgFe/g; and mild steatosis (PDFF 11–12%).
(5C) q-Dixon R2*effective and FF series: multiple ROIs positioned in right liver lobe confirm high R2* values (up to 221 sec^{-1}) and heterogeneous mild steatosis (PDFF 10–16%).
(5D) HISTO acquisition report confirms iron overload and steatosis: R2 water 55 sec^{-1} (normal values < 30 sec^{-1}) in the single voxel measured in right lobe. PDFF is 32% in the same voxel. According to literature, steatosis can be overestimated in presence of iron overload [14].
(5E) After bloodletting therapy, q-Dixon acquisitions demonstrate reduction in iron overload and steatosis: R2* is 145 sec^{-1}, corresponding to LIC of 4.64 mgFe/g. Steatosis is reduced (PDFF 7–8%).

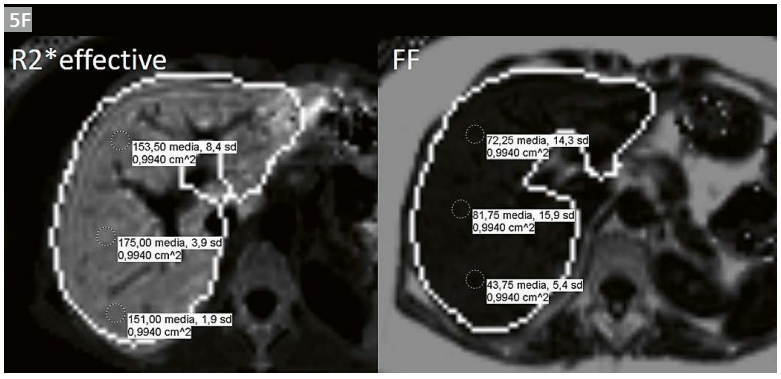

(5F) q-Dixon R2*effective and FF series: multiple ROIs in right liver lobe confirm high R2* values (up to 175 sec^{-1}) and mild steatosis (PDFF 7–8%) with areas of relative spare (PDFF 4.3% in S6). **(5G)** HISTO confirms the effect of the therapy: R2 water is 50.7 sec^{-1} (normal values < 30 sec^{-1}) in the single voxel measured in right lobe. PDFF is 15% in the same voxel.

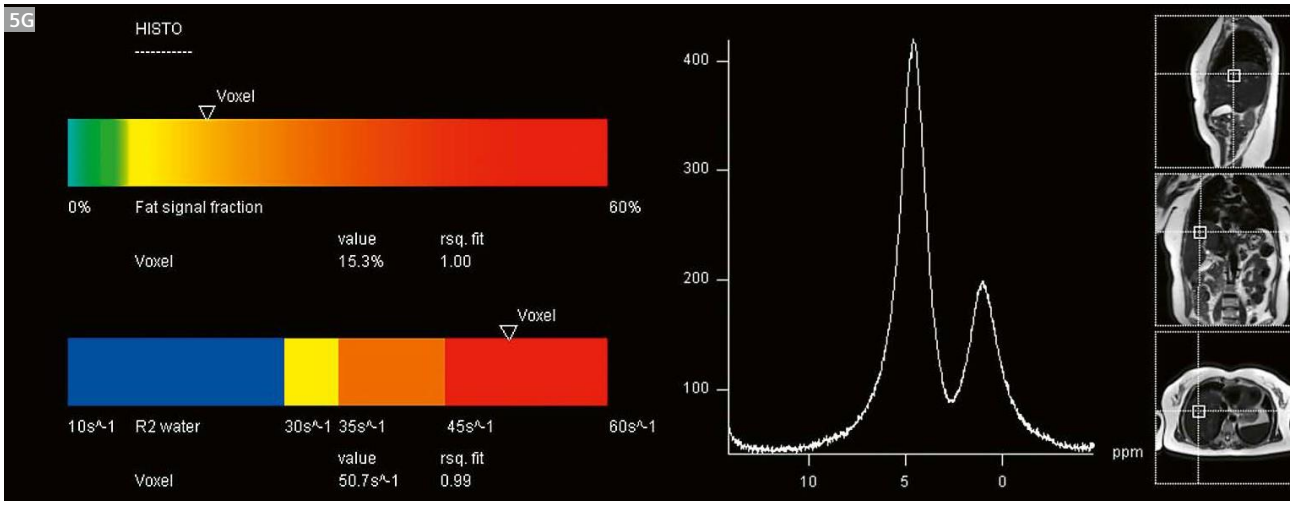

Technique

The first sequence is an e-Dixon, obtained in a single 15–20 second breath-hold acquisition, which returns four series of images: in/opp/fat suppression/water suppression. It gives a semi-quantitative evaluation of fat and iron buildup by estimating the total number of voxels (and the volume in mL of the hepatic parenchyma) and the presence of fat and/or iron in the parenchyma.

The six-point acquisition q-Dixon, obtained in a 18–20 second breath-hold acquisition, is a 3D multi-echo gradient echo sequence with Dixon reconstructions and correction for T2* in the presence of iron. It returns five series of images: FF (fat fraction), WF (water fraction), effective R2*, effective T2* and goodness-of-fit map for quality control. It also plots the distribution of measured echo times, and gives a graphical representation with color bars or colorimetric maps of the two biomarkers: PDFF (proton density fat fraction) and R2 * (1/T2*), both as average values calculated over the entire liver volume and as single voxel measurements.

During postprocessing, PDFF and R2* can also be measured in each desired voxel of the liver, by placing the region of interest (ROI) in the most interesting hepatic segments in the FF and effective R2* series. In this way an estimate of steatosis can be made for each part or lobe, which is useful if the patient must undergo liver resection [9].

The FF value multiplied by 10^{-1} corresponds to the PDFF value in that location. This makes it possible to classify steatosis in a very accurate manner: grade 0 (normal liver PDFF: 0–5%), grade 1 (mild PDFF: 5–17%), grade 2 (moderate PDFF: 17–22%), and grade 3 (severe PDFF: ≥ 22%).

The effective R2* is measured in Hertz (or sec^{-1}) and correlates to the value of LIC (liver iron concentration) through a specific conversion factor for each device. The LIC is the ratio of intrahepatic iron to the dry weight of the parenchyma. Normal LIC is < 1.8 mg/g (dry weight). Values between 3 and 7 indicate a mild iron overload, > 7 moderate, and > 15 severe. A LIC value of 7 mg/g is an indication for chelation therapy in patients with iron overload due to repeated blood transfusions [10–12].

Case 6

66-year-old male with recent detection of liver cirrhosis; no viral causes were documented and the patient denied any alcohol abuse. NASH-related cirrhosis was suspected, so LiverLab evaluation was requested.

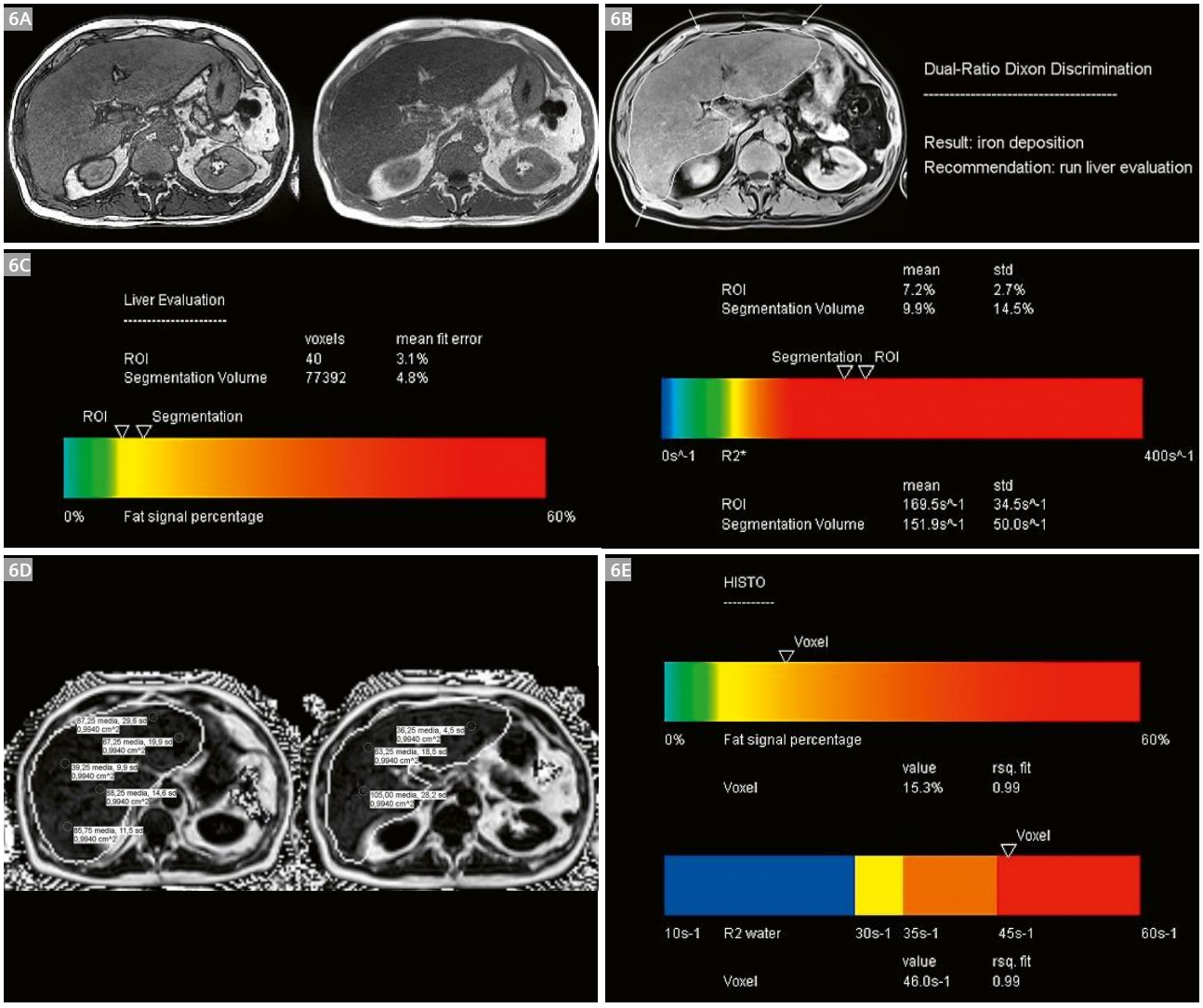

6 (6A) T1 GRE in/opp sequences: the signal intensity of liver parenchyma is low in both series of images, especially in-phase.
(6B) e-Dixon liver segmentation is not perfect (arrows) because of low signal intensity of the parenchyma, but it can only influence segmentation volume values of PDFF and R2* at q-Dixon acquisition, but not ROIs measurements of these parameters.
(6C) q-Dixon report confirms PDFF = 7–10% (mild steatosis but with heterogeneous distribution) and R2* = 169.5 sec^{-1} corresponding to LIC of 5.44 mgFe/g (mild iron overload).
(6D) q-Dixon FF sequence: multiple ROIs in right and left lobes confirm very heterogeneous PDFF values, ranging between 4% and 10%.
(6E) HISTO acquisition report confirms iron overload (R2 water 46 sec^{-1}; normal values <30 sec^{-1}) in the single voxel measured in right lobe. PDFF is 15% in the same voxel.

The HISTO spectroscopy sequences are multi-echo sequences corrected for the T2 signal, at high speed, acquired on a single voxel. These sequences are based on the principle that there is a strong nonlinear correlation between the water R2 signal and the iron concentration, independent of the lipid concentration. The sequence contains an algorithm that integrates the water and fat signal for each TE acquired, and can be used to obtain the values of fat fraction and water R2 [13].

Three localizer sequences define the location of the voxel, and then an apnea sequence of about 18–20 seconds returns a spectrum of the shorter TEs to perform quality control of the values obtained at TE = 12 seconds, where two distinct peaks must be appreciated: water and fat. The sequence also shows the measured values of fat fraction and R2 water on color bars. If desired, the acquisition can be repeated in another voxel of your choice.

A T2* colored map can also be obtained by acquiring multi-echo T2* sequences.

Conclusion

These cases show how LiverLab can give a wealth of information to clinicians, useful for diagnosis, management and follow-up of patients with fat and/or iron liver overload. With its rapid acquisition (5–7 minutes) it can easily be integrated in a standard liver MRI protocol. Radiologists' skills in using and interpreting LiverLab acquisitions and measurements can improve rapidly once these sequences are added to the standard protocol in patients with hepatopathy. In our experience clinicians appreciate the information given about fat and/or iron liver overload, and ask for this type of evaluation more and more frequently.

Contact

Barbara Frittoli, M.D.
Radiologia 1 ASST-Spedali Civili di Brescia
p.le Spedali Civili 1
25123 Brescia
Italy
bfrittoli@gmail.com

References

1 Xiaozhou M, Nagaraj-Setty H, Kambadakone R, Kenudson-Mino M, Hahn PF, Sahani DV. Imaging based Quantification of Hepatic Fat: Methods and Clinical Applications. RadioGraphics. 2009;29(5):1253-1280.
2 Caussy C, Reeder SB, Sirlin CB, Loomba R. Noninvasive, Quantitative Assessment of Liver Fat by MRI-PDFF as an Endpoint in NASH Trials, Hepatology. 2018;68(2):763-772.
3 Mouzaki M, Trout AT, Arce-Clachar AC, Bramlage K, Kuhnell P, Dillman JR et al. Assessment of Nonalcoholic Fatty Liver Disease Progression in Children Using Magnetic Resonance Imaging. The Journal of Pediatrics. 2018;201:86-92.
4 Yu EL, Golshan S, Harlow KE, Angeles JE, Durelle J, Goyal NP et al. Prevalence of Nonalcoholic Fatty Liver Disease in Children with Obesity. The Journal of Pediatrics. 2018; in press, available online since 14 Dec 2018 from https://www.sciencedirect.com/journal/the-journal-of-pediatrics/articles-in-press.
5 Deng J, Zhong X, Fishbein M et al. Hepatic Fat Quantification in Pediatric Patients using Multi-echo Dixon VIBE: Early Experience. MAGNETOM Flash. 2015;2(62):23-25.
6 Hutton C, Gyngell ML, Milanesi M, Bagur A, Brady M. Validation of a standardized MRI method for liver fat and T2 quantification. PLoS ONE. 2018;13(9):e0204175. https://doi.org/10.1371/journal.pone.0204175
7 Sharma P, Martin D. An Efficient Workflow for Quantifying Hepatic Lipid and Iron Deposition using LiverLab. MAGNETOM Flash. 2014;3(58):12-17.
8 Sellers R. MR LiverLab. MAGNETOM Flash. 2016;3(66):39-43.
9 Kim HJ, Cho HJ, Kim B, You MY, Lee JH, Huh J et al. Accuracy and precision of proton density fat fraction measurement across field strengths and scan intervals: A phantom and human study. Journal of Magnetic Resonance Imaging. 2018; in press, available online since 14 Nov 2018 from https://onlinelibrary.wiley.com/toc/15222586/0/0
10 Wood JC. Use of magnetic resonance imaging to monitor iron overload. Hematol Oncol Clin North Am. 2014;28(4):747-64.
11 Henninger B, Zoller H, Rauch S, Finkenstedt A, Shocke M, Jaschke W et al. R2* relaxometry for the quantification of hepatic iron overload: biopsy based calibration and comparison with the literature. RoFo. 2015;187(6): 472-479.
12 Quinn C, St Pierre T. MRI Measurements of Iron Load in Transfusion-Dependent Patients: Implementation, Challenges, and Pitfalls. Pediatr Blood Cancer. 2016;63:773–780.
13 Reeder SB, Cruite I, Hamilton G, Sirlin CB. Quantitative assessment of liver fat with magnetic resonance imaging and spectroscopy. J. Magn. Reson. Imaging. 2011;34:729-749.
14 Pineda N, Sharma P, Qin Xu, Hu X, Vos M, Martin DR. Measurement of Hepatic Lipid: High-Speed T2-Corrected Multiecho Acquisition at 1H MR Spectroscopy—A Rapid and Accurate Technique. Radiology. 2009;252(2):568-576. https://doi.org/10.1148/radiol.2523082084.

The Prostate Dot Engine – a System-Guided and Assisted Workflow to Improve Consistency in Prostate MR Exams

Wilhelm Horger, Gregor Thoermer, Elisabeth Weiland, Bernd Kuehn, Berthold Kiefer

Siemens Healthineers, Magnetic Resonance Imaging, Erlangen, Germany

The "PROMISe" of mpMRI

PROMIS, PRECISION, 4M and MRI-FIRST [1–4] are four landmark studies that are changing the way we screen for prostate cancer.

Evidence presented in these studies has already impacted guidelines on imaging prostate cancer issued by the European Association of Urology and national guidelines in the UK (NICE) and the Netherlands toward a scheme where prostate MRI serves a first-line triage test in biopsy-naïve men with elevated PSA levels.

These studies consistently provide Level 1A evidence that using multiparametric MRI (mpMRI) of the prostate can reduce the number of biopsies required in men with elevated PSA levels.

Due to the excellent negative predictive value of prostate mpMRI, men without suspicious MRI findings do not require further examinations. At the same time, the mpMRI pathway does not result in an under-detection of clinically significant cancer, but will reduce the number of clinically insignificant cancers picked up by chance in a "systematic TRUS-biopsy-only" care scheme (see Table 1). It has been shown for – quite differently organized – healthcare systems that the MRI pathway will reduce the overall healthcare expenditure per clinically significant cancer diagnosed. This advantage is largely driven by the reduced number of biopsies [5–7], resulting in fewer infections and sepsis, the latter presenting a huge financial burden [8]. The potential long-term effects on patient management of reduced detection of clinically insignificant disease have not even been modelled in studies of this kind.

Performance of mpMRI pathway in comparison with TRUS-bx pathway	PRECISION[1] (500 men)	MRI-FIRST[2]	4M Study[3]	PROMIS[4]
Avoid biopsy after negative mpMRI in (%) of patients	28 %	18 – 21 %	49 %	27 %
Increase in detection of significant cancers (%)	+12 %	No difference in significant cancer (+2 %)	No difference in significant cancer (+2 %)	No difference in significant cancer (+2 %)
Diagnosis of insignificant cancer	-13 %	-14 %	-11 %	-5 %
Reduction of biopsy cores per patient (relevant for infections and side effects	11 → 4 (= -64 %)	12 → 3 (= -75 %)	12 → 3 (= -75 %)	n.a.

Table 1: Summary of recently published landmark mpMRI prostate cancer detection studies and their impact on patient management.

The challenge in scaling up mpMRI

Expert panels are, however, aware that the MRI pathway puts an additional burden on radiologists and imaging providers and the potential risks and challenges associated with the increasing demand. Most radiologists have limited expertise in interpreting and reporting prostate MRI, and the consistent acquisition of high-quality mpMRI prostate examinations is a challenge for technologists not used to performing the exam routinely according to the PI-RADS recommendations.

In 2019, Engels et al. [9] and Barrett et al. [10] published excellent papers on how to perform high-quality mpMRI and which pitfalls to consider. They concluded that training of skilled professionals is key; but also that imaging vendors should provide tools and workflows that help tailor and optimize the exam for the individual patient, to maximize scan quality and consistency.

Respective software automatically detecting characteristic landmarks with machine learning trained algorithms to adjust size and angulation of FOVs to the individual anatomical conditions with high consistency and reproducibility has been successfully established for various applications, literarily ranging from head to toe with the Brain, Spine, Hip, Knee, Breast, Cardiac, Abdomen, and Whole-Body Dot Engines. Studies specifically investigating the value of such software for assisted and guided brain, liver and whole-body examinations have clearly shown relevant reduction of examination time compared to standard workflows [11–13]. In addition, for liver examinations, assisting features including automated bolus detection (ABLE) with an automatically positioned bolus tracker in the descending aorta allow technologists to achieve optimal arterial phase quality in dynamic contrast-enhanced scans in 94% of cases, where a fixed-time approach only achieves 73% of optimally timed arterial phase images [12].

Prostate Dot Engine[1] – from prototype to product

Such novel automated scanner software has recently been prototyped and evaluated for MRI examinations of the prostate. The aim is to standardize scan volume positioning, tilting and coverage, in order to ensure high consistency between operators, and to better support Active Surveillance with repeated MR scans [14]. Although the evaluation did not show a statistically significant time advantage of the assisted workflow over the manual workflow (26 versus 28 minutes median examination time), the overall imaging quality was superior with the assisted MRI scans, achieving an average rating of 4.6 out of 5 versus 3.8 out of 5 points for the manual workflow.

In the light of developing evidence and changing guidelines, the planned introduction of the Prostate Dot Engine as part of the software version *syngo* MR XA30A is timely.

The Prostate Dot Engine is designed for fast, reproducible and standardized prostate MR examinations and supports multi-parametric, multi-plane MR imaging according to the latest PI-RADS v2.1 recommendations [15]. The operator is guided through one comprehensive workflow with decision points to adapt the strategy to individual patient conditions (see Figure 1), while artificial intelligence aids in planning and performing the procedure steps.

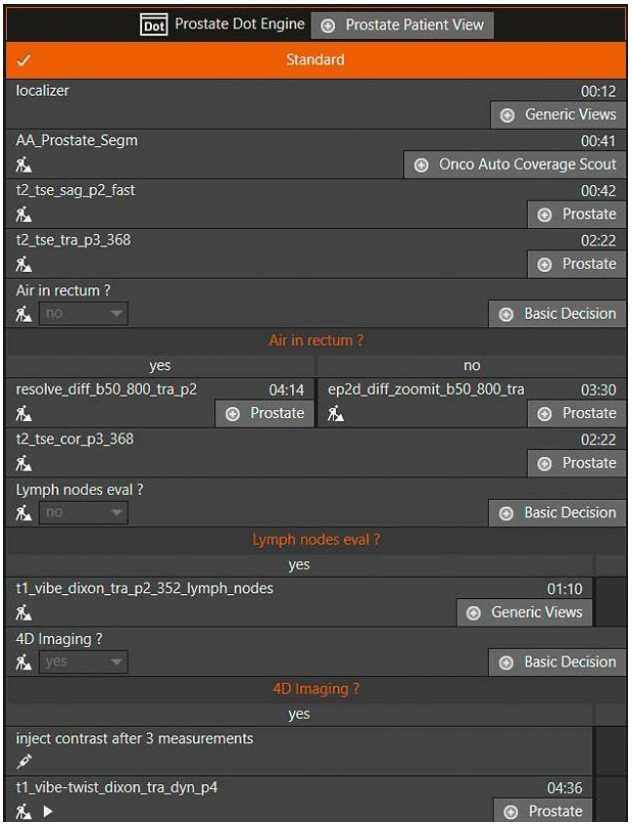

1 Workflow of the Prostate Dot Engine with different decision points.
For example, based on initial morphological scans the operator may be asked to decide whether a patient has a lot of gas in the rectum. If there is considerable gas, a highly robust RESOLVE DWI scan is acquired. If not, zoomed diffusion-weighed images are acquired. These are more prone to distortions, but offer higher spatial resolution and better contrast in shorter time.

Work in progress: the product is currently under development and is not for sale in the U.S. and in other countries. Its future availability cannot be ensured.

AI-assisted planning, angulation, and coverage

Before image acquisition, the operator has the choice between two general approaches for acquiring the data. In "Patient View" (Fig. 2) slice orientation can be chosen to be either "Anatomical" or "Axial". Anatomical means that the acquisition volumes are tilted to match the actual, individual angulation of the prostate in the body, which can be affected by factors such as bladder and rectal filling, or how the patient lies on the bed. Most recommendations and committees suggest acquiring either axial scans "perpendicular to the long axis of the prostate" or "true axial" images, the latter aimed at improving reproducibility in Active Surveillance [9, 15, 16].

A recent study has investigated the robustness of AI-derived axial slice angulation with the Prostate Dot Engine. Subjects underwent MRI scans of the prostate with full and empty bladder, with excellent reproducibility of the angulation [17], indicating that the assisted planning approach might increase consistency in Active Surveillance without compromising fidelity in anatomical coverage. The preferred angulation strategy can be predefined and set as a default, so it does not have to be selected in every patient.

The short AutoAlign prostate segmentation scan at the beginning of the exam facilitates the detection of certain landmarks in the small pelvis to derive the angulation and coverage required for the subsequent mpMRI of the prostate. For the angulation, the entry point of the bladder neck into the prostate and the exit of the urethra from the apex of the prostate are used as highly reproducible landmarks. In addition, the prostate gland is automatically segmented, and if the PSA value has been specified an estimate of PSA density (ng/ml) is provided in the generated report. Another feature of the Prostate Dot Engine is to support asymmetric anatomical coverage or a shift in the field-of-view direction as illustrated in Figure 3.

By default, images in the sagittal plane are acquired before the axial T2-weighted and diffusion-weighted images. This approach has repeatedly been reported to be beneficial as it gives the patient some time to relax and calm down, so they are less likely to move during the most relevant axial scans.

Diffusion-weighted imaging

After acquiring T2-weighted images in sagittal and transverse orientation, diffusion-weighted images are automatically pre-planned and acquired, using either RESOLVE or a

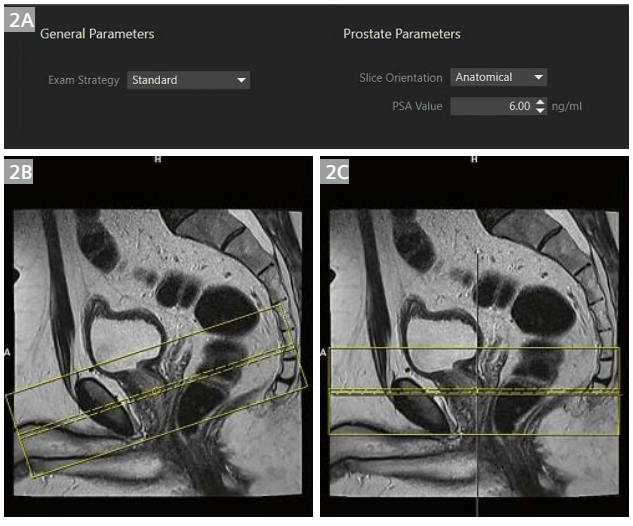

2 The Patient View of the Prostate Dot Engine **(2A)** is displayed before the examination. The operator can specify the desired slice orientation ("Anatomical" or "Axial"), which will result in the acquisition orientations shown in **2B** and **2C**, respectively. Coronal and sagittal acquisitions are acquired perpendicular to the chosen axial orientation. The PSA value can be entered in order to get an automated estimation of the PSA density.

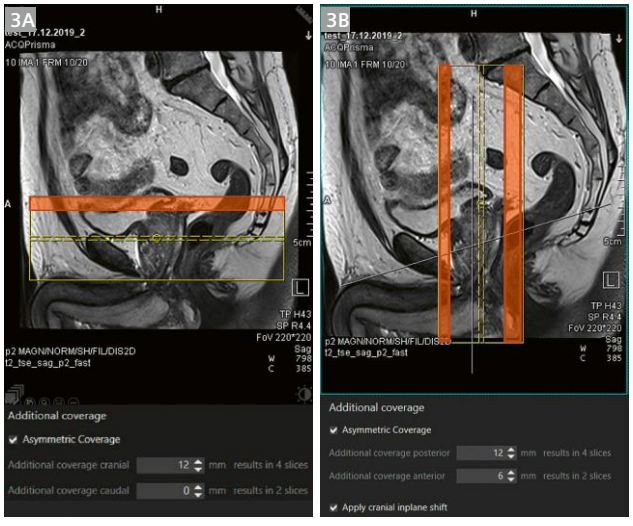

3 Based on the segmentation of the prostate gland, the required number of slices to cover the entire organ is automatically derived and adjusted. In particular with straight axial acquisitions, the seminal vesicles may expand more in the cranial direction than the prostate base **(3A)**. To ensure complete coverage of the seminal vesicles, the user interface allows to specify additional "asymmetric coverage", for example with 4 more slices in the cranial direction (corresponding to the orange area). The same can also be applied to other orientations, e.g., to coronal planes **(3B)**. In addition, a FOV shift to better cover lymph nodes in the small pelvis can be achieved by ticking the option "Apply cranial inplane shift" thus ending the FOV 5 cm below the apex of the prostate.

single-shot EPI method with reduced FOV (ZOOMit^{PRO}). The strengths of both techniques are specified in Table 2 and an illustrative case can be found in Figure 4.

Following the PI-RADS v2.1 recommendation, two *b*-values (b = 50 s/mm^2 and b = 800 s/mm^2) are scanned and ultra-high *b*-value images at b = 1400 s/mm^2 are automatically calculated. The often-suggested additional acquisition of a supporting *b*-value in the range of 400–500 s/mm^2 for improved ADC calculation is not recommended here, since a linear fitted ADC value is hardly influenced by this choice and the scan time may more effectively be invested in additional averages at the higher *b*-value.

With regards to the ultra-high *b*-value (> 1400 s/mm^2) there is some disagreement in the international community whether to acquire or extrapolate images, and on the optimal choice of the ultra-high *b*-value [18]. UK consensus guidelines are most specific in proposing b ≥ 1400 s/mm^2 at 1.5T and b ≥ 2000 s/mm^2 at 3T, both "preferentially acquired". Rosenkrantz et al. [20] provide some guidance on the choice of an optimal *b*-value, suggesting that "computed *b*-values in the range of 1500–2500 s/mm^2 (but not higher) are optimal for prostate cancer detection" providing high sensitivity for lesions and sufficient anatomical clarity.

The Prostate Dot Engine provides a flexible framework where protocol steps can be modified and added to best serve individual institutional expectations.

Dynamic contrast-enhanced imaging

After acquiring diffusion-weighted and coronal T2-weighted images, T1-weighted scans of the small pelvis and dynamic contrast-enhanced (DCE) images may be acquired. Some studies [20, 21] suggest that the detection rate of clinically significant cancer may not be negatively affected with a bi-parametric screening protocol, but the detection rate of insignificant cancer and the number of biopsies may go up due to a tendency to upgrade indecisive cases without DCE information. On the other hand, bi-parametric protocols have the clear advantage of being completely non-invasive and substantially shorter, there-

	ZOOMit^{Pro}	RESOLVE
TE (ms)	72	51
FOV (mm x mm)	100 x 100	200 x 200
Resolution (mm^3)	0.82 x 0.82 x 3.0	0.85 x 0.85 x 3.0
Acquisition time (min:sec)	3:30	4:14

Table 2: Comparison of protocol parameters of ZOOMit^{Pro} and RESOLVE with b = 50, 800 s/mm^2 at 3T (MAGNETOM Prisma). While ZOOMit provides higher SNR and resolution in shorter acquisition time, the readout segmented RESOLVE is more robust in patients with susceptibility issues (especially caused by gas in rectum) due to a substantially shorter echo train.

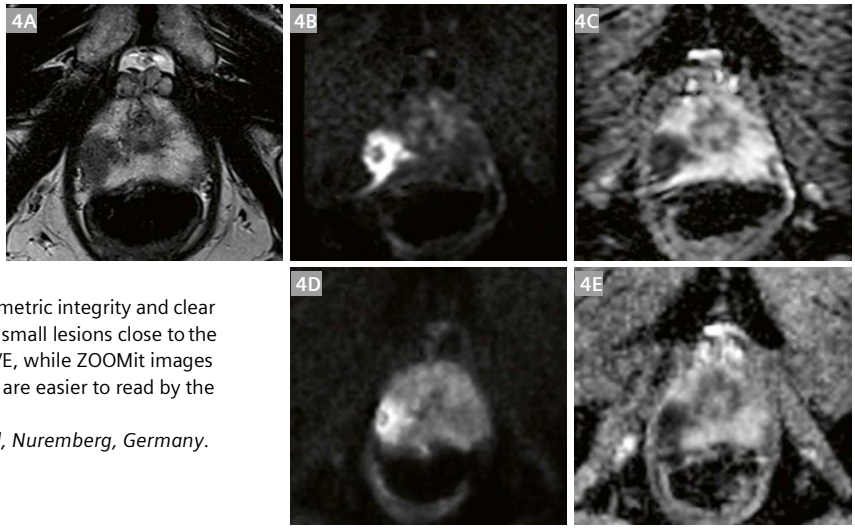

4 72-year-old patient with suspected prostate cancer. A clearly visible lesion in the right peripheral zone in the apical aspect of the prostate **(4A)** represented with a corresponding diffusion restriction in calculated high *b*-value images and ADC maps. Due to a substantial amount of gas in the rectum, ZOOMit images **(4B, D)** suffer from a distortion in phase-encoding-direction (here: L-R), sometimes also referred to as "comet tail sign" while the RESOLVE images **(4C, E)** expose high geometric integrity and clear lesion delineation. It can be argued that very small lesions close to the capsule may only be seen properly in RESOLVE, while ZOOMit images appear to have higher lesion conspicuity and are easier to read by the radiologists.
Images courtesy of Prof. Karlheinz Engelhard, Nuremberg, Germany.

fore more cost efficient. While the role of DCE in prostate cancer detection is debated and may be subject to change in a later version of PI-RADS, DCE remains integral part of PI-RADS v2.1 conform mpMRI for now. This is also reflected in the workflow of the Prostate Dot Engine: by default, DCE imaging is included but may be deselected (i.e. in follow-ups) or removed if this is the institutional preference. As for the other scans, positioning of the imaging volume is automatically adjusted and imaging parameters, such as temporal and spatial resolution, are kept constant to fulfill the requirements of the PI-RADS standard.

Summary

The Prostate Dot Engine aims to standardize mpMRI of the prostate, to assist less experienced users in performing the scans with consistent high quality, and to facilitate high reproducibility in repeated scans, for example in Active Surveillance. The Prostate Dot Engine is one of several intelligent solutions designed to scale up prostate MRI in the light of a globally rising demand for this procedure.

References

1 Kasivisvanathan V, Rannikko AS, Borghi M, et al. PRECISION Study Group Collaborators. MRI-Targeted or Standard Biopsy for Prostate-Cancer Diagnosis. N Engl J Med. 2018;378(19):1767-1777.
2 Rouvière O, Puech P, Renard-Penna R, et al. Use of prostate systematic and targeted biopsy on the basis of multiparametric MRI in biopsy-naive patients (MRI-FIRST): a prospective, multicentre, paired diagnostic study. Lancet Oncol 2018; http://dx.doi.org/10.1016/S1470-2045(18)30569-2.
3 van der Leesta M, Cornelb E, Israëla B, et al. Head-to-head comparison of transrectal ultrasound guided prostate biopsy versus multi-parametric prostate resonance imaging with subsequent MR-guided biopsy in biopsy-naïve men with elevated PSA; a large prospective multicenter clinical study. Eur Urol. 2018; in press.
4 Ahmed HU, El-Shater Bosaily A, Brown LC, et al. Diagnostic accuracy of multi-parametric MRI and TRUS biopsy in prostate cancer (PROMIS): a paired validating confirmatory study. Lancet. 2017;389: 815–22.
5 de Rooij M, Crienen S, Witjes JA, et al. Cost-effectiveness of magnetic resonance (MR) imaging and MR-guided targeted biopsy versus systematic transrectal ultrasound-guided biopsy in diagnosing prostate cancer: a modelling study from a health care perspective. Eur Urol. 2014;66(3):430-436.
6 Pahwa S, Schlitz NK, Ponsky LE, et al. Cost-effectiveness of MR Imaging-guided Strategies for Detection of Prostate Cancer in Biopsy-Naive Men. Radiology. 2017;285(1):157-166.
7 Faria R, Soares MO, Spackman E, et al. Optimising the Diagnosis of Prostate Cancer in the Era of Multiparametric Magnetic Resonance Imaging: A Cost-effectiveness Analysis Based on the Prostate MR Imaging Study (PROMIS). Eur Urol. 2018;73(1):23-30. doi: 10.1016/j.eururo.2017.08.018. Epub 2017 Sep 19.
8 Gross MD, Alshak MN, Shoag JE, et al. Healthcare Costs of Post-Prostate Biopsy Sepsis. Urology. 2019;133:11-15.
9 Engels RRM, Israël B, Padhani AR, et al. Multiparametric Magnetic Resonance Imaging for the Detection of Clinically Significant Prostate Cancer: What Urologists Need to Know. Part 1: Acquisition. Eur Urol. 2019 in press; DOI: https://doi.org/10.1016/j.eururo.2019.09.021.
10 Caglic I, Barrett T. Optimising prostate mpMRI: prepare for success. Clin Radiol. 2019 ;74(11):831-840.
11 Moenninghoff C, Umutlu L, Kloeters C, et al. Workflow efficiency of two 1.5T MR scanners with and without an automated user interface for head examinations. Acad Radiol. 2013;20(6):721-30.
12 Sharma P, Kalb B, Kitajima HD, et al. Optimization of single injection liver arterial phase gadolinium enhanced MRI using bolus track real-time imaging. J Magn Reson Imaging. 2011;33(1):110-8.
13 Stocker D, Finkenstaedt T, Kuehn B, et al. Performance of an Automated Versus a Manual Whole-Body Magnetic Resonance Imaging Workflow. Invest Radiol. 2018;53(8):463-471.
14 Esser M, Zinsser D, Kündel M, et al. Performance of an Automated Workflow for Magnetic Resonance Imaging of the Prostate: Comparison With a Manual Workflow. Invest Radiol. 2019. doi: 10.1097/RLI.0000000000000635
15 American College of Radiology. PI-RADS® Prostate Imaging – Reporting and Data System 2019, Version 2.1. https://www.acr.org/-/media/ACR/Files/RADS/Pi-RADS/PIRADS-V2-1.pdf
16 Appayya MB, Adshead J, Ahmed HU. National implementation of multi-parametric magnetic resonance imaging for prostate cancer detection – recommendations from a UK consensus meeting. https://doi.org/10.1111/bju.14361.
17 Cui Y, Han S, Li C, et al. Performance and Reproducibility of a Day Optimizing Throughput (Dot) Workflow Engine in Automated Prostate MRI Positioning. Proceedings of the 28th Annual Meeting of the ISMRM, Abstract No. #4546.
18 Kordbacheh H, Seethamraju RT, Harisinghani MG, et al. Image quality and diagnostic accuracy of complex-averaged high b value images in diffusion-weighted MRI of prostate cancer. Abdominal Radiology. 2019 June;44(6):2244-2253.
19 Brizmohun AM, Adshead J, Ahmed HU, et al. National implementation of multi-parametric magnetic resonance imaging for prostate cancer detection – recommendations from a UK consensus meeting. BJU Int. 2018;122:13-25. https://doi.org/10.1111/bju.14361.
20 Rosenkrantz AB, Parikh N, Kierans AS, et al. Prostate Cancer Detection Using Computed Very High b-value Diffusion-weighted Imaging: How High Should We Go? Acad Radiol. 2016;23(6):704-11.
21 Kuhl CK, Bruhn R, Krämer N, et al. Abbreviated Biparametric Prostate MR Imaging in Men with Elevated Prostate-specific Antigen. Radiology. 2017;285(2):493-505.
22 Van der Leest M, Israël B, Cornel EB, et al. High Diagnostic Performance of Short Magnetic Resonance Imaging Protocols for Prostate Cancer Detection in Biopsy-naïve Men: The Next Step in Magnetic Resonance Imaging Accessibility. Eur Urol. 2019;76(5):574-581.

Contact

Wilhelm Horger
MR Application Development
Siemens Healthineers
wilhelm.horger@siemens-healthineers.com

A Fully Automated, End-to-End Prostate MRI Workflow Solution Incorporating Dot, Ultrashort Biparametric Imaging and Deep-Learning-based Detection, Classification, and Reporting

David J. Winkel, M.D.[1]; Robert Grimm, Ph.D.[2]; Thomas Benkert, Ph.D.[2]; Berthold Kiefer, Ph.D.[2]; Daniel T. Boll, M.D.[1]

[1]Department of Radiology, University Hospital Basel, Switzerland
[2]MR Applications Predevelopment, Siemens Healthineers, Erlangen, Germany

Introduction

For more than a decade, magnetic resonance imaging (MRI) has been established as a powerful tool for prostate cancer diagnosis. The PROMIS study has demonstrated that prostate MRI is a suitable triage tool for biopsy-naïve men, reducing the number of unnecessary biopsies by a quarter while improving the detection of clinically significant cancer [1]. The PRECISION study randomized patients to either systematic biopsies or MRI; with no biopsy if MRI was negative, and targeted biopsy if MRI was positive. Targeted biopsies guided by MRI detected significantly more clinically significant cancers while reducing the number of clinically insignificant cancers [2]. Because of these findings, MRI for prostate cancer diagnosis has been integrated into established guidelines [3].

Increasing demand for prostate MRI examinations can be expected, as the incidence of prostate cancer increases with age and life-expectancy in developed countries is rising. Furthermore, prostate MRI has been discussed in the literature as a screening tool, similar to breast cancer screening [4]. However, several limitations need to be addressed in order to prepare for this increasing prostate MRI workload. Variation in MRI data acquisitions could be reduced [5]. Another limitation is the relatively long acquisition time of multiparametric MRI examinations (mpMRI) employing T2-weighted (T2w), diffusion-weighted imaging (DWI) and dynamic-contrast enhanced (DCE) MRI. Several studies have shown that an approach without DCE MRI, called biparametric MRI (bpMRI), yields comparable results to mpMRI of the prostate [6]. Potentially even more important topic is the varying interpretation performance based on the expertise level. However, even among expert radiologists, agreement on prostate cancer classification based on established guidelines is imperfect [7, 8].

This all points to a clear need for

1. Efficient, reproducible, and robust data acquisition workflow
2. Optimized and fast sequence design
3. Automated detection, classification, and reporting workflows in prostate MRI examinations

1 Image acquisition using the Prostate Dot Engine[1] including automated prostate contour detection, prostate centering, field of view adaption and three-dimensional correction of spatial axes.

This is a chain of independent, yet highly interlinked stages. Well-registered and reformatted images with reproducible high image quality are a key prerequisite for optimal and reproducible artificial intelligence-based analyses.

In this article, we outline an end-to-end solution that addresses all the limitations above, incorporating day optimizing throughput (Dot), ultrashort bpMRI and deep-learning-based lesion detection, classification and reporting. We present two example cases using the proposed workflow in order to illustrate its feasibility.

Material and methods

Prostate Dot Engine

The Prostate Dot Engine[1] is a prototype software tool designed to provide a fast, robust, and standardized image acquisition workflow. After acquiring the Turbo-Spin Echo (TSE) scout, the Prostate Dot automatically centers the prostate in the field of view, adapts the size of the field of view and performs a three-dimensional correction of spatial axes. Slices can be aligned either strictly orthogonal or automatically defined by the orientation of the urethra, i.e., perpendicular to the urethra for the axial planes. Furthermore, the prostate is segmented for standardized volume assessment. After coil placement, the Dot workflow does not require further adaptations by technicians, and it allows interruptions and corrections of the scan process at any time. A screenshot of the Prostate Dot Engine can be found in Figure 1.

[1] *Work in progress: the application is currently under development and is not for sale in the U.S. and in other countries. Its future availability cannot be ensured.*

Sequence specifications

The biparametric protocol consists of a T2-weighted turbo spin-echo (TSE) pulse sequence in axial, sagittal and coronal orientations and an improved single shot DWI EPI sequence (ZOOMit^{PRO}, Siemens Healthcare, Erlangen, Germany) with consecutive computation of the apparent diffusion coefficient. Unlike other DWI techniques, ZOOMit^{PRO} magnifies the prostate (in the phase-encoding direction) and is free of infolding artifacts. Either a smaller quadratic FOV or only a reduced FOV in the phase-encoding direction ('stripe') is excited (see Figure 2A). As there is no signal from the non-excited regions, only the small stripe needs to be encoded (see Figures 2B, C). That means the encoding time can be decreased while maintaining spatial resolution, or the spatial resolution can be increased, or a combination of the two. Furthermore, decreased encoding time reduces spatial distortion.

Prostate AI

The output of the Prostate Dot Engine goes into the AI prototype (Prostate AI[1], Siemens Healthcare, Erlangen, Germany) for fully automatic prostate lesion detection, classification and reporting.

As illustrated in Figure 3, Prostate AI contains two parts:

1. A preprocessing pipeline
2. A component for lesion detection and classification, based on deep learning

The preprocessing pipeline takes the acquired bpMRI sequences and generates the required well-formatted and transformed data volumes. From the DWI series, a logarithmic extrapolation method is adopted to compute a new DWI volume with *b*-value of 2000 s/mm^2. This step

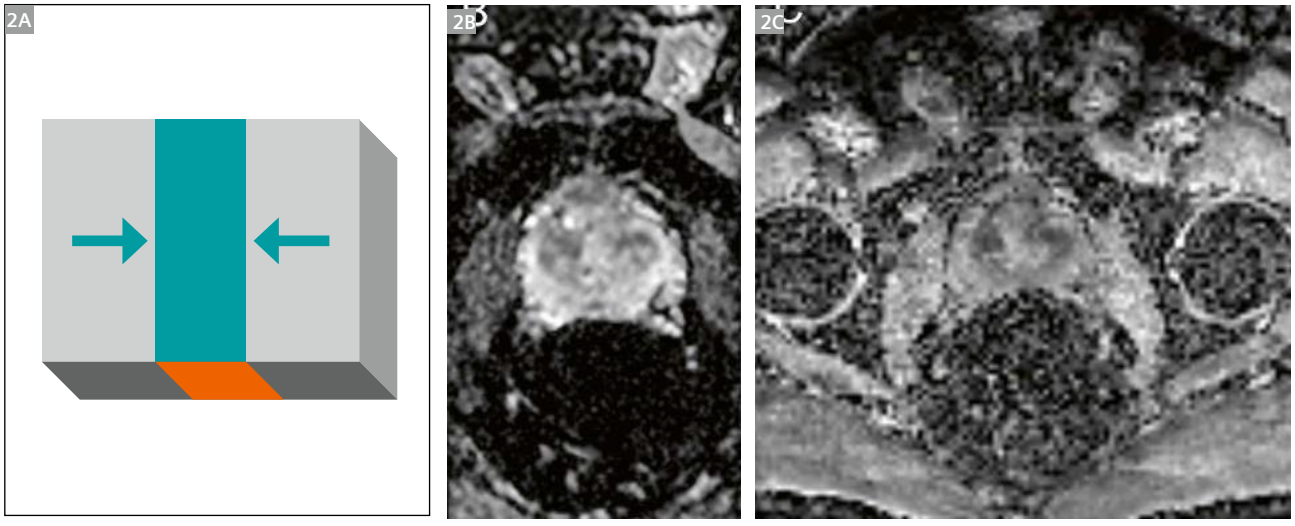

2 Single-shot DWI EPI sequence (ZOOMit^{PRO}) with image examples from one study object: **(2A)** reduced FOV in phase-encoding direction (blue stripe); **(2B)** resulting image in comparison to **(2C)** the conventional RESOLVE technique.

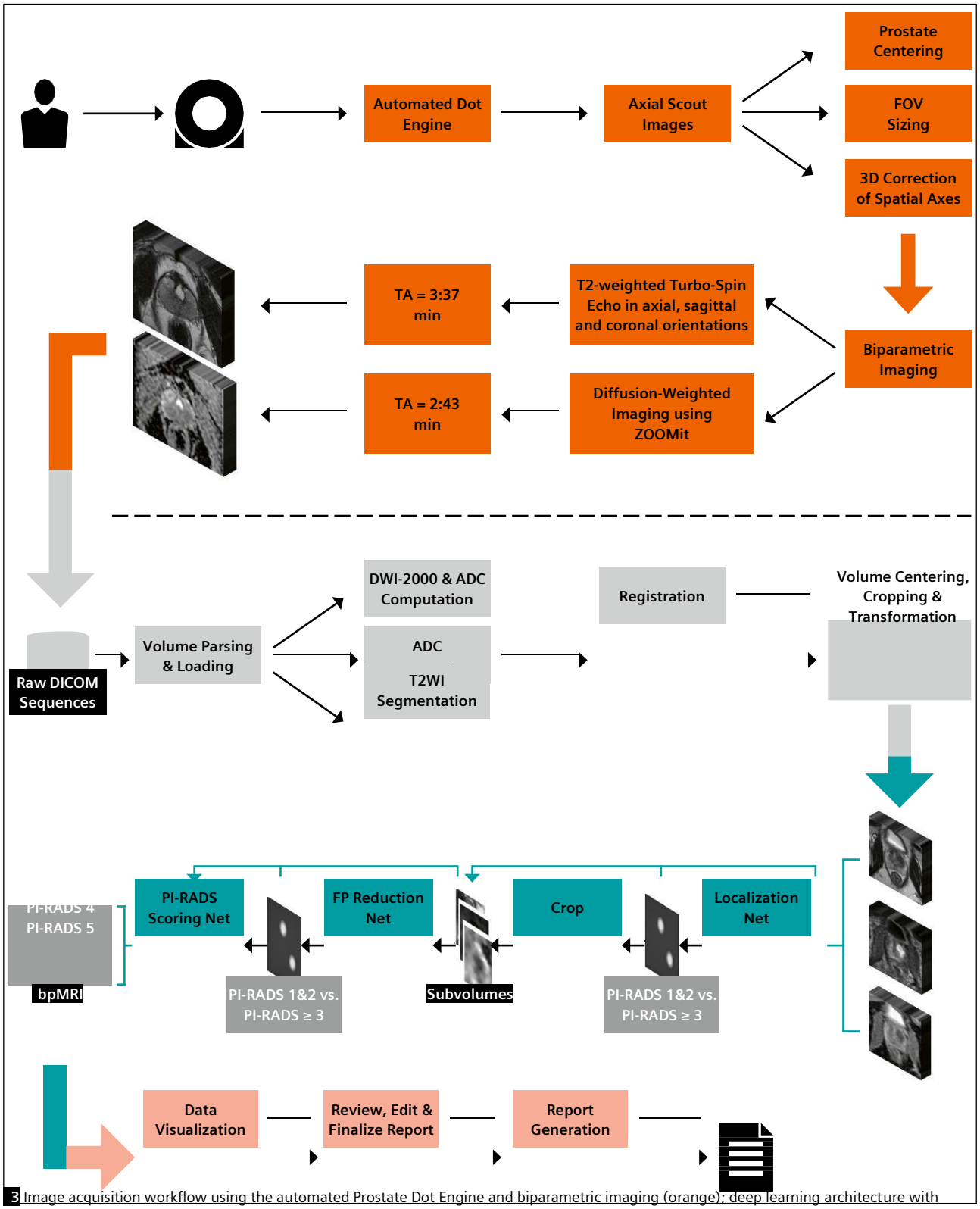

3 Image acquisition workflow using the automated Prostate Dot Engine and biparametric imaging (orange); deep learning architecture with preprocessing pipeline (gray); deep learning-based lesion detection and classification component (blue).

Dot = day optimizing throughput, FOV = field of view, 3D = three-dimensional, TA = time of acquisition, DICOM = Digital Imaging and Communications in Medicine, ADC = apparent diffusion coefficient, FP = false positive, PI-RADS = Prostate Imaging Reporting- and Data System

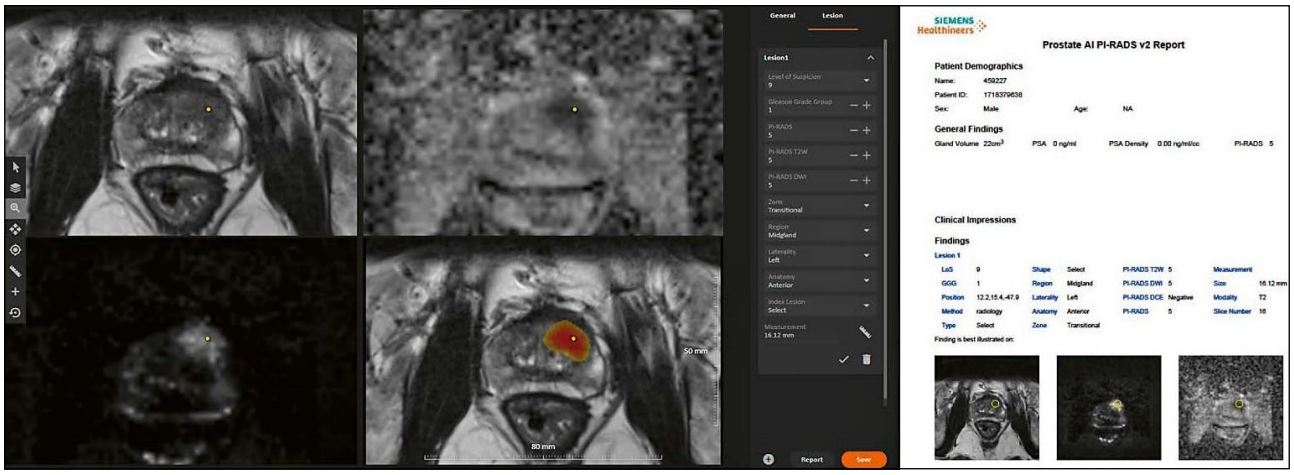

4 Data visualization platform with the T2w images, ADC map, and high *b*-value image as well as the T2w image overlaid with the AI-generated heatmap (in red and yellow). Prostate AI automatically detected the suspect lesion in the transition zone (TZ, yellow dot) and pre-populated all relevant information according to current PI-RADS guidelines. Next, a machine-readable report based on this information is generated.

can eliminate the *b*-value variances among the datasets and also improve lesion detection performance [10]. Also, apparent diffusion coefficient (ADC) maps are computed. Next, whole-organ gland segmentation is performed on the T2w volume using a learning-based method as presented in Yang et al. [11]. After segmentation, a rigid registration is conducted to align T2w and DWI images. The preprocessing pipeline can eliminate both geometric and intensity variances across sequences and patient studies.

Prostate AI then automatically detects clinically relevant lesions and classifies each detected lesion according to PI-RADS categories. This is achieved by a sequence of coupled deep neural networks that are trained separately. First, a fully convolutional localization net is able to generate a semantic lesion candidate heatmap (see Figures 5 and 6); then a sub-volume-based false positive reduction net further improves detection accuracy by removing the false positives; finally another sub-volume-based PI-RADS scoring net stages the level of malignancy for each detection according to PI-RADS categories.

In a last step, Prostate AI displays the detection and classification results on a dedicated platform. As the ability of the interpreting radiologist to accept or reject AI-based findings has been identified as a prerequisite for adoption of these techniques [12], these capabilities have been implemented. The user is then able to create a machine-readable report with all relevant information for the referring physician (see Figure 4). This report can be sent to the local RIS/PACS system.

Cases

Case 1

Figures 5A-D demonstrate a lesion in the right midgland PZpl/PZa of a 62-year-old man, with a maximum diameter of 30.2 mm and a mean ADC-value of 758 µm²/s. Prostate AI detected the lesion and assigned a PI-RADS 5 category. Biopsy results revealed a Gleason 4+3 = 7 pattern.

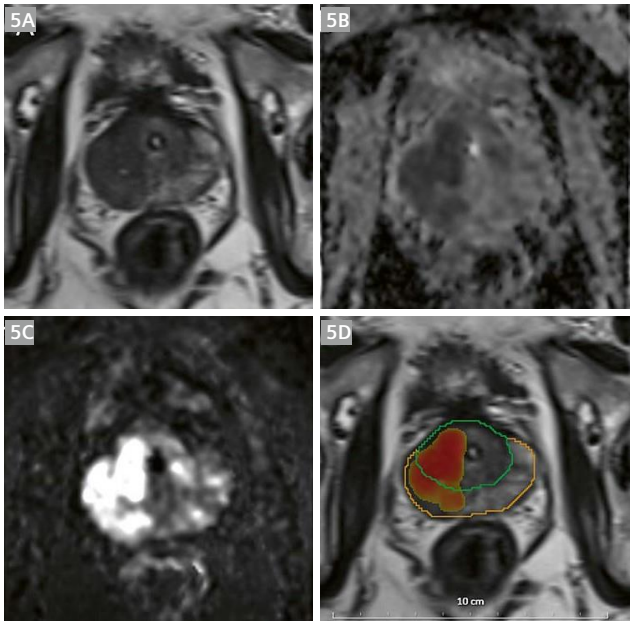

Case 2
Figures 6A-D demonstrate a lesion in the left apical PZpl of a 51-year-old man, with a maximum diameter of 10.2 mm and a mean ADC-value of 961 µm²/s. Prostate AI detected the lesion and assigned a PI-RADS 4 category. Biopsy results revealed a Gleason 3+3 = 6 pattern.

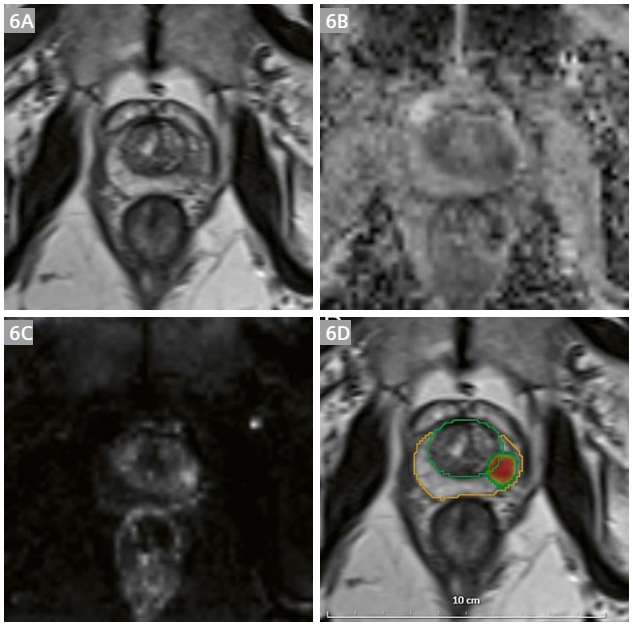

Conclusion

In this article, we outlined an end-to-end concept to allow a standardized workflow with a reproducible and fast data acquisition with optimized imaging sequences and an AI-empowered data analysis including automated detection, classification and reporting of suspicious lesions in biparametric prostate MRI examinations.

Reproducible and fast data acquisition concepts are not only contributing to a standardized reporting performed by human readers but would also help artificial intelligence-based solutions to reliably process input data. Preliminary results from a study conducted at the University of Innsbruck in Austria including 50 patients referred for a prostate MRI examination, compared the tilting angle of the auto-alignment of the Prostate Dot Engine against axes determined manually by an experienced radiologist, serving as the reference-standard. The investigators were able to show a mean ± SD deviation of the tilting angle of 5.5 ± 4.4 degrees (Ch. Kremser, W. Judmaier, Med. Uni Innsbruck, unpublished results). However, to date, there is no study investigating workflow differences, such as time-saving metrics, between Dot-guided and conventional, technician-guided workflows. Those studies are currently planned, and their results will contribute to reveal the value of Dot engines in clinical routine.

Concerning the use of abbreviated protocols consisting of T2-weighted and DWI only – so-called biparametric prostate MRI – several studies [6, 13, 14] have shown comparable results as obtained with conventional, mpMRI protocols including DCE-MRI. We added another component to our suggested workflow, that is performing DWI with the ZOOMit^{PRO}. As shown in Figure 2, ZOOMit^{PRO} uses a reduced FOV in the phase-encoding direction compared with either standard single shot DWI EPI or RESOLVE (REadout Segmentation Of Long Variable Echo trains). The resulting decreased acquisition time can be invested in a superior spatial resolution. Future studies are needed to systematically investigate differences between different types of DWI acquisition schemes compared to the ZOOMit^{PRO} technique.

The last component in our workflow is the use of AI-based lesion detection and classification. Schelb et al. [15] used the input from T2w sequences and DWI to train a deep learning algorithm (Unet) on the histopathological outcome, serving as ground truth. They were able to show that this algorithm achieved a similar performance to human readers using the PI-RADS assessment score. Cao et al. [16] used the input of mpMRI images to build a convolutional neural network trained on histopathological data and used this algorithm to detect suspicious lesions and to predict the Gleason score. The results were promising, with a high sensitivity for lesion detection – comparable to expert human readers – and a high classification performance with regards to clinically significant cancer. However, the usefulness of these algorithms needs to be proven in larger multi-reader, multi-case (MRMC) studies, systematically examining their influence on interpretation performance and speed, with and without those solutions.

We have identified a need to re-structure existing prostate MRI workflows, as patient or – in case of screening approaches – participant throughput is expected to increase. In our vision, current workflows need more reliable, reproducible and fast data acquisition steps. Furthermore, recent research has shown that deep learning algorithms can compete with human intelligence in prostate MRI reporting. We outlined a possible end-to-end solution and demonstrated its feasibility with two case examples. Future research will investigate what impact the individual components or the combination of those components will have on the future of prostate MRI.

References

1 Ahmed HU, El-Shater Bosaily A, Brown LC, et al. Diagnostic accuracy of multi-parametric MRI and TRUS biopsy in prostate cancer (PROMIS): a paired validating confirmatory study. Lancet. 2017;389:815–822. https://doi.org/10.1016/S0140-6736(16)32401-1

2 Kasivisvanathan V, Rannikko AS, Borghi M, et al. MRI-Targeted or Standard Biopsy for Prostate-Cancer Diagnosis. N Engl J Med. 2018;378:1767–1777. https://doi.org/10.1056/NEJMoa1801993

3 EAU Guidelines. Presented at the EAU Annual Congress Barcelona 2019. ISBN 978-94-92671-04-2.

4 Kim SJ, Vickers AJ, Hu JC. Challenges in Adopting Level 1 Evidence for Multiparametric Magnetic Resonance Imaging as a Biomarker for Prostate Cancer Screening. JAMA Oncol. 2018;4:1663–1664. https://doi.org/10.1001/jamaoncol.2018.4160

5 Padhani AR, Barentsz J, Villeirs G, et al. PI-RADS Steering Committee: The PI-RADS Multiparametric MRI and MRI-directed Biopsy Pathway. Radiology. 2019;292:464–474. https://doi.org/10.1148/radiol.2019182946

6 Weiss J, Martirosian P, Notohamiprodjo M, et al. Implementation of a 5-Minute Magnetic Resonance Imaging Screening Protocol for Prostate Cancer in Men with Elevated Prostate-Specific Antigen before Biopsy. Invest Radiol. 2018;53:186–190. https://doi.org/10.1097/RLI.0000000000000427

7 Weinreb JC, Barentsz JO, Choyke PL, et al. PI-RADS Prostate Imaging - Reporting and Data System: 2015, Version 2. Eur Urol. 2016;69:16–40. https://doi.org/10.1016/j.eururo.2015.08.052

8 Rosenkrantz AB, Ginocchio LA, Cornfeld D, et al. Interobserver Reproducibility of the PI-RADS Version 2 Lexicon: A Multicenter Study of Six Experienced Prostate Radiologists. Radiology. 2016;280:793–804. https://doi.org/10.1148/radiol.2016152542

9 Maas MC, Fütterer JJ, Scheenen TW. Quantitative evaluation of computed high b value diffusion-weighted magnetic resonance imaging of the prostate. Invest Radiol. 2013;48:779.

10 Rosenkrantz AB, Parikh N, Kierans AS, et al. Prostate Cancer Detection Using Computed Very High b-value Diffusion-weighted Imaging: How High Should We Go? Acad Radiol. 2016;23:704–711. https://doi.org/10.1016/J.ACRA.2016.02.003

11 Yang D, Xu D, Zhou SK, et al. Automatic Liver Segmentation Using an Adversarial Image-to-Image Network. In: Descoteaux M, Maier-Hein L, Franz A, et al (eds) Medical Image Computing and Computer Assisted Intervention – MICCAI 2017. Springer International Publishing, Cham. 2017; pp 507–515.

12 Padhani AR, Turkbey B. Detecting Prostate Cancer with Deep Learning for MRI: A Small Step Forward. Radiology. 2019;192012. https://doi.org/10.1148/radiol.2019192012

13 Kuhl CK, Bruhn R, Krämer N, et al. Abbreviated Biparametric Prostate MR Imaging in Men with Elevated Prostate-specific Antigen. Radiology. 2017;282:493–505. https://doi.org/10.1148/radiol.2017170129

14 Woo S, Suh CH, Kim SY, et al. Head-to-head comparison between biparametric and multiparametric MRI for the diagnosis of prostate cancer: A systematic review and meta-analysis. Am J Roentgenol. 2018;211:W226–W241. https://doi.org/10.2214/AJR.18.19880

15 Schelb P, Kohl S, Radtke JP, et al. Classification of Cancer at Prostate MRI: Deep Learning versus Clinical PI-RADS Assessment. Radiology. 2019;190938. https://doi.org/10.1148/radiol.2019190938

16 Cao R, Bajgiran AM, Mirak SA, et al. Joint Prostate Cancer Detection and Gleason Score Prediction in mp-MRI via FocalNet. IEEE Trans Med Imaging. 2019;38:2496–2506. https://doi.org/10.1109/TMI.2019.2901928

Contact

David J. Winkel, M.D.
Department of Radiology
University Hospital Basel
Spitalstrasse 21
4031 Basel
Switzerland
Tel.: +41 61 328 65 22
davidjean.winkel@usb.ch

Assessing Breast Cancer Phenotypes with MRI Biomarkers in Clinical Practice

Elizabeth Morris, M.D.

Chief, Breast Imaging Service, Larry Norton Chair & Professor of Radiology,
Memorial Sloan Kettering Cancer Center (MSKCC), New York, NY, USA

Introduction

Advances in our understanding of the human genome have transformed the way we understand and treat breast cancer. Today, oncologists and gynecologists are no longer saying "this is invasive ductal carcinoma," but they can classify each breast cancer as one of four molecular subtypes based on its genetic expression. In this context, breast MRI provides a highly valuable and non-invasive tool to differentiate between subtypes due to the differences in imaging phenotypes between subtypes. In addition, as the cancer subtype has a significant impact on the individual patient's response to the currently available treatment options, MRI biomarkers may be used to predict complete response to therapy including non-surgical options and improve patient outcomes.

Breast cancer subtypes

While every breast cancer is unique, breast cancer can be classified into one of four distinct subtypes: luminal A, luminal B, human epidermal growth factor receptor 2 (HER2) positive, and basal-like. Luminal cancers are the most prevalent breast cancer subtype, representing 70% (55% luminal A, and 15% luminal B) of all breast cancers. Non-luminal cancers are less common but still substantial, representing 30% (15% basal-like and 15% HER2) of all breast cancers (Fig. 1).

The breast cancer subtype that is present in an individual patient has a significant impact on the cancer's aggressiveness. HER2-positive cancers and triple negative cancers are more highly aggressive whereas luminal A cancers (which are the most frequently diagnosed breast cancer) have a relatively good prognosis. In addition to the subtype, it must also be noted that intracellular receptors that respond to estrogen (ER) and progesterone (PR) hormones as well as HER2 receptors have been shown to also impact cancer aggressiveness. All cells have HER2 receptors on them, but if they overexpress these receptors to a certain degree, then they are associated with a much more aggressive form of breast cancer with uncontrolled growth.

Luminal A

Luminal A cancers are low-grade cancers that are strongly ER positive and/or PR positive as well as HER2 negative. They show no amplification of HER2, the proto-oncogene for increased growth, or Ki-67, a biomarker for cellular proliferation.

Luminal A cancers have a five-year survival rate of over 80%, which is highest among the subtypes. Luminal A cancers respond favorably to hormone therapy with tamoxifen or aromatase inhibitors (AI). Nonetheless, they are associated with the risk of late mortality more than ten years after the original diagnosis. It is hypothesized that the cancer cells remain inactive for a long time, probably suppressed by the immune system, before late relapse takes place. Late relapse is not uncommon with this subtype and luminal A cancers are highly likely to metastasize to the bone.

On MRI, luminal A presents as a typical spiculated mass with significant desmoplastic response (Fig. 2).

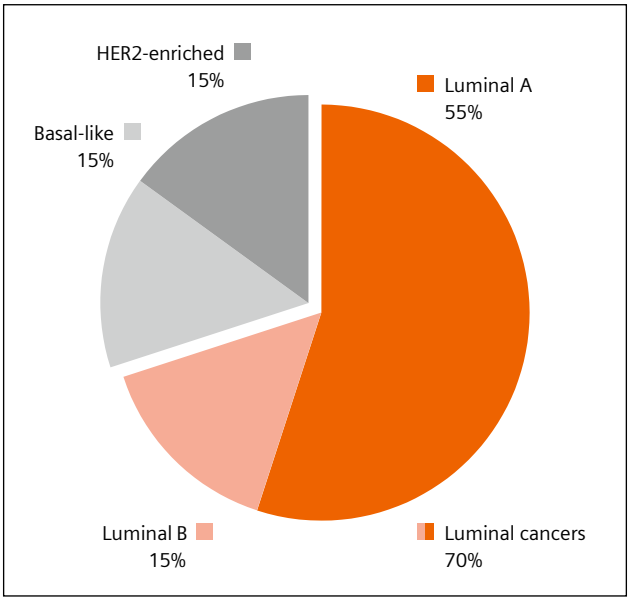

1 Breast cancer subtypes and their respective prevalence.

Luminal B

Luminal B cancers have a lower level of expression of ER and PR than luminal A cancers, and 20–30% of these cancers have a concomitant amplification of HER2. Compared with luminal A cancers, luminal B cancers are higher grade (always medium- to high-grade), showing a higher Ki-67 index and likely having lymph node involvement. Hence, luminal B cancers have a definite decrease in long-term survival, with a five-year survival of approximately 40%. Like luminal A cancers, luminal B cancers metastasize to the bone.

Mammoprint, Oncotype DX, and PAM-50 multigene assays identify breast cancers with an increased risk of recurrence based on gene expression arrays using formalin-fixed paraffin-embedded (FFPE) specimens. They help to identify which patient can forego chemotherapy. For luminal B cancers, a low Oncotype DX recurrence score permits the recommendation of hormonal therapy alone, whereas a high recurrence score indicates that chemotherapy is required as an adjunct treatment.

On imaging, luminal A and luminal B cancers look very similar. Tumor grading is the preferred mechanism for differentiating luminal A and luminal B cancers. Ki-67 can also provide great assistance but is not routinely recommended. Ki-67 as a prognostic marker is associated with larger tumor size, lymph node involvement, and shorter disease-free survival (DFS) and overall survival (OS). Ki-67 has shown to be positively associated with response to neoadjuvant chemotherapy (NAC).

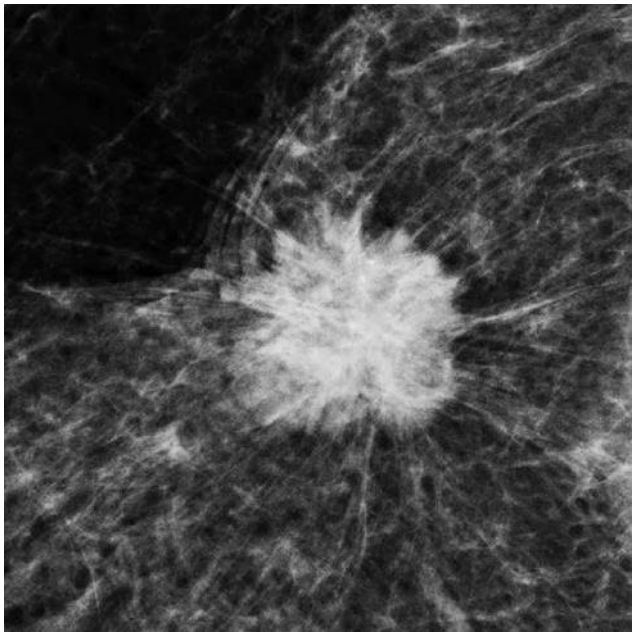

2 Zoomed T1-weighted post-contrast images (subtracted from T1-weighted pre-contrast) showing the typical representation of a luminal A breast cancer: a hyperdense, spiculated mass with irregular margins and significant desmoplastic response.

HER2 positive

15% of all breast cancers are HER2 positive. These tumors usually have an intermediate to high nuclear grade. Prior to the introduction of traztuzumab (brand name Herceptin) and pertuzamab (brand name Perjeta), the untreated clinical five-year survival rate was 31%; with these treatments, treating physicians have achieved a 33% reduction in mortality and a 52% reduction in recurrence.

Patients with HER2 positive cancers are more likely to have metastases that go to the viscera and the brain.

Basal-like

The fourth subtype of breast cancer is basal-like. Basal-like cancers have cells that are similar to epithelial cells (i.e., basal cells) that line the surface of the basement membranes along the ducts.

While there are many different types of basal cell cancer, the clinical focus is on triple-negative invasive ductal cancers. The discussion of triple-negative cancers generally centers on the very aggressive nature of this cancer and that it is more common in African-American women. In this population, this cancer represents 27% of the overall cancer burden and 41% of the cancer mortality.

Adenoid cystic carcinoma is a rare type of invasive ductal cancer; however, while it is triple negative, it has very positive prognosis and outcome.

Basal-like breast cancer is usually high grade with an aggressive clinical course. Recurrence normally occurs in the first five years after diagnosis. Once a patient is beyond the five-year mark, the prognosis is normally positive; this is in stark contrast to luminal A type breast cancer. Basal-like breast cancer also has a high occurrence of metastases to brain, lung, and viscera. This subtype of cancer has the highest mortality rate.

The role of MRI and radiomics

Over the past few decades, breast MRI capabilities have improved dramatically. With radiomics and radiogenomics, MR images can now be analyzed so that the image is related to the genome, rendering a host of data that might positively affect patient outcome. Radiologists can identify volumes to be segmented on MR images. Computers can then extract hundreds of descriptive and quantitative features that, when combined with medical and genomic data, create a comprehensive database. Clinicians can compare pixels with adjacent pixels and analyze them in this context to render many different datasets.

As opposed to traditional human interpretation where radiologists interpret the shape, margin, internal enhancement patterns, and kinetic curve of the lesion, computers can automatically segment abnormal lesions and parenchyma in the MR image, produce data on kinetic features, and analyze morphological texture features rendering a

more quantitative phenotype analysis. Radiomics has provided deeper analytic features in datasets, e.g., inter- and intra-tumor heterogeneity, site entropy, kurtosis, and site cluster dissimilarity, by extracting information from images that is imperceptible visually. This information is combined with clinical data and genomic profiles to facilitate the establishment of a clinically applicable prognosis prediction model. For example, MR images of a patient pre- and post-NAC as shown in in Figure 3 could render feature data that provide the clinician with a greater ability to predict pathologic complete response (pCR) by showing whether viable tumor persists.

While radiomics encompasses numerous potential features, these features tend to be standardizable and quantifiable. Many research organizations have been investigating the utility of radiomics to determine breast cancer phenotype groups. At Memorial Sloan Kettering Cancer Center (MSK), we have found that clinicians are able to predict breast cancer phenotypes with radiomics nearly as accurately as Oncotype DX and PAM50. Therefore, it is possible that in the future radiomics could establish oncologic signatures in the same way that tissue sampling currently does but without the need for invasive procedures.

Neoadjuvant Chemotherapy

Neoadjuvant Chemotherapy (NAC) is increasingly used to treat breast cancer because it enables breast-conserving surgery in women who traditionally require a mastectomy. The goal of NAC is pCR, defined as the absence of any residual in-situ or invasive cancer. pCR has served as a surrogate of DFS and OS for a long time.

Currently, the most accurately predictive test for pCR is MRI. MRI is more accurate in determining residual disease than physical examination, mammography, and ultrasound [3, 6]. However, MRI is not universally utilized as it still renders many false positives and false negatives. The absence of enhancement on MRI is called a radiologic complete response (rCR) even when there is a residual mass, and the pattern of the residual tumor is defined as contiguous or scattered to allow for better surgical selection.

With radiomics, it is possible that clinicians will achieve better response prediction with MRI, and MRI could potentially be used to replace surgery in the identification of patients with a complete response. Preliminary studies at MSK have shown that radiomics may be able to differentiate responders from non-responders.

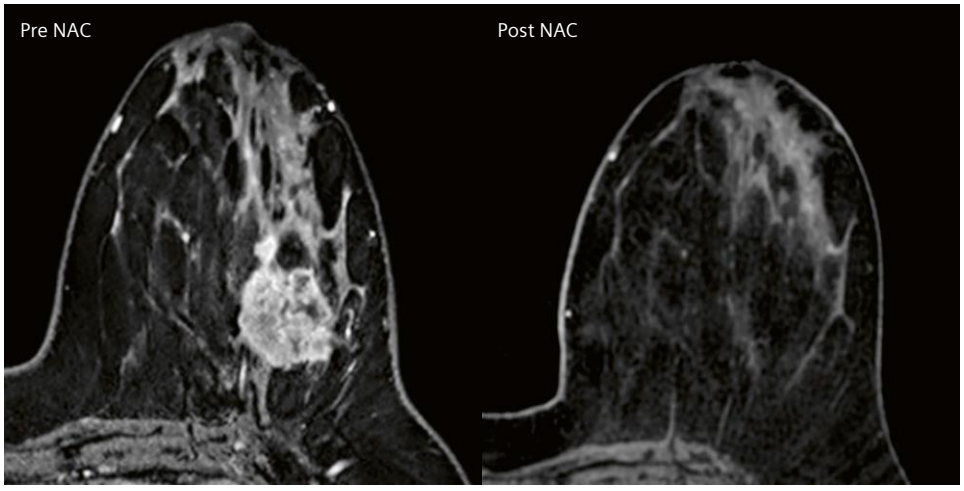

3 Subtracted, post-contrast T1-weighted images pre and post neoadjuvant chemotherapy. Patient showing complete imaging response which was confirmed as complete pathological response by biopsy. Highest response rates are seen in patients with TNBC and HER2+.

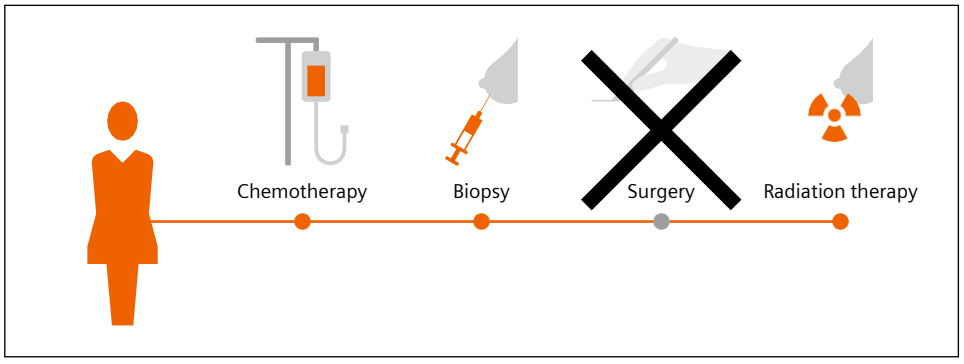

4 Proposed Care Pathway for patients with predicted pCR based on radiomic MRI profiling and biopsy-derived genetic profiling. In a planned trial patients shall proceed directly to radiation therapy without surgery.

New study conducted by Memorial Sloan Kettering Cancer Center

Currently, the NAC course of treatment involves MRI monitoring at critical points. We have been conducting a trial to perform a percutaneous MRI-guided biopsy in patients who have had an rCR as determined on MRI with radiomic analysis prior to surgery. We hypothesized that MRI-guided biopsy will accurately diagnose a pCR in women with complete response on MRI comparable to surgery, thus allowing us to avoid unnecessary surgery in these patients.

For the pilot phase, so far ten patients have undergone the MRI-guided biopsy (with a marker to allow targeting of the biopsy) post NAC but prior to surgery. Results from the pilot phase indicate that MRI-guided biopsy can yield a high level of accuracy in diagnosing a pCR.

Therefore, we are currently proposing a full trial where the management of breast cancer in women with a pCR (as diagnosed by MRI-guided biopsy post-NAC) will proceed without surgery to the indicated duration of radiation therapy (Fig. 4). The salient open question is what quantity of residual disease precludes bypassing the surgical option for the less invasive method. Also, given that this would represent a new treatment protocol, the type of follow-up that would be required has yet to be determined.

Topics for further research

Another topic that is also worthy of further investigation is the association between parenchymal enhancement using contrast-enhanced MRI and the outcome of patients with breast cancer, as studied earlier by van der Velden et al. [4]. This study found that parenchymal enhancement is associated with long-term outcomes and higher parenchymal enhancement is associated with better outcomes. Women who have higher background enhancement who are treated experience better outcomes than women with lower background enhancement even though high background enhancement is associated with higher risk of developing breast cancer [4]. These results have been reproduced [5].

MRI features can also be investigated to predict cancer aggressiveness. For example, Lee et al. [1] found that spiculated margins were an indicator low grade ($p < 0.001$) and a low Ki-67 ($p = 0.007$); these are typical of luminal A breast cancers which have a high chance of pCR. Lee et al. also found that tumors with a high grade ($p < 0.001$) and that were ER negative were associated with poor patient outcome ($p = 0.001$).

Lastly, peritumoral edema, which indicates increased vascular permeability with local cytokines, is associated with early metastatic disease and can also be investigated for its clinical utility [2].

Conclusion

MR imaging is moving into an era of technology where the status quo is being disrupted. Artificial intelligence (AI) and machine learning will produce marked advancements in risk prediction and cancer detection.

As advances continue to be made in the tools available to clinicians, clinicians must ask themselves to find uses for these advancements that will improve treatment options, patient outcomes, and quality of life. Clinicians must be intellectually agile to use these tools to create new possibilities for the treatment of patients as individuals, guiding clinical practice toward personalized medicine.

Contact

Elizabeth Morris
Chief, Breast Imaging Service,
Larry Norton Chair & Professor of Radiology
Memorial Sloan Kettering Cancer Center
1275 York Avenue
New York, NY, 10065
USA
Tel. +1 646 888 4510
morrise@mskcc.org

References

1 Lee SH, Cho N, Kim SJ, Cha JH, Cho KS, Ko ES, Moon WK. Correlation between high resolution dynamic MR features and prognostic factors in breast cancer. Korean J Radiol. 2008 Jan-Feb;9(1):10-8.

2 Rao A, Net J, Brandt K, Huang E, Freymann J, Burnside E, Kirby J, Morris E, Bonaccio E, Giger M, Jaffe C, Ganott M, Sutton E, Le-Petross H, Zuley M, Dogan B, and Whitman G. TU-CD-BRB-07: Identification of Associations Between Radiologist-Annotated Imaging Features and Genomic Alterations in Breast Invasive Carcinoma, a TCGA Phenotype Research Group Study. Med Phys. 2015;42:3603-4.

3 Rosen EL, Blackwell KL, Baker JA, Soo MS, Bentley RC, Yu D, Samulski TV, Dewhirst MW. Accuracy of MRI in the detection of residual breast cancer after neoadjuvant chemotherapy. AJR Am J Roentgenol. 2003 Nov;181(5):1275-82.

4 van der Velden BH, Dmitriev I, Loo CE, Pijnappel RM, Gilhuijs KG. Association between Parenchymal Enhancement of the Contralateral Breast in Dynamic Contrast-enhanced MR Imaging and Outcome of Patients with Unilateral Invasive Breast Cancer. Radiology. 2015 Sep;276(3):675-85.

5 van der Velden BH, Sutton EJ, Carbonaro LA, Pijnappel RM, Morris EA. Contralateral parenchymal enhancement on dynamic contrast-enhanced MRI reproduces as a biomarker of survival in ER-positive/HER2-negative breast cancer patients. Euro Radiology. 2018 Nov;28(11):4705-16.

6 Yeh E, Slanetz P, Kopans DB, Rafferty E, Georgian-Smith D, Moy L, Halpern E, Moore R, Kuter I, Taghian A. Prospective comparison of mammography, sonography, and MRI in patients undergoing neoadjuvant chemotherapy for palpable breast cancer. AJR Am J Roentgenol. 2005 Mar;184(3):868-77.

teamplay – Streamline Clinical Operations to Unlock Productivity Gains

Annelinde Veen

Siemens Healthineers, Erlangen, Germany

Get more out of your imaging data

In the age of digitalization, optimal use of data is key to success. Imaging modalities generate an abundance of clinical data to help diagnose a disease or for follow-up treatment of patients; and there is a lot more value behind imaging data when it comes to operational insights. However, this kind of data does not provide any advantage until you can turn it into actionable information. Today, the majority of operational data is not used, or is fragmented in data silos, or is simply lost – all of which prevents users from being able to derive improvement measures. At the same time, the Internet of Medical Things (IoMT)[1] is growing by approximately 25% every year[2], accelerating the digital transformation of the healthcare industry and emphasizing the importance of connected data.

So how can you benefit from digitalization to get more out of your data?

teamplay is your starting point. teamplay performance management applications grant instant access to analytics derived from operational data from your imaging fleet. This will enable you to make objective, well-informed decisions quickly by offering a clear overview of radiology performance data. Monitor quantities such as imaging throughput, dose levels, staff utilization, rooms, and department resources – down to each device and procedure. teamplay allows you to simplify your reporting and gain insights to reveal improvement potentials. In addition to that, you can link with other teamplay users and their data for comparable benchmarks[3], and exchange images with little effort.

Continued on page 90.

[1]*The Internet of Medical Things refers to the connected system of medical devices and applications that collect data that is then provided to healthcare IT systems through online computer networks.*
Source: https://www.forbes.com/sites/bernardmarr/2018/01/25/why-the-internet-of-medical-things-iomt-will-start-to-transform-healthcare-in-2018/#600bf0df4a3c
[2]*Source: Statista, Estimated Healthcare IoT Device Installations Worldwide 2018*
[3]*Depending on privacy settings.*

How does it work?

The teamplay performance management applications run on the teamplay digital health platform, which is the main enabler of digital connectedness. Healthcare providers can gain easy access to operational, clinical and shared decision-making solutions developed by Siemens Healthineers (SHS) and our partners – greatly enabling scalability and flexibility and supporting future-readiness.

The platform effectively integrates and interconnects data and knowledge from a global and diverse network of healthcare professionals, and already comprises more than 5,000 connected institutions[4].

teamplay Receiver software connects your organization to the teamplay cloud and serves as your central data gateway, allowing the exchange of health data in a secured environment – inside or outside your network.

The receiver serves as a DICOM node and fetches data from the connected scanners and/or the PACS, according to your institution's data privacy policy. Regardless of manufacturer, your entire imaging device fleet (MRI, CT, SPECT, PET/CT, X-ray interventional radiology and cardiology, ultrasound) can be connected and monitored remotely. teamplay's cloud infrastructure is based on Microsoft Azure, meets industry best practices of security and privacy, and supports HIPAA and is compliant with GDPR, and ISO 27001.

Streamline your operations with the following teamplay performance management applications:

- **teamplay Protocols** – speed up your protocol management by facilitating remote access[5]
- **teamplay Usage** – increase your efficiency and optimize your imaging fleet utilization
- **teamplay Dose** – simplify your radiation dose management
- **teamplay Insights** – maximize your insights, optimize your value
- **teamplay Images** – share and discuss cases in a secured environment[6]

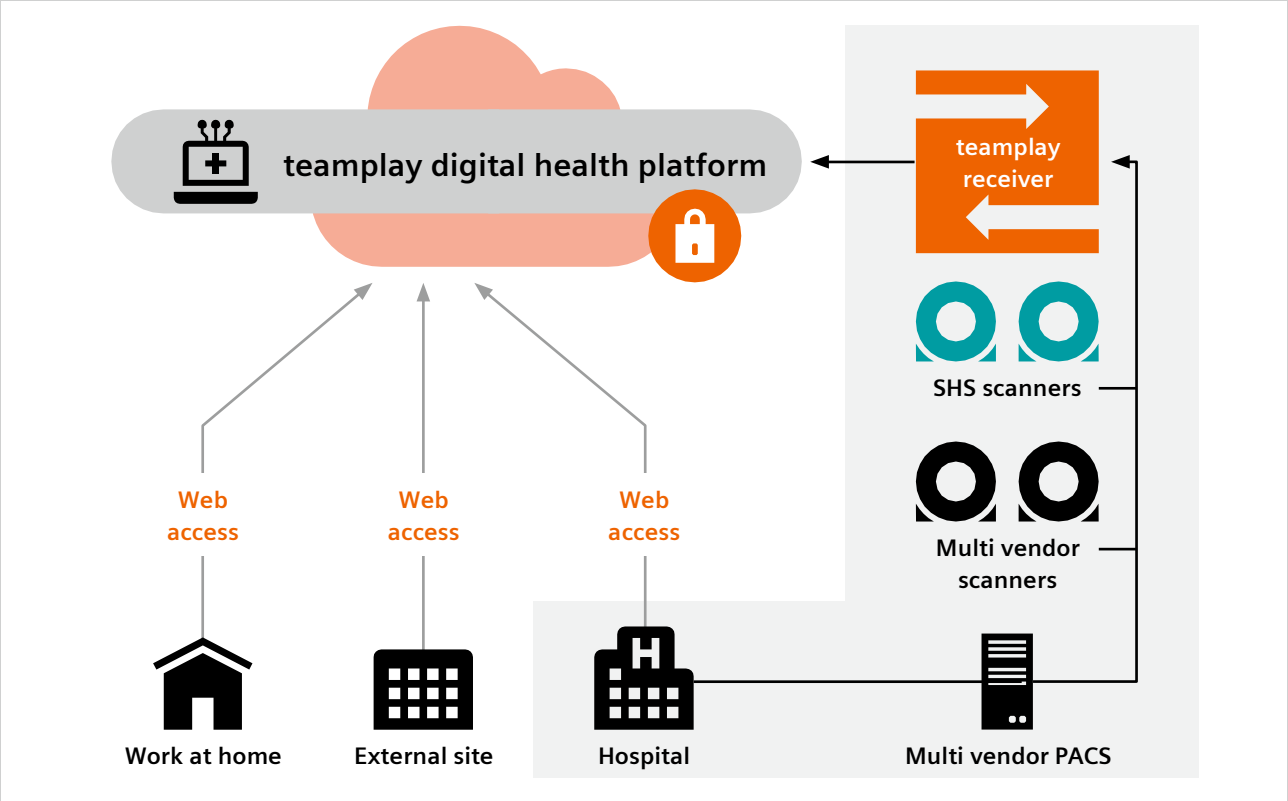

1 Technical set-up for teamplay digital health platform.

[4]*Due to regulations, data exchange between data center regions is restricted. The products/features/service offerings are not commercially available in all countries. If the services are not marketed in countries due to regulatory or other reasons, the service offering cannot be guaranteed. Please contact your local Siemens organization for further details.*

[5]*teamplay Protocols supports selected Siemens Healthineers scanners.*

[6]*The DICOM viewer is not intended for diagnostic display.*

Streamlining operations to reduce wait times

Huge patient backlog and increasing wait times are a significant concern for many imaging departments. Patients often face several weeks of waiting to get an MRI appointment. How could teamplay help you?

One possible solution is offering more exam slots. How can you achieve this without extending opening hours or hiring extra staff? teamplay performance management applications give insights on how to improve workflows in order to increase patient throughput, scanning more patients with the same number of scanners and within a given time.

With teamplay Usage you can see all the MRI scanners in your department, institution or hospital chain at a glance. Key performance indicators (KPIs) such as throughput, patient change time, exams per hour, and table occupancy help you understand your workflow and detect potential for improvement. To achieve the goal of scanning more patients within the same period of time, the two KPIs 'exam duration' and 'patient change time' are of particular interest and could be shortened.

Identify which exam durations can be shortened

Multiple protocols are installed on every MRI scanner, which might make it quite difficult to know where to start optimizing your protocols and to shorten your average exam duration. This task becomes even more complex if your imaging fleet consists of numerous MRI scanners, spread over several locations.

teamplay can support you in identifying the protocols that have the biggest impacts on your workflow, and which are therefore good starting points for optimization. With teamplay you can see which protocols are used, their frequency of use and the respective average exam duration. Combining these three types of information helps you to select the protocols that are used most regularly and show the most potential for shortening exams (Fig. 2).

Optimize patient change times

Another way to increase the efficiency of your radiology department is to focus on the KPI 'change time between patients'.

Patient change times can be quite long when a patient is prepared directly on the MRI scanner. For example, whenever contrast is required for an MRI scan, the process of preparing the patient and placing IVs typically takes considerable time. Often this procedure is performed inside the MRI room, which means a waste of valuable scan time, as the scanner cannot be used on another patient while it is happening.

With teamplay you can easily identify the average patient change times on each scanner, and even filter them for specific exam type (Fig. 3). The patient change time is calculated as the time between the end of the last scan and the start of a new scan, independent of any other manual actions. If this KPI seems relatively long, the next step should be learning what exactly is happening with your scanners and in the examination (MR) rooms during this time. With this knowledge, you can then find strategies to change the workflow in a way that minimizes patient change times. For example, teamplay Usage helped one of our customers to identify long patient change times on their two MRI systems. The root causes were staff availability, inefficient lay-out of the MRI rooms, and that patients were lacking information about what to expect during the scan. By assigning enough technologists, changing the lay-out of the MRI rooms, and providing educational videos to patients, the average patient change time has decreased by 50%. As a result, 30% more patients can be scanned.[7]

Standardize care and save costs

Standardization of operations helps improve clinical and operational outcomes. Once best practices – for example specific protocol settings – are identified, it is key to quickly spread them across your fleet. But delivering standardized care throughout your entire imaging fleet can be difficult, time consuming, and hard work. For example, it is projected that up to 520 hrs per year are spent by a chief technologist for harmonizing MRI protocols and travelling to the scanners across five different sites, resulting in average labor costs of approximately US$ 46,800 a year[8] – not to mention exacerbating the staff shortage many healthcare providers are facing.

teamplay performance management applications facilitate remote access and help minimize the effort needed for standardization.

It all starts with accessible intelligence. By getting a transparent view of your imaging device utilization with teamplay Usage, you can identify processes that take up an exceptionally large amount of time. You can easily

[7]The statements by Siemens Healthineers' customers described herein are based on results that were achieved in the customer's unique setting. Because there is no 'typical' hospital or laboratory and many variables exist (e.g., hospital size, samples mix, case mix, level of IT and/or automation adoption) there can be no guarantee that other customers will achieve the same results.

[8]Assumptions: average annual income of a Chief Radiographer = 75k USD; 75k USD + estimated employee on-costs = 180k USD; average 8h/d at 250 working days = 2000h/year → 90 USD/h; 10h/week travelling time to harmonize MR protocols across five sites → 520h/year*

**Source: http://www1.salary.com/Chief-MRI-Technologist-Salary.html*

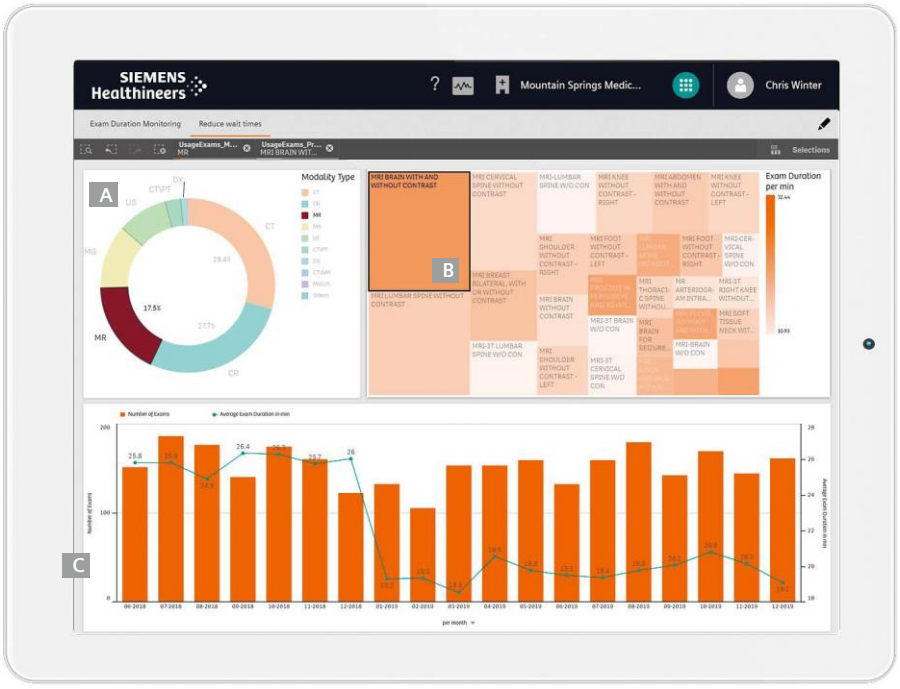

A Filter on Modality type
Select MR

B Identify protocol
In this overview of protocols you can identify which protocol is used most often (size of box) and has a long duration (darkest color is longest duration)

C Track progress over time
See how number of exams and average exam duration has evolved over time for selected protocol.

2 Identify which protocol has the most potential to be shortened, to scan more patients in a given time.

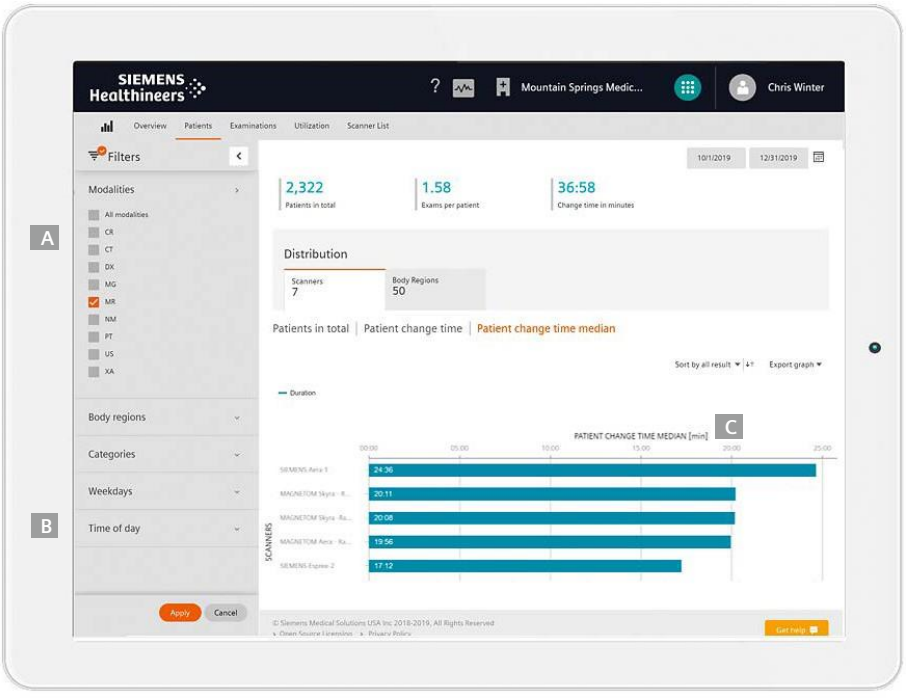

A Filter on Modality type
Select MR

B Select working hours
To get the patient change time during your most productive hours

C See your patient change times
Get an overview of patient change time per scanner

3 Learn which scanners have relatively long patient change time, to adapt your workflow to scan more patients in a given time.

compare different KPIs from all your imaging modalities in your institution, even when you have multiple locations. For example, if you compare average exam durations per body region per scanner, you will be able to see whether there are differences between scanners and identify outliers. Inefficient scan protocols are often the reason for those variations. Once you have identified these differences, you want to make sure that your entire organization benefits from the improved settings.

teamplay Protocols facilitates convenient remote access to all protocols, and allows you to adjust and distribute the optimized scan protocols to other scanners instantly (Fig. 4). Moreover, our latest generation of Siemens Healthineers' MRI scanners allows for uninterrupted protocol management. While scanning patients, the lead technologist can manage and adapt protocols remotely, in parallel. This leads to additional flexibility as well as time and cost savings.

Overall, teamplay's convenient, remote protocol management helps you to provide standardized, high-quality care throughout your entire fleet.

Siemens Healthineers collects best practice protocols for MR from all around the world on the MAGNETOM World website (www.siemens.com/magnetom-world). From here you can easily import these best practice protocols into teamplay to distribute them to the scanners in your fleet. For example, to aid standardization of cardiovascular MR imaging, the Society for Cardiovascular Magnetic Resonance (SCMR) released CMR exam protocol recommendations for the most frequent procedures. Based on the Cardiac Dot Engine, we have prepared clinically optimized exam protocols for 1.5 and 3T MAGNETOM MR scanners from Siemens Healthineers.

Fleet management across your imaging modalities

teamplay covers and connects your entire imaging fleet from Siemens Healthineers and other manufacturers, from MRI, CT imaging, PET/CT, X-ray, and mammography to interventional angiography. With one powerful tool you have all the data at your fingertips to improve performance and enable standardized care.

Another very important topic for radiology departments is to keep provided radiation doses as low as reasonably achievable (ALARA). With teamplay, you can monitor dose levels and identify and analyze outliers. This allows you to provide the best quality of care to your patients, and also ensures compliance with national dose regulations.

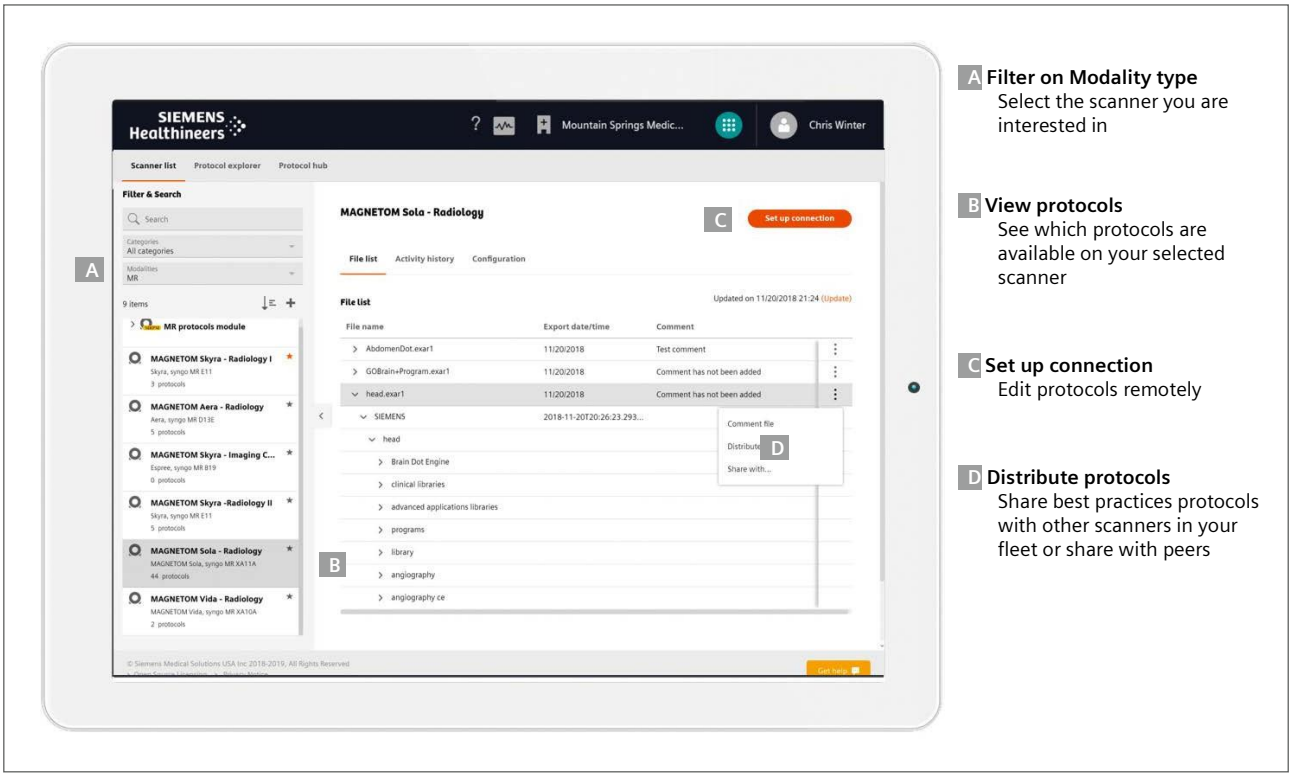

4 View your protocols, edit them remotely, and distribute your best-practice protocol throughout your fleet.

"We went from hours down to minutes to get the same protocols out to the fleet."[7]

Robert Day
Chief Operating Officer,
Zwanger-Pesiri Radiology, New York, USA

Zwanger-Pesiri Radiology Snapshot
For over 60 years, Zwanger-Pesiri Radiology has focused on patient-centered care, research, and education. Led by Steven L. Mendelsohn, M.D., the team of 1,100 professionals with over 60 radiologists, 45 nurses, 300 receptionists, 75 MRI technologists, 15 nuclear technologists, 150 X-ray and CT technologists, 110 schedulers, 80 billers, and 30 IT staff members is dedicated to providing state-of-the-art radiology services. The radiologists work closely with referring physicians to ensure optimal outcomes for patients. To support them in their clinical work, they use high-end imaging equipment including one Siemens Biograph mMR PET-MRI, 25 3T Siemens MRIs (22 MAGNETOM Skyra, 1 MAGNETOM Vida, and 2 MAGNETOM Verio), nine 1.5T Siemens MRIs (6 MAGNETOM Aera, 2 MAGNETOM Espree, 1 MAGNETOM Amira), five Siemens PET/CTs, and a myriad of other units from 3D mammography, to open-sided MRIs as well as countless ultrasound, X-ray, DEXA and ABUS units.

Summary

Healthcare professionals, hospitals, and institutions of higher learning come together in teamplay's rich digital network to access the metrics from their own imaging.

Streamlining your clinical operations with teamplay enables an increase in productivity, while also reducing wait times and giving higher-quality care. This means you can provide more time and attention to your patients, and improve patient satisfaction – an increasingly relevant factor in the reimbursement of healthcare services.

For more information and to try teamplay yourself, visit: www.siemens-healthineers.com/teamplay and select the 'Try teamplay!' button in the upper-right corner.

Contact

Annelinde Veen
Siemens Healthineers
Global Marketing Manager teamplay – performance management solutions
annelinde.veen@siemens.healthineers.com

Glen Roberts
Siemens Healthineers
Global Segment Manager MRI in Therapy and teamplay for MRI
glen.roberts@siemens-healthineers.com

*MAGNETOM Espree is Not Licensed for Sale in Canada.

An Attempt to Reconstruct the History of Gradient-System Technology at Siemens

Franz Schmitt, Ph.D.; Stefan Nowak; Eva Eberlein

Siemens Healthineers, Erlangen, Germany

In 1983, the first Siemens MRI system bearing the MAGNETOM name was installed at the Mallinckrodt Institute of Radiology, in St. Louis, Missouri, USA. Ever since those early days, the name MAGNETOM has been associated with technological innovation and advances, such as the first wide bore 70-cm MRI system, new coil concepts like Tim and Tim4G ("from local to total") and, most recently, with the innovations of the BioMatrix platform. This allows the operator to adapt scanning to patient individuality via special sensors and interfaces and, thanks to the most modern acceleration techniques, also makes MRI faster and more patient friendly, for example with free-breathing examinations.

This is the second part in a series of articles that take a retrospective view to see how we got to MRI of today.

Introduction

The development of clinical MRI was a journey into engineering terra incognita. Although the basic components were known through building MRI prototypes in the early 1980s [1], driving this technology to perfection demanded innovations aplenty. Entirely new technological paths had to be navigated to perfect magnets, gradients, and RF excitation and reception.

This article explores how Siemens learned to make good gradients. It charts the amazing technological advances from 1983, when Siemens Medizintechnik, as it was called then, began to develop their first MRI product, the MAGNETOM; until today, when Siemens Healthineers provide MAGNETOM Prisma, MAGNETOM Terra, and MAGNETOM Connectom[1] to the clinical and research community.

To get the story straight, we have read old memos and lab books, and consulted colleagues from the early days of MR at Siemens. Technological progress comes through the ingenuity of many people, so we also tell the personal stories that reveal why one and not another path was taken.

Gradient performance over the years

Since the introduction of MRI as a commercially available diagnostic tool in 1983, dramatic improvements have been achieved in all features defining image quality, such as resolution, signal-to-noise ratio (SNR), and speed. Initially, spin echo (SE) images with 128 x 128 pixels per slice were acquired in several minutes.

Nowadays, the standard matrix size for musculoskeletal and neuro studies using TSE-based techniques is 512 x 512 with similar imaging times, but covering the entire volume of interest. Echo-planar imaging (EPI) [2] techniques has made it possible to acquire 128 x 128 images in less than 100 ms. Most recently, Simultaneous Multi-Slice (e.g., SMS-EPI for BOLD fMRI) allows the acquisition of an entire volume of 100 slices with resolution of (1.2 mm)^3 at a repetition time (TR) of 1.3 seconds. That is CT-like speed [3, 4]. Here, high-speed gradients and novel RF excitation and reception techniques are combined, allowing resolution and throughput only dreamed of a few years ago.

At the beginning of clinical MRI, maximum achievable gradients G_{max} were typically in the range of 1 to 2 mT/m amplitude, with rise times of 1 to 2 ms. In terms of slew rate (SR), in units of T/m/s, that is on the order of SR 1. Over almost four decades, amplitudes and slew rates have increased by orders of magnitude. Present-day technology gives gradient pulses up to 80 mT/m for whole-body applications, with SR 200 T/m/s. This is the physiological limit for peripheral nerve stimulation (PNS) in whole-body applications, but not a technical limit. Higher SR is possible through higher voltages in principle, although it would present other technical challenges such as high voltage resilience of the entire gradient system. More on this later.

By reducing the linearity volume of a gradient coil, faster switching at higher amplitudes is possible. This has been introduced with the MAGNETOM Sonata [5] and with the SC72 gradient coil (70 mT/m at SR 200 T/m/s)

[1] *MAGNETOM Connectom is ongoing research. All data shown are acquired using a non-commercial system under institutional review board permission. Siemens does not intend to commercialize the system.*
**MAGNETOM Sonata is Not Licensed for Sale in Canada.*

in our 7T whole-body system [6]. This development has been pushed furthest for the Human Connectome project [7–9], with two gradient systems: the Connectom-S, a redesign of the SC72 for the 3T MAGNETOM Skyra magnet performing with 100 mT/m at SR 200 T/m/s; and the Connectom-A, also for the MAGNETOM Skyra magnet, which has a peak performance of 300 mT/m at SR 200 T/m/s [10]. Both systems sacrificed the patient bore, reducing it to 580 mm diameter.

So the performance of gradient systems has improved enormously. The product of maximum gradient strength times the slew rate, GP = G_{max} * SR, reflects the gradient performance GP [11]. The entire evolution of gradient performance is demonstrated in Figure 1 **...**

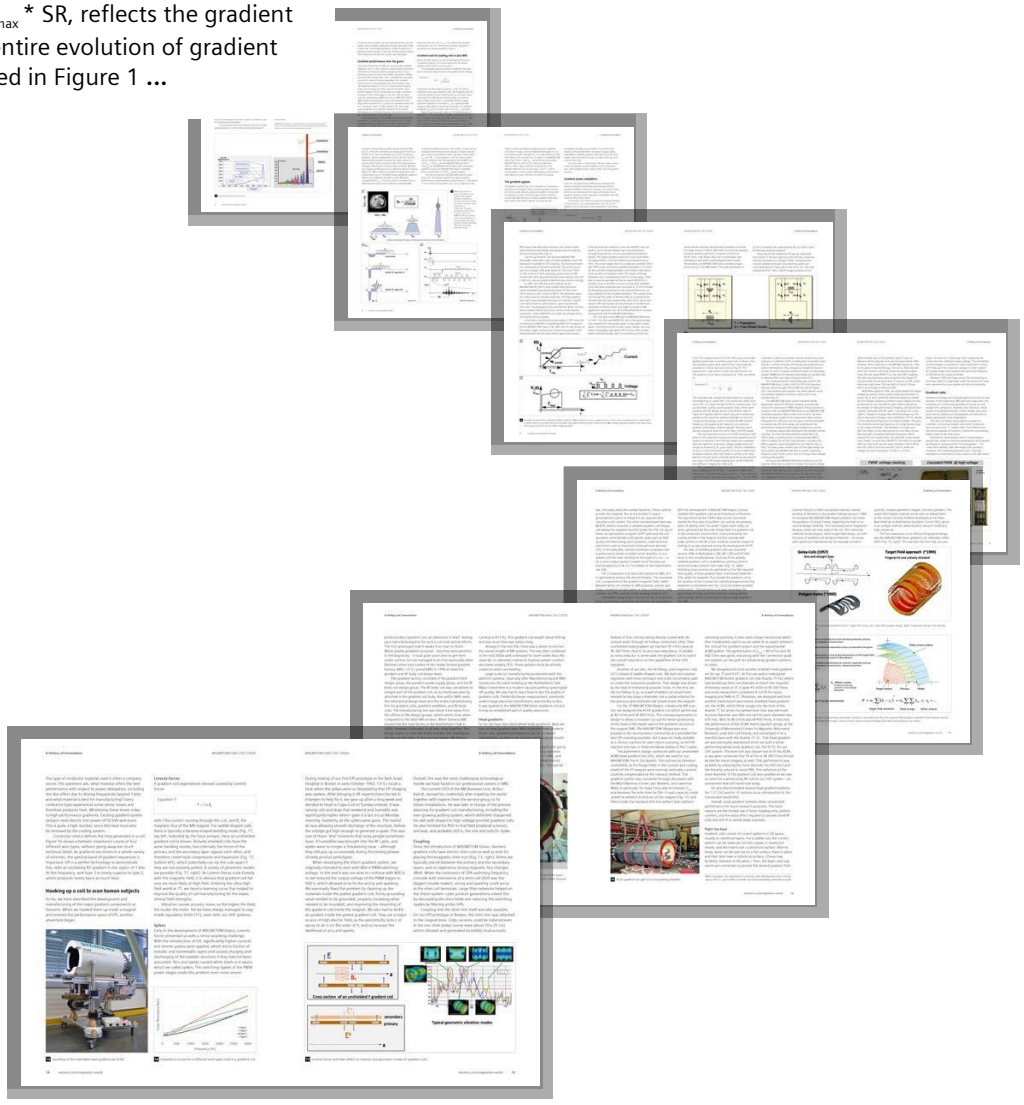

... continue reading this comprehensive article at

siemens.com/magnetom-world

Meet Siemens Healthineers

Siemens Healthineers: Our brand name embodies the pioneering spirit and engineering expertise that is unique in the healthcare industry. The people working for Siemens Healthineers are totally committed to the company they work for, and are passionate about their technology. In this section we introduce you to colleagues from all over the world – people who put their hearts into what they do.

Cordell Fields, Esq.

Cordell started his career in Regulatory Affairs ten years ago, after graduating from Law School. While studying law, he participated in a Health Law Clinic and discovered his passion for the Healthcare industry. He joined Siemens in 2010 as a Regulatory Affairs Specialist, supporting the Health Information Technology portfolio globally. In 2013, he transitioned to the modality side of the business and began supporting the MR business line from a U.S. Regulatory perspective. He has been supporting the MR business line ever since, and has been involved in several major product and technology launches for the U.S. market.

Malvern, PA, USA

How did you first come into contact with MRI?
My first involvement with MRI was from a personal perspective. My father routinely undergoes MRI scans for his Multiple Sclerosis treatment plans, so I was aware of the technology from an early age.

What role do you play in the MR business line?
Regulatory serves many functions for MR systems and technologies at Siemens Healthineers. We help ensure that the systems and technologies are cleared or approved with the appropriate country Regulatory authority; in the U.S. the authority is the Food and Drug Administration (FDA). The systems cannot be sold in the U.S. without FDA clearance or approval, so Regulatory plays a vital role for the business in this regard. We also support Marketing by reviewing and approving the materials to ensure compliance prior to external distribution. If there are issues with initial marketing language, we collaborate with Marketing by offering feedback and guidance on revising the wording as necessary.

What is most fascinating about your job?
I enjoy learning about the new MRI systems, techniques, and sequences, and about their benefit to healthcare. It's particularly fascinating to know I contribute to making these technological advances available in the U.S. marketplace; innovations that will contribute to enhancing the lives of patients and help make the jobs of healthcare professionals easier.

What do you think are the most important developments in MRI and in healthcare?
I believe some of the most important developments in MRI will be those geared toward involvement (from a workflow perspective) in detecting prostate cancer, and also MRI technologies to assist physicians in reviewing brain scans linked to Multiple Sclerosis and Alzheimer's disease.

If you could do anything you wanted for a month, what would it be?
Outside of work I enjoy spending time with my family, reading, watching and playing sports, and working out.

The entire editorial staff at Medical University of Vienna and at Siemens Healthineers extends their appreciation to all the radiologists, technologists, physicists, experts, and scholars who donate their time and energy – without payment – in order to share their expertise with the readers of MAGNETOM Flash.

MAGNETOM Flash – Imprint

Publisher:
Siemens Healthcare GmbH
Magnetic Resonance,
Karl-Schall-Str. 6, D-91052 Erlangen, Germany

Editor-in-chief:
Antje Hellwich
(antje.hellwich@siemens-healthineers.com)

Guest editor:
Univ. Prof. Dr. med Siegfried Trattnig,
Full Professor for Radiology with
Special Focus on High Field MR,
High Field MR Center,
Department of Biomedical Imaging and
Image Guided Therapy,
Medical University of Vienna, Austria

Editorial Board:
Rebecca Ramb, Ph.D.; Sunil Kumar S. L., M.D.;
Wellesley Were; Jane Kilkenny; Nadine Leclair, M.D.

Review Board:
André Fischer, Ph.D.; Daniel Fischer;
Berthold Kiefer, Ph.D.; Heiko Meyer, Ph.D.;
Gregor Thörmer, Ph.D.

Copy Editing:
Sheila Regan, Jen Metcalf, UNIWORKS,
www.uni-works.org
(with special thanks to Kylie Martin)

Layout:
Agentur Baumgärtner,
Friedrichstr. 4, D-90762 Fürth, Germany

Production:
Norbert Moser,
Siemens Healthcare GmbH

Printer:
G. Peschke Druckerei GmbH,
Taxetstr. 4, D-85599 Parsdorf b. Munich, Germany

We welcome your questions and comments about the editorial content of MAGNETOM Flash. Please contact us at magnetomworld.team@siemens-healthineers.com

Manuscripts as well as suggestions, proposals and information are always welcome; they are carefully examined and submitted to the editorial board for attention. MAGNETOM Flash is not responsible for loss, damage, or any other injury to unsolicited manuscripts or other materials. We reserve the right to edit for clarity, accuracy, and space. Include your name, address, and phone number and send to the editors, address above.

MAGNETOM Flash is also available online:

www.siemens.com/magnetom-world

Not for distribution in the US

On account of certain regional limitations of sales rights and service availability, we cannot guarantee that all products included in this brochure are available through the Siemens sales organization worldwide. Availability and packaging may vary by country and is subject to change without prior notice. Some/All of the features and products described herein may not be available in the United States.

The information in this document contains general technical descriptions of specifications and options as well as standard and optional features which do not always have to be present in individual cases, and which may not be commercially available in all countries.

Due to regulatory reasons their future availability cannot be guaranteed. Please contact your local Siemens organization for further details.

Siemens reserves the right to modify the design, packaging, specifications, and options described herein without prior notice. Please contact your local Siemens sales representative for the most current information.

Some of the Medical Devices Listed in the Magazine May Not Yet be Licensed for Sale in Canada, in Accordance with Canadian Law.

Note: Any technical data contained in this document may vary within defined tolerances. Original images always lose a certain amount of detail when reproduced.

Siemens Healthineers Headquarters
Siemens Healthcare GmbH
Henkestr. 127
91052 Erlangen, Germany
Phone: +49 9131 84-0
siemens-healthineers.com

Published by Siemens Healthcare GmbH · Order No. A91MR-1000-144C-7600 · Printed in Germany · 8705 0420 ·